



EUROPEAN
COMMISSION

Community Research

TIMODAZ

**Thermal Impact on the Damaged Zone
Around a Radioactive Waste Disposal in Clay Host Rocks**

(Contract Number: FI6W-CT-2007-036449)

Deliverable D13 – Annex 6

**Large scale excavation and heater in-situ experiment:
the PRACLAY experiment modelling.**

Editors: **Robert Charlier**

Co-authors: **Robert Charlier, Frédéric Collin, Arnaud Dizier, Suzanne Fauriel, Antonio Gens, Chen Guangjing, Lyesse Laloui, Thibaut Meynet, Frédéric Pascon, Jean-Pol Radu, Philippe Van Marcke, Jean Vaunat**

Laboratories: **CIMNE, ESV EURIDICE GIE, EPFL, ULg**

Reporting period: **01/10/2006 - 30/09/2010**

Date of issue of this report: **30/09/2010**

Start date of the project: **01/10/2006**

Duration: **48** months

Project co-funded by the European Commission under the Euratom Research and Training Programme on Nuclear Energy within the Sixth Framework Programme (2002-2006)		
Dissemination Level		
PU	Public	
RE	Restricted to a group specified by the partners of the TIMODAZ project	RE
CO	Confidential, only for partners of the TIMODAZ project	

TIMODAZ

Deliverable **D13 – Annex 5**

Dissemination level: **RE**

Date of issue of this report: **30/09/2010**

1/129



1	<i>Executive summary</i>	3
1.1	Experiment description	3
1.2	Experiment idealisation	5
1.3	Results: Comparison of 2D and 3D models	8
1.4	Conclusions	17
2	<i>Introduction: the PRACLAY experiment</i>	19
2.1	PRACLAY gallery excavation	21
2.2	PRACLAY Seal Test	23
2.3	PRACLAY Heater Test	25
3	<i>Exercise, idealisation proposed</i>	27
3.1	General framework of the benchmark	27
3.2	Geometry of PRACLAY gallery	28
3.3	2D plane strain modelling	30
3.4	2D axisymmetric modelling	36
3.5	3D modelling	45
4	<i>General form of numerical results</i>	46
4.1	2D plane strain modelling	46
4.2	2D axisymmetric modelling	61
4.3	3D modelling	84
5	<i>Comparison of 2D and 3D models</i>	94
6	<i>Specific aspects highlighted by different labs</i>	99
6.1	EPFL	99
6.2	ULg	104
6.3	Euridice	111
6.4	CIMNE	119
7	<i>References</i>	129



1 Executive summary

1.1 Experiment description

Praclay is an experiment in progress within the Boom underground laboratory at a depth of some 200m, in a poorly indurated Boom Clay layer (Figure 1). The Praclay project was initiated in the middle of the 90'ties and intends to achieve several experiments, including the drilling of the connecting gallery, some on surface tests, and the Praclay gallery project, which is concerned in the Timodaz project.

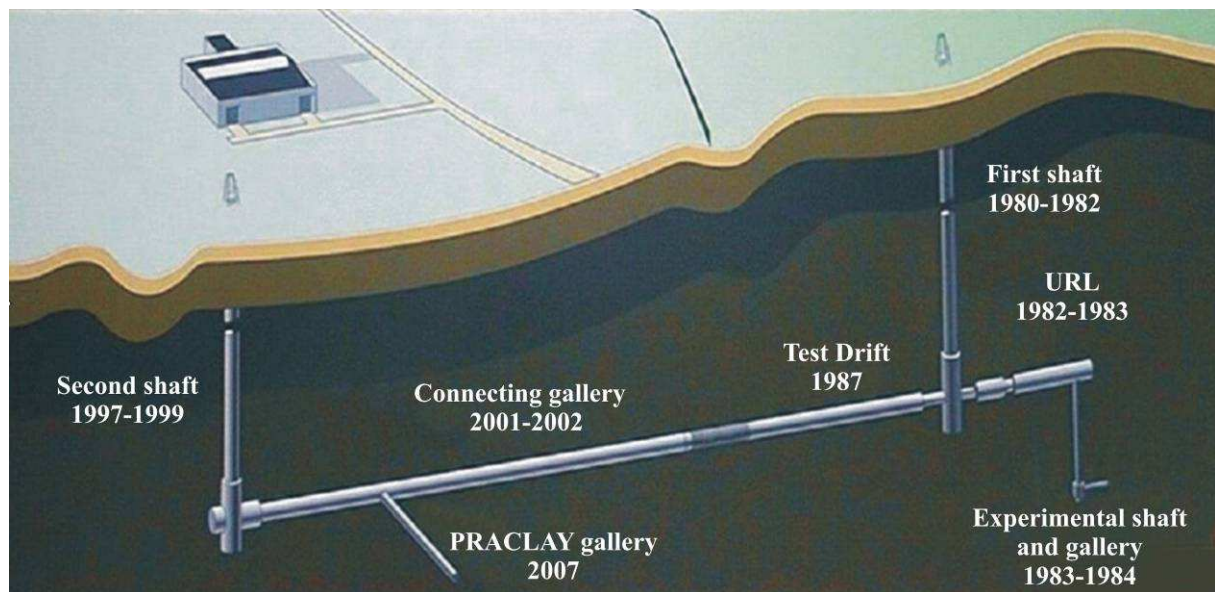


Figure 1: History and layout of the underground research facility HADES

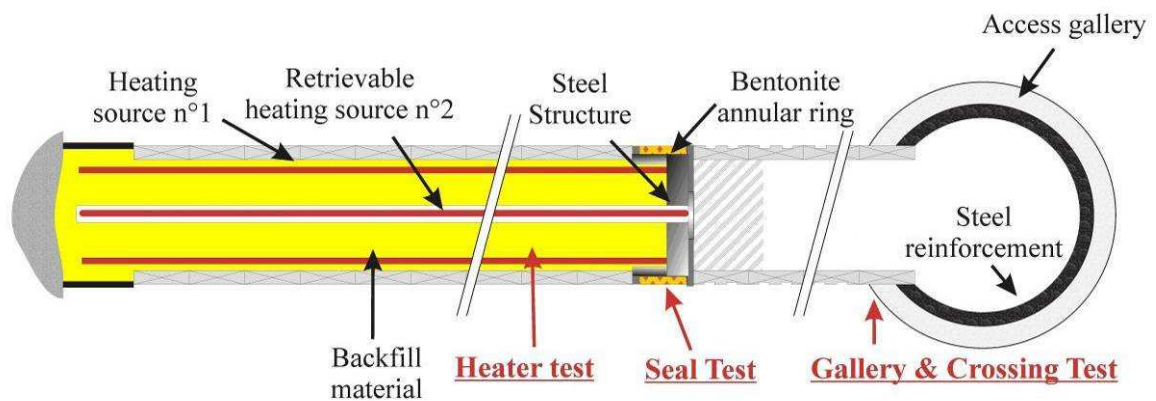


Figure 2: The PRACLAY in-situ experiment comprises three tests: the "Gallery&Crossing Test", the "Seal Test" and the "Heater Test"

The large In-Situ Experiment (Figure 2) comprises three tests:

1. the Gallery and Crossing Test further examining and demonstrating the construction of an underground repository by industrial method and examining the feasibility to construct a crossing between galleries;

2. the Seal Test examining the feasibility of hydraulically sealing the heated part of the PRACLAY gallery from the rest of the underground;
3. the Heater Test studying the response of the Boom Clay to a thermal impact.

The same excavation technique and type of lining as applied for the construction of the Connecting Gallery were selected for the PRACLAY gallery: excavating by an open-face tunnelling machine and installing a concrete wedge block lining. The design of the lining had to take into account a geotechnical loading due to the pressure exerted by the clay massif on the lining and a thermal loading due to the increased stresses in and on the lining during the Heater Test. The diameter of the PRACLAY gallery is set at 2.50 m. A reinforcement ring is placed in the Connecting Gallery prior to the excavation works to assure the stability of the lining of the Connecting Gallery.

The underground works started on 01.10.2007 with the cutting of the lining of the Connecting Gallery, and the construction of the PRACLAY gallery was successfully completed in 2007. A hydraulic seal was successfully installed in the PRACLAY gallery in 2010. The installation is part of the PRACLAY In-Situ Experiment and its main purpose is the creation of an undrained hydraulic boundary at the intersection between the heated part of the PRACLAY gallery and the non-heated part. Such an undrained boundary is required to achieve the most penalizing conditions that are reasonably achievable during the Heater Test.

The bentonite placed in an annular ring against the Boom Clay has to exert a swelling pressure of ca. 5 MPa against the Boom Clay to locally reduce the hydraulic conductivity of the Boom Clay around the seal and in that way create an undrained hydraulic boundary. It was decided to use MX80 bentonite compacted into bentonite blocks.

The last phase in the installation of the PRACLAY In-Situ Experiment will be accomplished in 2010 by the installation of the heating system and backfill material. The requirement for the heating system is that it has to impose a constant temperature of 80°C in the clay at the gallery extrados. The heater consists of a primary heater close to the gallery intrados and a secondary heater inside a central tube (Figure 2). Both heaters consist of electrical heaters.

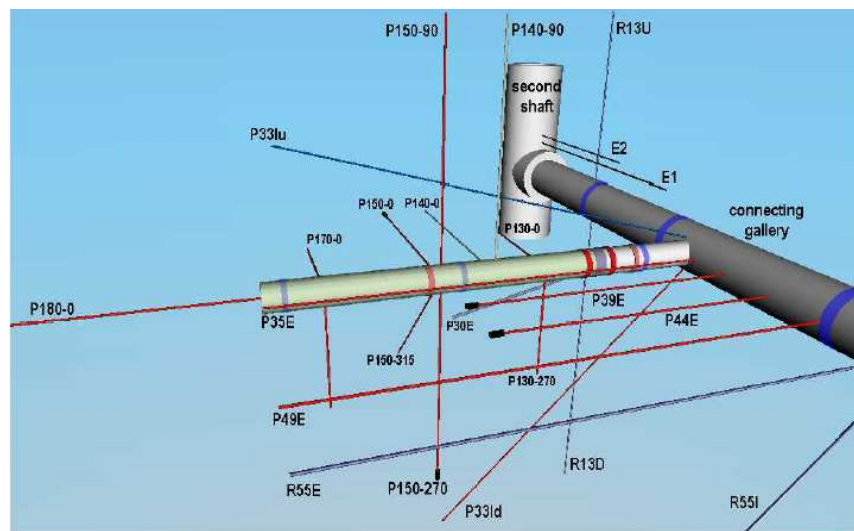


Figure 3: Lay-out of the instrumented boreholes around the PRACLAY gallery

The Figure 28 below gives an overview of the instrumentation program including temperature, pore water, total stresses and displacements measurements as well as the follow-up of the chemical evolution in the Boom Clay around the test.

1.2 Experiment idealisation

The main idea of the reported simulations is to reproduce the excavation of the PRACLAY gallery and the heating phase of the PRACLAY experiment with a coupled thermo-hydro-mechanical model. This modelling may be considered as a plane strain two-dimensional problem (this simple geometry allows taking into account anisotropy in 2D), a two-dimensional problem in axisymmetric condition or a three dimensional problem. This last geometry allows taking into account the effect of the anisotropy of the clay for all the processes. The Figure 4 illustrates the 2D plane strain model. The inner radius is equal to 0.95 m, the thickness of the liner is equal to 30 cm as seen in Figure 4.

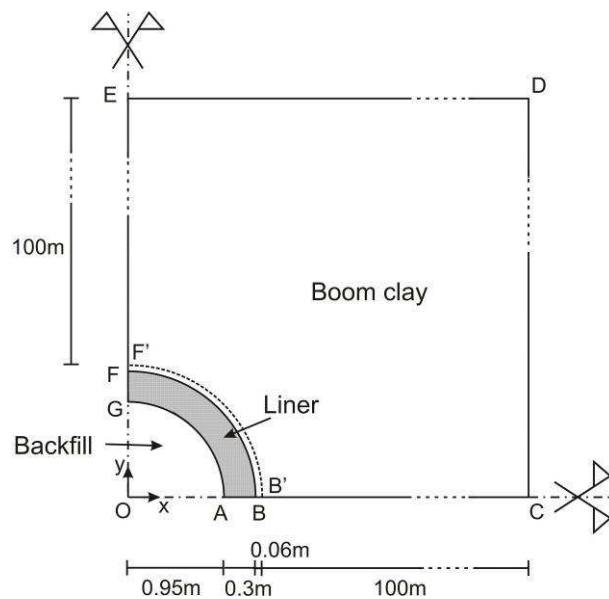
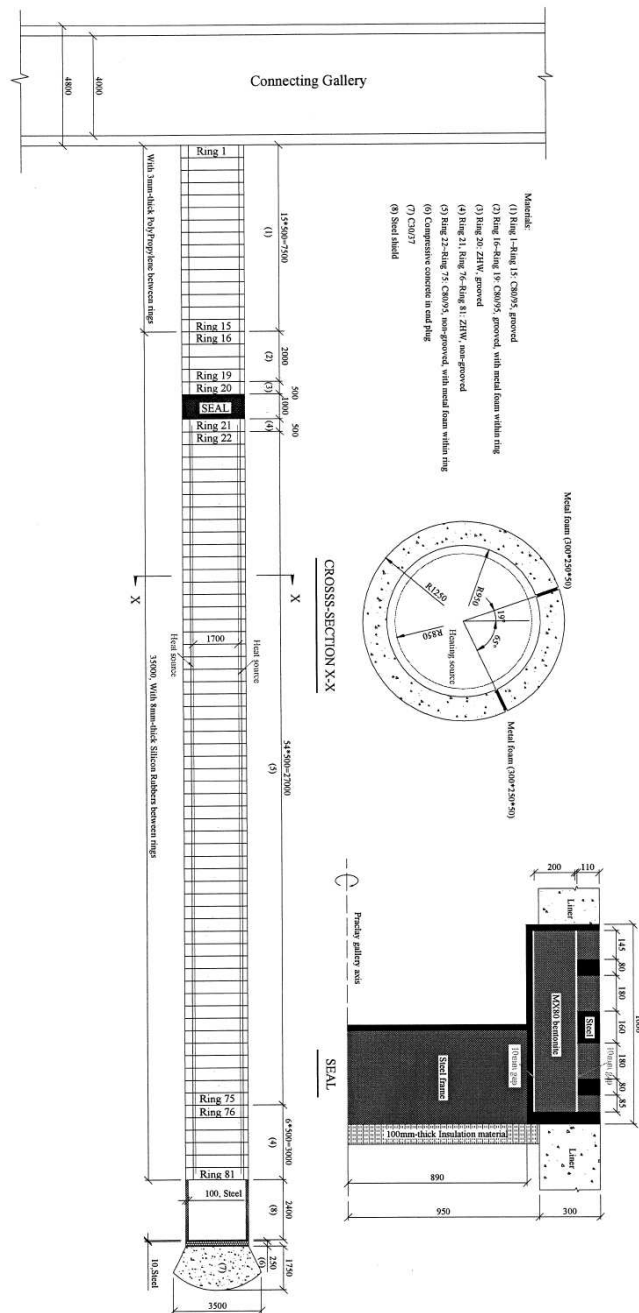


Figure 4: Schematic representation of the 2D plane strain modelling

The geometry of the modelling for the bi-dimensional axisymmetric conditions is based on the geometry of the PRACLAY gallery, provided in Figure 5. The geometry of the 3D modelling is inspired of the plane strain and axisymmetric cases (Figure 6).



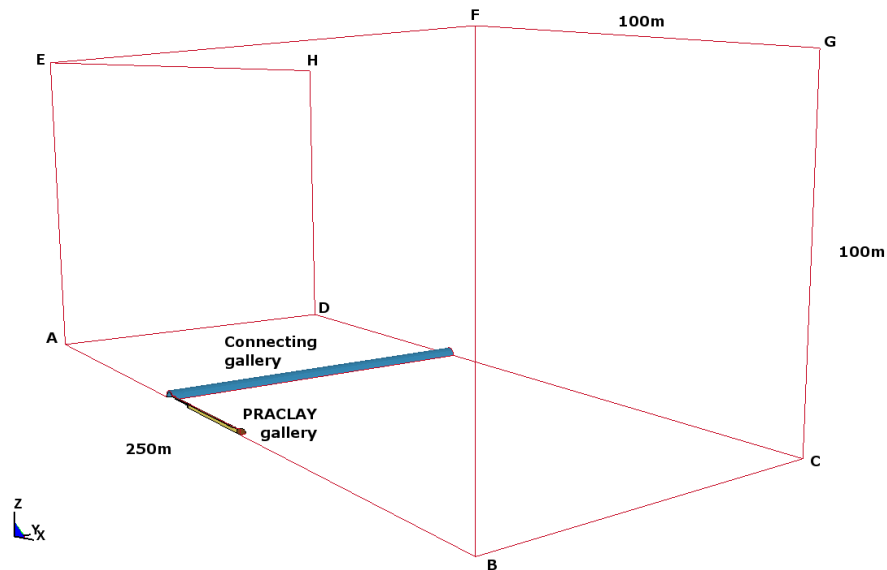


Figure 6: 3D model extent

Seven different materials are involved in the construction of the gallery. Most of the liner rings are made of concrete elements, but some steel components are also used for the seal and, at the end of the gallery, for the lost shield and the stiffened steel end.

The clay is initially considered as homogeneous and isotropic. It is supposed to be fully saturated. Initial state of stresses is anisotropic, unless for the axisymmetric modelling.

In the concrete liner, the initial conditions assume that the concrete is saturated at a temperature corresponding to the one of the host formation. The liner is composed of concrete C80/95. Due to joints, its permeability is taken 10 times greater than the clay permeability. The friction coefficient between the ring and the host clay depends on the external geometry of the concrete liner: some of them are grooved. The liner is supposed to be put after a convergence of 0.06 m.

The backfill material, constituted of sand with a 40% porosity and saturated in water, was taken into account in the 2D axisymmetric and 3D models, but not the 2D plane strain model for sake of simplicity.

The seal element is modelled with a steel ring (with the same thickness as the concrete one), without representing explicitly the bentonite. However, the action of the bentonite is modelled by imposing a total stress history corresponding to the swelling pressure and considering impervious condition at the steel extrados.

The modelling first consists in the excavation of the gallery and, in a second step, a thermal loading is applied at the extrados of the liner:

- Phase 1: Duration: 20 days: Excavation of the gallery; Temperature fixed at initial value on the whole domain.
- Phase 2: Duration: 2.5 years: Waiting phase: pore pressure fixed at 100 kPa on the liner intrados; Temperature fixed at initial value on the whole domain.
- Phase 3: Duration: 1 year: Installation of the seal (total stress increase, impervious boundary); Waiting phase: pore pressure fixed at 100 kPa on the liner intrados; Temperature fixed at initial value on the whole domain.

- Phase 4: Duration: 6 months. Heater phase: temperature linearly increasing from initial value to 85°C at the intrados of the liner; Water undrained conditions at the liner intrados in the part of the gallery after the seal. The hydraulic conditions remain the same as the ones in the previous phases, in the part of the gallery between the connecting gallery and the seal.
- Phase 5: Duration: 10 years. Stabilised heater phase: temperature fixed to 85°C at the intrados of the liner; Water undrained conditions at the liner intrados in the part of the gallery after the seal. The hydraulic conditions remain the same as the ones in the previous phases, in the part of the gallery between the connecting gallery and the seal.

The actual heater system is constituted of a pipes network with heat water flow inside; it is located 10 cm inside the intrados of the liner and imposes a temperature, as constant as possible, of about 80°C at the extrados gallery wall. This complex system is idealised simply by imposing an increase of the temperature directly at the intrados of the liner.

1.3 Results: Comparison of 2D and 3D models

Results were proposed by ULg, Euridice, CIMNE and NRG for 2D plane strain simulations, by EPFL, ULg, Euridice and CIMNE for axisymmetric simulations and by ULg and CIMNE for 3D simulations.

1.3.1 Pore water pressure

The comparison of the p_w profiles obtained using the 3 different approaches leads to two main conclusions summarized on the following figures:

- At the end of the gallery excavation (Figure 7), the anisotropy of the initial stresses implies a higher p_w along the horizontal profile. Both 2D plane strain and 3D models include this anisotropy and they provide very similar results: the same difference between horizontal and vertical p_w profiles and the same overpressure (peak) along the horizontal profile (the same maximum value as well as the same location). With the 2D axisymmetric model, which does not take into account the anisotropic initial stresses, the p_w profile is in-between.
- At the end of the experiment (Figure 8), the difference between the horizontal and vertical profiles is not so large anymore, as predicted by those models including this anisotropy, i.e. 2D plane strain and 3D models. The main difference is now between the 2D plane strain model that predicts a maximum p_w at the wall (about 2.7 MPa) and both 2D axisymmetric and 3D models that agree on a maximum p_w around 2.5 MPa and located at about 9 to 10 m from the gallery axis.

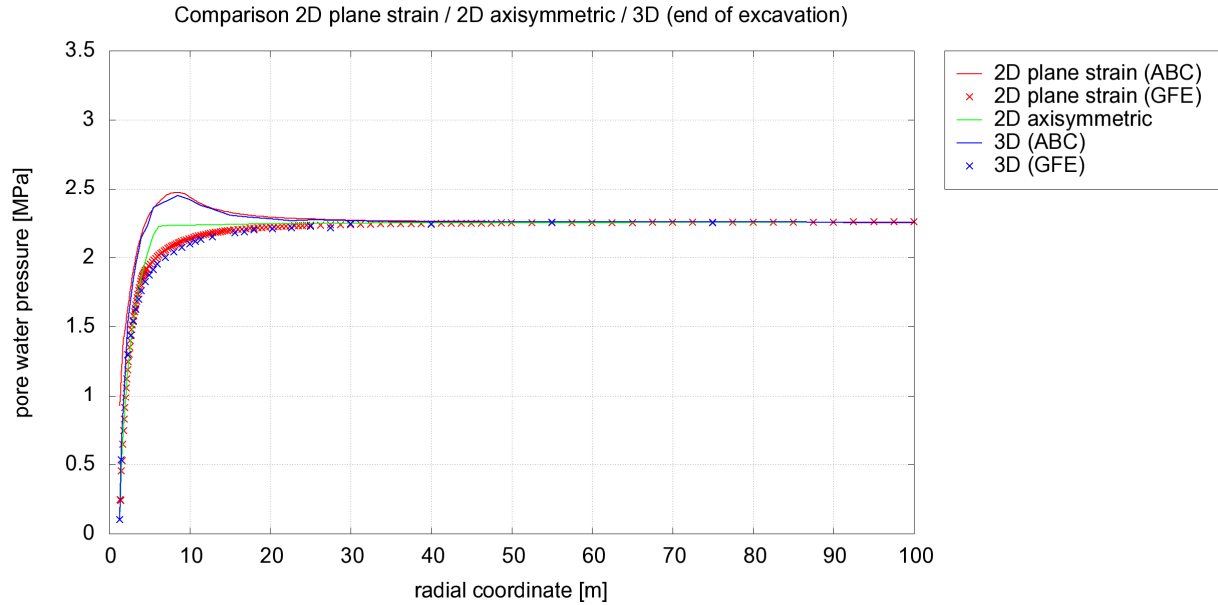


Figure 7: Comparison of the p_w horizontal and vertical profiles at the end of the excavation with the 2D plane strain, 2D axisymmetric and 3D models (using BC2 in all models)

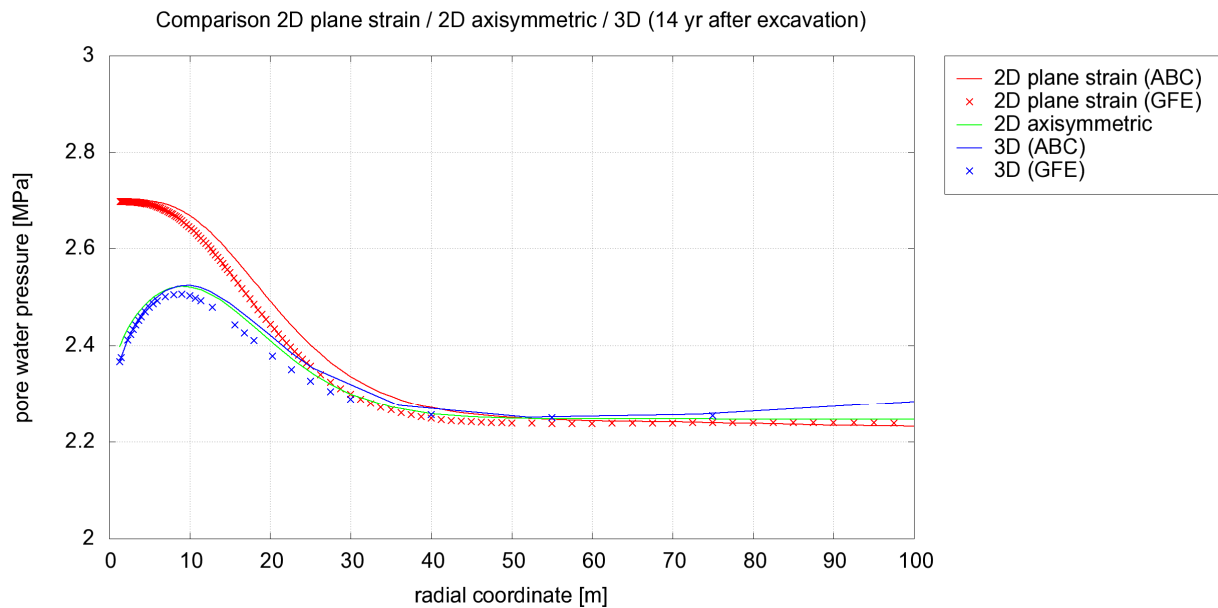


Figure 8: Comparison of the p_w horizontal and vertical profiles at the end of the experiment with the 2D plane strain, 2D axisymmetric and 3D models (using BC2 in all models)

Hence, the 3D model is more complete than 2D models and it should indicate the most realistic results among the three approaches. In the short term results, the 2D plane strain model is in good agreement with the 3D model (since the stress anisotropy could be introduced).

In the long term results, the effect of anisotropy of the initial stresses is not as important as just after excavation. The 2D axisymmetric and 3D models are therefore in good agreement, since the diffusion of p_w along the axial direction is allowed in the 2D axisymmetric model and not in the 2D plane strain one.

Nevertheless, we should keep in mind that no other anisotropy but initial stresses is included in the 3D model. Otherwise, if some other anisotropic properties were taken into account (such as intrinsic permeability or thermal conductivity), we would expect to see a difference between the 2D axisymmetric and the 3D approaches.

1.3.2 Temperature

The temperature profiles in all the models are very close, as illustrated in the Figure 9, and no anisotropy can be observed since thermal properties are isotropic in all models (hence vertical and horizontal profiles are superposed in the figure).

The main difference is observed when comparing the 2D plane strain model with the two other models. Since there is no heat diffusion in the direction of the gallery axis in this model, the temperature is a little bit higher than the temperature predicted by the 2D axisymmetric and 3D model, that are in very good agreement on this. The gap between the different approaches is maximum between 10 and 20 m and it reaches a few degrees (about 2°C).

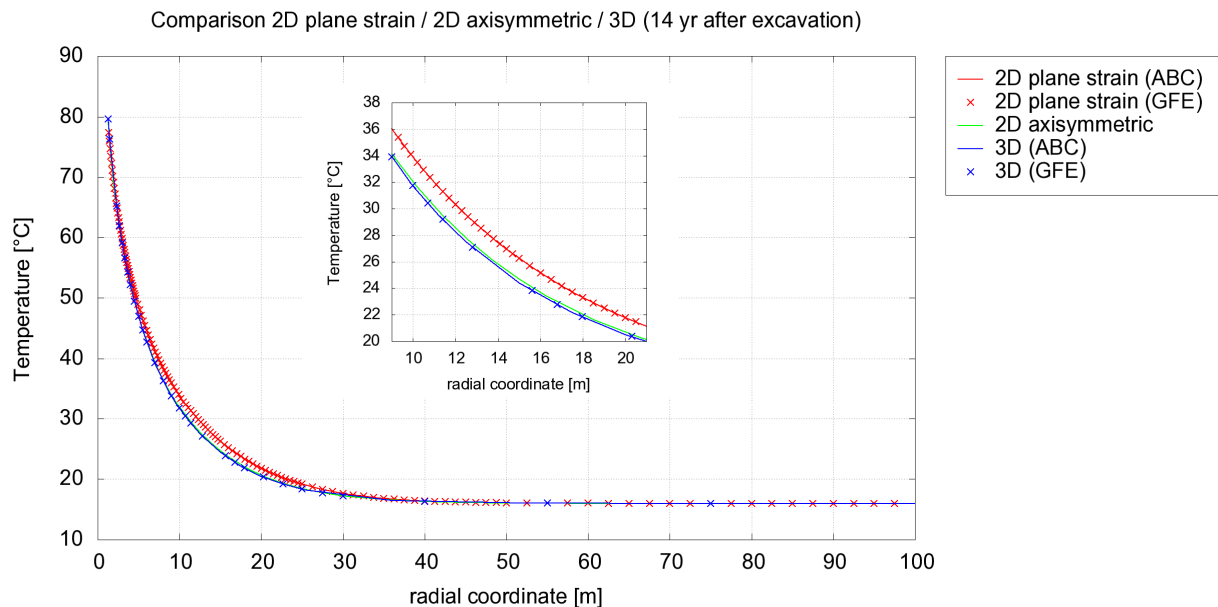


Figure 9: Comparison of the horizontal and vertical temperature profiles at the end of the experiment with the 2D plane strain, 2D axisymmetric and 3D models (using BC2 in all models)

1.3.3 Radial displacement

The comparison of the radial displacement at the end of the excavation using the different models (cf. Figure 10) is very similar to the analysis of the p_w profiles. The 2D plane strain and 3D models give the same different curves along the horizontal and vertical profiles and the 2D axisymmetric model is again in-between. The reason is still a question of anisotropic initial stresses.

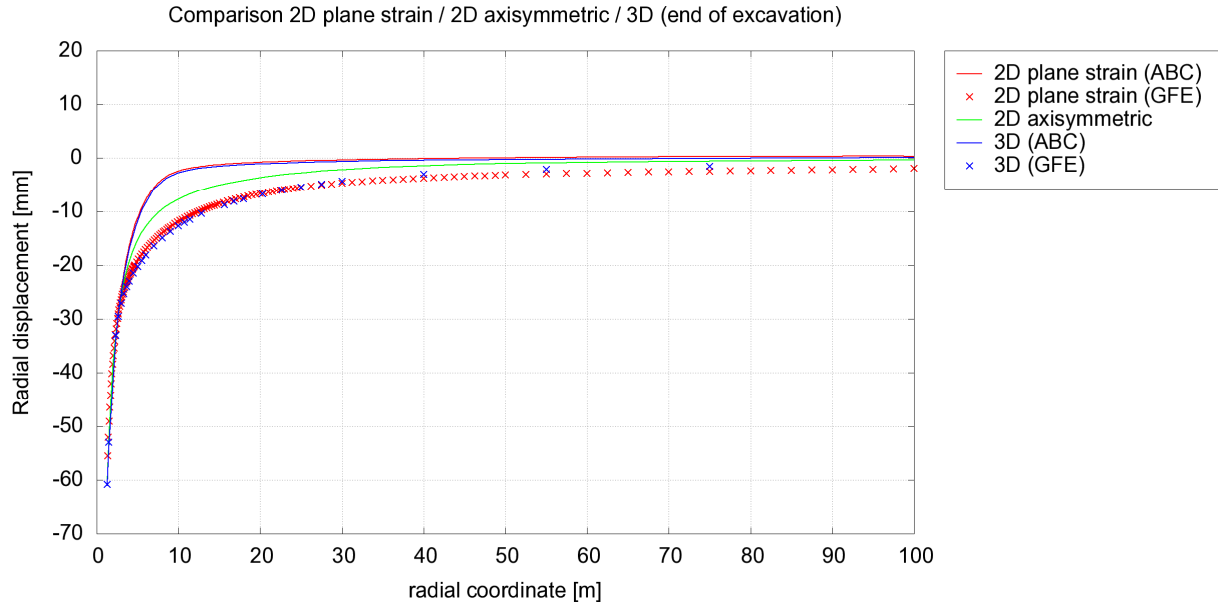


Figure 10: Comparison of the radial displacement along horizontal and vertical profiles at the end of the excavation with the 2D plane strain, 2D axisymmetric and 3D models (using BC2 in all models)

Observing the same profiles at the end of the experiment (Figure 11) is now different from the profiles of p_w 14 years after the excavation of the gallery: the agreement between 2D axisymmetric and 3D models is not as good as in the Figure 8. The reason comes from the fact that the radial displacement is a cumulated value during all the experiment and the history in the 2D axisymmetric and 3D models is not exactly the same, more especially in terms of plasticity as described in the next section. Even though similar pressure levels (and stress levels) can be observed at the end of the experiment in the two approaches (as in the Figure 8), the plastic strain might be very different and so the corresponding displacement profiles might do (Figure 11).

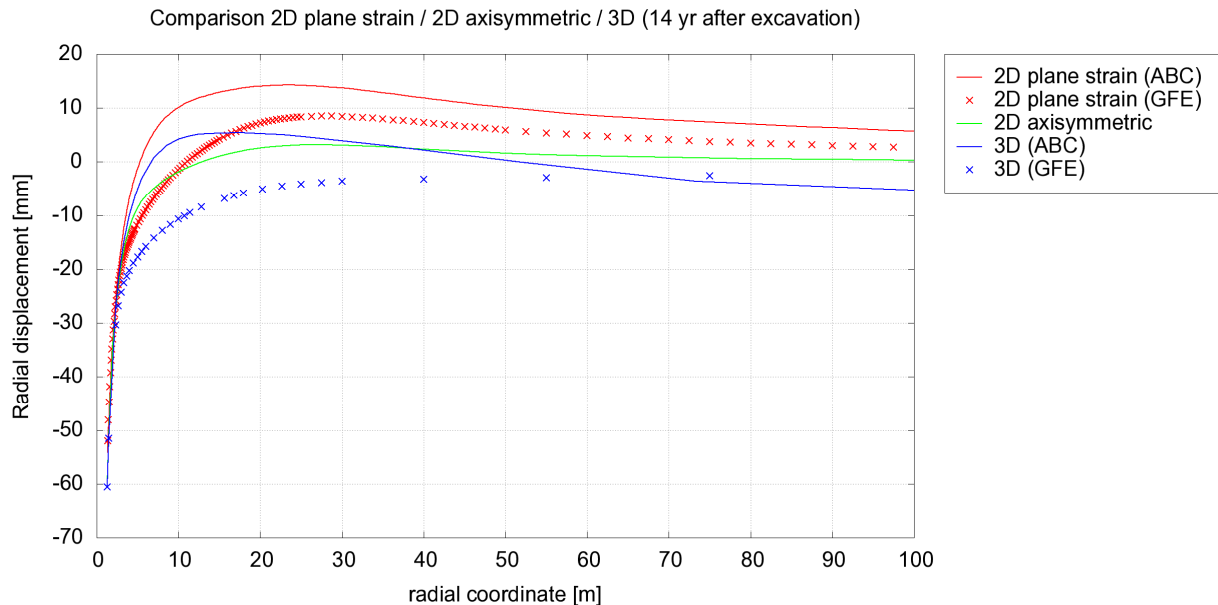


Figure 11: Comparison of the radial displacement along horizontal and vertical profiles at the end of the experiment with the 2D plane strain, 2D axisymmetric and 3D models (using BC2 in all models)

1.3.4 Effective stress path

The main difference between the models comes from the initial stress state. As the initial effective stresses are isotropic in the 2D axisymmetric model, the stress path start from another initial point in the invariants space:

- in the 2D plane strain and 3D models:

$$I_{1,ini} = -5.4 \text{ MPa} \quad \text{and} \quad I_{2,ini} = 0.675 \text{ MPa}$$

- in the 2D axisymmetric model:

$$I_{1,ini} = -6.75 \text{ MPa} \quad \text{and} \quad I_{2,ini} = 0 \text{ MPa}$$

Considering the initial drained friction angle $\phi_{ini} = 5^\circ$, the stress state reaches more quickly the plastic domain in the 2D plane strain and 3D models than in the 2D axisymmetric model. As a consequence, the sensor P42E remains in the elastic domain according to the 2D axisymmetric model, while it enters the plastic domain according the two other models, as shown in the Figure 14.

For all four sensors, the 2D plane strain and the 3D models are in relatively good agreement (cf. Figure 12 to Figure 15), the main drawback of the 3D model being the lack of a complete path during the excavation because of numerical reasons.

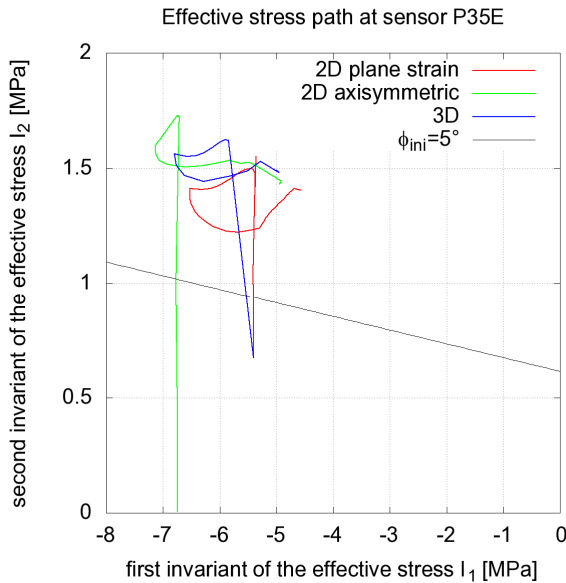


Figure 12: Stress path in the I_1 - I_2 invariants space at sensor P35E

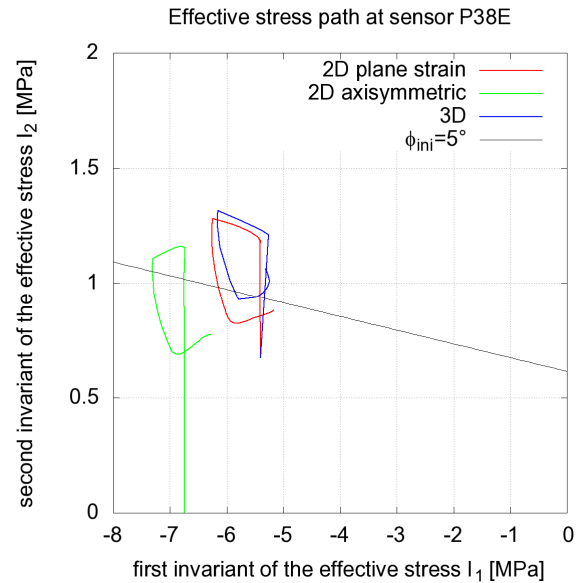


Figure 13: Stress path in the I_1 - I_2 invariants space at sensor P38E

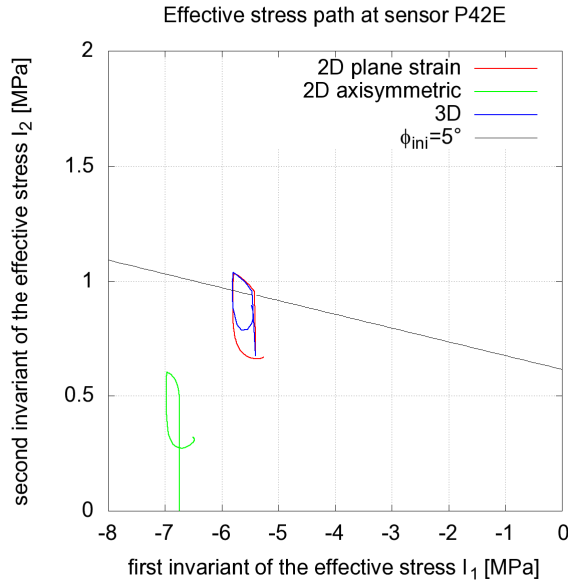


Figure 14: Stress path in the I_1 - I_2 invariants space at sensor P42E

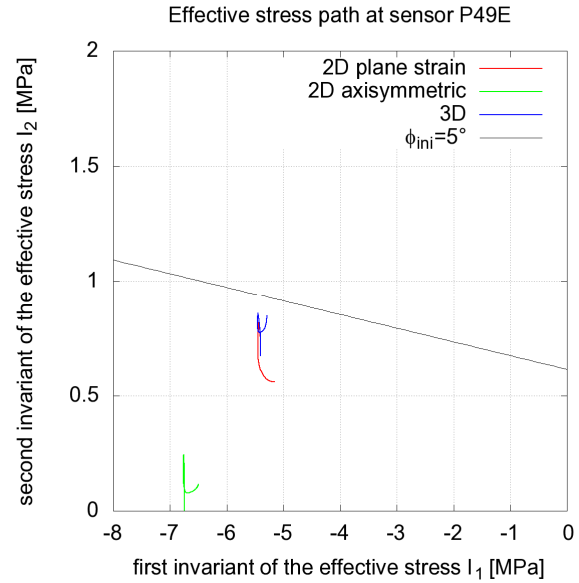


Figure 15: Stress path in the I_1 - I_2 invariants space at sensor P49E

1.3.5 Plastic zone extent

To illustrate the extent of the plastic zone, the figures below represent the contour levels of the Coulomb's friction angle ϕ at the end of the excavation. The initial value is 5° , represented in white in this figure. Due to plastic hardening, ϕ increases up to those colorized values in the scale, i.e. from blue (5° - 6°) to red (up to 16°).

The 2D axisymmetric model predicts a less extended plastic zone, the thickness of which being 2.6 m (cf. Figure 16).

The 2D plane strain and 3D models are in good agreement, predicting a plastic zone extending up to 3 m along the vertical direction and about 3 times deeper in the horizontal direction, up to 9 m - 11 m (cf. Figure 17 in 2D plane strain, and Figure 18 in 3D).

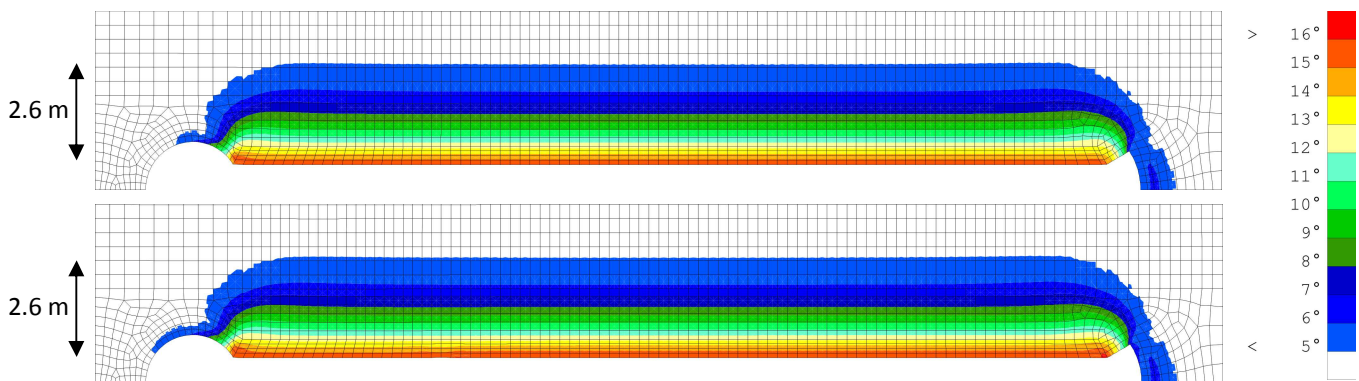


Figure 16: 2D axisymmetric model - Actualized ("hardened") Coulomb's friction angle at the end of the excavation (above) and at the end of the heater experiment (below). Initial value is 5° (in white).

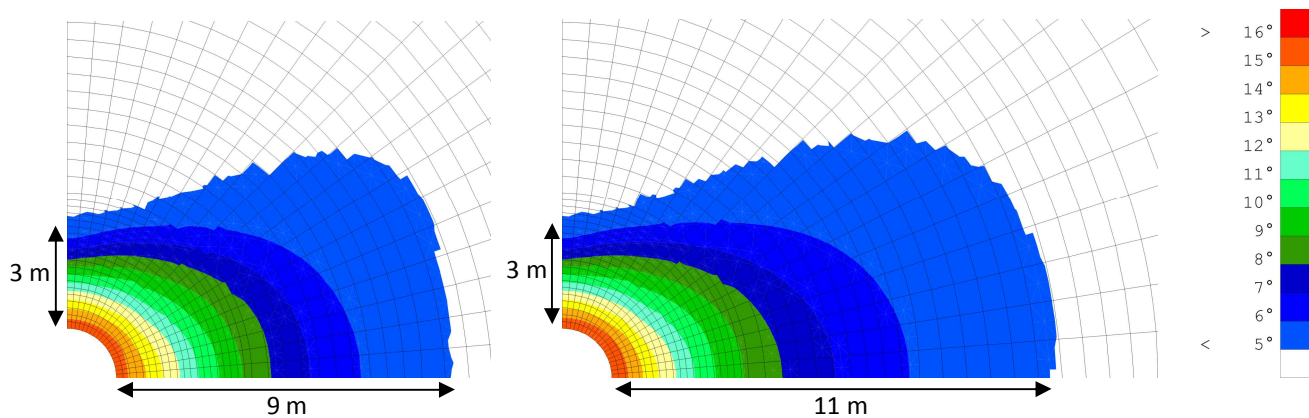


Figure 17: 2D plane strain model - Actualized ("hardened") Coulomb's friction angle at the end of the excavation (left) and at the end of the heater experiment (right). Initial value is 5° (in white).

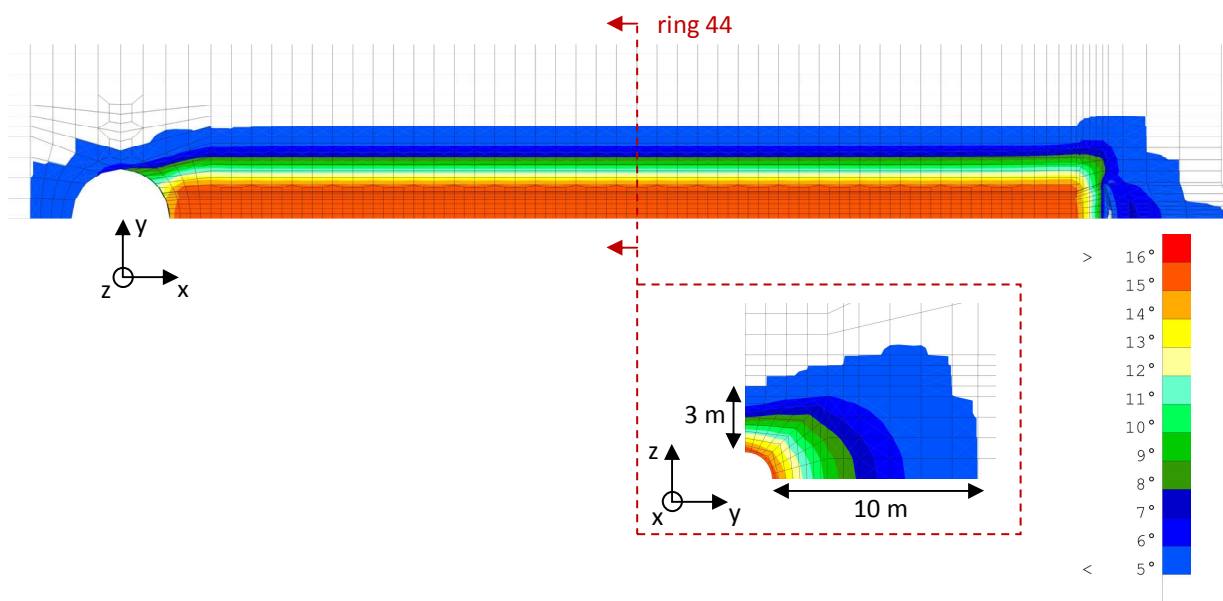


Figure 18: 3D model - Actualized Coulomb's friction angle at the end of the excavation. Initial value is 5° (in white).

1.3.6 Additional simulations

EPFL

EPFL carried out computations to assess the influence of non-linear thermo-elasticity and thermo-plasticity on the THM response of the repository, using the ACMEG-T constitutive law in both 1D axisymmetric and 2D axisymmetric models.

The obtained pore pressures and stress fields differ from those obtained with the other models. The differences are mainly due to the non-linear elasticity and the thermo-plasticity of the ACMEG-T model. An increase in rigidity as well as progressive plasticity induced by heating, causing an increase of the preconsolidation pressure, is considered in ACMEG-T. This causes an increase in excess pore water pressures, and consequently in effective stresses.

ULG

ULg has compared 2D plane strain simulation results based on 3 different thermoplastic laws, Drucker-Prager, TSOIL and ACMEG-T. Pore pressures are only slightly affected by the model of thermo-plasticity. This is probably due to the kind of thermo-plasticity involved by these models, which only affects the cap, i.e. the high isotropic stress states, and not the deviatoric mechanism.

ULg has also modelled in 3D the effect of anisotropy in thermal conductivity and in permeability. The main effect is observed on the pore water profile (Figure 19) where the anisotropic permeability (case 3D_{III}) is different from the others.

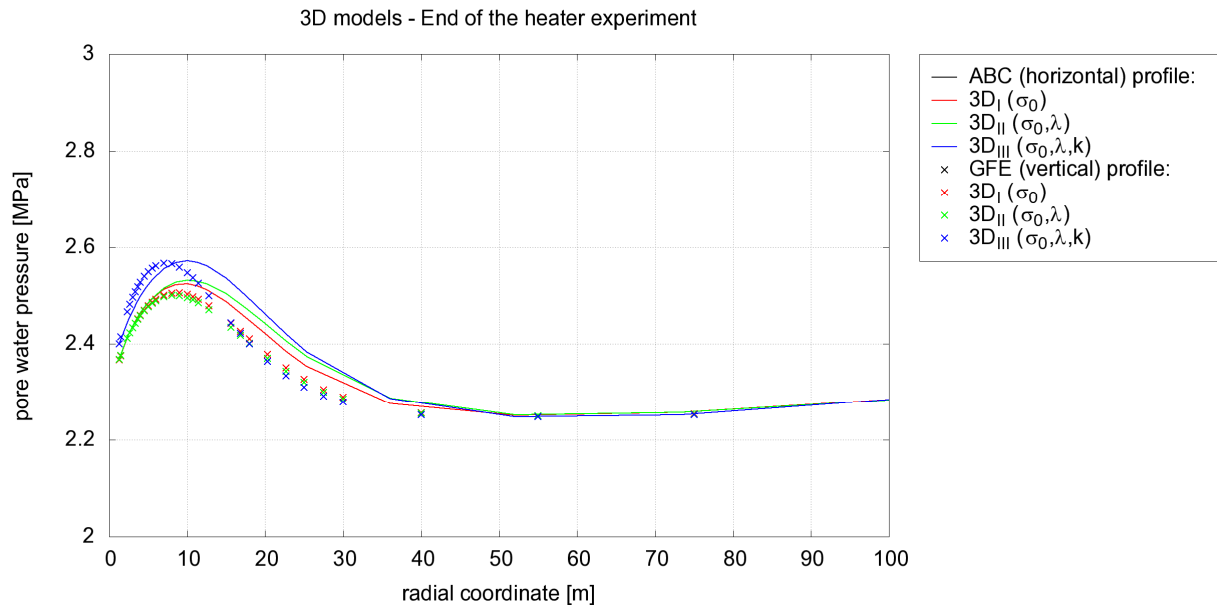


Figure 19: Pore water pressure profiles at the end of the heater experiment.
Effect of the anisotropic parameters.

Euridice

Euridice has tested the effect of the far field boundary conditions: fixed stress vs. fixed displacement, boundary at 100 or 300 m. As an example, the Figure 20 presents the pore water pressure profiles along boundary ABC after heating for 10.5 years. It appears that case 2 should be avoided. However in the actual case of Praclay boundary conditions in vertical direction are nearer then modelled.

Euridice has also analysed the effect of stress anisotropy, and has showed that it explains a number of features observed in situ, such as pore pressure evolution and gallery convergence, which are different on horizontal and vertical axis.

Eventually Euridice has shown that the large conductivity of the backfill material may significantly modify the longitudinal distribution of pore pressures in the near field.

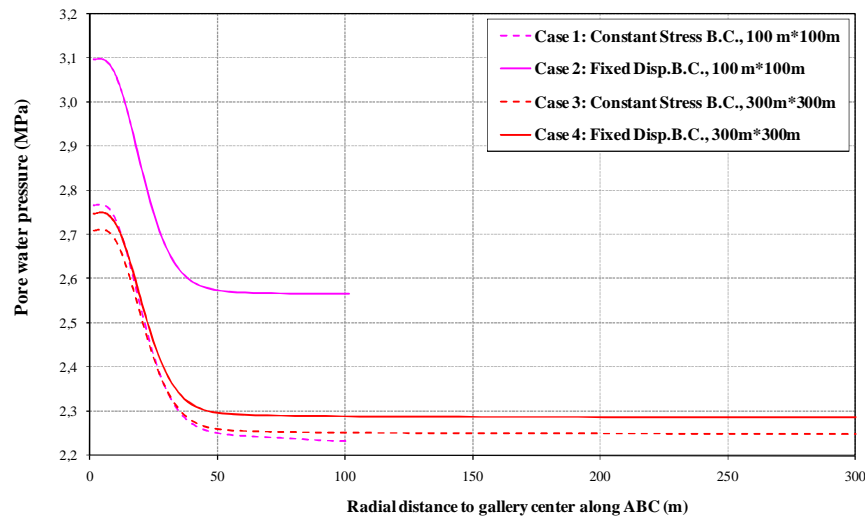


Figure 20: Pore water pressure profiles along boundary ABC for the four cases after heating for 10.5 years

CIMNE

CIMNE has analysed the initial state around PRACLAY experiment. It is known that the hydro-mechanical state is highly heterogeneous because it is influenced by the different excavations realized. Moreover, the low permeability of the clay rock delays significantly the reach of the steady state for pore pressure distribution, which affects in turn the stress distribution. The effect of the excavation of the connecting gallery on the hydro-mechanical state around Praclay experiment is studied.

An anisotropic model with a Mohr-Coulomb failure criterion has been used. Figure 21 shows a comparison between the pore pressure computed by the full anisotropic model and the isotropic model for one sensor located in a borehole in front of the test drift. It evidences the capability of the anisotropic model to capture the peak in pore pressure as the front approaches the sensors. This peak is mainly controlled by the anisotropy of elastic moduli.

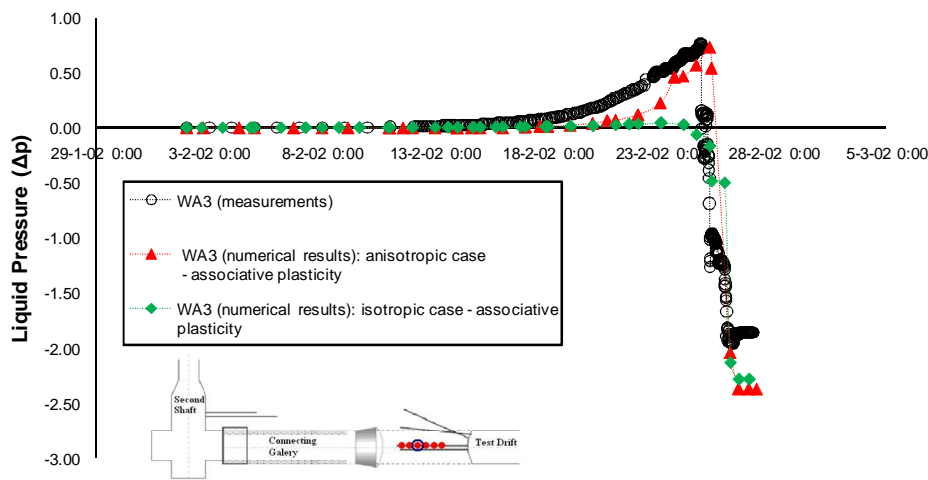


Figure 21: Computed pore pressure vs measurement at sensor A3 for the isotropic and full anisotropic model.

Figure 22 shows the profile of pore pressure along the centre axis of Praclay gallery previous to its excavation. It evidences an increase of pressure in a zone at a distance from the connecting

gallery wall between 20 and 50m, that is around the second middle of Praclay heater. Magnitude of the increase reaches a maximum of 500 kPa (with respect to value of pore pressure in the far field) at 28m from the connecting gallery.

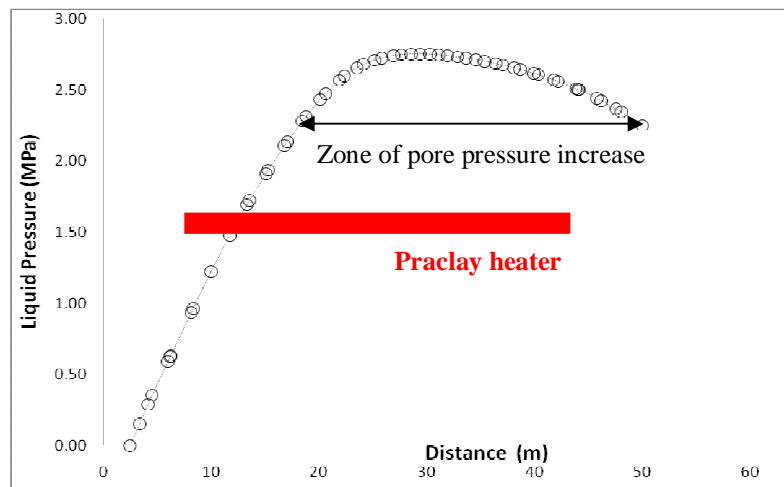


Figure 22: Profile of pore pressure along the centre axis of Praclay gallery previous to its excavation

The effect of anisotropy on the thermal field around PRACLAY experiment was also checked by CIMNE and found significant.

1.4 Conclusions

Globally, the results obtained by the different teams participating to the benchmark are in good agreement.

As expected, some differences are noticeable between the different 2D and 3D approaches, due to the inherent assumptions and limitations of each model:

- On one hand, the 2D plane strain model allows taking into account the anisotropy of the initial, leading to different behaviors in the horizontal and the vertical direction (this is mainly visible at the end of excavation in the pore water pressure profiles, the effective stresses field and the plastic zone extent). On the other hand, neither heat nor water flow is allowed in the out-of-plane direction, so the dissipation is only possible in the plane of the model. Hence, some values (such as the pore water pressure) are higher than in the 2D axisymmetric and 3D models, more especially in the vicinity of the PRACLAY gallery.
- The 2D axisymmetric model offers the possibility to model the PRACLAY experiment including details all along the axial direction, amongst which the bentonite sealing, the connecting gallery, the end plug, etc. Flows in the axial direction are also included and they clearly influence the results, i.e. the pore water pressure profiles. However, the lack of anisotropic properties in this approach constitutes the major drawback of the model when looking at the plastic behavior, leading to the differences observed in the stress paths and in the axisymmetric and less extended plastic zone extent.

- The 3D model appears as the ideal solution: both anisotropy and axial modeling can be included. However, this approach is much more resources consuming (computing time and required memory). To overcome this problem, a compromise must be found between a faster coarse mesh and a more precise and numerically stable refined mesh. The 3D model presented in this report is the fruit of several attempts to solve this problem within a few days of computation and getting results globally in accordance with the best predictions of the 2D plane strain and the 2D axisymmetric models.



2 Introduction: the PRACLAY experiment

(van Marcke et al.)

For more than 30 years Belgium has been actively studying the long-term management of high-level and/or long-lived radioactive waste. A research program has been launched by the Belgian Nuclear Research Centre (SCK•CEN) at Mol in the early 1970's. This program followed international recommendations to isolate radioactive waste from humans and the environment by geological disposal. This means that the waste is disposed of in a geologically stable formation with appropriate characteristics. SCK•CEN chose to concentrate its efforts on investigating the poorly-indurated Boom Clay layer beneath its own site as a potential host formation. Because of the lack of experience in the excavation of underground facilities at a depth of some 200 meters in this type of clay, one of the main objectives of the initial research and development (R&D) program has been the assessment and demonstration of the feasibility of constructing such a repository. This is why the construction of the underground research facility HADES (High-Activity Disposal Experimental Site) was started in 1980 (Figure 23).

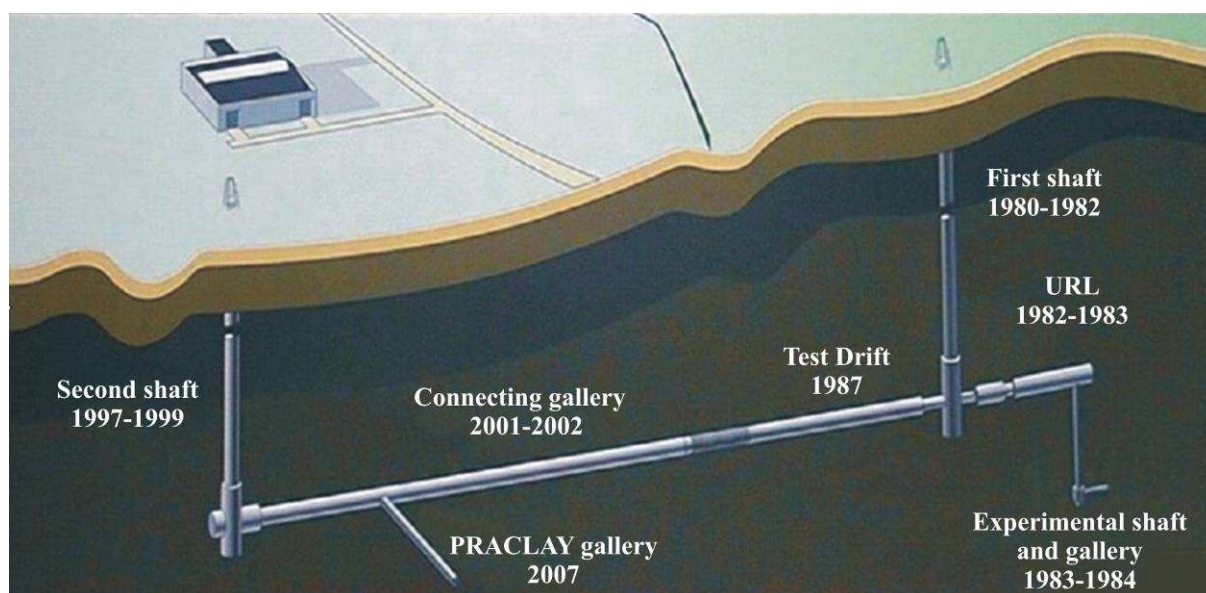


Figure 23: History and layout of the underground research facility HADES

In 1985 ONDRAF/NIRAS, the Belgian Agency for Radioactive Waste and Fissile Materials, took over the R&D program for the disposal of radioactive waste from SCK•CEN. The promising results already obtained made ONDRAF/NIRAS decide to confirm the Boom Clay beneath the Mol site as the reference host formation for the geological disposal of high-level and/or long-lived radioactive waste. The construction works carried out until then and the construction of the Test Drift a few years later (1987) showed that it was possible to construct shafts in frozen aquifer sands and to construct disposal galleries in unfrozen clay. But the feasibility of constructing galleries using an industrial technique had not yet been demonstrated. An expert assessment in the late 1980's confirmed that the poorly-indurated clays, and in particular the Boom Clay under the Mol site, could be considered for the disposal of high-level and/or long-lived waste, since they are able to offer effective protection in the very long term. The Boom Clay had been found to have a very low hydraulic conductivity, a plastic character that gives it good self-sealing properties and a high capacity to fix radionuclides and, hence, to delay their migration towards the biosphere.

These encouraging results prompted ONDRAF/NIRAS and SCK•CEN to launch an ambitious demonstration project: the PRACLAY project (NIRONDA, 1997). The PRACLAY project was to be managed by Euridice, the economic interest group created to that end in 1995 – though under the name “EIG PRACLAY” at that time – and grouping ONDRAF/NIRAS and SCK•CEN. This project had three main objectives:

1. Demonstrating the feasibility, from both a technical as an economic point of view, of constructing underground galleries similar, except in length, to the contemplated disposal galleries and using the industrial techniques that could be used for constructing a real geological repository;
2. Demonstrating the feasibility of constructing an intersection between main galleries and disposal galleries;
3. Carrying out the PRACLAY Heater Test, namely simulating the disposal of heat-emitting high-level waste in a geological repository in clay. This was to be done by installing electrical heaters in a pilot gallery similar in every respect, except the length, to the disposal galleries considered in the reference architecture of the repository.

The first goal – demonstrating the feasibility of constructing an underground gallery by an industrial technique – was fulfilled by the construction of the Connecting Gallery in 2001-2002 (Bastiaens et al., 2003).

The next step in the research program was the realization of the PRACLAY project which aimed demonstrating the feasibility of the reference design for the deep disposal of heat-emitting high-level vitrified radioactive waste. But in 2003 ONDRAF/NIRAS reviewed the design of the engineered barrier system (EBS) (NIRONDA, 2003). The EBS contains all engineered materials placed within the repository, including the waste forms, buffer materials, backfill and seals. Three new designs for the EBS were considered.

The supercontainer was selected as the reference design for the EBS (NIRONDA, 2004). However, ONDRAF/NIRAS considers the two other options as safe and valuable alternatives and therefore wishes to keep the possibility to switch over to these alternatives at a minimal cost. This implied that a unique large-scale demonstration experiment for one specific design was no longer an adequate R&D approach. Therefore the PRACLAY project was reorientated to be as design-independent as possible to maintain the validity and representativeness of the project in case of future changes in the repository design (Demarche and Bel, 2003). The original scope of the experiment – the demonstration of the reference design for vitrified high-level waste – was enlarged to the characterization, verification, confirmation and demonstration of relevant elements of the disposal system and their behaviour by means of a combination of small surface experiments and a large in-situ experiment.

The small surface experiments consist of tests characterising the host formation, the components of the disposal system and the interaction between them and tests demonstrating the feasibility of constructing these components of the disposal system. The OPHELIE mock-up (Van Humbeek et al., 2009) and the ESDRED mock-up make part of these PRACLAY surface experiments. The first aimed at testing the original, and later abandoned, design of a disposal gallery based on precompacted bentonite. The second aimed at demonstrating the feasibility of applying a grout backfill as considered in the supercontainer design. Furthermore tests examining and demonstrating the feasibility of constructing a supercontainer were setup and are still on-going.



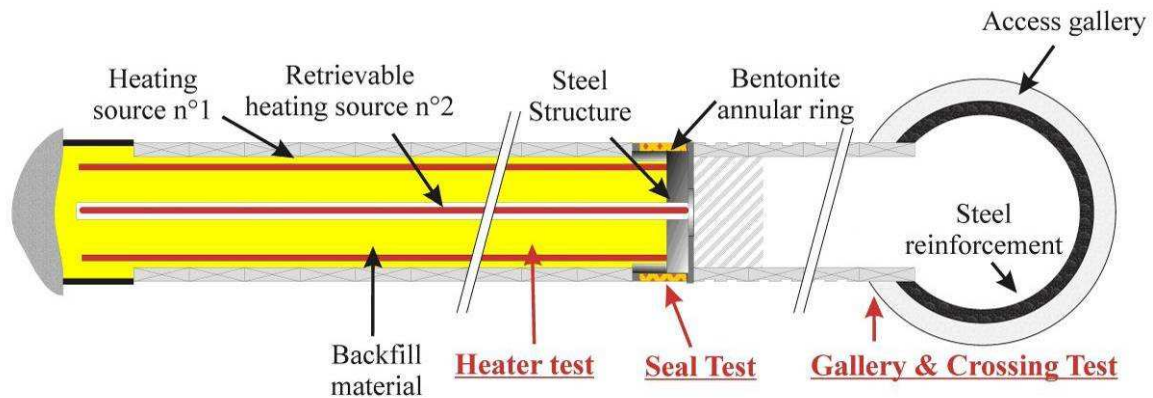


Figure 24: The PRACLAY in-situ experiment comprises three tests: the “Gallery&Crossing Test”, the “Seal Test” and the “Heater Test”

The large In-Situ Experiment (Figure 24) comprises three tests:

1. the Gallery and Crossing Test further examining and demonstrating the construction of an underground repository by industrial method and examining the feasibility to construct a crossing between galleries;
2. the Seal Test examining the feasibility of hydraulically sealing the heated part of the PRACLAY gallery from the rest of the underground;
3. the Heater Test studying the response of the Boom Clay to a thermal impact.

2.1 PRACLAY gallery excavation

To host the Heater Test the construction of a new gallery was needed. The existing galleries of HADES were not suitable to host this test for the following reasons:

1. The lining was not designed to sustain the thermal load resulting from the Heater Test.
2. The installation of instrumentation is complicated as the existing galleries are not designed for this purpose.
3. The period over which the clay massif remained drained before the start of the Heater Test is too long to reproduce the desired penalising conditions.
4. The experiment would disturb and complicate the operations and on-going experiments in HADES. The disturbed laboratory length would be too large and would limit the available space for other future experiments.

Constructing a new gallery perpendicular to the existing galleries also offered the possibility of realising a crossing between two galleries similar to the crossings foreseen in the reference repository design. The construction of the crossing between the PRACLAY and Connecting Gallery required a reinforcement ring because the lining of the latter is designed to allow openings of maximum 100 mm. It was decided to use a reinforcement ring with an internal diameter of 3.5 m not to narrow too much the Connecting Gallery at the crossing. Because of economical reasons and the presence of adjacent instrumentation in the clay, the length of the reinforcement ring was limited to 3.8 m. The maximum allowable diameter for an opening in the Connecting Gallery when using a reinforcement ring meeting these requirements was 2.55 m. The nominal diameter of the PRACLAY gallery on extrados was therefore fixed at 2.50 m.

The location of the PRACLAY gallery was chosen between rings 32 and 35 of the Connecting Gallery and the gallery was constructed towards the east. These choices were made considering the existing instrumentation in the Connecting Gallery, the interactions between the Heater Test, the other running experiments and the HADES infrastructure. Also the topography of the rings in the Connecting Gallery was taken into account as this determined the maximum external diameter of the reinforcement ring that could be installed.

The same excavation technique and type of lining as applied for the construction of the Connecting Gallery were selected for the PRACLAY gallery: excavating by an open-face tunnelling machine and installing a concrete wedge block lining. The design of the lining had to take into account a geotechnical loading due to the pressure exerted by the clay massif on the lining and a thermal loading due to the increased stresses in and on the lining during the Heater Test. A preliminary study on the stability of the gallery lining based on scoping calculations led to the following considerations and conclusions:

- The lining thickness was fixed at 0.30 m and thus the internal diameter of the PRACLAY gallery was set at 1.90 m. Increasing the lining thickness was considered not to be useful as this would only slightly affect the stresses in the lining and it would diminish the internal diameter of the gallery and the effective space inside the gallery.
- The length of the lining rings was set at 0.50 m in contrast to the lining rings of the Connecting Gallery which were 1.00 m long. The ring length was reduced to limit the frictional force between the ring and the clay. Moreover, shorter segments are easier to handle and result in a shorter unsupported zone behind the tunnelling shield.

Compressive materials are incorporated in the lining (in and between lining rings) allowing for thermal expansion of the lining and in that way limiting the thermally induced stresses.

Two types of high performance concrete (HPC) were considered for the concrete segments: a standard HPC (C80/95) and a heavy HPC. The heavy HPC has a higher elastic modulus and thermal conductivity than standard HPC. Both types have almost the same compressive strength of ca. 80 MPa. From scoping calculations it appeared that using a heavy HPC merely has advantages. For a given thermal loading the maximum tangential stress in a heavy HPC is only slightly smaller than in a standard HPC. Moreover it presents a brittle behaviour at high deformation which is unfavourable for the stability of the liner. It was therefore decided to use standard HPC rather than heavy HPC.

As the hydraulic seal is installed after the construction of the PRACLAY gallery, an alternative lining in the zone of the future hydraulic seal is needed. On the one hand, a maximal percentage of the clay sidewall has to remain accessible to make sure the bentonite properly seals off. On the other hand, a certain support of the clay sidewall is needed to prevent convergence and instability of the sidewall.

In conclusion, the following design criteria were defined for the PRACLAY gallery:

- The PRACLAY gallery is located between rings 32 and 35 of the Connecting Gallery and is constructed eastwards.
- The diameter of the PRACLAY gallery is set at 2.50 m. A reinforcement ring is placed in the Connecting Gallery prior to the excavation works to assure the stability of the lining of the Connecting Gallery.

- The excavation is done by an open-face tunneling machine and 0.30 m thick concrete wedge blocks (standard HPC) are used as lining. The length of the lining rings is limited to 0.50 m to limit the frictional force between the ring and the clay. Compressive materials are incorporated in the gallery lining allowing for some thermal dilatation and in that way limiting the thermally induced stresses. At the location of the hydraulic seal an alternative lining is placed.

The underground works started on 01.10.2007 with the cutting of the lining of the Connecting Gallery, and the construction of the PRACLAY gallery was successfully completed in 2007.

The tunnelling machine was then positioned in this opening and the excavation works were started. The construction of the PRACLAY gallery – 84 lining rings including the rings for the hydraulic seal –, between 04.10.2007 and 06.11.2007, more or less progressed as expected. Beside for the start-up phase (i.e. the construction of the first 11 rings), the stop-and-go test and the construction of the alternative lining at the location of the future hydraulic seal, a progress rate of 2 m/day was aimed for. From ring 15 on the achieved construction rate complied in general with the required rate. Only minor problems were encountered. These were mainly mechanical problems (e.g. oil leakage due to broken hoses) and delays due to limited working space for equipment and personnel which also complicated the repairing of these delays.

A stop-and-go-test was performed after the construction of ring 79 by stopping the excavation works for one week. The purpose of the stop-and-go test was testing the level of difficulty to restart the tunnelling machine as the friction between the clay and the shield increases during the stand-still due to the convergence of the Boom Clay around the shield. The thrust force required to push the shield forward after one week was about twice the normal thrust force. Still, this was only ~25% of the maximum available force and no problems restarting the excavation works were met.

Several measurements were carried out during and after the excavation of the PRACLAY gallery. They aimed at gaining as much information as possible on the performance of the excavation technique, the behaviour of the Boom Clay and the impact of the excavation on the clay. This information was obtained from observations and measurements of the clay, the lining and the tunnelling machine.

2.2 PRACLAY Seal Test

A hydraulic seal was successfully installed in the PRACLAY gallery in 2010. The installation is part of the PRACLAY In-Situ Experiment and its main purpose is the creation of an undrained hydraulic boundary at the intersection between the heated part of the PRACLAY gallery and the non-heated part. Such an undrained boundary is required to achieve the most penalizing conditions that are reasonably achievable during the Heater Test.

The design of the hydraulic seal is mainly determined by the design of the PRACLAY gallery and the Heater Test. The seal is installed at a distance of 10 m from the Connecting Gallery to limit the mutual interactions between the Heater Test and the Connecting Gallery. It consists of a steel structure closing off the heated part of the gallery from the rest of the underground infrastructure and an annular ring of bentonite placed against the clay. The bentonite is hydrated and its swelling pressure exerted against the clay will locally lower the hydraulic conductivity of the clay. Scoping calculations proved that a seal length of 1 m is sufficiently effective and that no significant gain is obtained by further increasing the length of the seal (Figure 25).



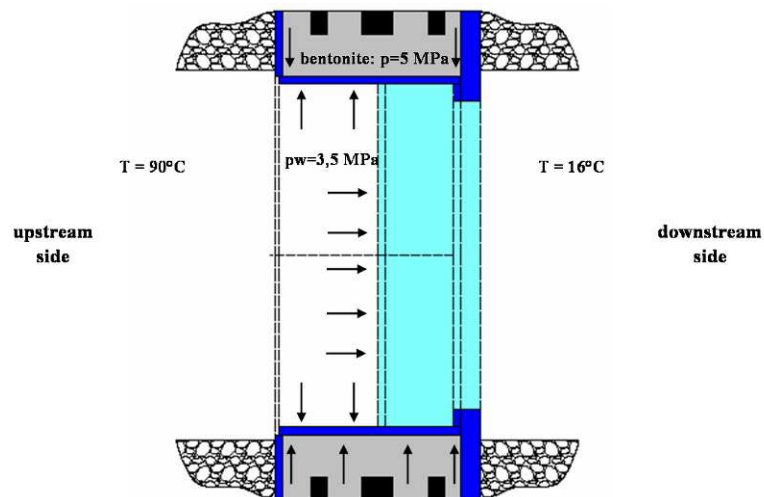


Figure 25: Structure of PRACLAY Seal

To maintain the accessibility of the clay sidewall at the location of the hydraulic seal, an alternative lining is installed. The alternative lining consisted of four steel rings making up the permanent part of the lining and wood placed behind these steel rings as a temporary component of the lining. The permanent part consists of 4 steel rings while the temporary part, mainly wood placed between these rings, was removed before the erection of the hydraulic seal.

The steel structure consists of two flanges that are placed against the concrete lining next to the hydraulic seal. Because the flanges are too large to be installed in one piece, they are constructed in four segments that are welded together on site. After both flanges are installed, an annular ring of bentonite blocks is erected between the flanges and the clay sidewall. Subsequently a cylinder is placed in the annular bentonite ring and between the two flanges. In that way the bentonite is enclosed between the two flanges, the cylinder and the Boom Clay. On the extrados of the cylinder filters are placed for the hydration of the bentonite

A circular plate placed in the cylinder closes off the opening of the cylinder and thus the heated part of the PRACLAY gallery. Because this part of the gallery still has to remain accessible before the start of the Heater Test – this is needed for the assembly of the cylinder to the flanges during the seal erection and for the installation of the heater and backfill material in the PRACLAY gallery after the seal erection – a manhole is placed in the center of the plate. Before the start of the Heater Test the manhole is closed by welding a closing plate on it. The plate in the cylinder has different openings for the feed-through of the instrumentation and the heating system placed in the upstream part of the gallery.

The bentonite placed in an annular ring against the Boom Clay has to exert a swelling pressure of ca. 5 MPa against the Boom Clay to locally reduce the hydraulic conductivity of the Boom Clay around the seal and in that way create an undrained hydraulic boundary. It was decided to use MX80 bentonite compacted into bentonite blocks. The choice of this type of bentonite was mainly based on literature data on its swelling pressure, water retention potential and permeability. Furthermore it is a Na-bentonite which makes it chemically compatible with the Boom Clay water and relevant experience and information with this type of bentonite exists from its use in other experiments in underground research facilities (Mont Terri, Bure, ASPO, AECL's URL) and in the laboratory (by CEA, CIEMAT, CERMES and SKB). The desired initial dry density of the bentonite which determines its swelling pressure and its final saturated permeability was determined by scoping calculations.

Instrumentation was placed in the bentonite blocks to gain information on the bentonite hydration and to be able to test and evaluate the performance of the hydraulic seal.

2.3 PRACLAY Heater Test

The main goal of the PRACLAY In-Situ Experiment is examining the impact of a large-scale thermal load on the Boom Clay. Such a thermal load leads to perturbations in the clay and can affect its performance as a host rock in the geological disposal concept for radioactive waste. The impact of the thermal load on the clay is examined and evaluated in the Heater Test. To overcome eventual future changes in the repository design and because it is not possible to simulate the time scale, the spatial scale and the boundary conditions that apply for a real repository, the test was designed to be as design-independent as possible and aims at imposing the most penalizing THM conditions that are reasonably achievable.

More specifically the goals of the Heater Test are:

- Demonstrating that liquefaction of Boom Clay will not occur around a repository of heat emitting waste;
- Assessing the heat dissipation from a repository containing heat emitting waste and determining in particular the thermal conductivity of the Boom Clay;
- Estimating the major consequences of the THM impact on the Boom Clay with a major focus on the effect of this impact on the transport mechanisms (i.e. whether or not fluid transport remains diffusion dominated);
- Increasing the understanding of the effects on Boom Clay characteristics after a thermal pulse with respect to radionuclide transport related parameters with a focus on the retention capacity of the clay;
- Assessing the stability of the concrete lining during the most penalizing conditions of a thermal transient for any design, taking into account the temperature criterion of $T_{\max} < 100^{\circ}\text{C}$ around the overpack (Bel and Bernier, 2001);
- Increasing our knowledge of the performance and reliability of monitoring devices under thermal stress and heater.

The purpose of the Heater Test is simulating the thermal impact generated by heat emitting high-level waste (HLW) on Boom Clay. Simulating the exact hydrothermal conditions as in a real disposal site is not possible. The time period over which the thermal load applies in a real repository is too long (several hundreds to thousands of years) and also the length of the repository galleries and the boundary conditions, such as the drainage conditions around the repository, are different. Therefore the most penalizing conditions in terms of the THM response of the clay are considered within the limits of what is reasonably achievable. In addition, the design of the Heater Test has to be as independent as possible of the repository design to avoid eventual future changes in the repository design jeopardizing the validity and representativeness of the test.

The last phase in the installation of the PRACLAY In-Situ Experiment will be accomplished in 2010 by the installation of the heating system and backfill material. The requirement for the heating system is that it has to impose a constant temperature of 80°C in the clay at the gallery extrados. This target temperature has to be achieved step-wise and slowly to limit the thermal gradient and thus the stresses in the concrete lining. The backfill material was needed to create



undrained conditions in the gallery. Therefore the backfill material had to be saturated as much as possible.

The heater consists of a primary heater close to the gallery intrados and a secondary heater inside a central tube (Figure 24). Both heaters consist of electrical heaters. The primary heater is inaccessible during the Heater Test and therefore needs to be installed in a redundant manner. The second heater is a backup and remains accessible and replaceable at all times during the test. Beside these heating elements, also a control system regulating the heating power as a function of measured and target temperatures makes part of the heating system.

The backfill material had to have a thermal conductivity higher than the thermal conductivity of the liner and clay massif to efficiently transfer the heat generated by the heating system towards the clay massif. It also has to have a sufficiently high hydraulic conductivity to allow a quick equalization of the pore pressures in the backfill material and finally it preferably has a narrow grain size distribution to limit the density differences between the top and bottom due to segregation. The selected material fulfilling these requirements was Mol Sand M34 of which ca. 200 ton was required to fill the gallery.

In a first phase all the cables of the instrumentation installed in the heated part of the PRACLAY gallery were grouped and passed through their designated openings in the hydraulic seal. Also a tube for the backfill installation and a tube for the later backfill saturation were installed in the gallery and passed through the hydraulic seal. Subsequently the primary heater cables at the bottom of the gallery are placed and the floor platform supporting the central tube and the central tube is built over these heater cables. These components are built in sections starting from the end of the gallery and continuing towards the hydraulic seal.



3 Exercise, idealisation proposed

3.1 General framework of the benchmark

This benchmark concerns the modelling of the large scale in situ experiment (PRACLAY for preliminary demonstration test for clay disposal of vitrified high-level radioactive waste) at the Underground Research Laboratory (URL) at Mol. The PRACLAY experiment is designed to simulate the construction and operation (mainly heating) of a waste disposal gallery in a clay host rock. One of the aims of the experiment is to better understand and quantify the thermal impact on the THM behaviour and the sealing capacity of clays and to verify the performance of Boom Clay submitted to a thermal load at large scale.

Indeed, the effect of a large scale thermal load on the behaviour of Boom Clay is one important remaining issue in the feasibility study of the disposal. Indeed, the impact of the thermal load generated by the waste is particularly important since it will significantly affect the temperature and the stress profiles on the whole thickness of Boom Clay in the short term after the disposal. The early transient thermo-hydro-mechanical (THM) perturbation might be the most severe impact that the repository system will undergo on a large spatial scale and in a relatively short period of time.

The PRACLAY experiments are performed within “The PRACLAY Gallery”, which is 45 m long with an internal diameter about 2 m, lined with concrete segments and perpendicular to the connecting gallery. The Boom Clay will be instrumented to characterize the THM behaviour around the gallery. The heater length will be about 30 m. The PRACLAY in-situ experiment regroups a set of three tests (see Figure 26): the gallery and crossing test, the heater test, the plug test.

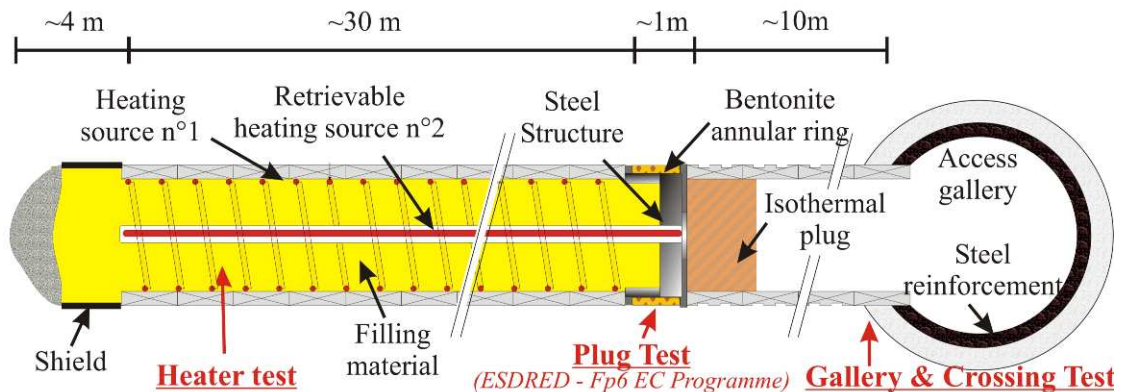


Figure 26: The PRACLAY experiments

The main idea of this benchmark is to reproduce the excavation of the PRACLAY gallery and the heating phase of the PRACLAY experiment with a coupled thermo-hydro-mechanical model. This modelling may be considered as a plane strain two-dimensional problem (this simple geometry allows taking into account anisotropy in 2D), a two-dimensional problem in axisymmetric condition and a three dimensional problem. This last geometry allows taking into account the effect of the anisotropy of the clay for all the processes. The choice of the geometry of the modelling is free and is let to the team.

3.2 Geometry of PRACLAY gallery

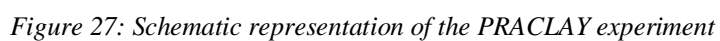
The excavation has been performed under the protection of a shield and using the wedge block system for the lining. The method has allowed an excavation rate (excavation + installation of the lining) of 2m/day. At the end of the gallery, a "stop and go" test was done to assess the feasibility to restart with the tunnelling machine after a stopping period. For the security of the connecting gallery, the construction of the PRACLAY gallery requires a steel reinforcement ring in the connecting gallery. The maximum possible diameter for the opening in the connecting gallery is 2.55 m. Consequently, the nominal diameter of the extrados of the PRACLAY gallery has been fixed to 2.5 m taking into account the convergence. A diameter about 2.5 m corresponds to the range of diameters considered for the repository designs. (The results of the crossing test will give additional information for the optimization of the tunnel excavation and will demonstrate the feasibility to construct a crossing between an access gallery and a disposal gallery.)

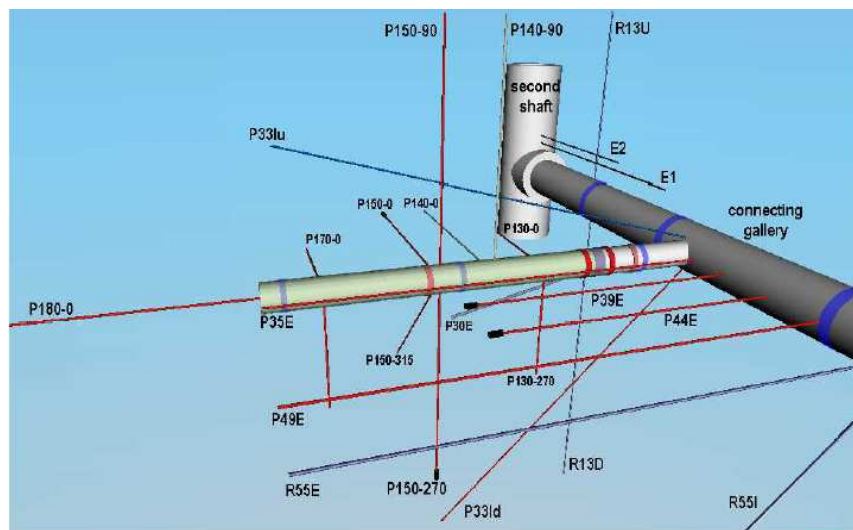
It has been chosen for the PRACLAY in-situ experiment, to use a heater system imposing a temperature about 80°C, as constant as possible, at the gallery wall (extrados of the lining). The heater system is located 10 cm (radius = 0.85 m) inside the intrados of the liner. However a second heater working at constant flux will be installed as a backup of the primary heater in case of failure. This back-up heater can be retrieved during the PRACLAY Heater Test.

Plugs (within disposal galleries, between disposal and main galleries, between main galleries and shafts) are considered, at least as a conservative measure, in the overall repository design in order to e.g., limit interactions between various repository zones (compartmentalization through cutting the hydraulic connection along the gallery lining and EDZ), increase the resilience of the repository to intrusion, and avoid gas migration. The "PRACLAY Plug Test" aims at demonstrating that it is possible to cut-off hydraulically the EDZ and the engineered barriers of the disposal galleries with a horizontal plug.

The geometry of the PRACLAY experiment is described in Figure 27. The heater which is delimited by a seal and a concrete end plug is 30 m long. The nominal internal diameter of the PRACLAY gallery is fixed to 1.9 m. The thickness of the liner is designed to 30 cm. The gap between the initial radius of the gallery (over-excavation) and the nominal radius 1.25 m (extrados of the liner) is equal to 0.06 m.

The Figure 28 below gives an overview of the instrumentation program including temperature, pore water, total stresses and displacements measurements as well as the follow-up of the chemical evolution in the Boom Clay around the test.





3.3 2D plane strain modelling

3.3.1 Geometry

This section describes the geometry of the modelling for the 2D plane strain condition. The studied cross view is situated near the middle of the heating zone, i.e. in the middle of ring n°44 (Figure 2) of the PRACLAY gallery.

This model is 100 m wide and 100 m high. Figure 4 illustrates the 2D plane strain model. The inner radius is equal to 0.95 m, the thickness of the liner is equal to 30 cm as seen in Figure 29. The liner is supposed to be put after a convergence of 0.06 m.

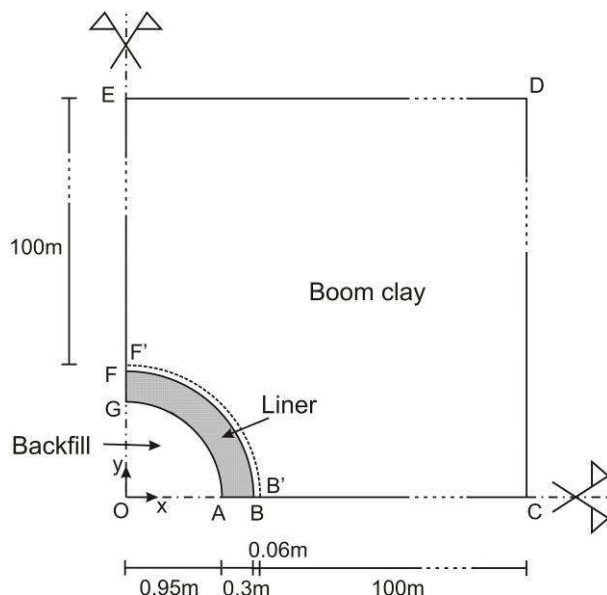


Figure 29: Schematic representation of the 2D plane strain modelling



3.3.2 Initial conditions

The clay is initially considered as homogeneous and isotropic. It is supposed to be fully saturated. Initial conditions are listed in Table 1. For Boom Clay, they are close to the ones encountered in the clay formation. The gravity will not be considered in this modelling.

Initial state		Boom Clay
Total stresses [MPa]	σ_{yy}	4.5
	$\sigma_{xx} = \sigma_{zz}$	3.825
Effective stresses [MPa]	σ'_{yy}	2.25
	$\sigma'_{xx} = \sigma'_{zz}$	1.575
	K'_0	0.7
Pore pressure [MPa]	p_{w0}	2.25
Temperature [°C]	T	16

Table 1: Initial state in the Boom clay – stresses, pore water pressure and temperature

In the concrete liner, the initial conditions assume that the concrete is saturated at a temperature corresponding to the one of the host formation.

Initial state		Concrete
Pore pressure [MPa]	p_{w0}	0.1
Temperature [°C]	T	16

Table 2: Initial state in the concrete – pore water pressure and temperature

3.3.3 Parameters

The Table 3 and Table 4 give the thermo-hydro characteristics of the water.

Hydraulic characteristics		Water
Fluid specific mass [kg/m³]	ρ_w	1000
Fluid dynamic viscosity [Pa.s]	μ_{w0}	10^{-3}
Liquid compressibility coefficient [MPa ⁻¹]	$1/\chi_w$	$5 \cdot 10^{-4}$

Table 3: Hydraulic characteristics for water

Thermal characteristics		Water
Volumetric liquid thermal expansion coefficient [K ⁻¹]	β_w	$3 \cdot 10^{-4}$
Liquid dynamic viscosity thermal coefficient [K ⁻¹]	α_w	0.01

Table 4: Thermal characteristics for water

The liquid dynamic viscosity varies linearly with the temperature following:

$$\mu_w(T) = \mu_{w0} - \alpha_w \mu_{w0} (T - T_0)$$

Here are presented, in Table 5 to Table 7, the thermo-hydro-mechanical characteristics of the Boom Clay. The properties are given for the initial temperature and pore pressure. The values of

these parameters are indicative and may be different according to the constitutive law used in this exercise.

Geomechanical characteristics		Boom Clay
Drained Young elastic modulus [MPa]	E_0	300
Drained Poisson ratio [-]	ν	0.125
Grain specific mass [kg/m ³]	ρ_s	2682
Drained cohesion [kPa]	c	300
Drained initial friction angle [°]	ϕ_0	5
Drained final friction angle [°]	ϕ_f	18
Hardening parameter [-]	β_ϕ	0.01
Drained dilatancy angle [°]	ψ	0
Biot's coefficient [-]	b	1

Table 5: Geomechanical characteristics for the Boom clay

The hardening rule for the friction angle is the following:

$$\phi = \phi_0 + \frac{(\phi_f - \phi_0) \varepsilon_{eq}^p}{\beta_\phi + \varepsilon_{eq}^p}$$

where the Von Mises equivalent plastic strain is obtained by the integration of the Von Mises equivalent plastic strain rate :

$$\varepsilon_{eq}^p = \int_0^t \dot{\varepsilon}_{eq}^p dt \quad \text{with} \quad \dot{\varepsilon}_{eq}^p = \sqrt{\frac{2}{3} \dot{\varepsilon}_{ij}^p \dot{\varepsilon}_{ij}^p}$$

The coefficient β_ϕ represents respectively the value of equivalent plastic strain for which half of the hardening on frictional angle is achieved.

Hydraulic characteristics		Boom Clay
Porosity [-]	n	0.39
Intrinsic permeability [m ²]	k_{int}^{sat}	4.10^{-19}

Table 6: Hydraulic characteristics for the Boom clay

Thermal characteristics		Boom Clay
Thermal conductivity [W.m ⁻¹ .K ⁻¹]	λ	1.35
Volumetric heat capacity [J.m ⁻³ .K ⁻¹]	ρC_p	$2.84 \cdot 10^6$
Linear solid thermal expansion coefficient [K ⁻¹]	β_s	10^{-5}

Table 7: Thermal characteristics for the Boom clay

The liner is composed of concrete C80/95. Due to joints, its permeability is taken 10 times greater than the clay permeability. Some characteristics of the liner are presented on Table 8 to Table 10.

Geomechanical characteristics		Concrete
Young elastic modulus [MPa]	E_0	43305
Poisson ratio [-]	ν	0.25
Specific mass [kg/m ³]	ρ	2500

Table 8: Geomechanical characteristics for the liner

Hydraulic characteristics		Concrete
Porosity [-]	n	0.15
Intrinsic permeability [m ²]	k_{int}^{sat}	4.10^{-18}

Table 9: Hydraulic characteristics for the liner

Thermal characteristics		Concrete
Thermal conductivity [W.m ⁻¹ .K ⁻¹]	λ	1.5
Volumetric heat capacity [J.m ⁻³ .K ⁻¹]	ρC_p	$2.2 \cdot 10^6$
Linear solid thermal expansion coefficient [K ⁻¹]	β_s	10^{-5}

Table 10: Thermal characteristics for the liner

The backfill material (Figure 29), constituted of sand with a 40% porosity and saturated in water, was not taken into account and not modelled in that benchmark for sake of simplicity.

3.3.4 Boundary conditions

Figure 30 represents the boundary conditions used in this 2D modelling.

Mechanical boundary conditions are defined as followed:

- X displacements are fixed on the boundaries DC, GF and F'E.
- Y displacements are fixed on the boundaries ED, AB and B'C.
- Boundary B'F': External forces decreasing during excavation phase and next contact with BF boundary.

Hydraulic boundary conditions:

- Boundaries GF, F'E, ED, DC, AB and B'C are impervious.
- Boundary B'F': pore pressure decreasing (excavation phase 1).
- Boundary AG: pore pressure fixed (excavation phase 1 and waiting phase 2) and impervious (heating phases 3 and 4).

Thermal boundary conditions:

- Boundaries BC, CD, DE and EF are adiabatic.
- Boundary AG: temperature increasing (heater phases 3 and 4).

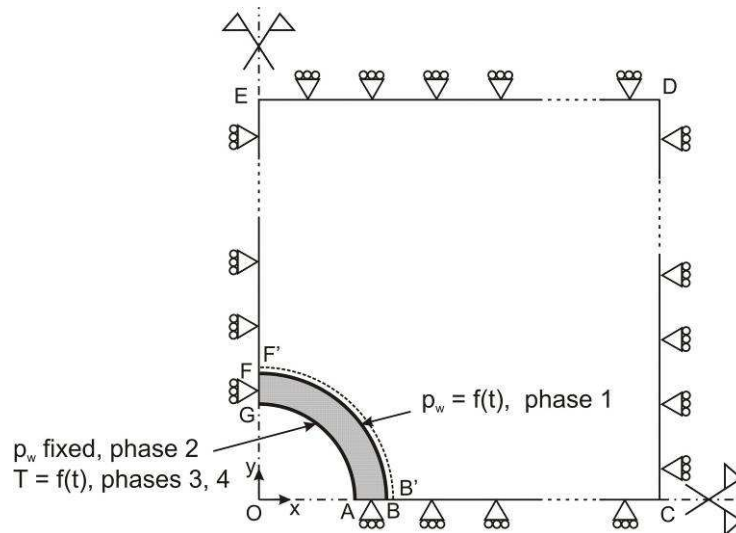


Figure 30: Schematic representation of the boundary conditions in the 2D plane strain modelling

3.3.5 Description of the calculation

The modelling first consists in the excavation of the gallery and, in a second step, a thermal loading is applied at the extrados of the liner:

Phase 1: Duration: 24 hours

- Excavation of the gallery: external forces decreasing on boundary B'F'.
- Decreasing pore pressure from initial value to 100 kPa on boundary B'F'.
- Temperature fixed at initial value on the whole domain.
- Pore pressure fixed at 100 kPa on the whole liner.

Phase 2: Duration: 3.5 years

- Waiting phase: pore pressure fixed at 100 kPa on boundary AG (liner intrados).
- Temperature fixed at initial value on the whole domain.

Phase 3: Duration: 6 months

- Heater phase: temperature linearly increasing from initial value to 85°C at the intrados of the liner (boundary AG).
- Water undrained conditions on the whole domain.

Phase 4: Duration: 10 years

- Stabilised heater phase: temperature fixed to 85°C at the intrados of the liner (boundary AG).
- Water undrained conditions on the whole domain.

The actual heater system is constituted of a pipes network with heat water flow inside; it is located 10 cm inside the intrados of the liner and imposes a temperature, as constant as possible, of about 80°C at the extrados gallery wall. In that proposition, this complex system is idealised simply by imposing an increase of the temperature directly at the intrados of the liner.

3.3.6 Output results

It is asked to supply the results (pore water pressure p_w , temperature T , effective stresses σ'_x , σ'_y and displacements u_x , u_y) along the two profiles ABC and GFE (Figure 31) for the 8 following times:

- End of the phase 1 (excavation phase): $t_1 = 24 \text{ h}$ = 86 400 sec.
- End of the phase 2 (waiting phase): $t_2 = t_1 + 3.5 \text{ years}$ = 110 462 400 sec.
- End of the phase 3 (heater phase): $t_3 = t_2 + 6 \text{ months}$ = 126 230 400 sec.
- Phase 4 (heater phase): $t_4 = t_3 + 0.5 \text{ year}$ = 141 998 400 sec.
- Phase 4 (heater phase): $t_5 = t_3 + 1 \text{ year}$ = 157 766 400 sec.
- Phase 4 (heater phase): $t_6 = t_3 + 2 \text{ years}$ = 189 302 400 sec.
- Phase 4 (heater phase): $t_7 = t_3 + 5 \text{ years}$ = 283 910 400 sec.
- End of the phase 4 (heater phase): $t_8 = t_3 + 10 \text{ years}$ = 441 590 400 sec.

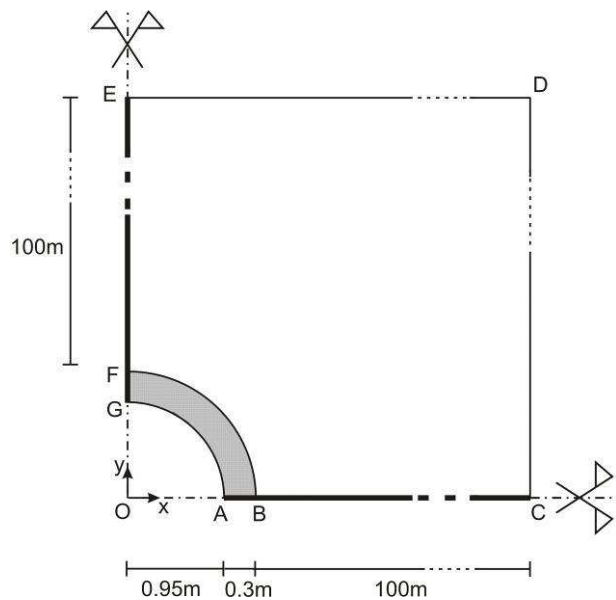


Figure 31: Two profiles output results for the 2D plane strain modelling

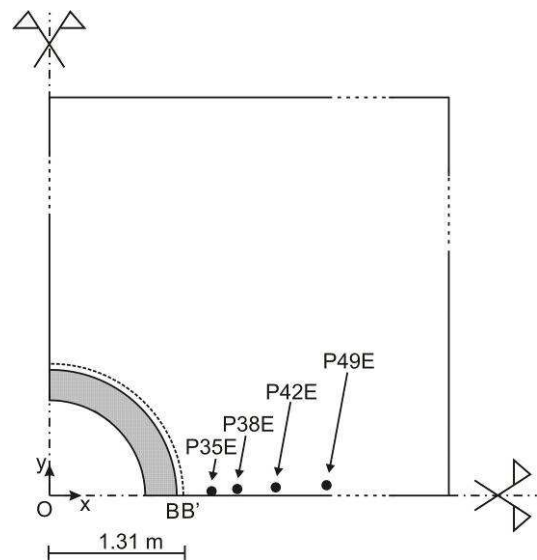


Figure 32: Sensors location for time evolution of results in the 2D plane strain modelling

It is asked also to supply the time evolution of some results (pore water pressure p_w , temperature T , mean effective stress p' and deviatoric effective stress q) for the 4 sensors (P35E, P38E, P42E and P49E) and the wall of the Boom clay (point B'=B), located on the Figure 32. The nominal radial distances from the centre of the gallery to the sensors P35E, P38E, P42E and P49E are respectively 2m, 5m, 9m and 16m but the correct distances taking borehole deviation into account are given on Table 11.

Sensors	Horizontal distance x [m]	Vertical distance y [m]	Radial distance r [m]
P35E	2.197	0.16	2.203
P38E	4.757	0.24	4.763
P42E	8.959	0.32	8.964
P49E	16.192	0.39	16.197

Table 11: Sensors location taking deviation into account (ring 44)

It is also asked to provide the temporal evolution of the dissipated power (per one meter thickness) all during the heating phase.

3.4 2D axisymmetric modelling

3.4.1 Geometry

This section describes the geometry of the modelling for the bi-dimensional axisymmetric conditions. The geometry of the PRACLAY gallery is provided in Figure 27. Seven different materials are involved in the construction of the gallery. Most of the liner rings are made of concrete elements, but some steel components are also used for the seal and, at the end of the gallery, for the lost shield and the stiffened steel end. The friction coefficient between the ring and the host clay depends on the external geometry of the concrete liner: some of them are grooved. All the data are summarized in the Table 12.

Ring	Material	External surface
1-15	C80/95 concrete	Grooved
16-19	C80/95 concrete (metal foam)	
20	ZHW C125/150 concrete	
Seal	Steel	Non-grooved
21	ZHW C125/150 concrete	
22-75	C80/95 concrete (metal foam)	
76-81	ZHW C125/150 concrete	
Steel shield	Steel	
Compressive end plug	C30/37 concrete	
End plug	C30/37 concrete	

Table 12: Description of the liner components

3.4.2 Initial conditions

The clay is initially considered as homogeneous and isotropic. It is supposed to be fully saturated. Initial conditions are listed in the Table 13. Be careful the initial stress conditions are isotropic.

Initial state		Boom Clay
Total stresses [MPa]	$\sigma_{\theta\theta} = \sigma_{rr} = \sigma_{zz}$	4.5
Effective stresses [MPa]	$\sigma'_{\theta\theta} = \sigma'_{rr} = \sigma'_{zz}$ K'_0	2.25 1
Pore pressure [MPa]	p_{w0}	2.25
Temperature [°C]	T	16

Table 13: Initial state in the Boom clay – stresses, pore water pressure and temperature

In the concrete liners, the initial conditions assume that the concrete is saturated at a temperature corresponding to the one of the host formation.

Initial state		Concrete
Pore pressure [MPa]	p_{w0}	0.1
Temperature [°C]	T	16

Table 14: Initial state in the concrete – pore water pressure and temperature

In the steel components, the initial temperature corresponds to the one of the host formation.

3.4.3 Parameters

Table 15 and Table 16 give the thermo-hydro characteristics of the water.

Hydraulic characteristics		Water
Fluid specific mass [kg/m³]	ρ_w	1000
Fluid dynamic viscosity [Pa.s]	μ_w	10^{-3}
Liquid compressibility coefficient [MPa ⁻¹]	$1/\chi_w$	5.10^{-4}

Table 15: Hydraulic characteristics for water

Thermal characteristics		Water
Volumetric liquid thermal expansion coefficient [K ⁻¹]	β_w	3.10^{-4}
Liquid dynamic viscosity thermal coefficient [K ⁻¹]	α_w	0.01

Table 16: Thermal characteristics for water

The liquid dynamic viscosity varies linearly with the temperature following:

$$\mu_w(T) = \mu_{w0} - \alpha_w \mu_{w0} (T - T_0)$$

Here are presented, in Table 17 to Table 19, the thermo-hydro-mechanical characteristics of the Boom Clay. The properties are given for the initial temperature and pore pressure. The values of these parameters are indicative and may be different according to the constitutive law used in this exercise.

Geomechanical characteristics		Boom Clay
Drained Young elastic modulus [MPa]	E_0	300
Drained Poisson ratio [-]	ν	0.125
Grain specific mass [kg/m ³]	ρ_s	2682
Drained cohesion [kPa]	c	300
Drained initial friction angle [°]	ϕ_0	5
Drained final friction angle [°]	ϕ_f	18
Hardening parameter [-]	β_ϕ	0.01
Drained dilatancy angle [°]	ψ	0
Biot's coefficient [-]	b	1

Table 17: Geomechanical characteristics for the Boom clay

The hardening rule for the friction angle is the following:

$$\phi = \phi_0 + \frac{(\phi_f - \phi_0) \varepsilon_{eq}^p}{\beta_\phi + \varepsilon_{eq}^p}$$

where the Von Mises equivalent plastic strain is obtained by integration of the Von Mises equivalent plastic strain rate :

$$\varepsilon_{eq}^p = \int_0^t \dot{\varepsilon}_{eq}^p dt \quad \text{with} \quad \dot{\varepsilon}_{eq}^p = \sqrt{\frac{2}{3} \dot{\varepsilon}_{ij}^p \dot{\varepsilon}_{ij}^p}$$

The coefficient β_ϕ represents respectively the value of equivalent plastic strain for which half of the hardening on frictional angle is achieved.

Hydraulic characteristics		Boom Clay
Porosity [-]	n	0.39
Intrinsic permeability [m ²]	k_{int}^{sat}	4.10^{-19}

Table 18: Hydraulic characteristics for the Boom clay

Thermal characteristics		Boom Clay
Thermal conductivity [W.m ⁻¹ .K ⁻¹]	λ	1.35
Volumetric heat capacity [J.m ⁻³ .K ⁻¹]	ρC_p	$2.84 \cdot 10^6$
Linear solid thermal expansion coefficient [K ⁻¹]	β_s	10^{-5}

Table 19: Thermal characteristics for the Boom clay

The nature of the liner varies along the Praclay gallery as depicted in Table 12. From ring 1 to 15, the liner is composed of concrete C80/95. From ring 16 to 19 and from ring 22 to 75, some metal foam is inserted within the concrete blocs. For sake of simplicity, these two types of concrete are supposed to have the same properties. Due to joints, the permeability of the liner is taken 10 times greater than the clay permeability. From ring 20 to 21 and from ring 76 to 81, the

liner is made of concrete ZHW C125/150. At the end of the gallery, the compressive end plug and the end plug are supposed to be both made of concrete C30/37.

The characteristics of different materials involved in the liner are presented in the Table 20 to the Table 30.

Geomechanical characteristics		C80/95 Concrete
Young elastic modulus [MPa]	E_0	43305
Poisson ratio [-]	ν	0.25
Specific mass [kg/m ³]	ρ	2500

Table 20: Geomechanical characteristics for the C80/95 liner

Hydraulic characteristics		C80/95 Concrete
Porosity [-]	n	0.15
Intrinsic permeability [m ²]	$k_{\text{int}}^{\text{sat}}$	4.10^{-18}

Table 21: Hydraulic characteristics for the C80/95 liner

Thermal characteristics		C80/95 Concrete
Thermal conductivity [W.m ⁻¹ .K ⁻¹]	λ	1.5
Volumetric heat capacity [J.m ⁻³ .K ⁻¹]	ρC_p	$2.2 \cdot 10^6$
Linear solid thermal expansion coefficient [K ⁻¹]	β_s	10^{-5}

Table 22: Thermal characteristics for the C80/95 liner

From ring 20 to 21 and from ring 76 to 81, the liner is composed of concrete ZHW C125/150.

Geomechanical characteristics		ZHW C125/150 Concrete
Young elastic modulus [MPa]	E_0	55500
Poisson ratio [-]	ν	0.25
Specific mass [kg/m ³]	ρ	2500

Table 23: Geomechanical characteristics for the ZHW C125/150 liner

Hydraulic characteristics		ZHW C125/150 Concrete
Porosity [-]	n	0.15
Intrinsic permeability [m ²]	$k_{\text{int}}^{\text{sat}}$	4.10^{-18}

Table 24: Hydraulic characteristics for the ZHW C125/150 liner

Thermal characteristics		ZHW C125/150 Concrete
Thermal conductivity [W.m ⁻¹ .K ⁻¹]	λ	1.5
Volumetric heat capacity [J.m ⁻³ .K ⁻¹]	ρC_p	2.2 10 ⁶
Linear solid thermal expansion coefficient [K ⁻¹]	β_s	10 ⁻⁵

Table 25: Thermal characteristics for the ZHW C125/150 liner

At the end of the gallery, concrete end plugs (C30/37) are used.

Geomechanical characteristics		C30/37 Concrete
Young elastic modulus [MPa]	E_0	32000
Poisson ratio [-]	ν	0.25
Specific mass [kg/m ³]	ρ	2500

Table 26: Geomechanical characteristics for the C30/37 liner

Hydraulic characteristics		C30/37 Concrete
Porosity [-]	n	0.15
Intrinsic permeability [m ²]	k_{int}^{sat}	4.10 ⁻¹⁸

Table 27: Hydraulic characteristics for the C30/37 liner

Thermal characteristics		C30/37 Concrete
Thermal conductivity [W.m ⁻¹ .K ⁻¹]	λ	1.5
Volumetric heat capacity [J.m ⁻³ .K ⁻¹]	ρC_p	2.2 10 ⁶
Linear solid thermal expansion coefficient [K ⁻¹]	β_s	10 ⁻⁵

Table 28: Thermal characteristics for the C30/37 liner

Steel components are also used in the seal and in the lost shield.

Geomechanical characteristics		steel
Young elastic modulus [MPa]	E_0	205000
Poisson ratio [-]	ν	0.3
Specific mass [kg/m ³]	ρ	7800

Table 29: Geomechanical characteristics for steel

Thermal characteristics		steel
Thermal conductivity [W.m ⁻¹ .K ⁻¹]	λ	50
Volumetric heat capacity [J.m ⁻³ .K ⁻¹]	ρC_p	3.9 10 ⁶
Linear solid thermal expansion coefficient [K ⁻¹]	β_s	1.2 10 ⁻⁵

Table 30: Thermal characteristics for steel

The grooved external surface of some parts of the liner allows a higher friction angle between the liner and the host clay. It is proposed to consider a friction angle of 16.7° for the grooved surface and of 5.7° for the non-grooved zone.

The backfill material, constituted of sand with a 40% porosity and saturated in water, may or may not be taken into account for sake of simplicity. In the case it is modelled, the properties of the backfill material given in the Table 31 to the Table 33 can be used.

Geomechanical characteristics		backfill material
Young elastic modulus [MPa]	E_0	1000
Poisson ratio [-]	ν	0.25
Specific mass [kg/m ³]	ρ	2500

Table 31: Geomechanical characteristics for the backfill material

Hydraulic characteristics		backfill material
Porosity [-]	n	0.40
Intrinsic permeability [m ²]	$k_{\text{int}}^{\text{sat}}$	1.10^{-12}

Table 32: Hydraulic characteristics for the backfill material

Thermal characteristics		backfill material
Thermal conductivity [W.m ⁻¹ .K ⁻¹]	λ	1.5
Volumetric heat capacity [J.m ⁻³ .K ⁻¹]	ρC_p	$2.2 \cdot 10^6$
Linear solid thermal expansion coefficient [K ⁻¹]	β_s	10^{-5}

Table 33: Thermal characteristics for the backfill material

3.4.4 Description of the calculation and the boundary conditions

The dimensions of the Finite Element Model are not imposed. The boundary conditions correspond to those of the 2D plane strain model (Figure 30). The excavation method has allowed an excavation rate (excavation + installation of the lining) of 2m/day. The liner is supposed to be put after a convergence of 0.06 m. For the seal element, it is proposed to model it with a steel ring (with the same thickness as the concrete one), without representing explicitly the bentonite. However, the action of the bentonite is modelled by imposing a total stress history corresponding to the swelling pressure and considering impervious condition at the steel extrados.

The history of the swelling pressure is given in the Table 34.

Time [yr]	Swelling pressure [MPa]
0	0
1	1.4
1.5	3
2.5 and later	4.5

Table 34: Time evolution of the swelling pressure after the installation of the seal

Figure 33 represents the schematic geometry in this 2D modelling, with the different materials. The participants are allowed to simplify this geometry for the modelling efforts.

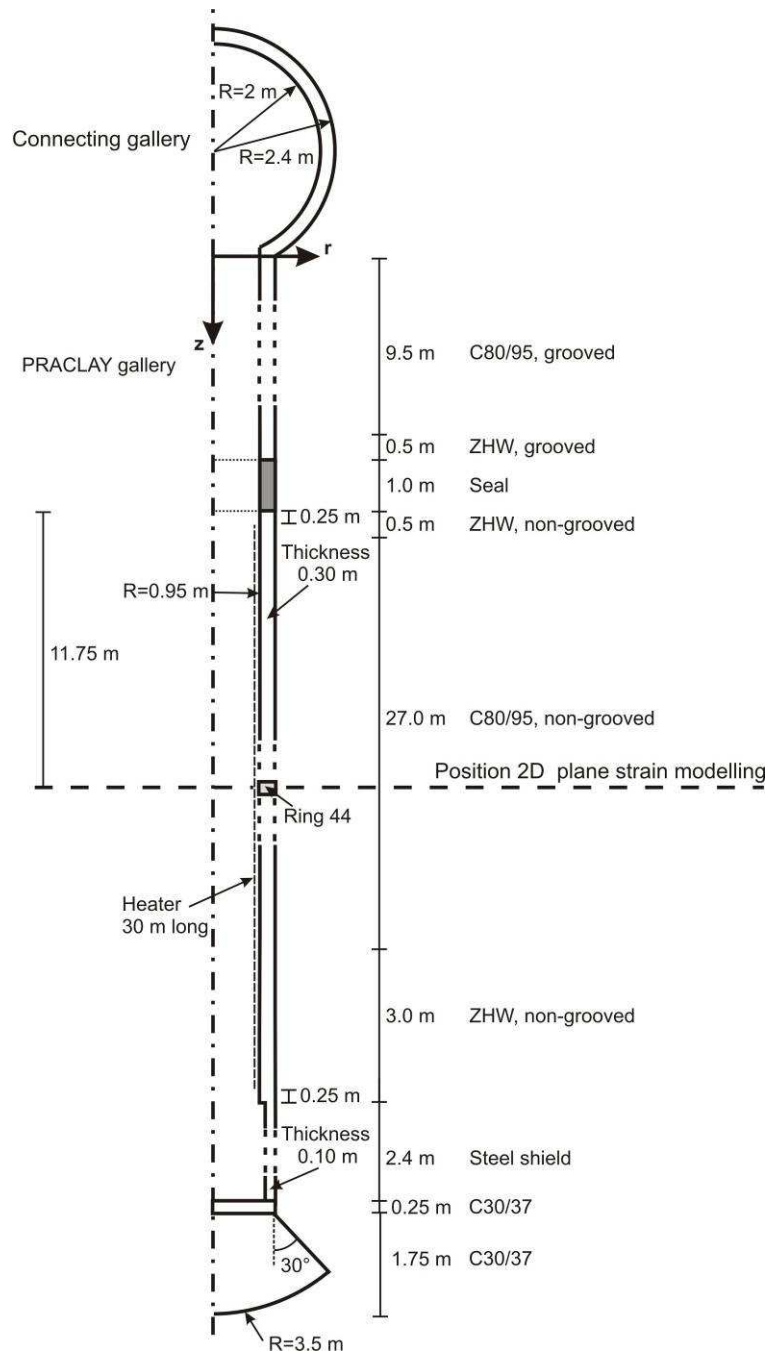


Figure 33: Schematic representation of geometry in the 2D axis-symmetric modelling

The modelling first consists in the excavation of the gallery and, in a second step, a thermal loading is applied at the extrados of the liner:

Phase 1: Duration: 20 days

- Excavation of the gallery.
- Temperature fixed at initial value on the whole domain.

TIMODAZ

The numerical modelling of the excavation process is not imposed (progressive, step by step, instantaneous) but, after 20 days, the total stress is equal to zero and the pore pressure is equal to 100 kPa.

Phase 2: Duration: 2.5 years

- Waiting phase: pore pressure fixed at 100 kPa on the liner intrados.
- Temperature fixed at initial value on the whole domain.

Phase 3: Duration: 1 year

- Installation of the seal (total stress increase, impervious boundary)
- Waiting phase: pore pressure fixed at 100 kPa on the liner intrados.
- Temperature fixed at initial value on the whole domain.

Phase 4: Duration: 6 months

- Heater phase: temperature linearly increasing from initial value to 85°C at the intrados of the liner (Be careful the heater is 30 m long).
- Water undrained conditions at the liner intrados in the part of the gallery after the seal. The hydraulic conditions remain the same as the ones in the previous phases, in the part of the gallery between the connecting gallery and the seal.

Phase 5: Duration: 10 years

- Stabilised heater phase: temperature fixed to 85°C at the intrados of the liner.
- Water undrained conditions at the liner intrados in the part of the gallery after the seal. The hydraulic conditions remain the same as the ones in the previous phases, in the part of the gallery between the connecting gallery and the seal.

The actual heater system is constituted of a pipes network with heat water flow inside; it is located 10 cm inside the intrados of the liner and imposes a temperature, as constant as possible, of about 80°C at the extrados gallery wall. In that proposition, this complex system is idealised simply by imposing an increase of the temperature directly at the intrados of the liner.

3.4.5 Output results

It is asked to supply the results (pore water pressure p_w , temperature T , effective stresses σ'_r , σ'_z and displacements u_r , u_z) along the five profiles (Figure 34) for the 9 following times:

- End of the phase 1 (excavation phase): $t_1 = 20$ days = 1 728 000 sec.
- End of the phase 2 (waiting phase): $t_2 = t_1 + 2.5$ years = 80 568 000 sec.
- End of the phase 3 (seal + waiting phase): $t_3 = t_2 + 1$ year = 112 104 000 sec.
- End of the phase 4 (heater phase): $t_4 = t_3 + 0.5$ year = 127 872 000 sec.
- Phase 5 (heater phase): $t_4 = t_3 + 0.5$ year = 143 640 000 sec.
- Phase 5 (heater phase): $t_5 = t_3 + 1$ year = 159 408 000 sec.
- Phase 5 (heater phase): $t_6 = t_3 + 2$ years = 190 944 000 sec.
- Phase 5 (heater phase): $t_7 = t_3 + 5$ years = 285 552 000 sec.



- End of the phase 5 (heater phase): $t_8 = t_3 + 10 \text{ years} = 443\,232\,000 \text{ sec.}$

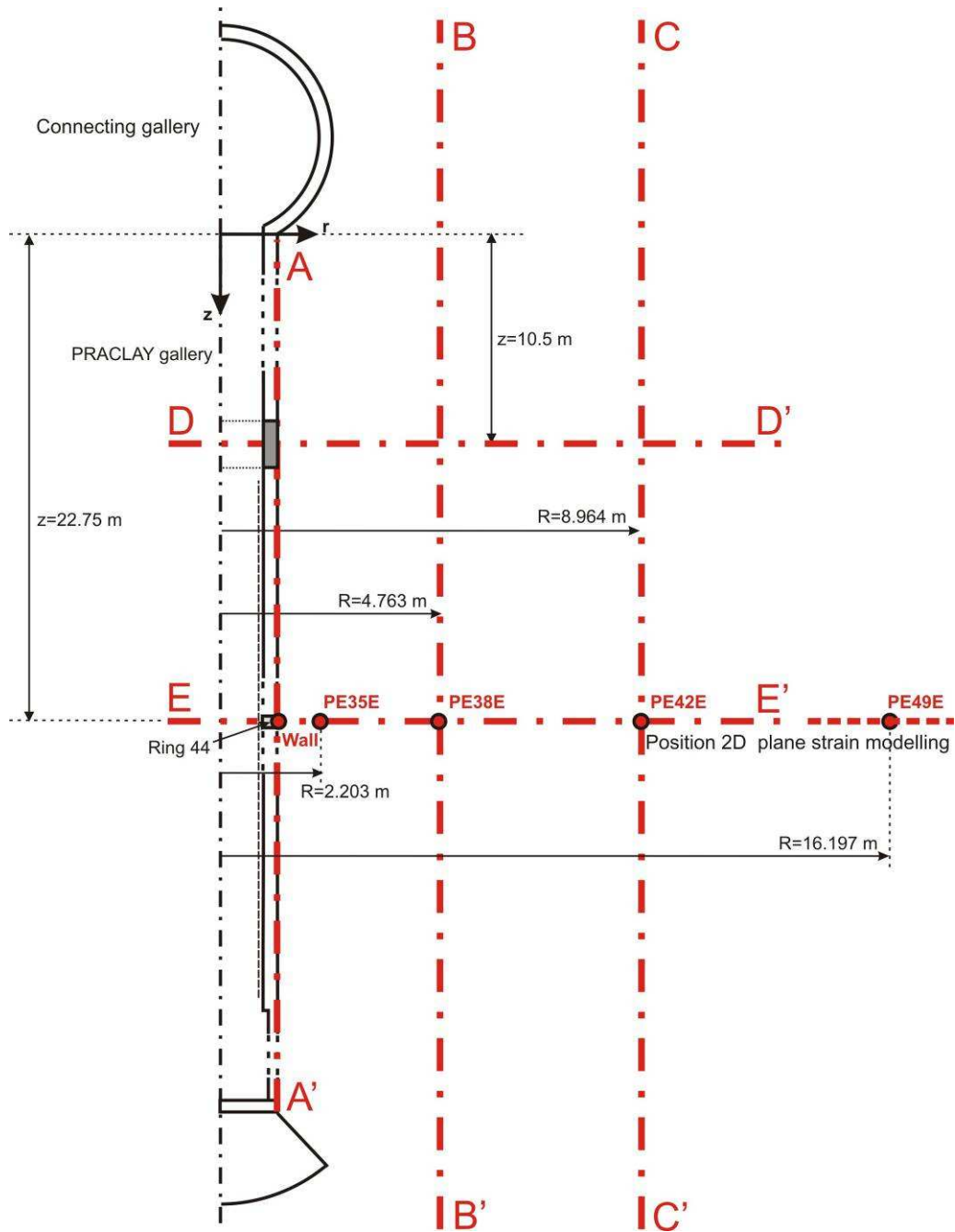


Figure 34: Five profiles output results for the 2D axis-symmetric modelling

It is asked also to supply the time evolution of some results (pore water pressure p_w , temperature T , mean effective stress p' and deviatoric effective stress q) for the 4 sensors (P35E, P38E, P42E and P49E) and the wall of the Boom clay, located on the Figure 34. The nominal radial distances from the centre of the gallery to the sensors P35E, P38E, P42E and P49E are respectively 2m, 5m, 9m and 16m but the correct distances taking borehole deviation into account are given in the Table 35.

Sensors	Radial distance r [m]
P35E	2.203
P38E	4.763
P42E	8.964
P49E	16.197

Table 35: Sensors location taking deviation into account (ring 44)

It is also asked to provide the temporal evolution of the global (2π radian) dissipated power (for one meter thickness) all during the heating phase.

3.5 3D modelling

The geometry of the 3D modelling should be inspired by the geometry of the two preceding cases. This modelling effort should concentrate on the anisotropic effects in the Boom clay.

4 General form of numerical results

4.1 2D plane strain modelling

Partners active in this model: NRG – ULg – Euridice – CIMNE

4.1.1 Pore water pressure

In the 2D plane strain modelling, the anisotropy of the initial stresses is taken into account. The effect on the pore water pressure field can be seen as soon as the excavation takes place.

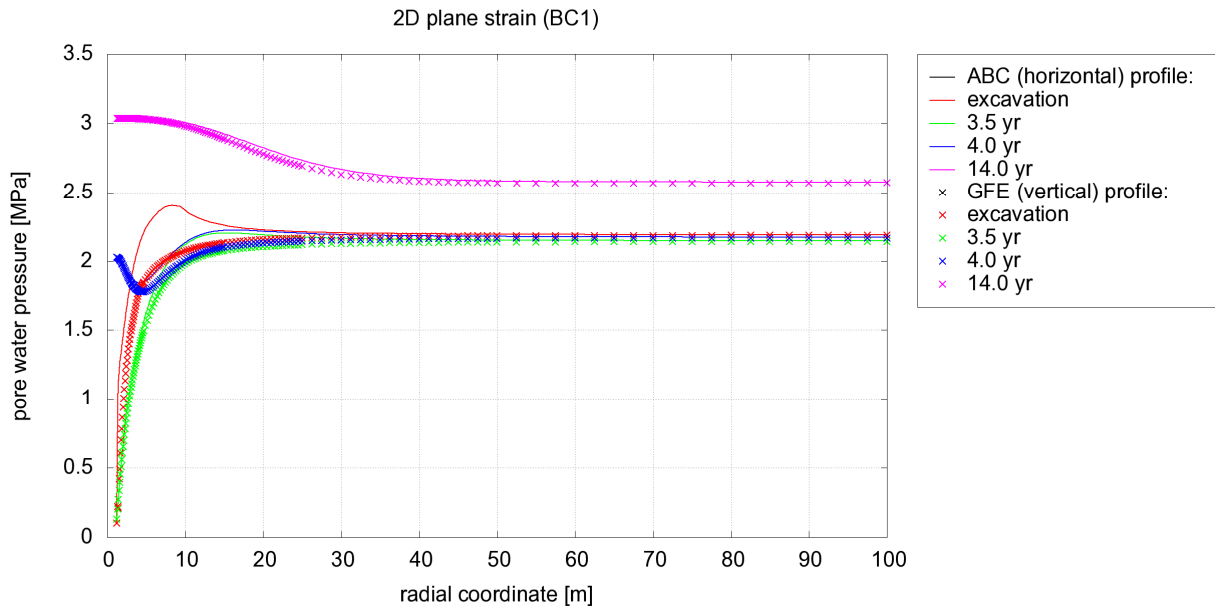


Figure 35: Pore water pressure along ABC (horizontal) and GFE (vertical) profiles

The Figure 35 shows the evolution in time of the pore water pressure (p_w) profiles along the horizontal and vertical directions (ABC and GFE, respectively). This figure corresponds to the far-field boundary conditions considered in a first time (denoted BC1), that are no x- and y-displacement.

Just after the excavation (in red), p_w decreases in the vicinity of the excavated tunnel due to the drainage boundary condition (100 kPa). The difference of behaviour in the horizontal and vertical directions is the most visible at that moment: while p_w is monotonically increasing from the excavated gallery to the far-field in the GFE vertical direction (red x-marks in the figure). The curve representing p_w in the ABC horizontal direction (continuous red curve) exhibits a peak equal to 2.4 MPa around 8m from the gallery axis, and then it decreases to 2.25 MPa, the initial value. The Figure 36 is another illustration of the non-uniform pore water pressure field at the end of the excavation.

After a period of time equal to 3.5 years (green x-marks and curve, Figure 35), the PRACLAY gallery is closed and heater test begins. The difference between vertical and horizontal profiles is not as pronounced as just after the excavation.

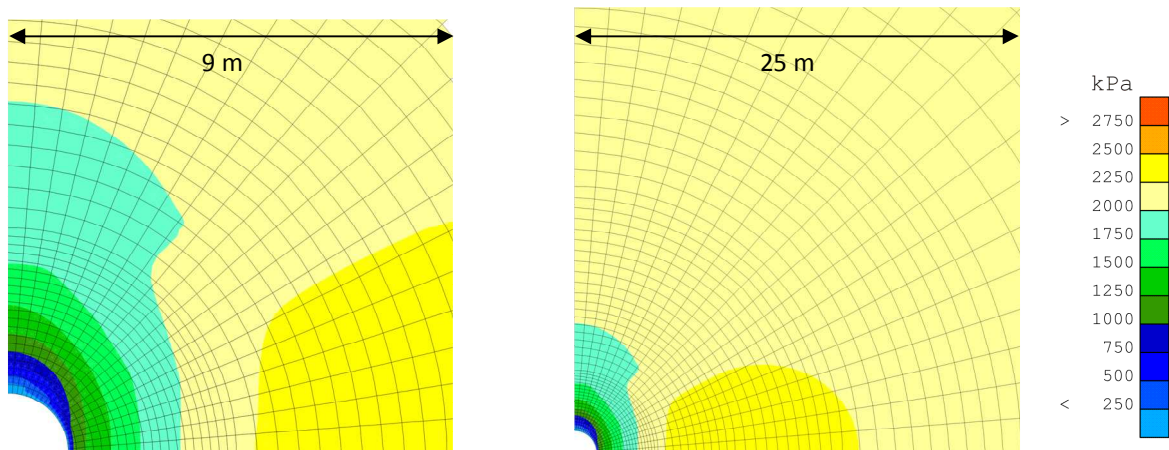


Figure 36: Pore water pressure at the end of the excavation.
Detailed view of the same contour levels at two different scales.

Due to the heating, p_w increases, first in the vicinity of the gallery, then further. The blue x-marks and curve represent p_w 4 years after the excavation, or 6 months after the beginning of the heater test, i.e. when the temperature of the heater device reaches the nominal temperature (85°C).

The magenta x-marks and curve correspond to the end of the heater experiment, 10 years after constant heating, or 14 years after the excavation. As it clearly appears on Figure 35:

- the pore water pressure is much larger than in the initial conditions, reaching 3 MPa in the vicinity of the gallery, and decreasing to about 2.55 MPa in the far-field;
- the difference between the vertical and horizontal profiles is still visible, but much smaller compared to the difference during the first period modeled.

Effect of the far-field boundary conditions:

As suggested by Euridice, a second type of mechanical far-field boundary conditions (denoted BC2) has been investigated. Instead of zero x- and y-displacements on CD and DE boundaries (cf. Figure 30), displacements are free and a loading condition is applied, assuming total stresses equal to:

- $q_y = -4.5$ MPa in the vertical y-direction along DE (compressive load)
- $q_x = -3.825$ MPa in the horizontal x-direction along CD (compressive load)

Using these BC2, one gets slightly different results, as depicted on Figure 37. Globally, the remark concerning the effect of anisotropy of the initial effective stresses is still valid (difference between horizontal and vertical profiles).

The main difference with respect to BC1 is the final level of the p_w :

- in the vicinity of the PRACLAY gallery, p_w reaches up to 3 MPa using BC1, while the maximum value is about 2.65 MPa when BC2 are used ;
- in the far-field, p_w increases significantly, exceeding 2.5 MPa, with BC1, while it remains at the initial value (2.25 MPa) when using BC2.

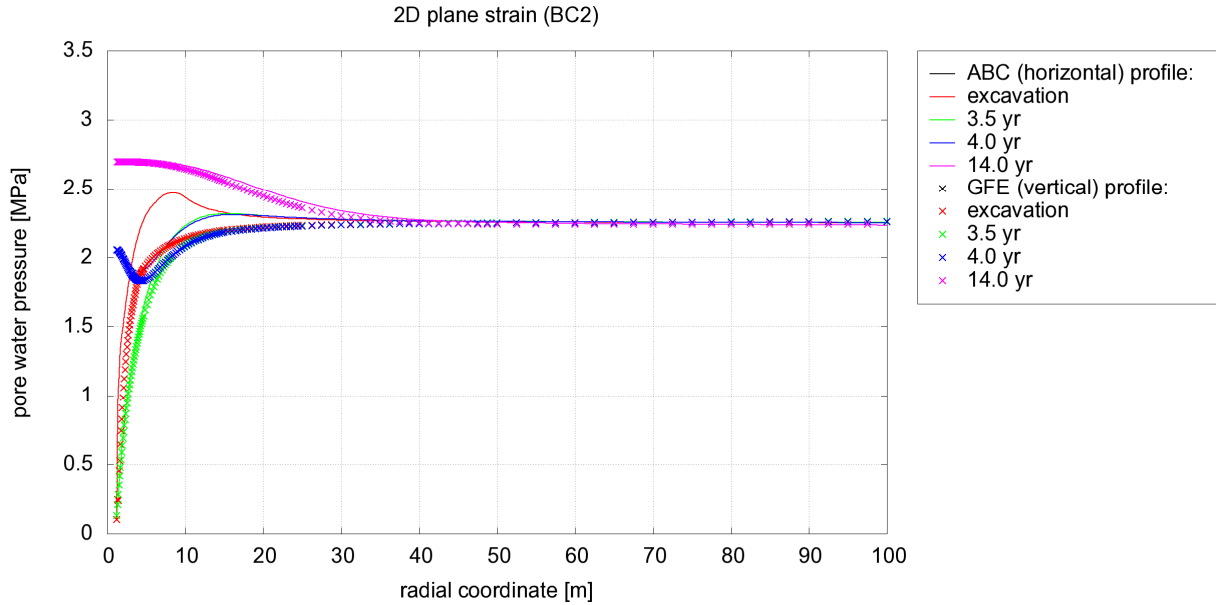


Figure 37: Pore water pressure along ABC (horizontal) and GFE (vertical) profiles using BC2

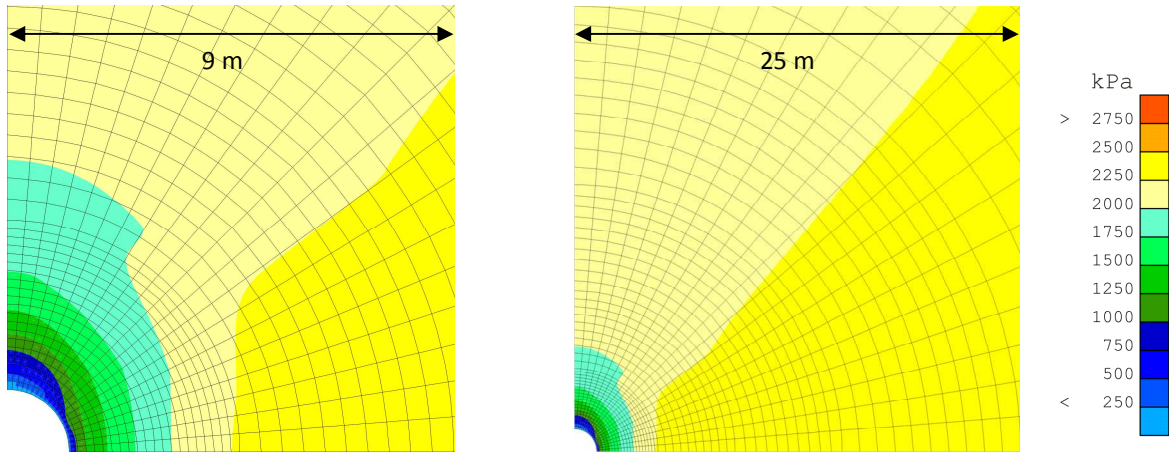


Figure 38: Pore water pressure at the end of the excavation using BC2.
Detailed view of the same contour levels at two different scales.

Evolution in time of p_w at the sensors location

The evolution of p_w is plotted in the Figure 39, using BC1. Three main phases can be identified:

- First, a quasi-instantaneous p_w decrease corresponds to the excavation. The drop amplitude is obviously larger for sensors close to the gallery wall, where p_w decreases down to 100 kPa that is a drainage boundary condition. For P35E sensor, p_w stops decreasing when the contact occurs between Boom clay and the liner (convergence of the clay), modifying mechanical stresses.
- Then, during the next 3.5 years, p_w is still decreasing, but the rate of decrease is lower, more especially for sensors further from the gallery (P49E, which is about 16 m far from the gallery axis). Due to the “building” of the liner, the drainage conditions are a little bit different: the 100 kPa boundary condition is now applied at the inner surface of the concrete liner instead of the outer surface (the excavation wall). That is the reason why p_w at the wall is quickly rising first, and then decreases again.

- The third phase corresponds to the heater test. From 3.5 years to 4 years, the temperature at the inner surface of the liner is increasing from 16°C to 85°C, and then it remains constant at 85°C for 10 additional years. Due to the heating, p_w increases. The rate of increase is higher in the vicinity of the gallery. It can be observed that p_w at the wall and sensors P35E, P38E, and P42E is approximately the same during the 10 last years. The value of p_w at sensor P49E is slightly lower (about 0.15 MPa) that the value at the other locations.

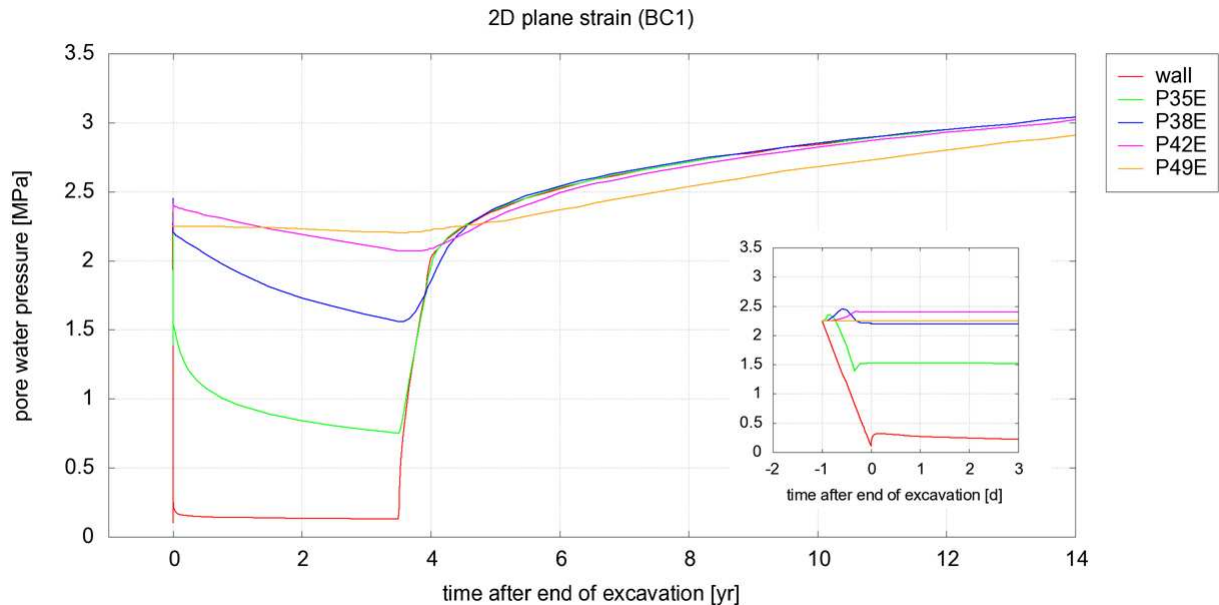


Figure 39: Evolution in time of the pore water pressure at sensors location

Considering now the second type of boundary conditions, one gets the curves in Figure 40. The behaviour is similar to the one using BC1. The main difference is a lower rate of increasing p_w during the heater test using BC2. The final p_w is also lower: 2.65 MPa vs. 3 MPa using BC1.

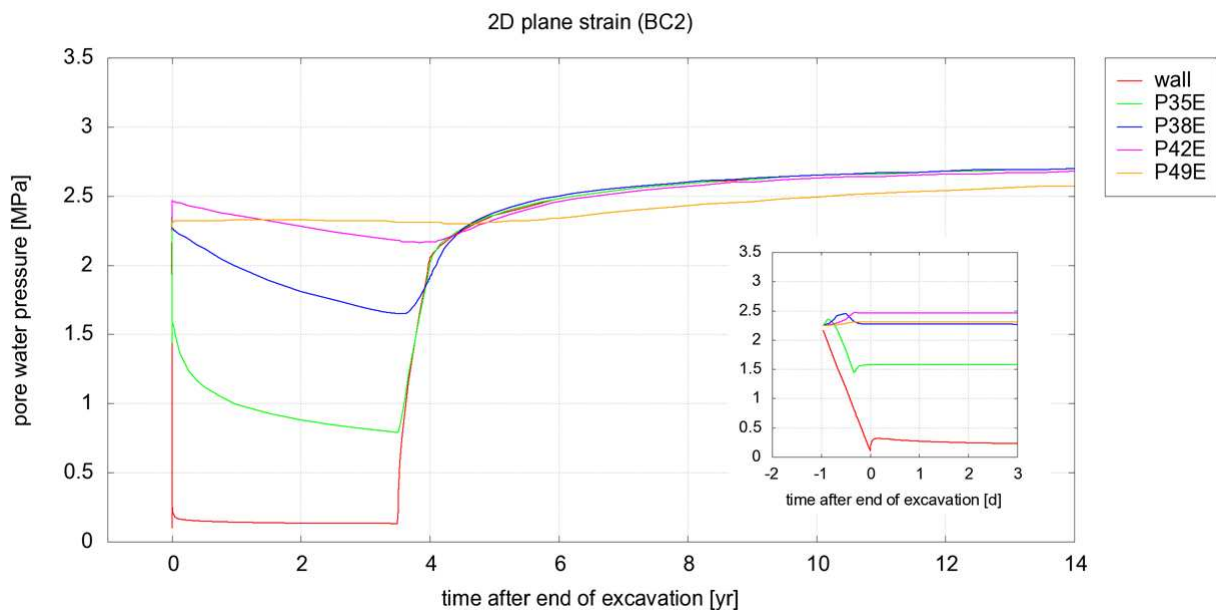


Figure 40: Evolution in time of the pore water pressure at sensors location using BC2

4.1.2 Temperature

The temperature is uniform and equal to 16°C before the heater test begins, i.e. during the 3.5 first years.

Then, during the heater test, the profiles in the vertical and horizontal directions remain equal, as it could be expected: there is no influence of the only anisotropy introduced in the model (which is the anisotropy of initial effective stresses).

The increase of temperature is almost equal to zero in a large domain: even at the end of the test, the temperature remains at 16°C from the far-field up to 50 m from the gallery axis (cf. Figure 41).

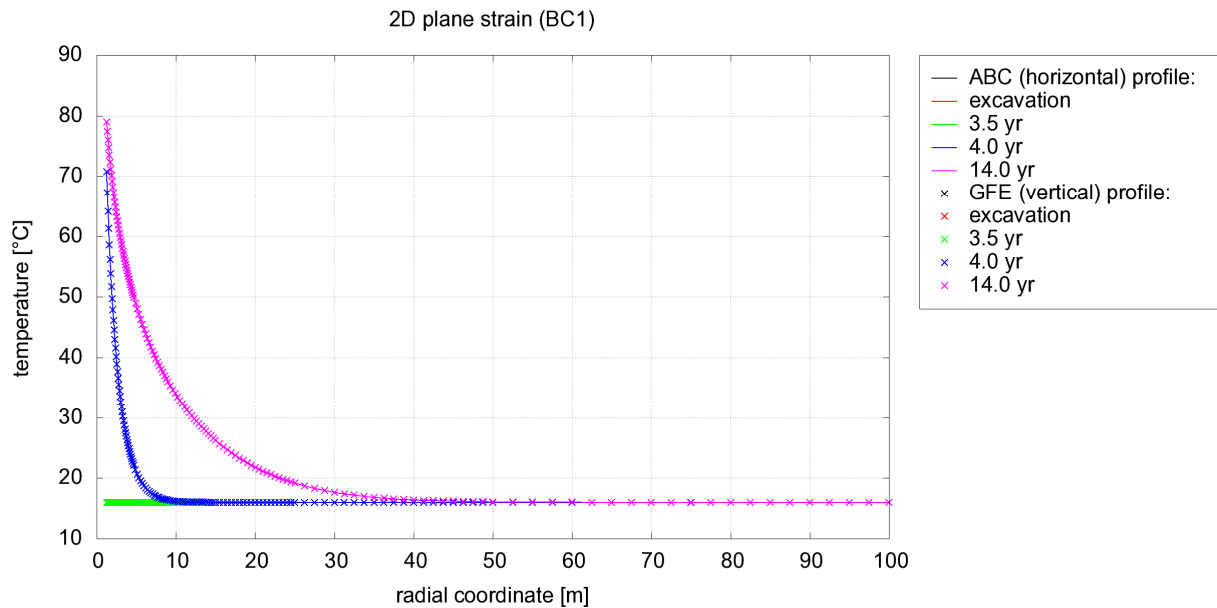


Figure 41: Temperature profiles

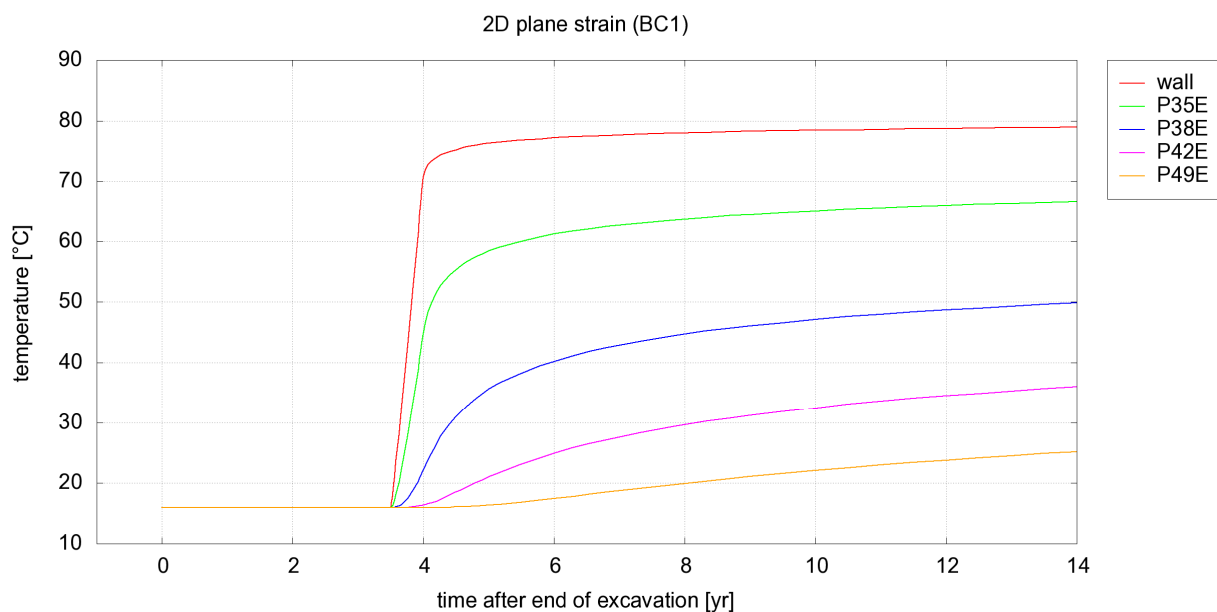


Figure 42: Evolution in time of the temperature at sensors location

The increase of temperature is lower than 10°C at 20 m (at the end of the test), and the temperature is about 25°C at sensor P49E location (16 m from the gallery axis), as shown in Figure 42. Higher temperatures are observed in the vicinity of the gallery: almost 80°C at the wall, and more than 50°C up to sensor P42E (4.7 m from gallery axis).

Effect of the far-field boundary conditions:

The modification of far-field mechanical boundary conditions (BC2) has absolutely no influence on the temperature field, so only figures using BC1 are depicted here.

4.1.3 Radial displacement

The radial displacement at the wall of the excavated gallery reaches immediately -6 cm in both vertical and horizontal directions, which correspond to the convergence of the Boom clay (excavation radius = 1.31 m) entering in contact with the concrete liner (external radius = 1.25 m).

Going deeper inside the Boom clay, the radial displacement decreases and becomes anisotropic, as shown in the Figure 43. In fact, the radial displacement is anisotropic (due to the anisotropic initial effective stresses), but the shape of the liner (a circular section) induces the same radial displacement in both vertical and horizontal direction in the very close vicinity of the gallery, as long as the Boom clay is in contact with the liner. The fact is that the Boom clay enters in contact in the vertical direction before it enters in the horizontal direction, but this is not noticeable at the time-scale of the figure.

Due to the heating, the radial displacement decreases (more precisely it becomes less negative) and even a positive radial displacement can be observed at the end of the test for radial coordinates higher than 5 m. For the coordinates under 5 m, the radial displacement remains negative, the effect of the Boom clay convergence being larger than the effect of thermal dilatation.

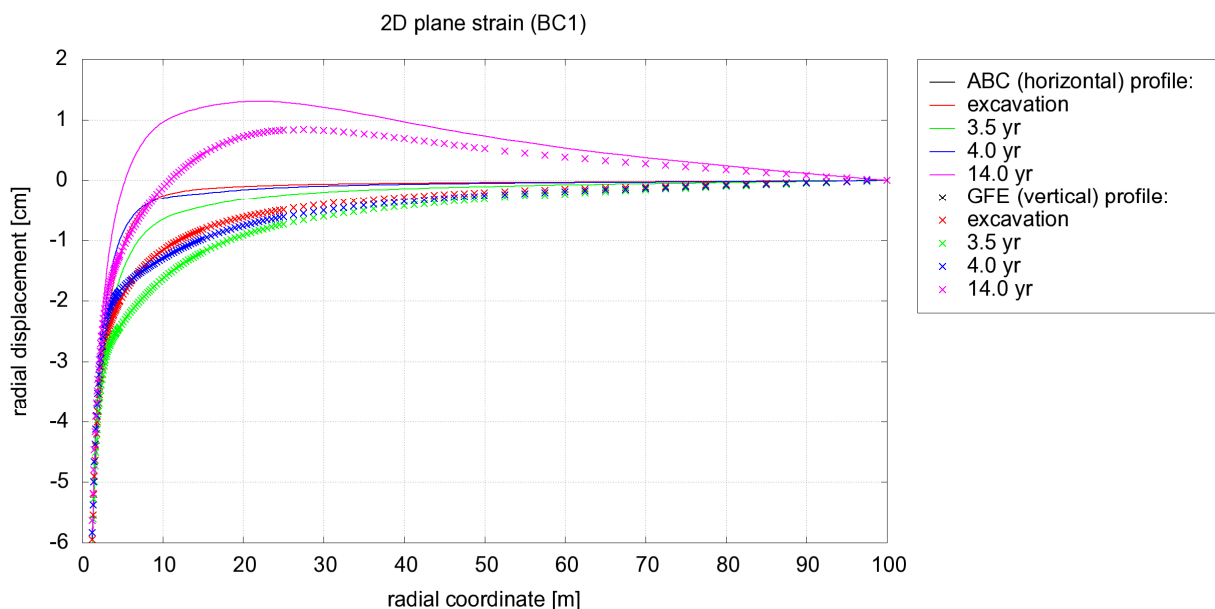


Figure 43: Radial displacement along ABC (horizontal) and GFE (vertical) profiles

In the Figure 43, the influence of the far-field mechanical boundary conditions can clearly be observed: since zero-displacement is prescribed at the boundary in both directions, the radial

displacement tends to zero during the whole test (from the excavation until 14 years after) and for both vertical and horizontal profiles.

In the Figure 44, the radial displacement is plotted when using the second type of boundary conditions. The main difference with respect to using BC1 is that the displacement being free at the far-field boundaries, it remains anisotropic all along the profiles including at the far-field boundaries, where the amplitude of the displacement is less than 0.5 cm.

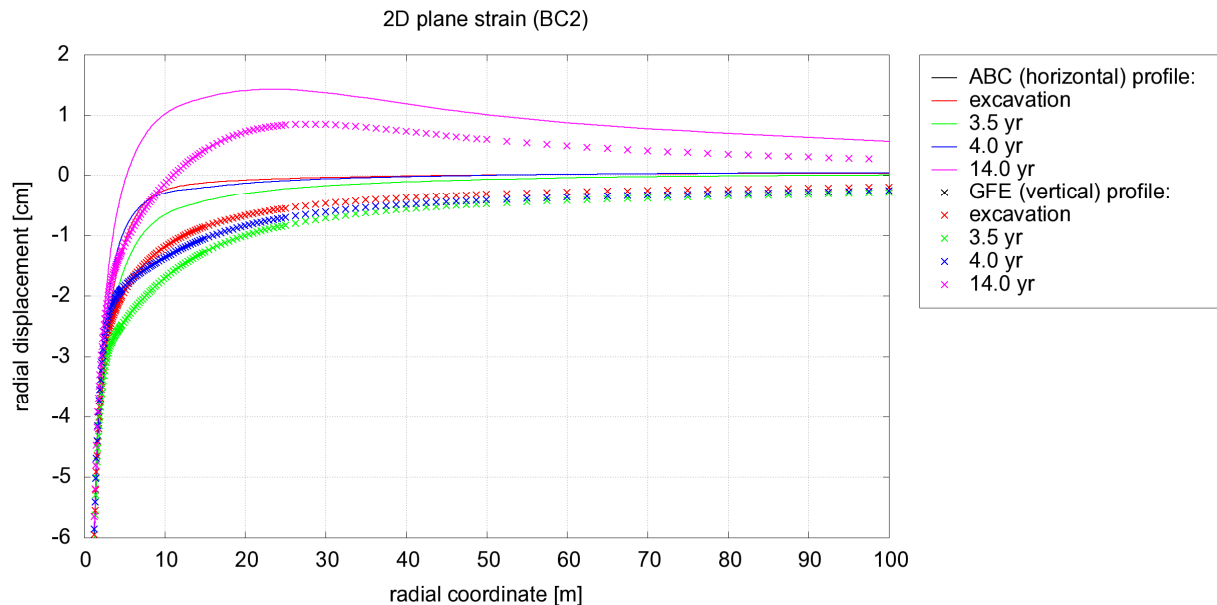


Figure 44: Radial displacement along ABC (horizontal) and GFE (vertical) profiles using BC2

4.1.4 Effective stresses

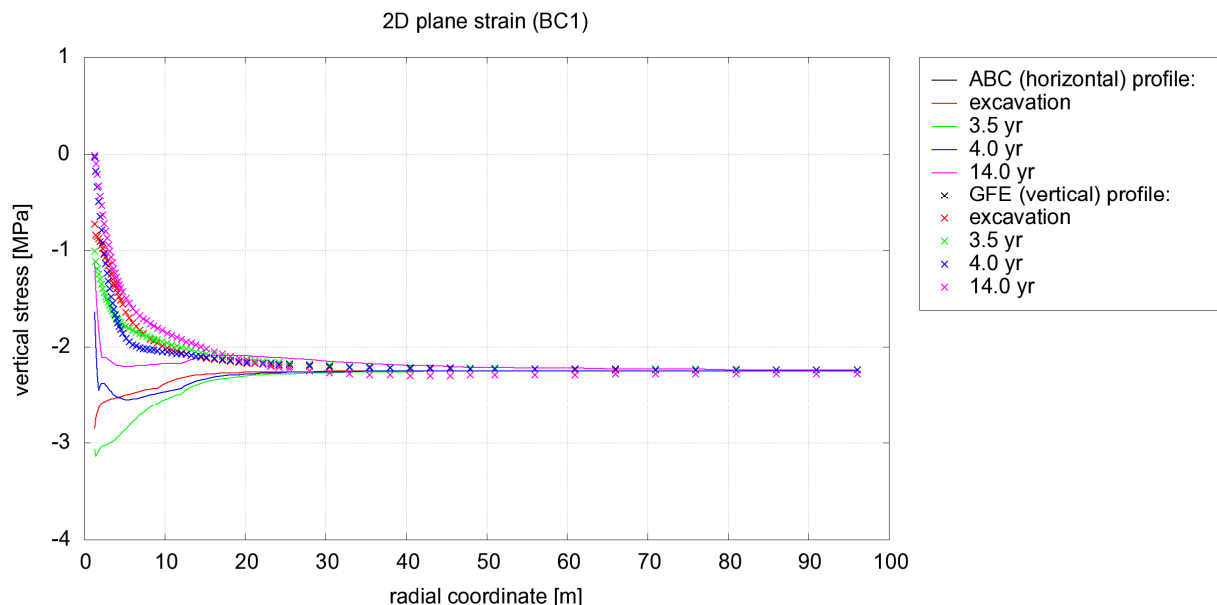


Figure 45: Vertical effective stress along ABC (horizontal) and GFE (vertical) profiles

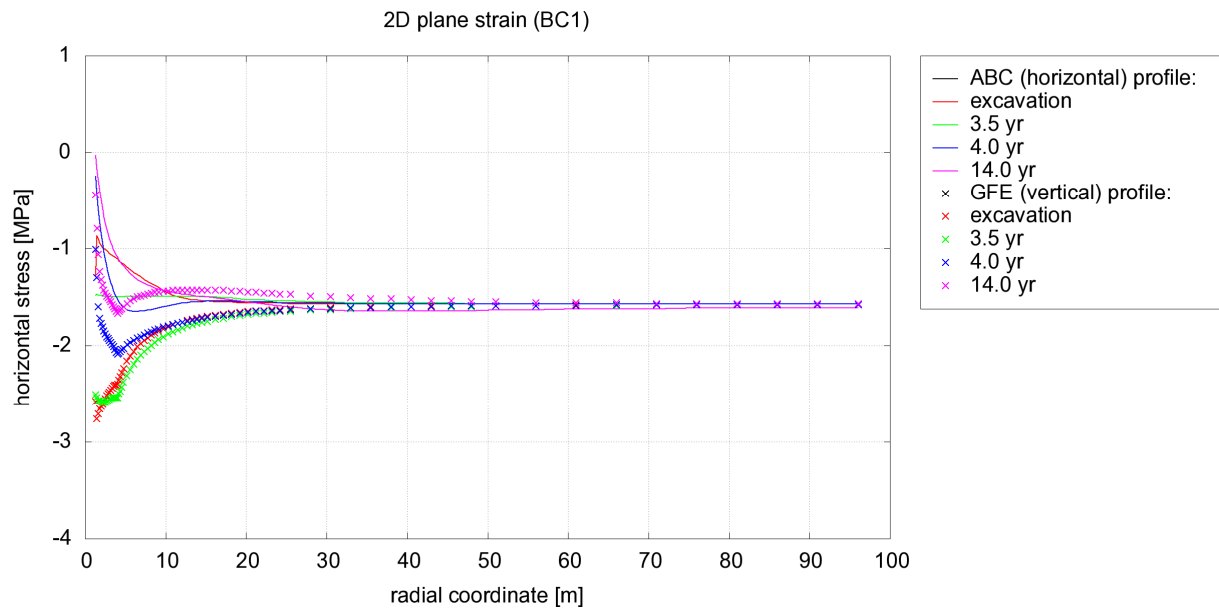


Figure 46: Horizontal effective stress along ABC (horizontal) and GFE (vertical) profiles

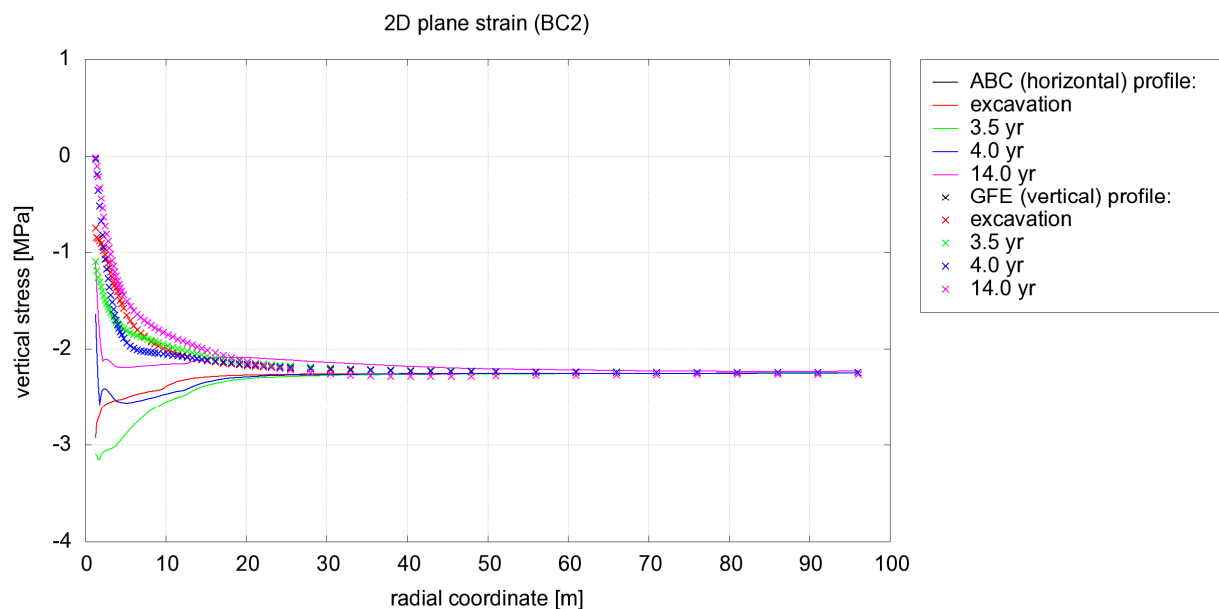


Figure 47: Vertical effective stress along ABC (horizontal) and GFE (vertical) profiles using BC2

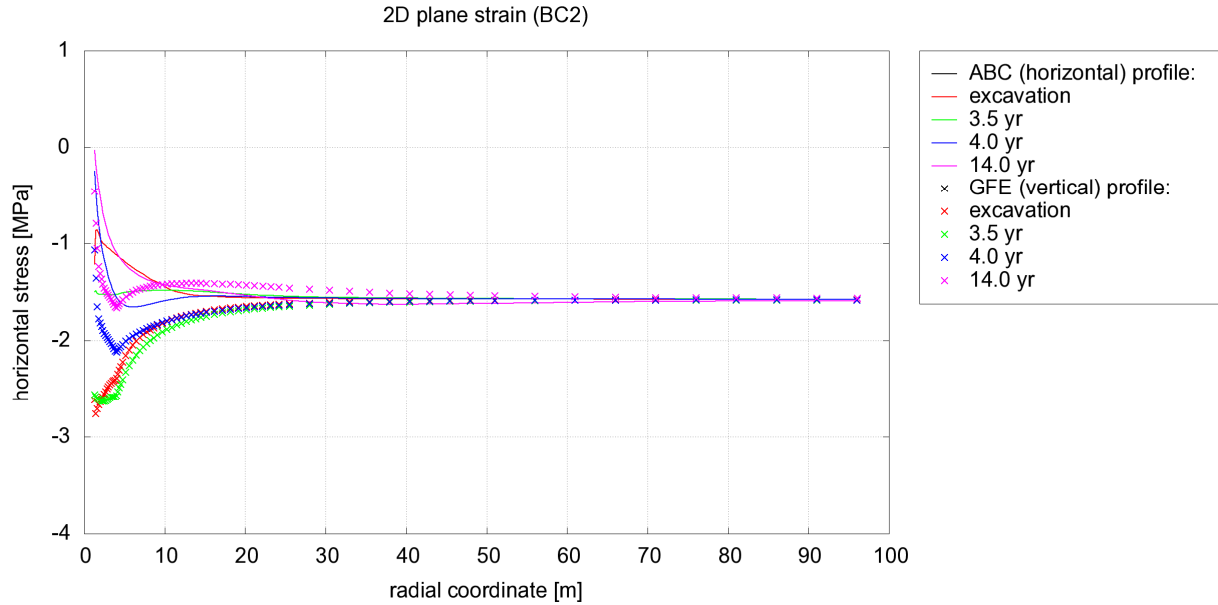


Figure 48: Horizontal effective stress along ABC (horizontal) and GFE (vertical) profiles using BC2

Mean and deviatoric effective stresses and stress path at sensors location

The Figure 49 and Figure 50 represent the evolution of the mean and deviatoric effective stresses, p' and q respectively defined as below, at sensors location. The initial values are:

- mean effective stress $p' = \frac{1}{3} \sigma'_{ii} = -1.8$ MPa
- deviatoric effective stress $q = \sqrt{\frac{1}{2} \hat{\sigma}'_{ij} : \hat{\sigma}'_{ij}} \approx 0.39$ MPa

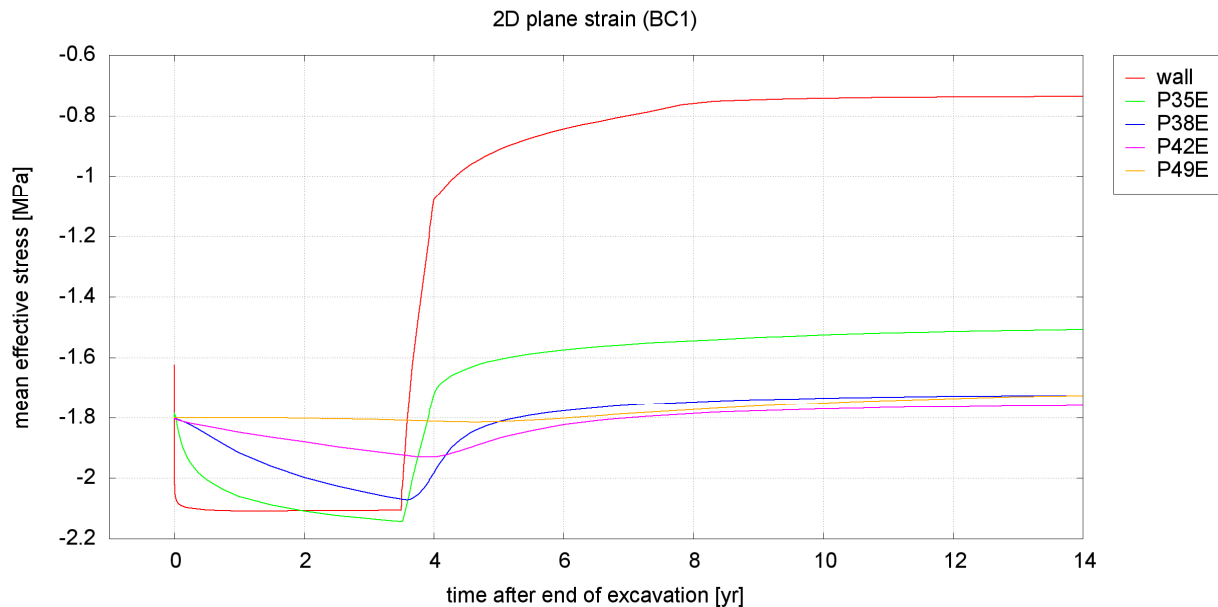


Figure 49: Evolution in time of mean effective stress p' at sensors location

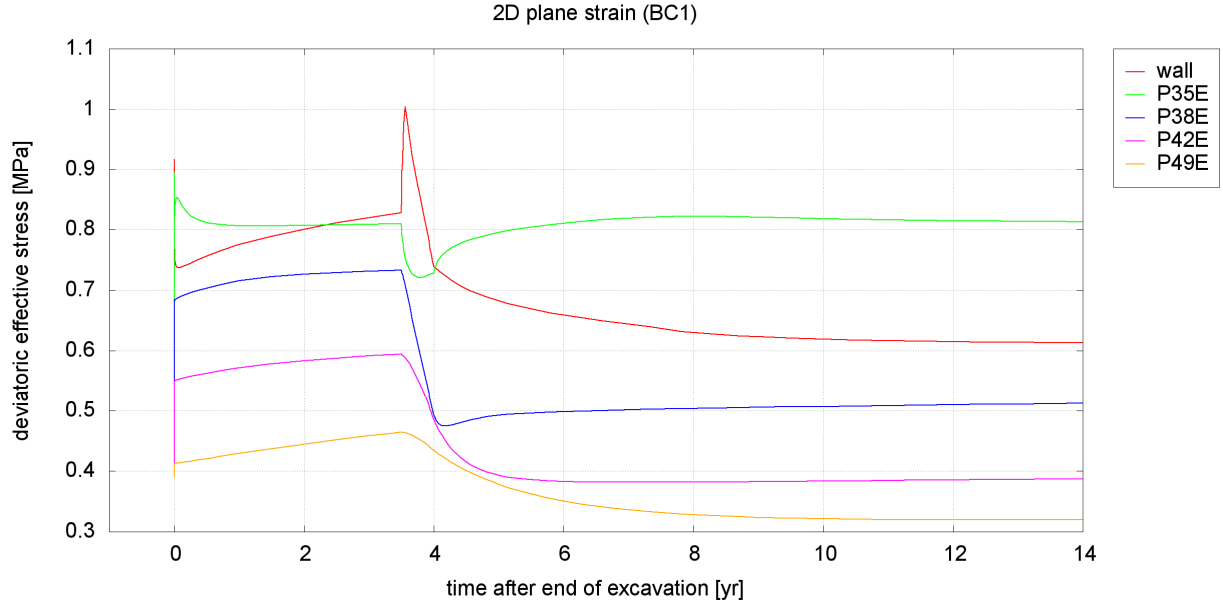


Figure 50: Evolution in time of deviatoric effective stress q at sensors location

The Figure 51 illustrates the stress path at sensors location in the plane of the two (effective) stress invariants I_1 and I_2 defined as:

$$I_1 = \sigma'_{ii} = 3p' \quad (1)$$

$$I_2 = \sqrt{\frac{3}{2} \hat{\sigma}'_{ij} : \hat{\sigma}'_{ij}} = \sqrt{3}q \quad (2)$$

The yield surface is defined as:

$$I_2 = \sqrt{3}m \left(\frac{3c}{\tan \phi} - I_1 \right) \quad \text{with} \quad m = \frac{2 \sin \phi}{\sqrt{3}(3 - \sin \phi)} \quad (3)$$

The Figure 51 shows that the plastic domain is reached at the location of all sensors, except P49E, which is located about 16 m far from the gallery axis and remains in the elastic domain.

The stress path during all successive phases (excavation, stabilization, heating) is detailed in Figure 52 to Figure 56 for each of the sensor locations.

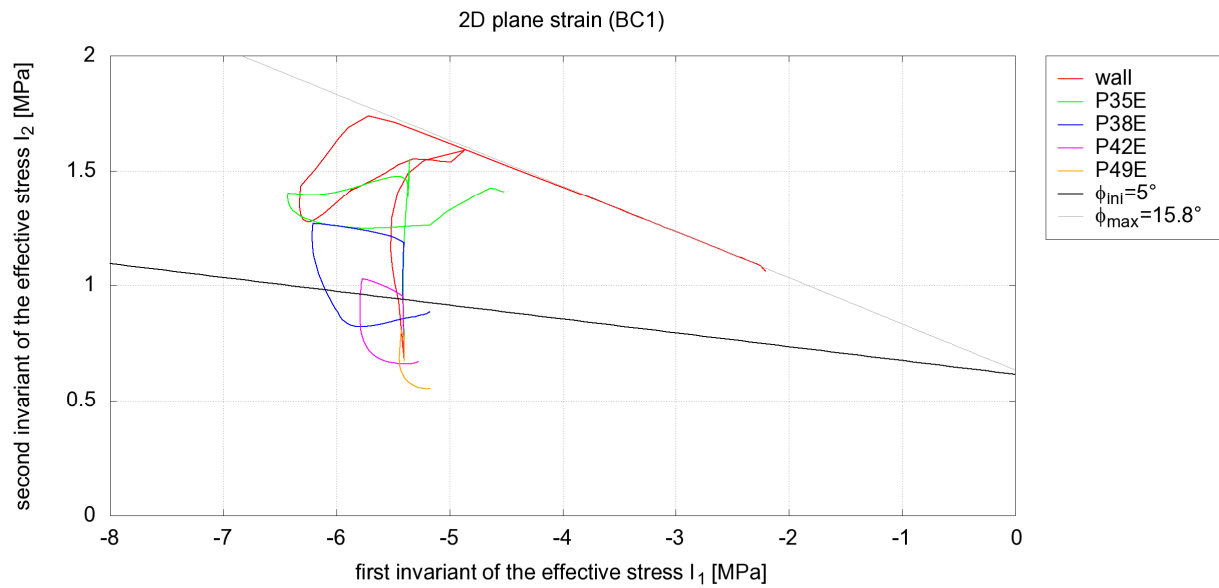


Figure 51: Stress path in the I_1 - I_2 invariants space at sensors location

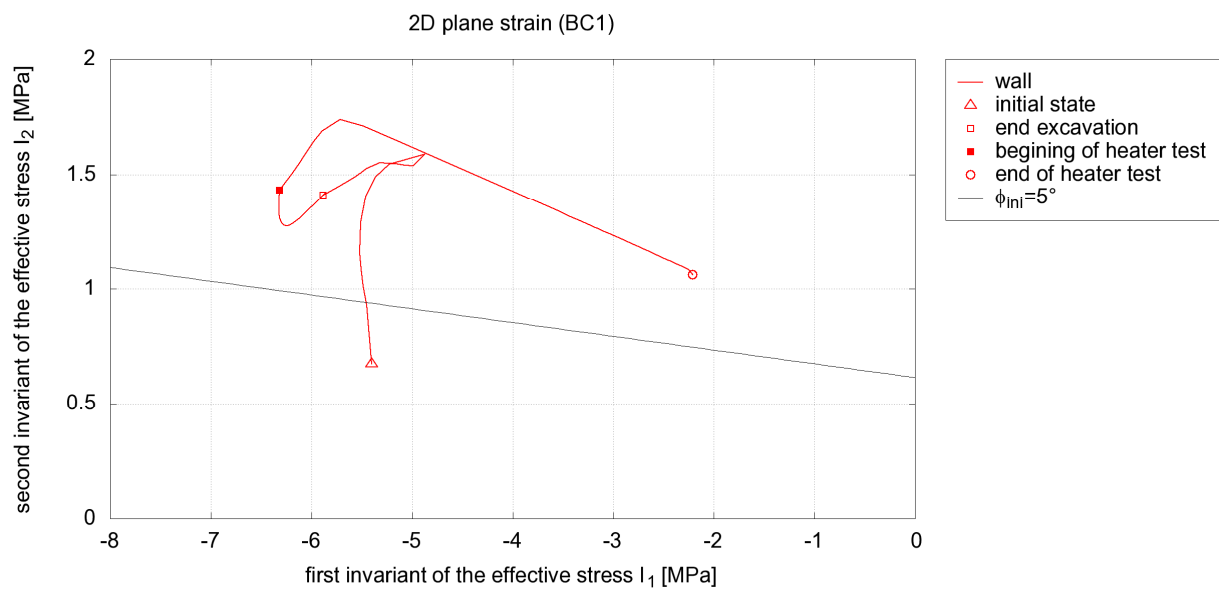


Figure 52: Stress path in the I_1 - I_2 invariants space at the wall (Boom clay / PRACLAY gallery interface)

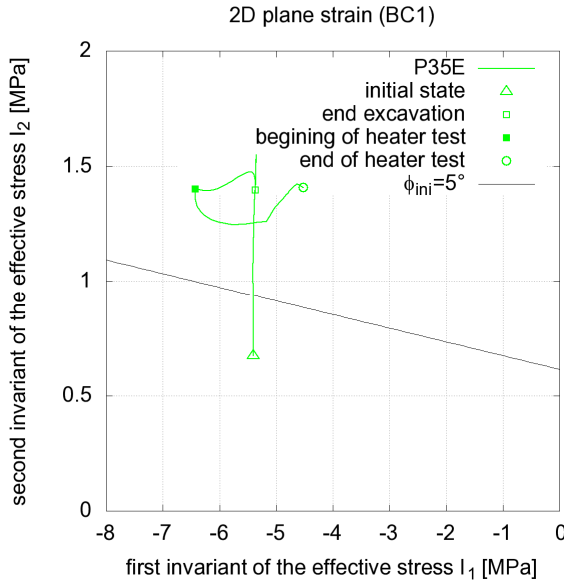


Figure 53: Stress path in the I_1 - I_2 invariants space at sensor P35E

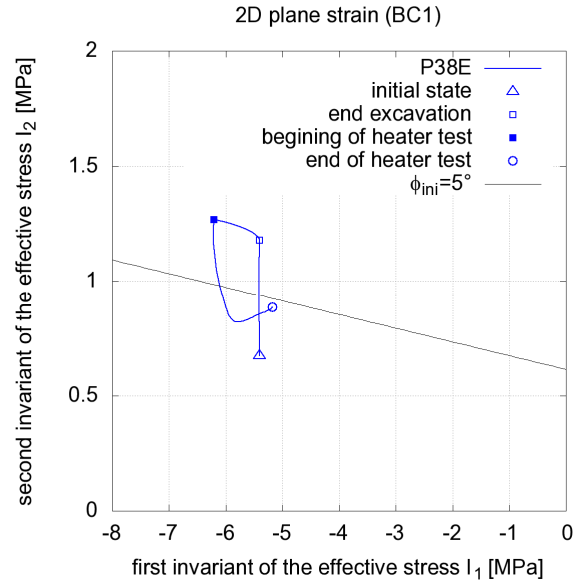


Figure 54: Stress path in the I_1 - I_2 invariants space at sensor P38E

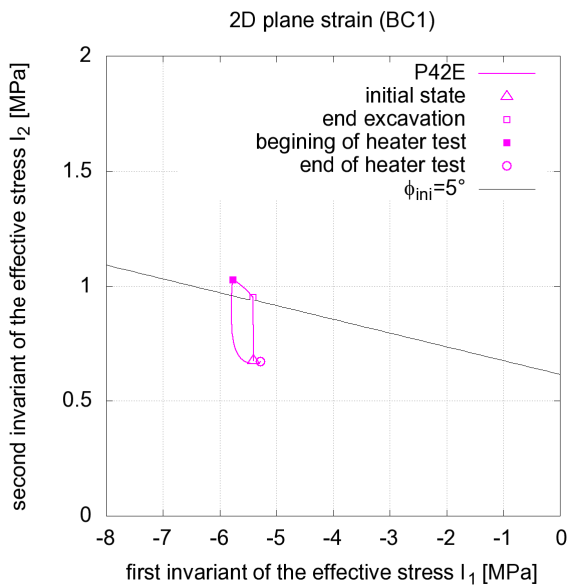


Figure 55: Stress path in the I_1 - I_2 invariants space at sensor P42E

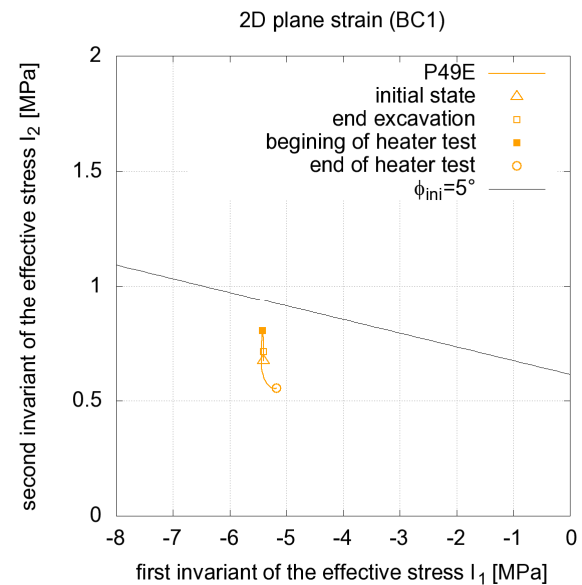


Figure 56: Stress path in the I_1 - I_2 invariants space at sensor P49E

Influence of the boundary conditions

The Figure 57 and Figure 58 show the evolution of the mean and deviatoric effective stress at the sensors location using BC2. The Figure 59 shows the stress path in the space of I_1 - I_2 stress invariants, using BC2. The results are quite similar to those obtained using BC1, since the sensors are located relatively close to the gallery (maximum 15 m) and far from the boundaries of the model (the extent of which being a square 100 m wide).

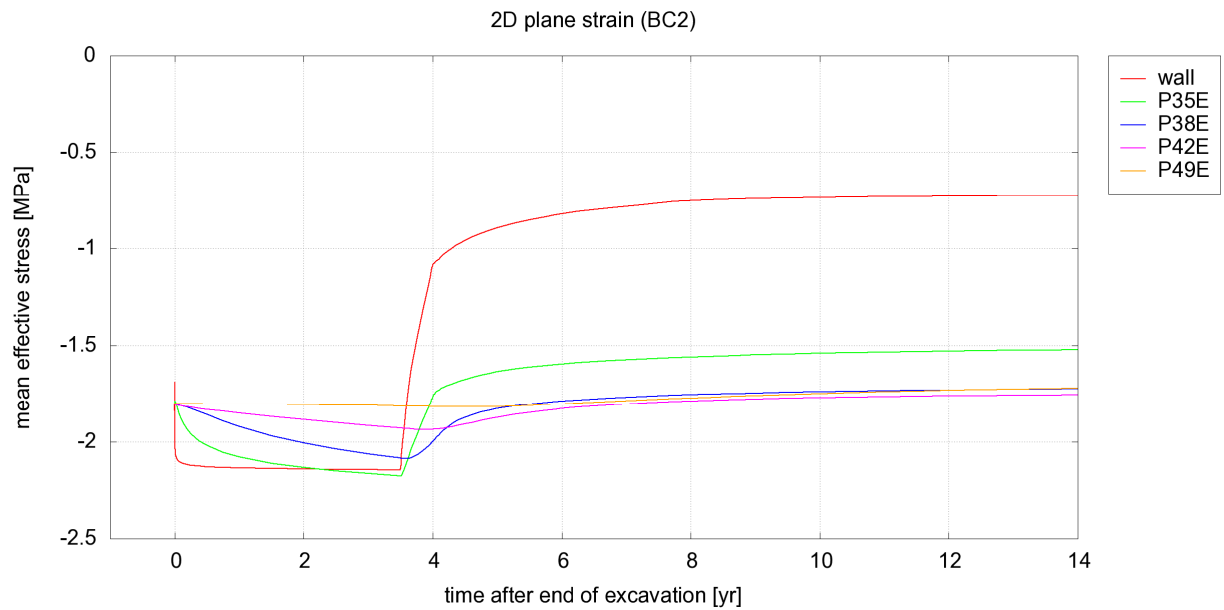


Figure 57: Evolution in time of mean effective stress p' at sensors location using BC2

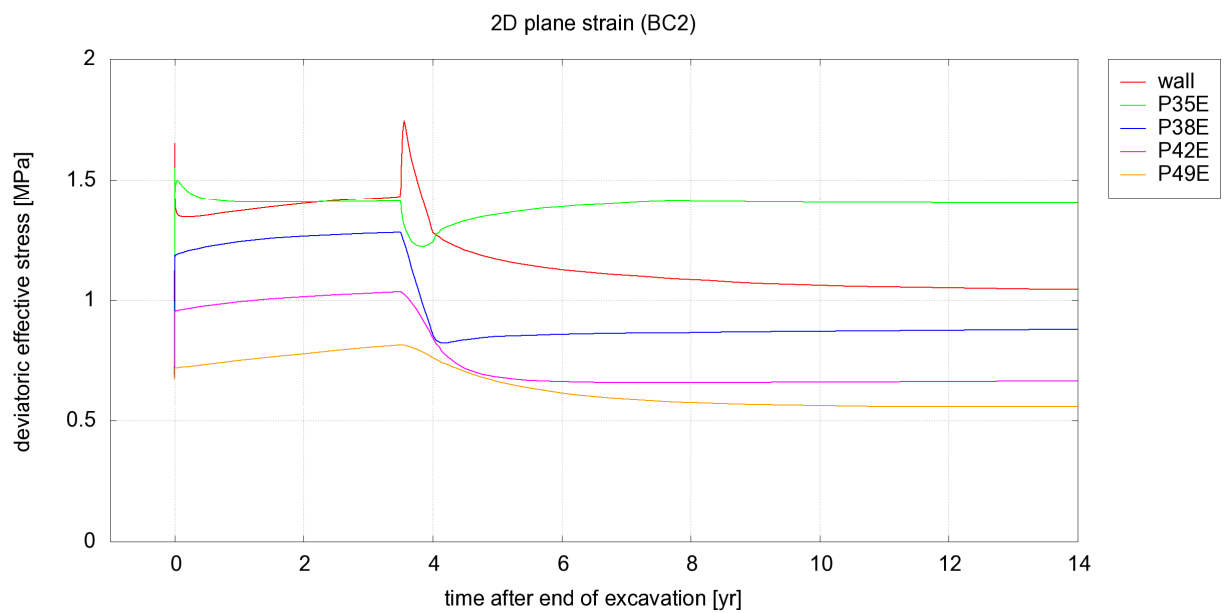


Figure 58: Evolution in time of deviatoric effective stress q at sensors location using BC2

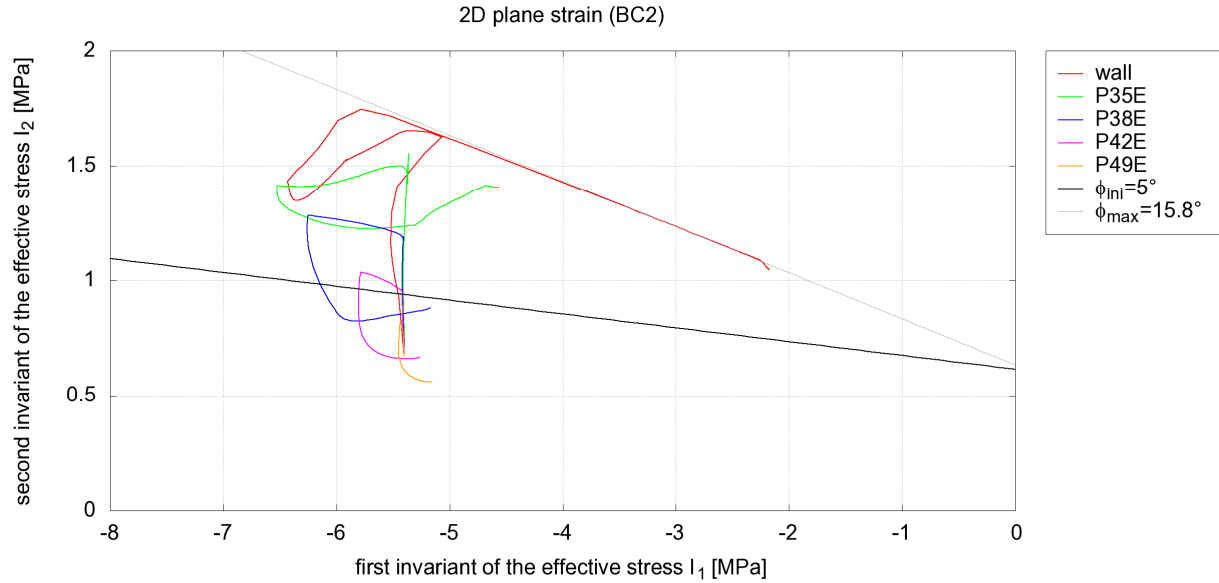


Figure 59: Stress path in the p' - q space at sensors location using BC2

Plastic zone extent

To illustrate the extent of the plastic zone, the Figure 60 represents the contour levels of the Coulomb's friction angle ϕ at the end of the excavation. The initial value is 5° , represented in white in this figure. Due to plastic hardening, ϕ increases up to those colorized values in the scale, i.e. from blue (5° - 6°) to red (up to 16°).

As the Figure 60 shows, the plastic zone is not axisymmetric, but influenced by the anisotropy of the initial stresses and its consequences on the effective stress and strain fields. The extent of the plastic zone is about 9 m in the horizontal direction and 3 m in the vertical direction.

The use of the first or the second type of far-field mechanical boundary conditions does not affect the plastic zone, as shown on the left (BC1) and right (BC2) figures that are very similar.

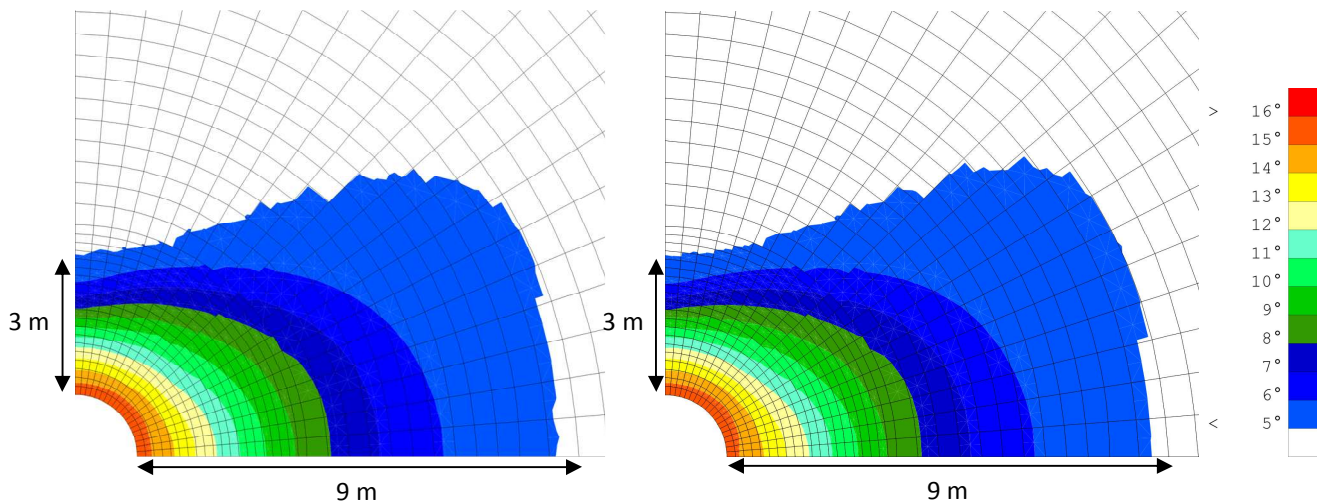


Figure 60: Actualized ("hardened") Coulomb's friction angle at the end of the excavation. Initial value is 5° (in white). Left: using BC1 – Right: using BC2

At the end of the heater experiment (14 years after the end of the excavation), the plastic zone extent is not significantly modified, as shown in the Figure 61. It is simply a little more extended in the horizontal direction. The remaining white zones are the zones where the stress state is permanently in the elastic domain all of the time.

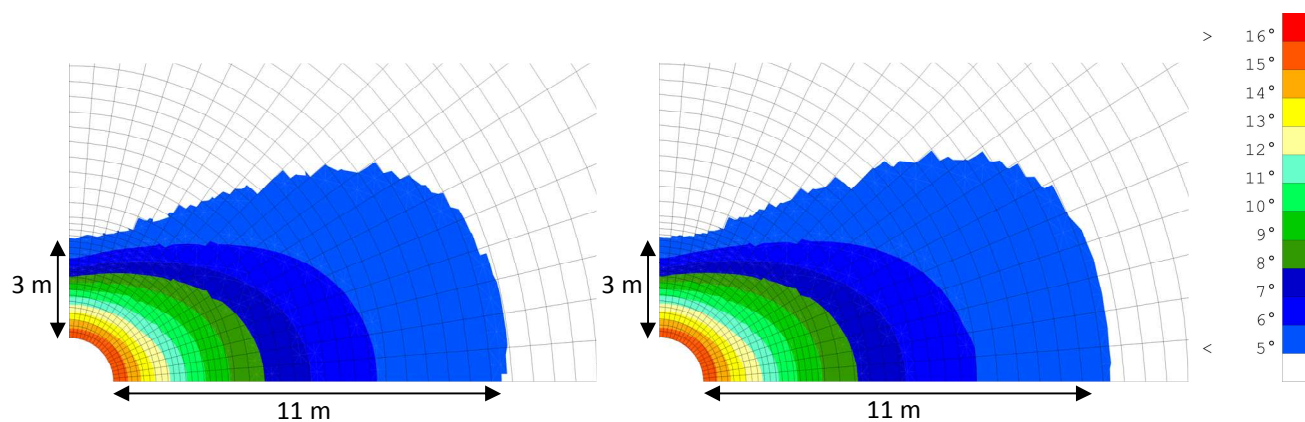


Figure 61: Actualized (“hardened”) Coulomb’s friction angle at the end of the excavation.
Initial value is 5° (in white). Left: using BC1 – Right: using BC2

4.2 2D axisymmetric modelling

Partners active in this model: EPFL – ULg – Euridice – CIMNE

4.2.1 Pore water pressure

In the 2D axisymmetric modelling, the anisotropy of the initial effective stresses cannot be taken into account. In return, the extent of the model in the direction of the gallery axis allows including some elements that are not present in the 2D plane strain model, e.g. the sealing (and thus also the bentonite), the concrete plug and steel shield at the end of the gallery, the connecting gallery ... In the present model, the sand filling is also modelled.

All these elements impact on the different values, the first one to be shown is the pore water pressure. The Figure 62, Figure 63 and Figure 64 represent p_w profiles along axial direction, the origin of the coordinates corresponding to the entry of the PRACLAY gallery.

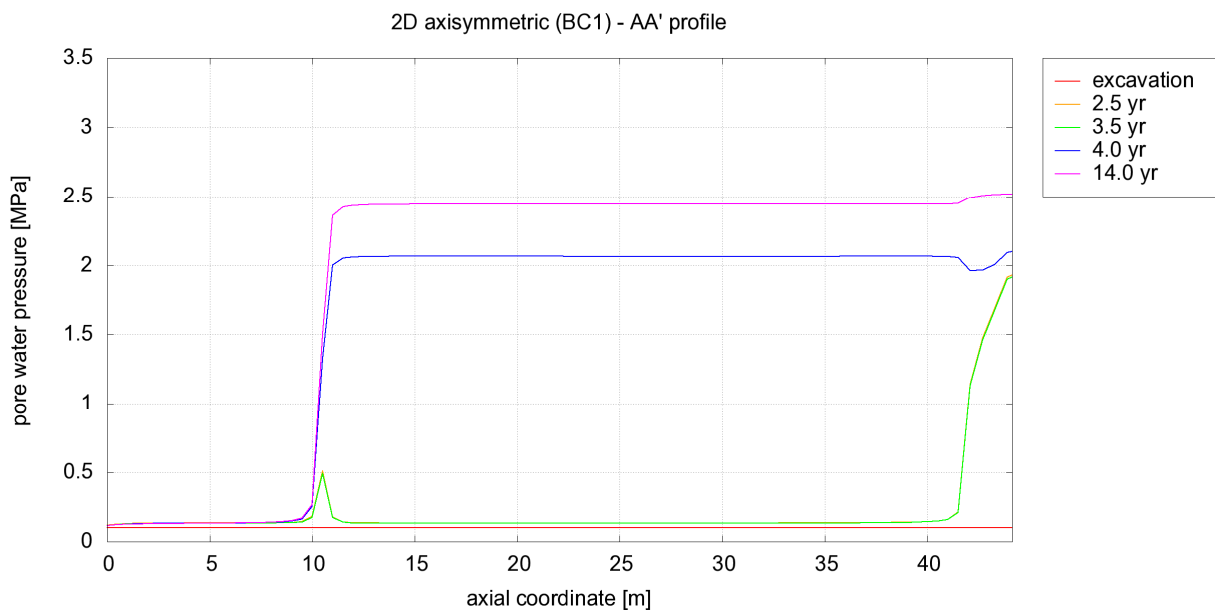


Figure 62: Pore water pressure along AA' (axial) profile

The first profile (AA', Figure 62) is located just along the wall of the excavated gallery:

- At the end of the excavation, p_w is equal to 100 kPa, this value being prescribed as a boundary condition during the excavation phase.
- After 2.5 years and 3.5 years, the p_w profiles are (almost) identical. The value of p_w along the profile is about 190 kPa, except in the first meter (due to the vicinity of the connecting gallery, hence the drainage is larger), between 10 and 11 m (because of the sealing using a steel structure which has been considered impervious, hence less drainage in this zone), and over 41.5 m (where the steel shield is located, the concrete elements of the gallery stopping there and the drainage boundary condition also).
- The next plotted time corresponds to 4 years after the end of the excavation, i.e. after 0.5 year of heating, when the temperature of the heater reaches the nominal value of 85°C. The value of p_w is quite homogeneous along the heater (between 13 m and 40 m), while border effects are visible near the sealing and at the end of the gallery.

- The final value of p_w is similar to the previous curve. The maximum p_w after 10 years of heating (end of the heater test) is close to 2.5 MPa, which is a 0.25 MPa overpressure with respect to the initial pore water pressure (before excavation).

The two next profiles BB' and CC' (Figure 63 and Figure 64, respectively) exhibit a similar evolution, but the observed phenomena are less marked as the distance from the gallery increases, i.e. for CC' profile (about 9 m from the gallery axis) than for BB' (about 4.75 m from the gallery axis):

- At the end of the excavation, the profile of p_w is approximately symmetrical, being lower where the effect of the drainage is more important, i.e. along the PRACLAY gallery.
- As time goes by (2.5 years and 3.5 years after excavation), the drainage from the gallery to those further profiles continues and p_w continues to decrease. The drainage from the connecting gallery and the presence of the impervious steel shield at the gallery extremity generate a slightly asymmetric p_w profile.
- Then, during the heater test (4 years and 14 years after excavation), the effect of the temperature increase becomes visible, first along the (closer) BB' profile, then along the (further) CC' profile where the p_w remains almost unchanged after 4 years (p_w profile after 4 years is similar to the one after 3.5 years), since the temperature along CC' profile after 6 months of heater test is still around 16°C, as it will be shown in the next section of this report (cf. Figure 74).

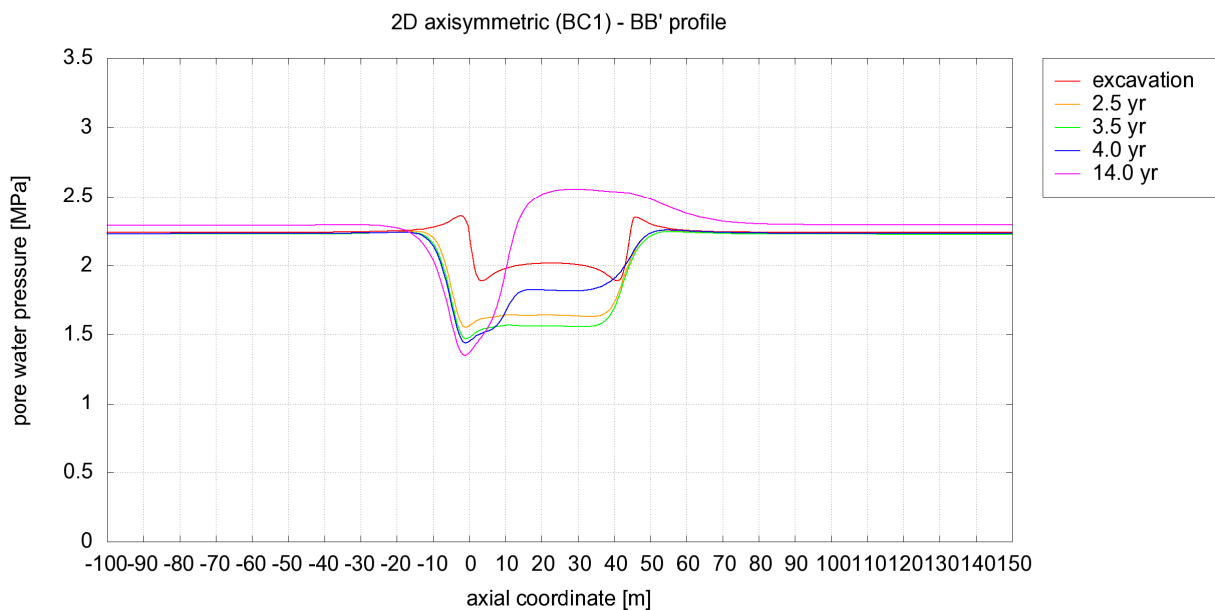


Figure 63: Pore water pressure along BB' (axial) profile

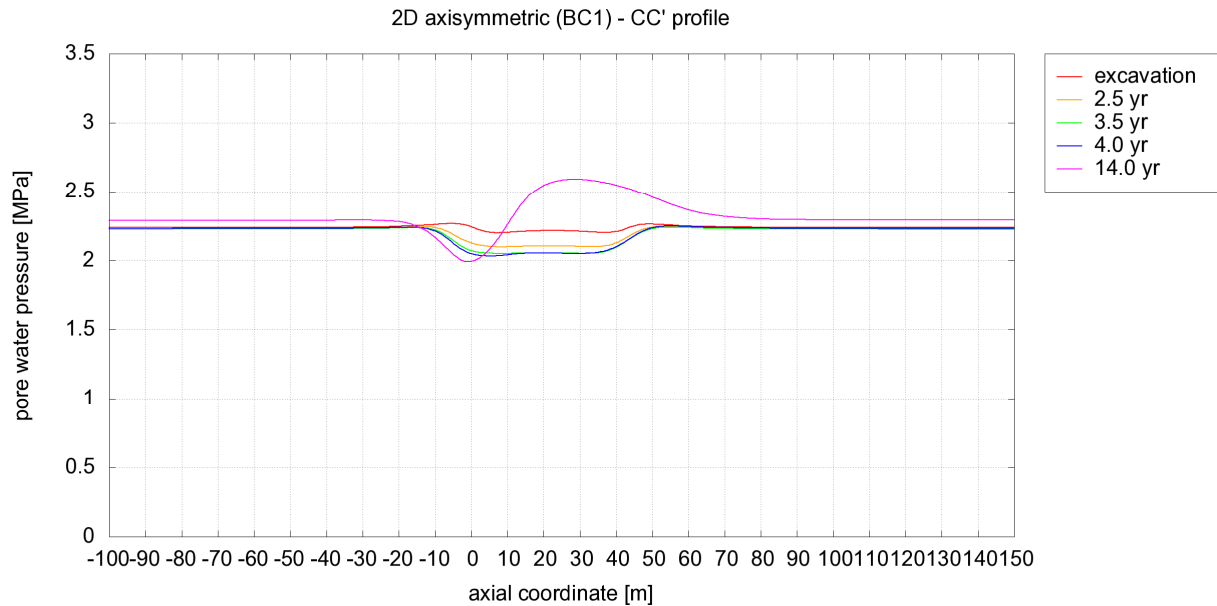


Figure 64: Pore water pressure along CC' (axial) profile

The Figure 65 and Figure 66 represent p_w profiles along radial direction:

- the Figure 65 corresponds to the DD' profile, located in the vertical plane of the sealing (axial coordinate = 10.5 m) ;
- the Figure 66 corresponds to the EE' profile, located in the vertical mid-plane of ring 44 (axial coordinate = 22.75 m), i.e. in the same plane as the 2D plane strain model.

In both cases and before heating (until 3.5 years), the decrease of p_w extends to a radius less than 20 m. During the heating and until the end of the heater test, p_w increases, the rising being larger along the EE' profile. The maximum p_w is located about 9 to 10 m from the gallery axis (along EE' profile) and this peak is around 2.57 MPa. The far-field p_w reaches 2.28 MPa.

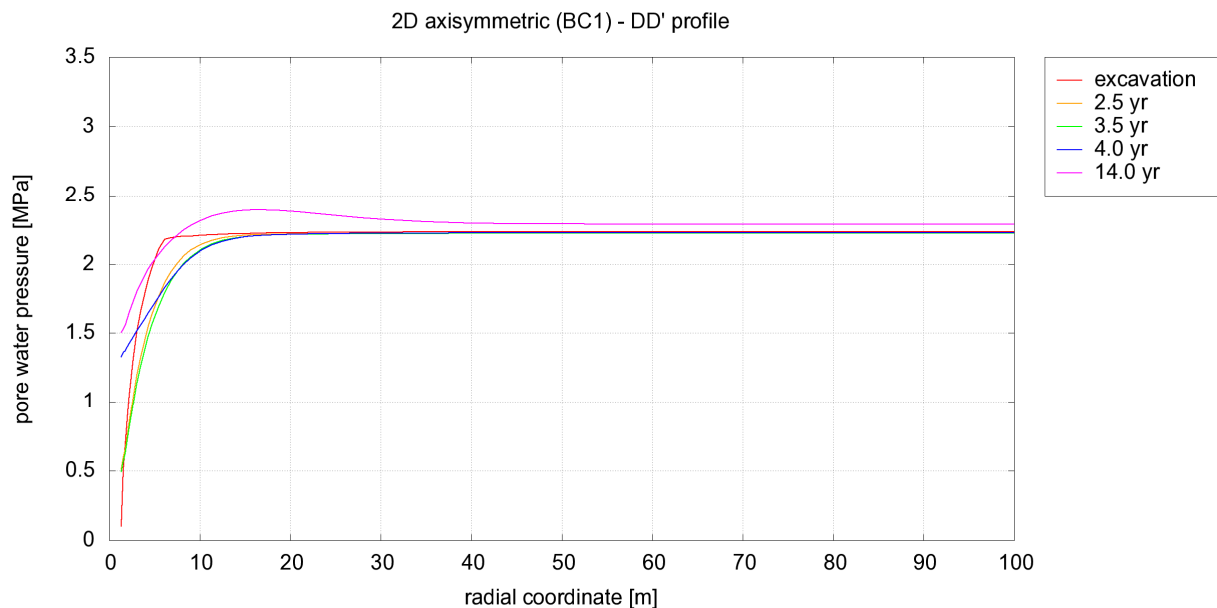


Figure 65: Pore water pressure along DD' (radial) profile

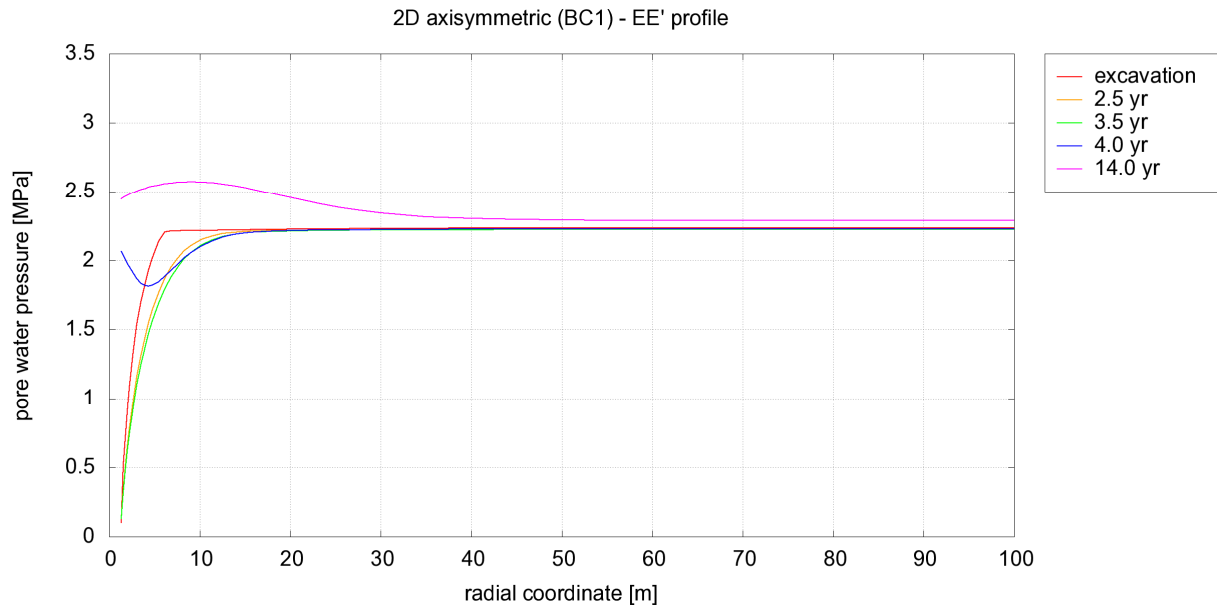


Figure 66: Pore water pressure along EE' (radial) profile

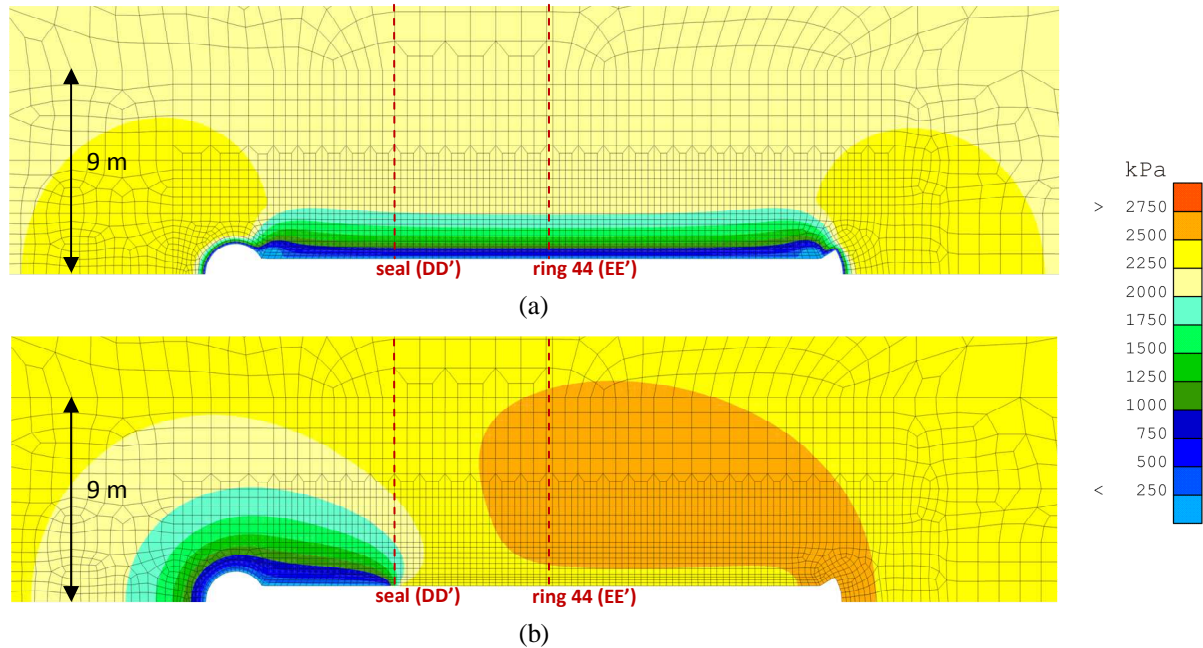


Figure 67: Pore water pressure fields at the end of the excavation (a) and at the end of the heater test (b)

Influence of the far-field mechanical boundary conditions

Just like for the 2D plane strain model, the second type of far-field mechanical boundary conditions has been investigated (free displacements + loading $q_{ax} = q_{rad} = 4.5$ MPa).

The results in terms of pore water pressure profiles using BC2 are very similar to those got with BC1. The most visible difference is shown in Figure 68: from 50 m and further, p_w remains equal to 2.25 MPa during all the time. The peak value is little bit lower using BC2 and equal to 2.52 MPa (to be compared to 2.57 MPa using BC1).

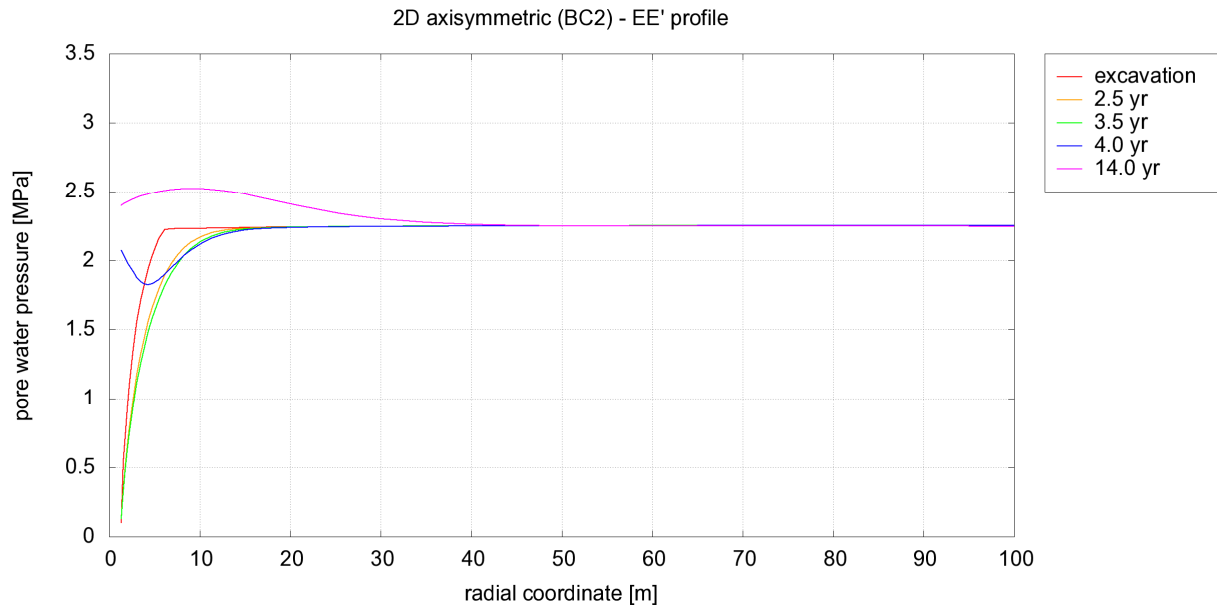


Figure 68: Pore water pressure along EE' (radial) profile using BC2

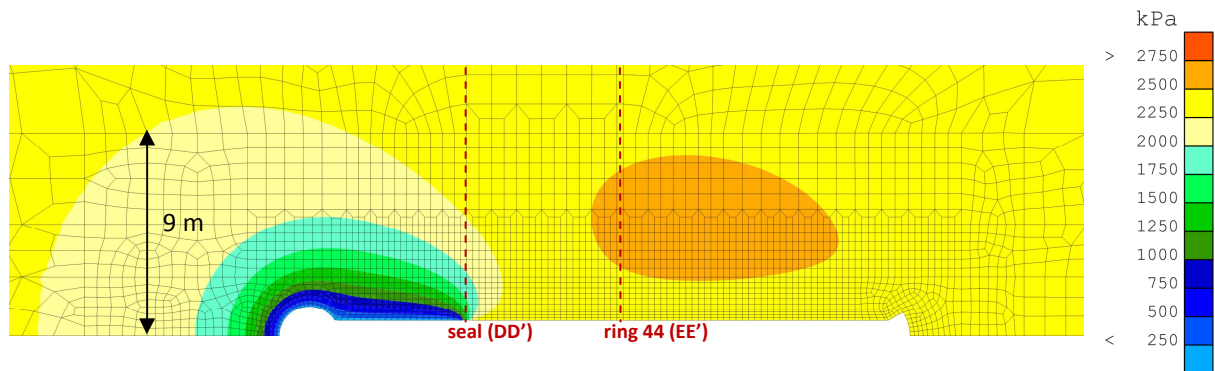


Figure 69: Pore water pressure field at the end of the heater test using BC2

Evolution in time of p_w at the sensors location

The evolution of p_w is plotted in the Figure 70, using BC1. The behaviour is similar to what is observed in the 2D plane strain model:

- First, a quasi-instantaneous p_w decrease corresponding to the excavation which takes place in 20 days in the 2D axisymmetric model (while it was in 1 day in the 2D plane strain model). The same decrease of p_w down to 100 kPa is the drainage boundary condition at the wall, and at the P35E sensor, p_w also stops decreasing when the contact occurs between Boom clay and the liner.
- Then, during the next 3.5 years, p_w is still decreasing, but the rate of decrease is lower, more especially for sensors further from the gallery. Due to the “building” of the liner, the drainage conditions are a little bit different: the 100 kPa boundary condition is now applied at the inner surface of the concrete liner instead of the outer surface (the excavation wall). That is the reason why p_w at the wall is rising at the very beginning (during the first day), and then it decreases again.

- The third phase corresponds to the heater test. From 3.5 years to 4 years, the temperature at the inner surface of the liner is increasing from 16°C to 85°C, and then it remains constant at 85°C for 10 additional years. Due to the heating, p_w increases. The rate of increase is higher in the vicinity of the gallery. The values of p_w at the different sensors are distributed in the range 2.4 MPa to 2.6 MPa and they remain quite constant during the last 6 years of the heater experiment.

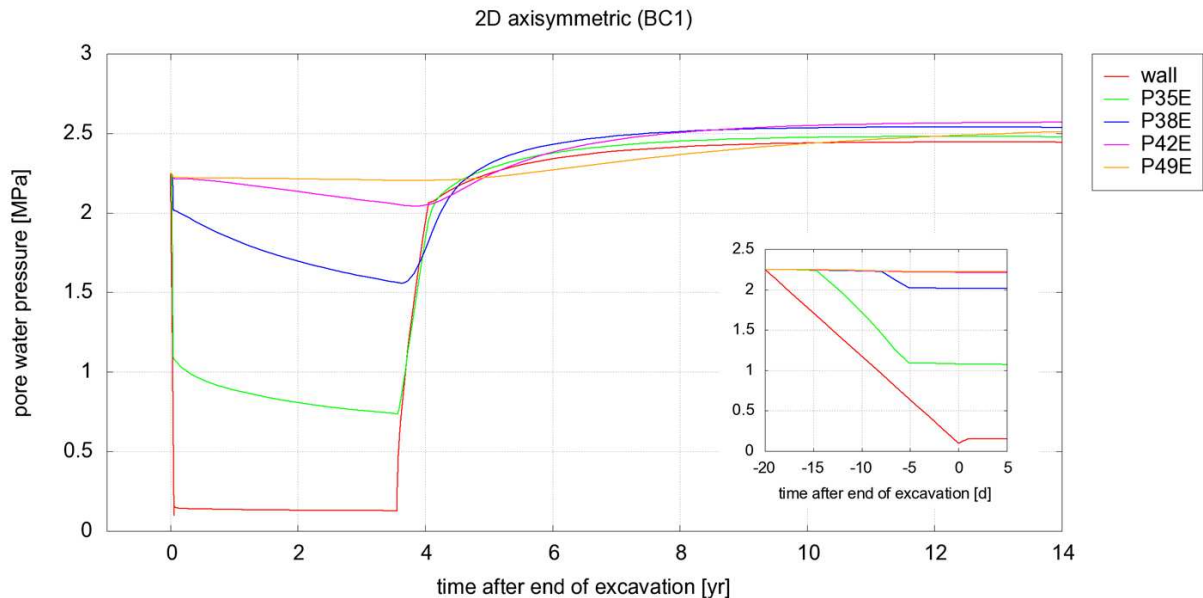


Figure 70: Evolution in time of the pore water pressure at sensors location

Looking at the evolution in time of p_w using BC2, one gets the curves in Figure 71. The difference with respect to results using BC1 (Figure 70) is almost invisible (despite p_w is a little bit lower using BC2) and much less pronounced as the difference observed between the use of BC1 and BC2 with the 2D plane strain model (cf. Figure 39 and Figure 40).

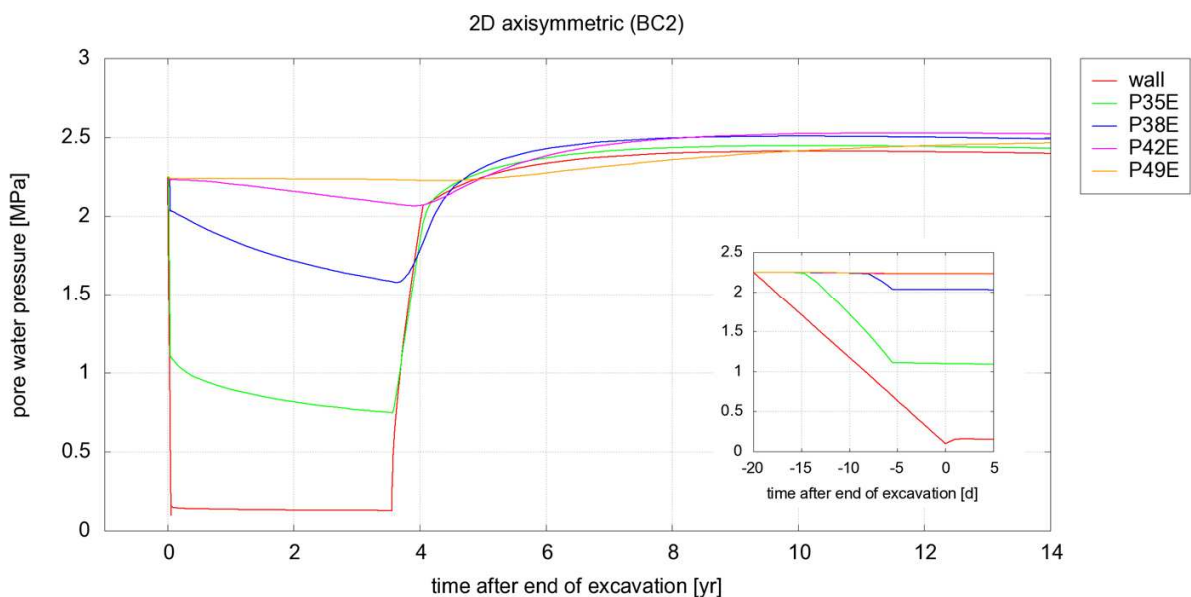


Figure 71: Evolution in time of the pore water pressure at sensors location using BC2

4.2.2 Temperature

The Figure 72 illustrates the temperature profile along the wall of the excavated gallery (AA' profile), in the axial direction. Since Boom clay is in contact with the PRACLAY gallery (the 6 cm gap has been bridged by the convergence of the Boom clay after excavation), the temperature along the AA' profile is also the temperature of the outer surface of the liner.

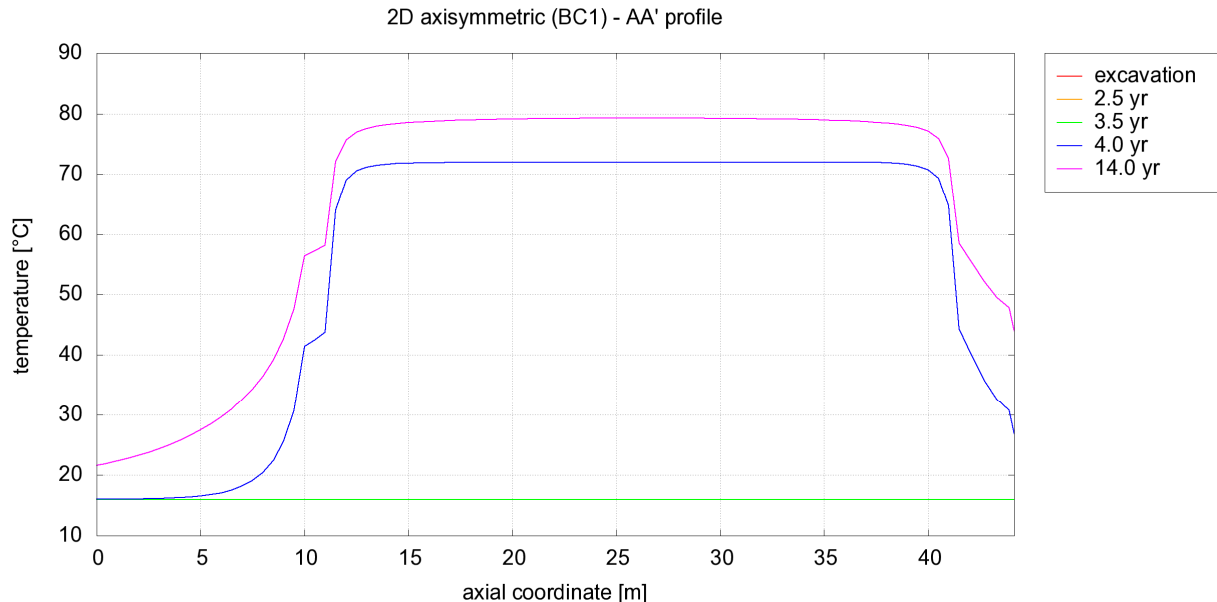


Figure 72: Temperature along AA' (axial) profile

The temperature increase is approximately uniform along the gallery between coordinates 13 m and 38 m, i.e. corresponding to the heater chamber. It is about 72°C when the heater is at the nominal temperature (4 years after excavation), and it tends to 80°C at the end of the heater experiment. Closer and beyond the heater chamber (axial coordinates <12m and >41 m, respectively), the temperature decreases. The gradient is lower where the thermal conductivity of the liner is higher, i.e. between 10 and 11 m (steel seal) and between 41.5 and 44 m (steel shield).

The Figure 73 and Figure 74 represent the temperature along further (axial) profiles BB' and CC'. The heating is delayed (with respect to AA' profile) and the maximum temperature is lower. As already mentioned above (in the pore water pressure analysis), the temperature remains close to 16°C after 6 months heating along CC' profile.

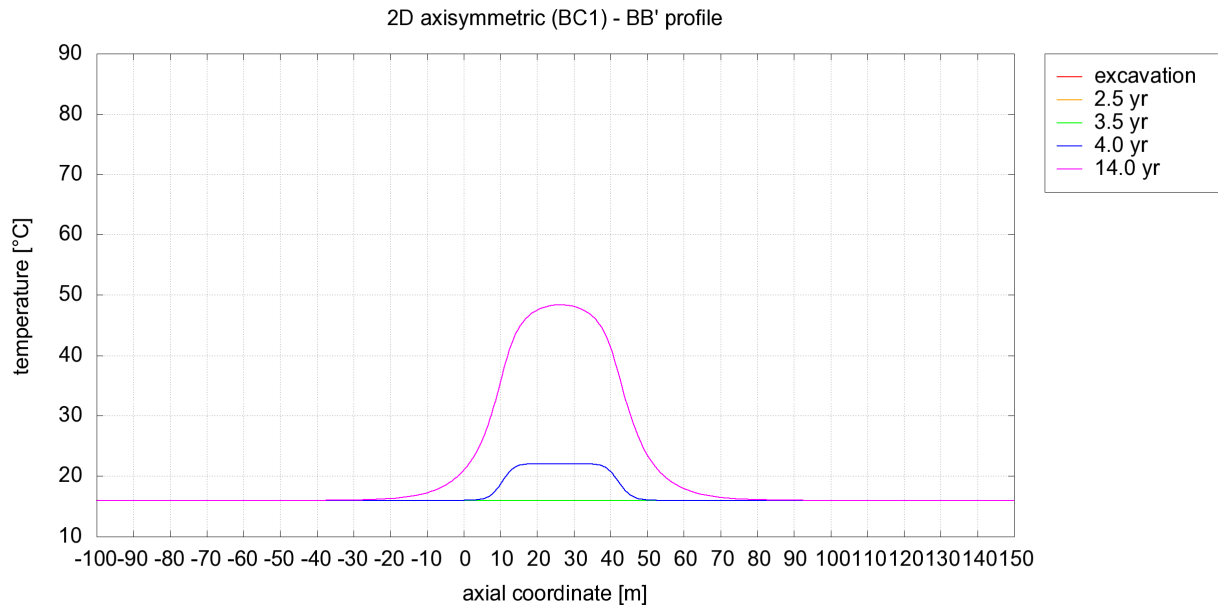


Figure 73: Temperature along BB' (axial) profile

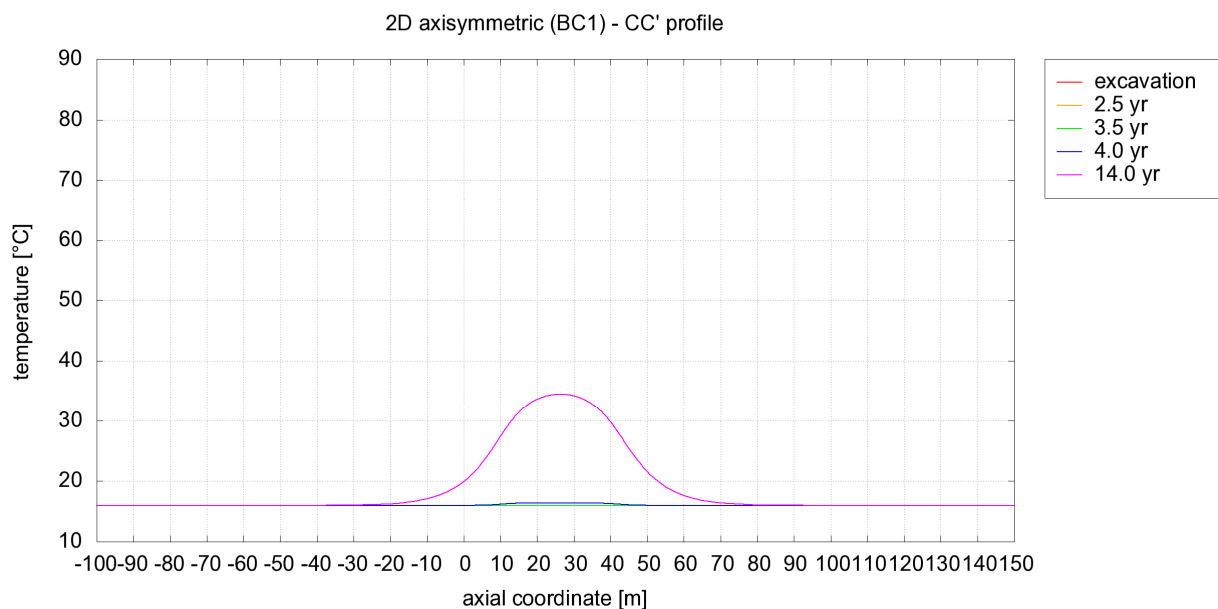


Figure 74: Temperature along CC' (axial) profile

The two profiles in the radial direction DD' and EE' (Figure 75 and Figure 76, respectively) exhibit a rapid decrease of the temperature in this direction. The heating of Boom clay is limited to approximately 5°C at a radius equal to 20 m and further, and almost no temperature increase can be observed from 40 m to the boundary of the model, even after 10 years of heating (14 years after excavation – end of the heater test). The maximum temperature along the DD' profile (in the plane of the seal) is about 58°C, in the vicinity of the seal.

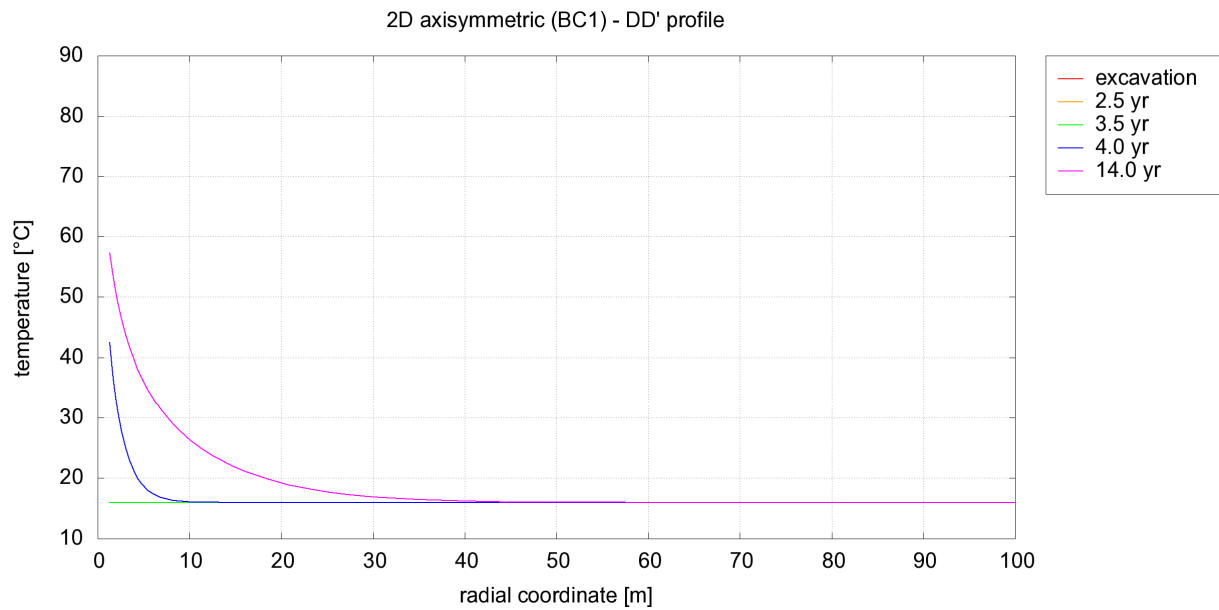


Figure 75: Temperature along DD' (radial) profile

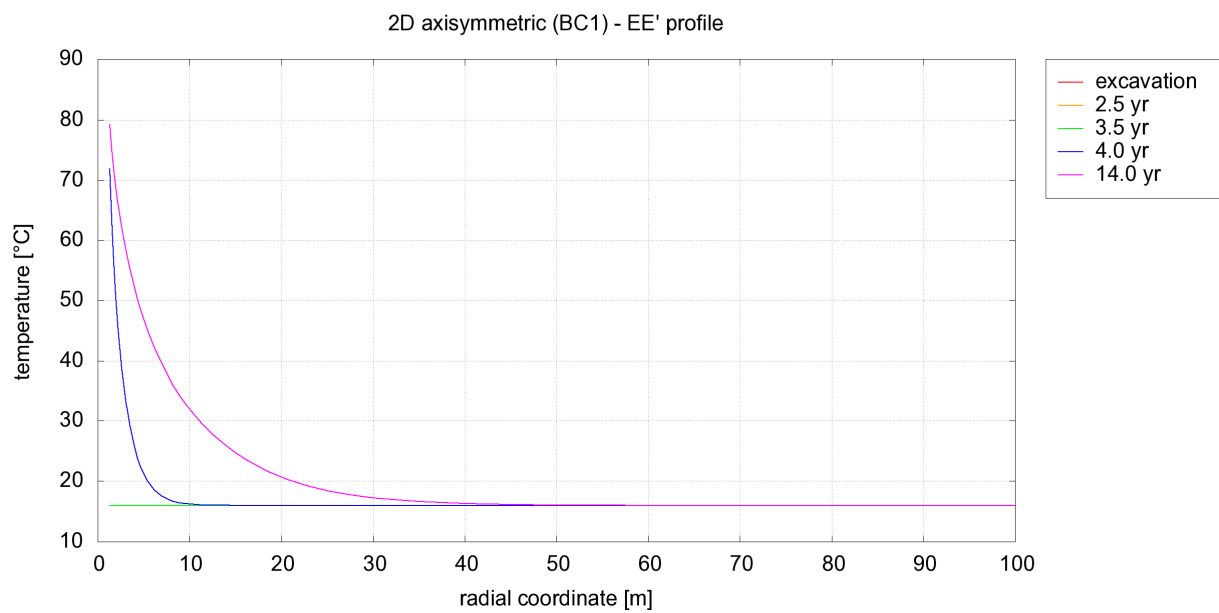


Figure 76: Temperature along EE' (radial) profile

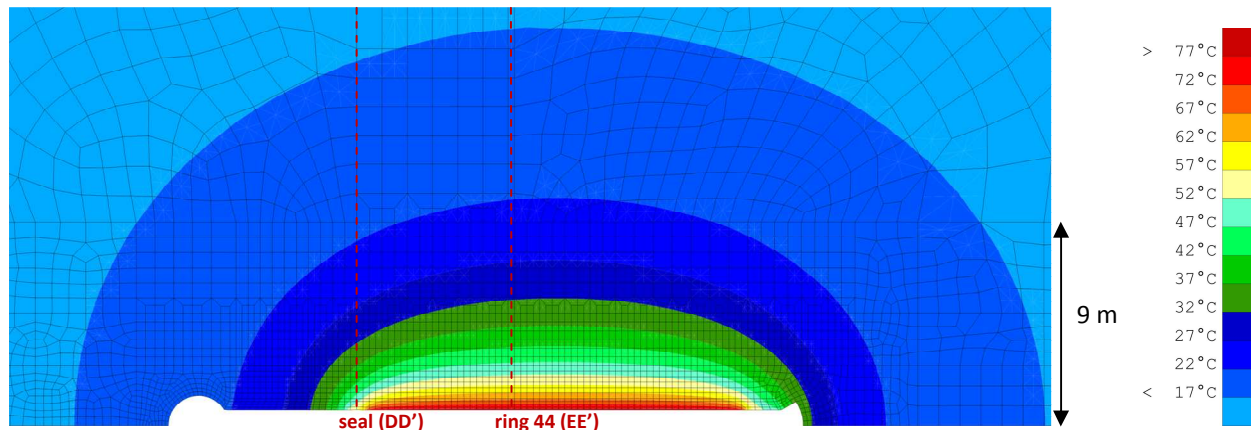


Figure 77: Temperature field in the Boom clay at the end of the heater test

The Figure 78 shows the temperature at sensors. It remains between 77°C and almost 80°C at the wall during the last 8 years of the heater experiment. The heating is more progressive as the distance to the gallery increases.

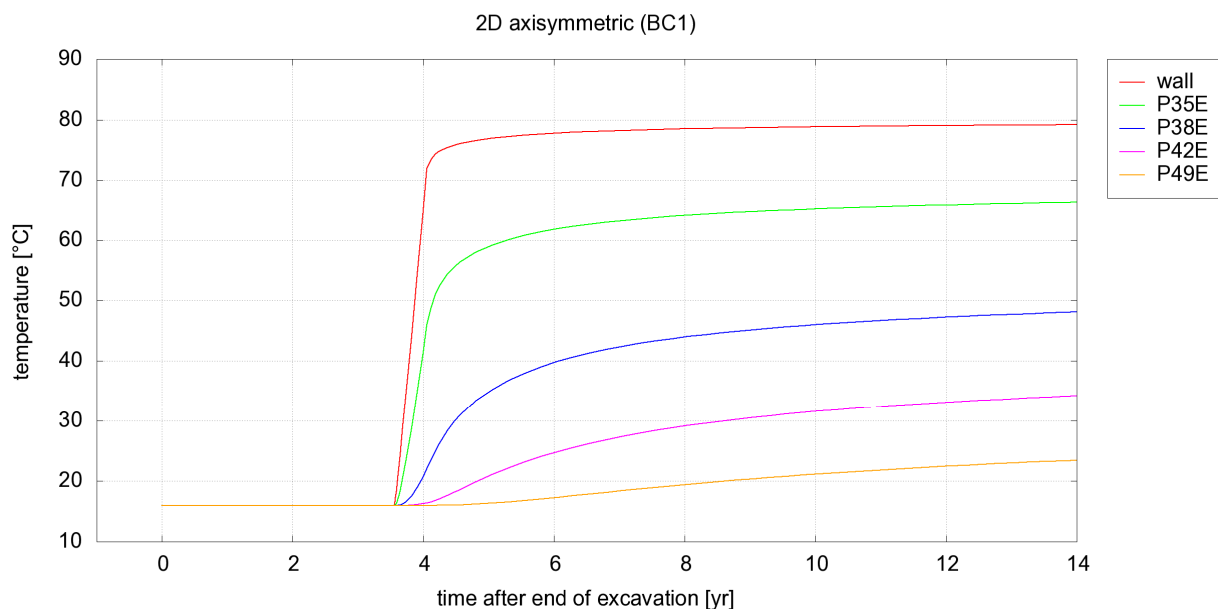


Figure 78: Evolution in time of the temperature at sensors location

Using BC2 instead of BC1 has no influence on the temperature (at sensors location as well as along profiles).

4.2.3 Radial displacement

The Figure 79 shows the radial displacement along the wall of the excavated gallery (AA' profile). It is equal to -60 mm all along the profile, i.e. the Boom clay converges and enters in contact with the liner (the initial gap is 6 cm). Some border effects are visible, the lack of contact in these places being due to the mesh, but without serious consequences.

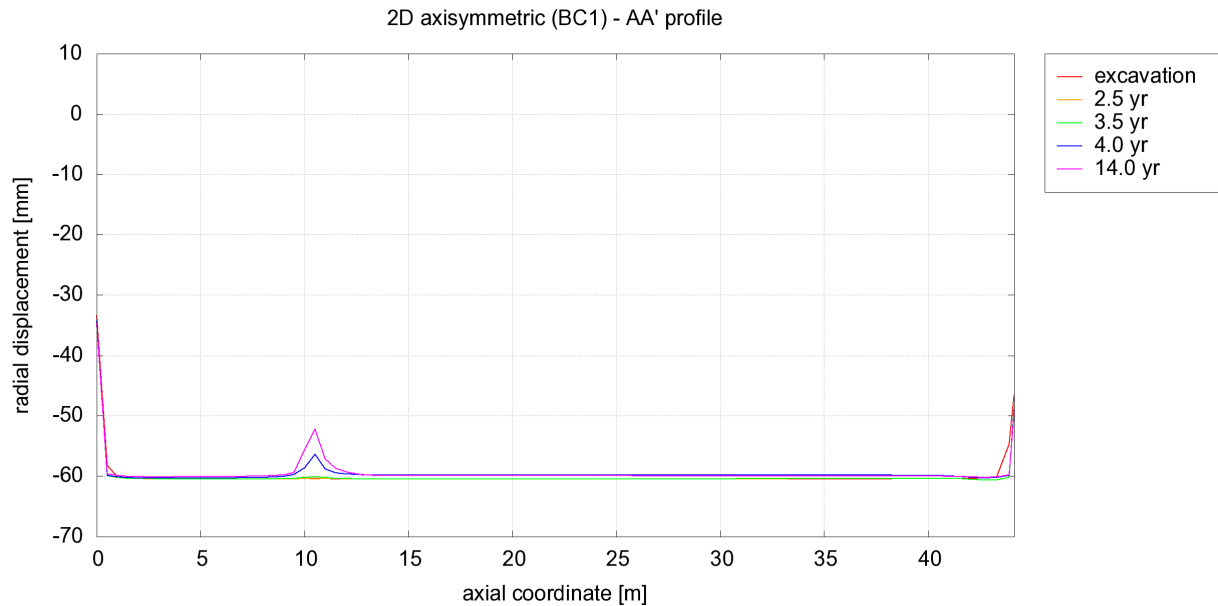


Figure 79: Radial displacement along AA' (axial) profile

After 2.5 years, the bentonite becomes active in the model and starts to swell. The effect of bentonite swelling can be observed between axial coordinates 10 m and 11 m, where the radial displacement decreases (it is less negative) for 3.5, 4.0, and 14.0 years after excavation.

In Figure 80 and Figure 81, the radial displacement is plotted for BB' and CC' axial profiles. The amplitude of the displacement is lower as the profile is further (less than 20 mm for BB' and less than 15 mm for CC'). The displacement profiles are almost symmetric before the heater experiment starts. Then, the effect of heating is clearly visible with a decreasing of the radial displacement (less negative) most of all "in front" of the heater (between 10 and 40 m).

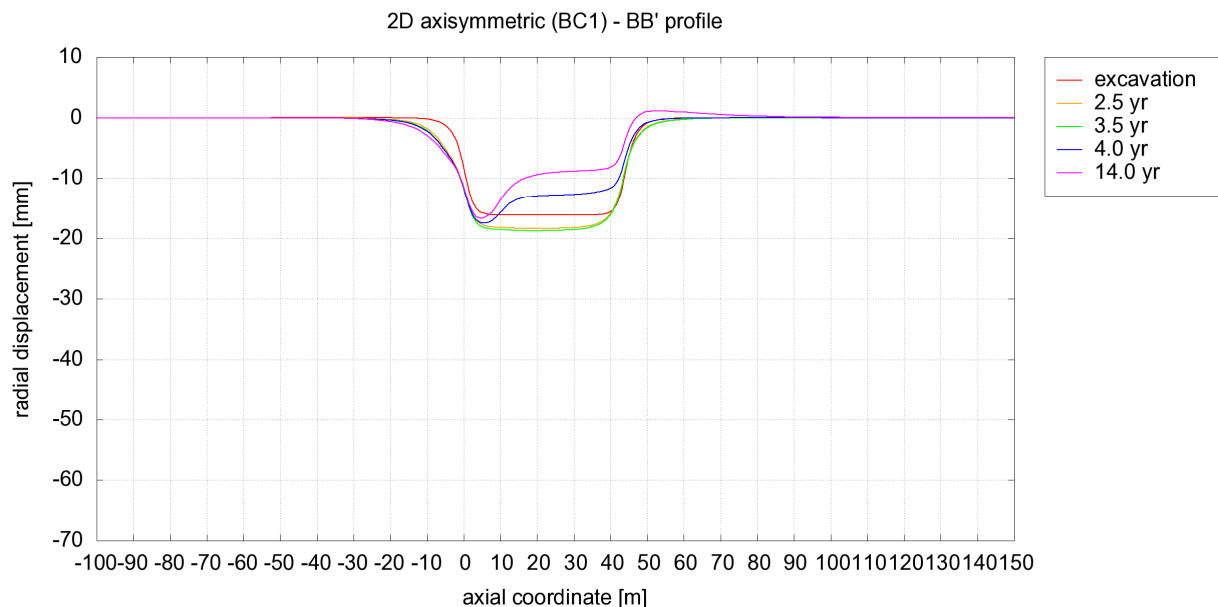


Figure 80: Radial displacement along BB' (axial) profile

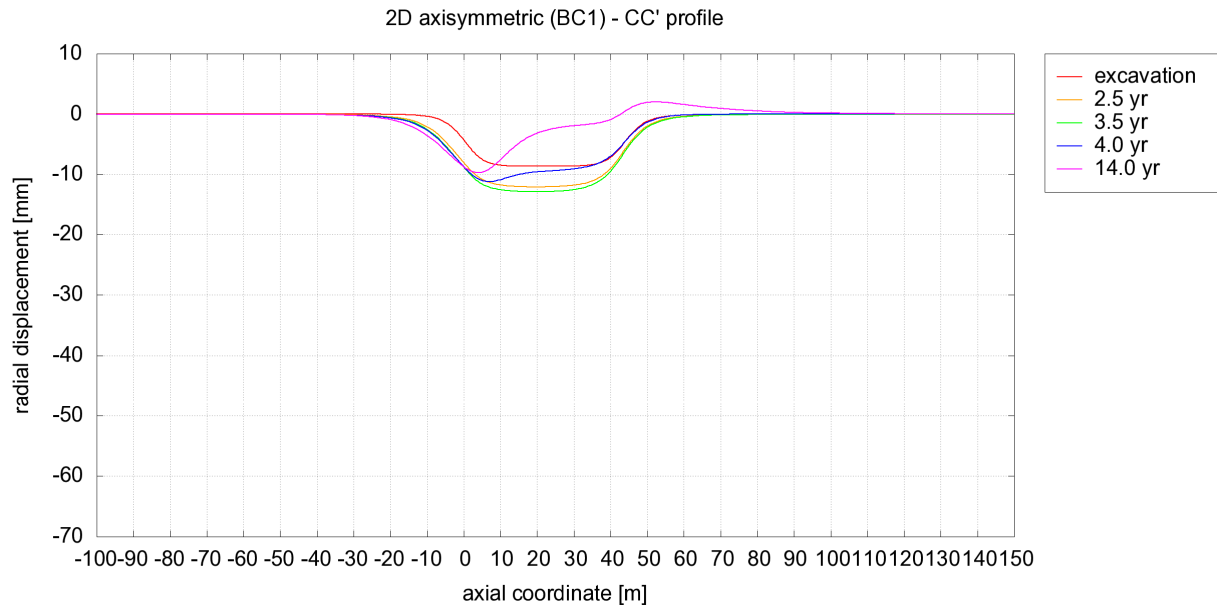


Figure 81: Radial displacement along CC' (axial) profile

The Figure 82 represents the radial displacement along DD' profile (in the mid-plane of the seal). It is equal to -6 cm at the wall (convergence of the Boom clay up to contact with the liner). The heating tends to produce a radial displacement in the opposite direction. At the end of the heater test, the radial displacement is slightly positive for radii greater than 20 m. The boundary conditions BC1 imply a zero-displacement at the boundary of the model, at any time of the computation.

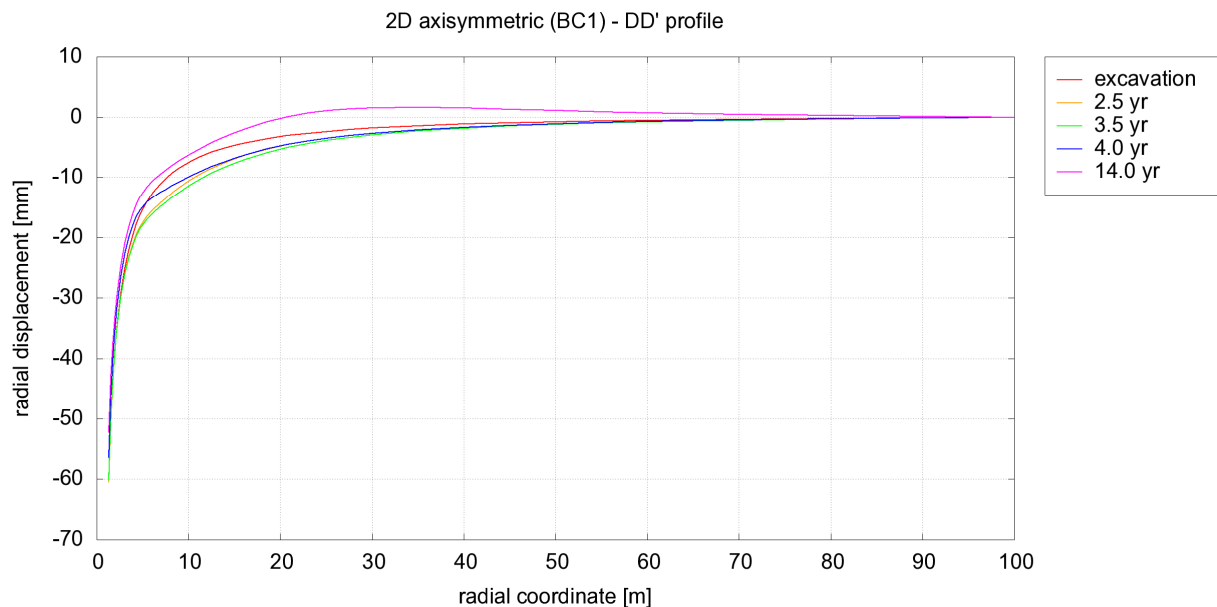


Figure 82: Radial displacement along DD' (radial) profile

The Figure 83 shows radial displacements along EE' profile. They are very similar to those observed for DD' profile. The positive radial displacement at the end of the heater test occurs for closer distances (around 12 m and more) and it is a little bit larger, but still less than 0.5 cm.

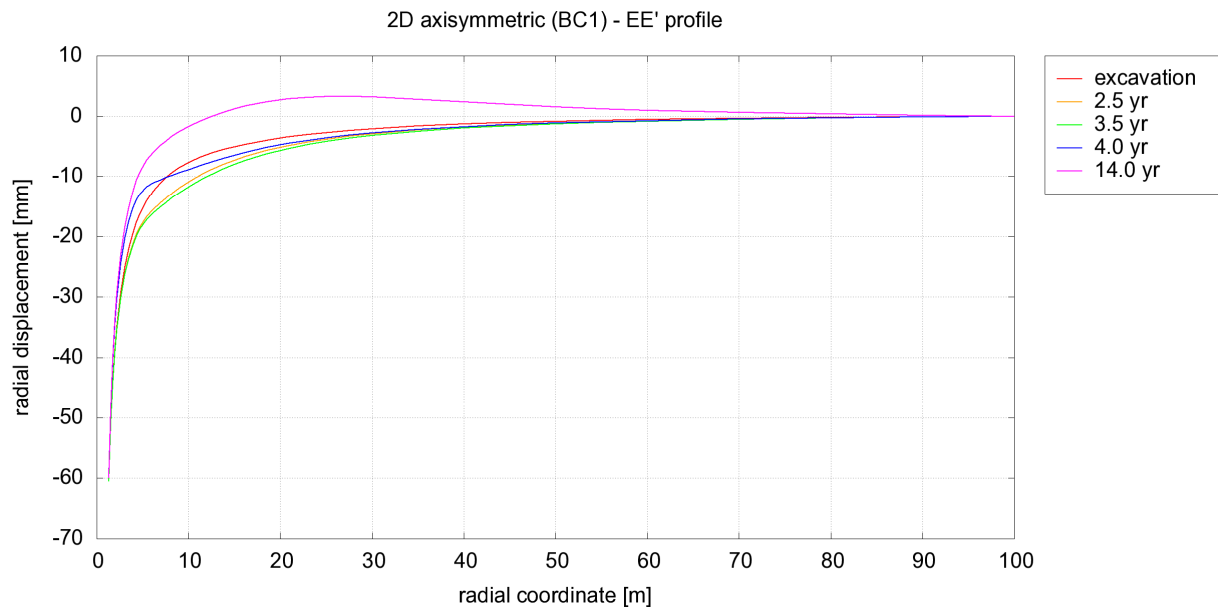


Figure 83: Radial displacement along EE' (radial) profile

Effect of the boundary conditions

Now considering the second type of boundary conditions, the radial displacements at the boundaries of the model are free and they differ from those obtained with BC1. Nevertheless, these differences are small, as the Figure 84 shows for EE' profile (to be compared with Figure 83).

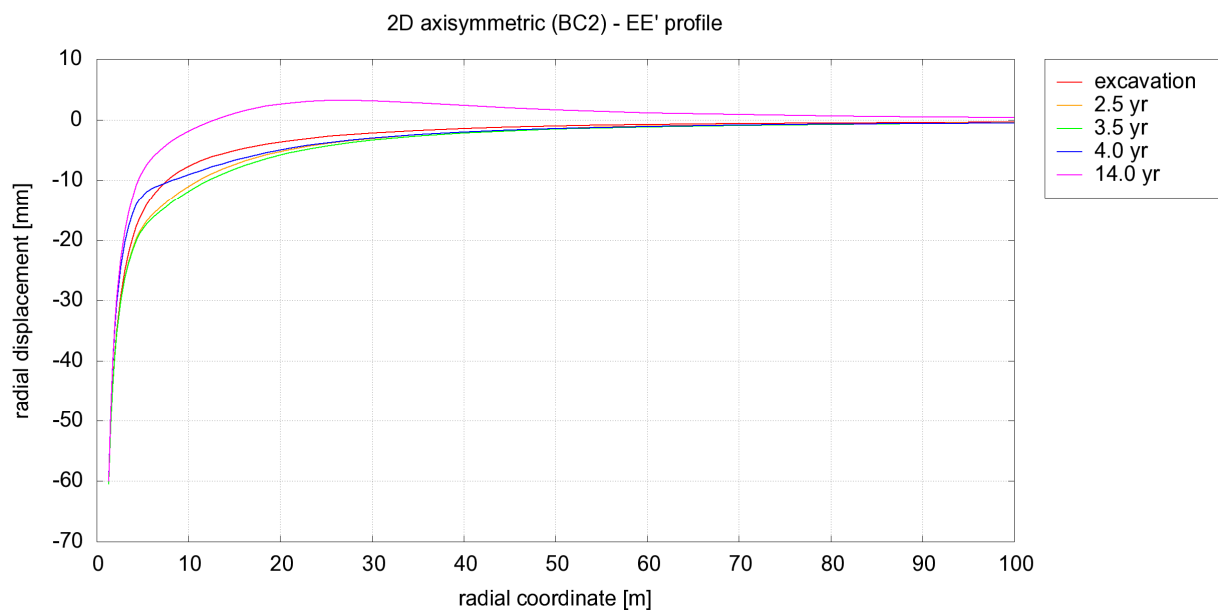


Figure 84: Radial displacement along EE' (radial) profile using BC2

4.2.4 Effective stresses

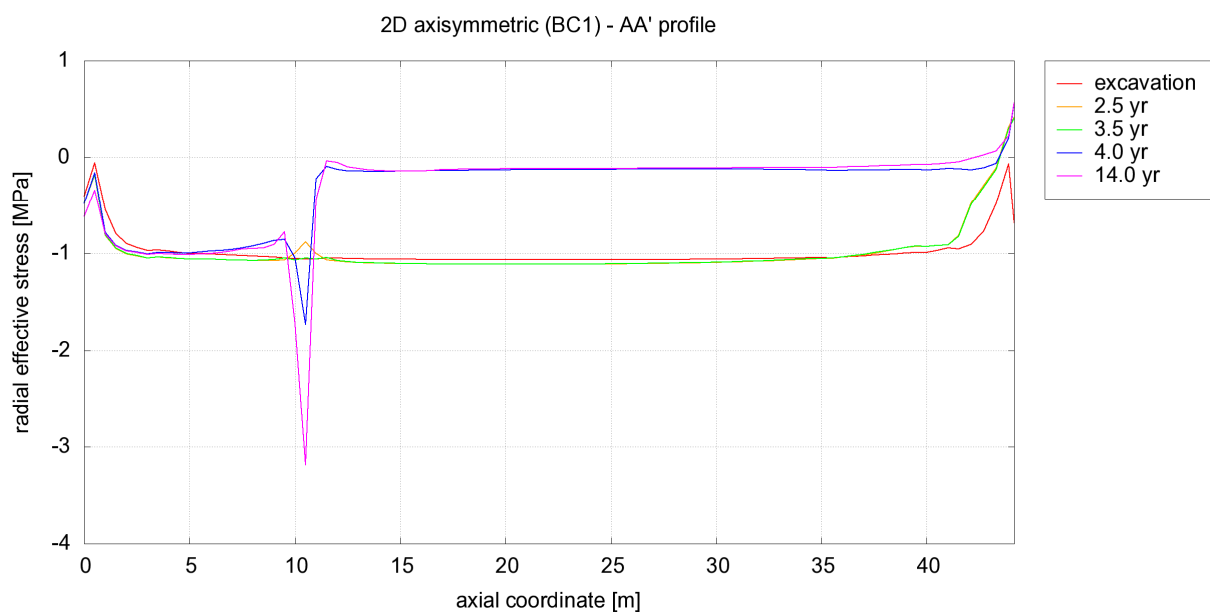


Figure 85: Radial effective stress along AA' (axial) profile

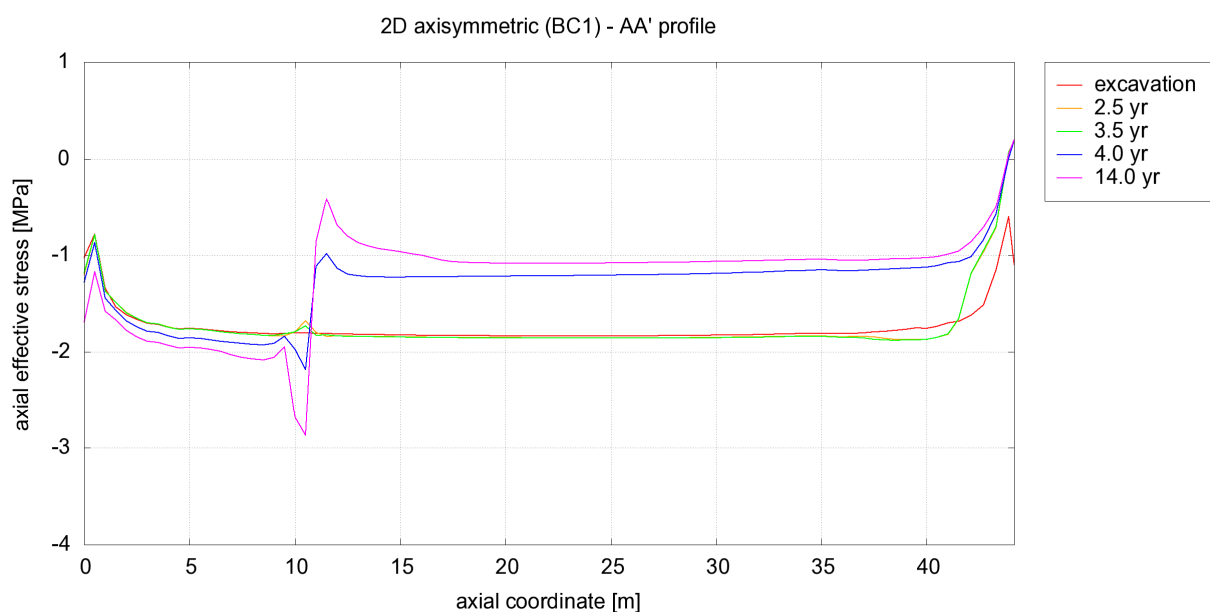


Figure 86: Axial effective stress along AA' (axial) profile

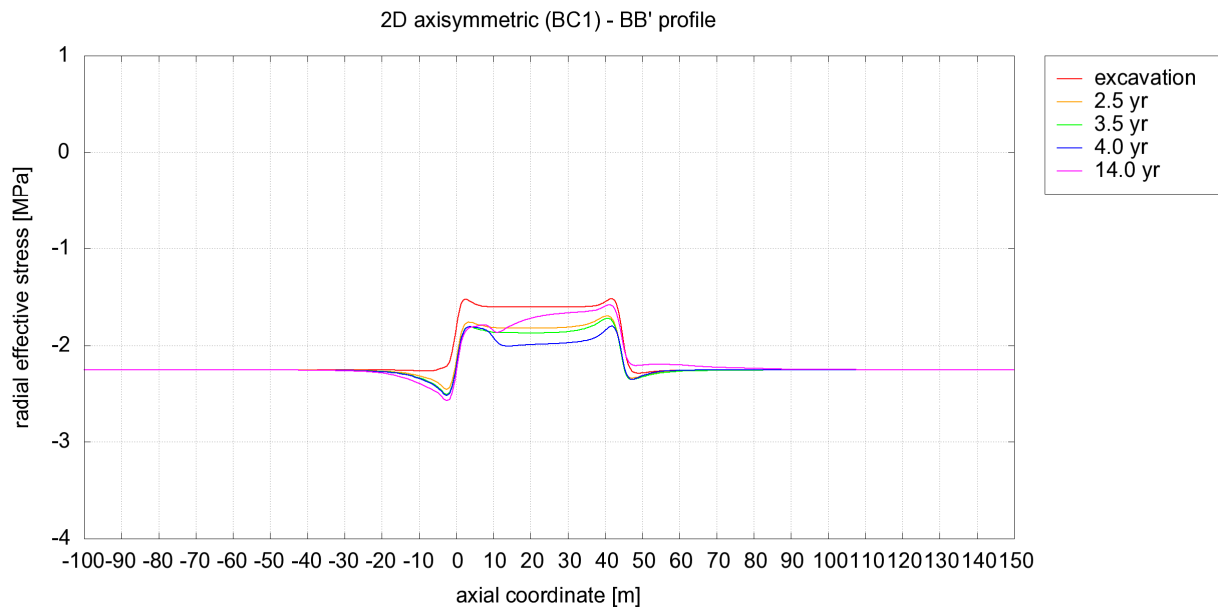


Figure 87: Radial effective stress along BB' (axial) profile

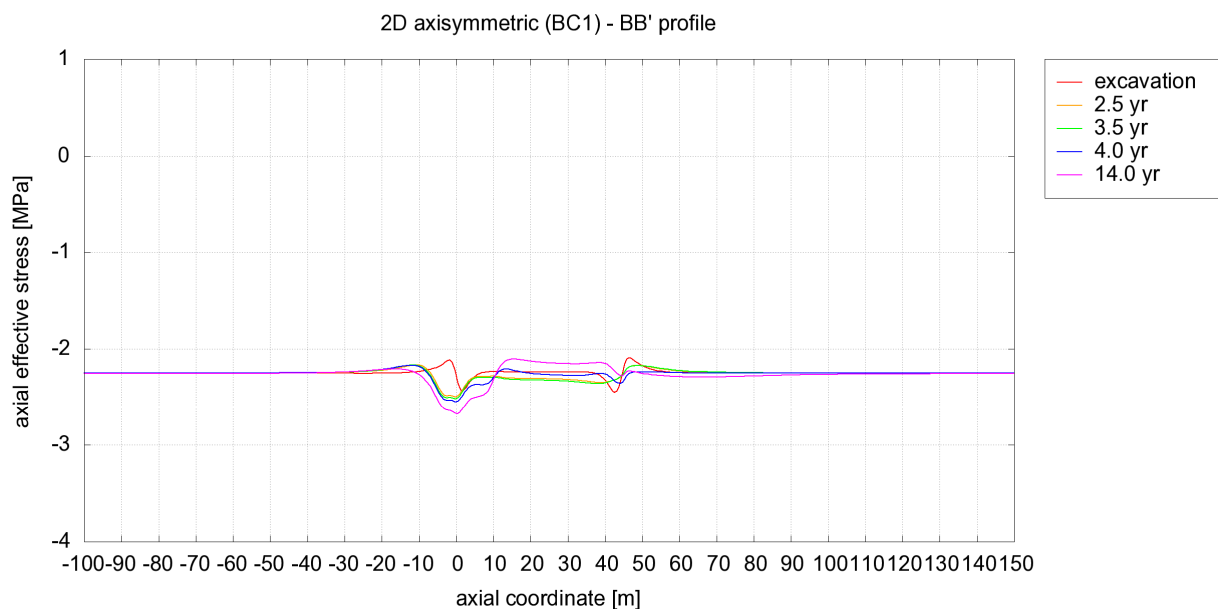


Figure 88: Axial effective stress along BB' (axial) profile

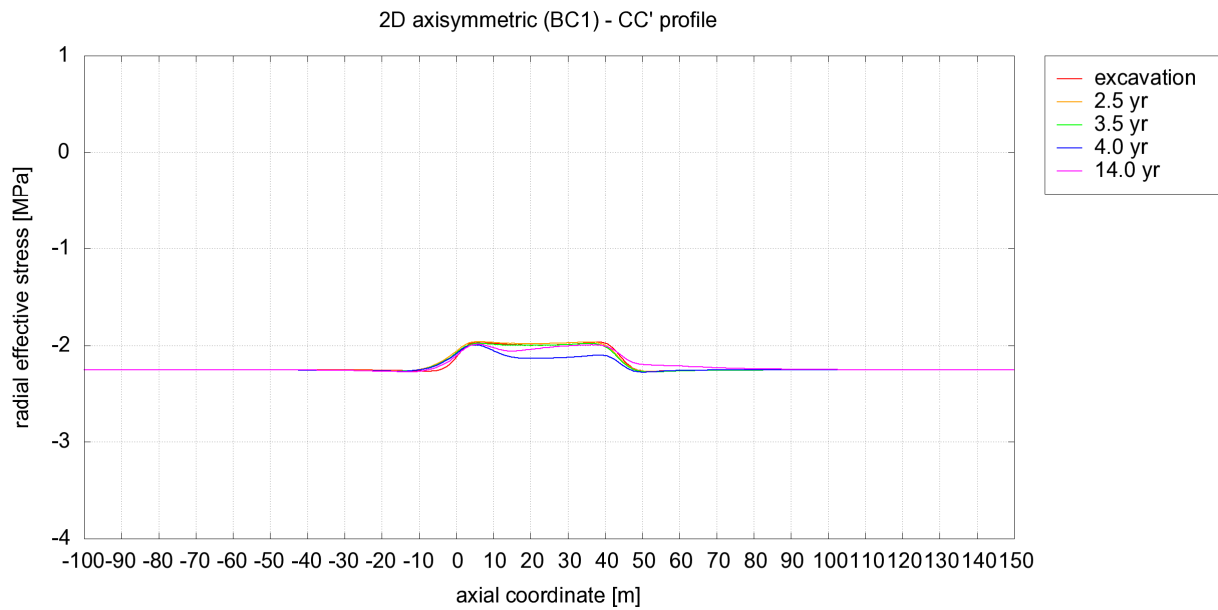


Figure 89: Radial effective stress along CC' (axial) profile

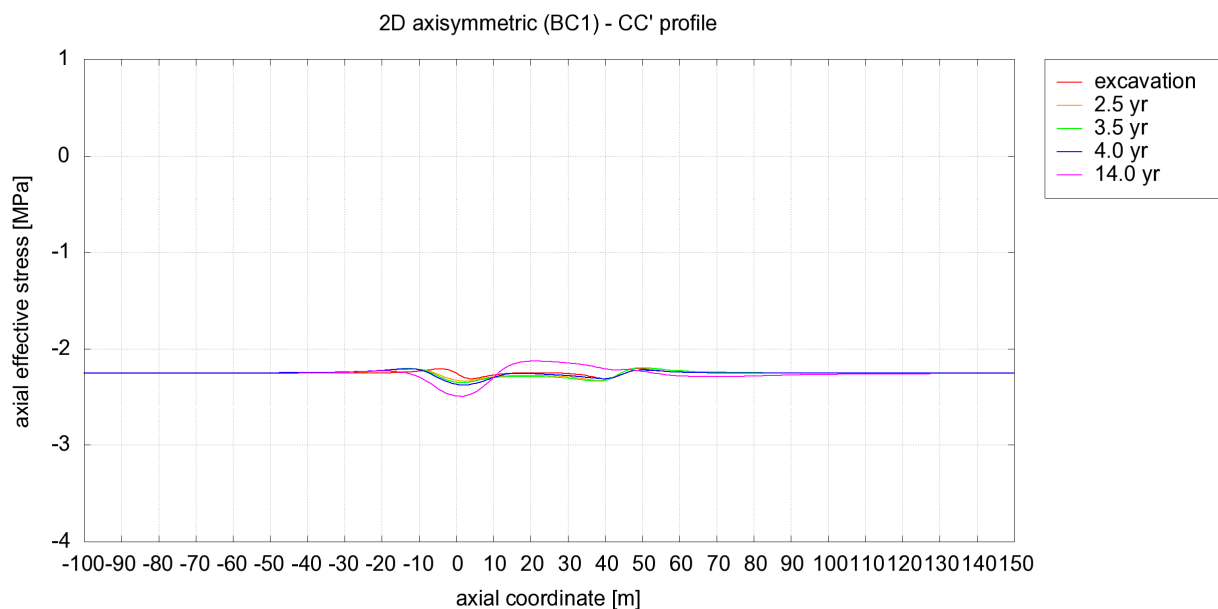


Figure 90: Axial effective stress along CC' (axial) profile

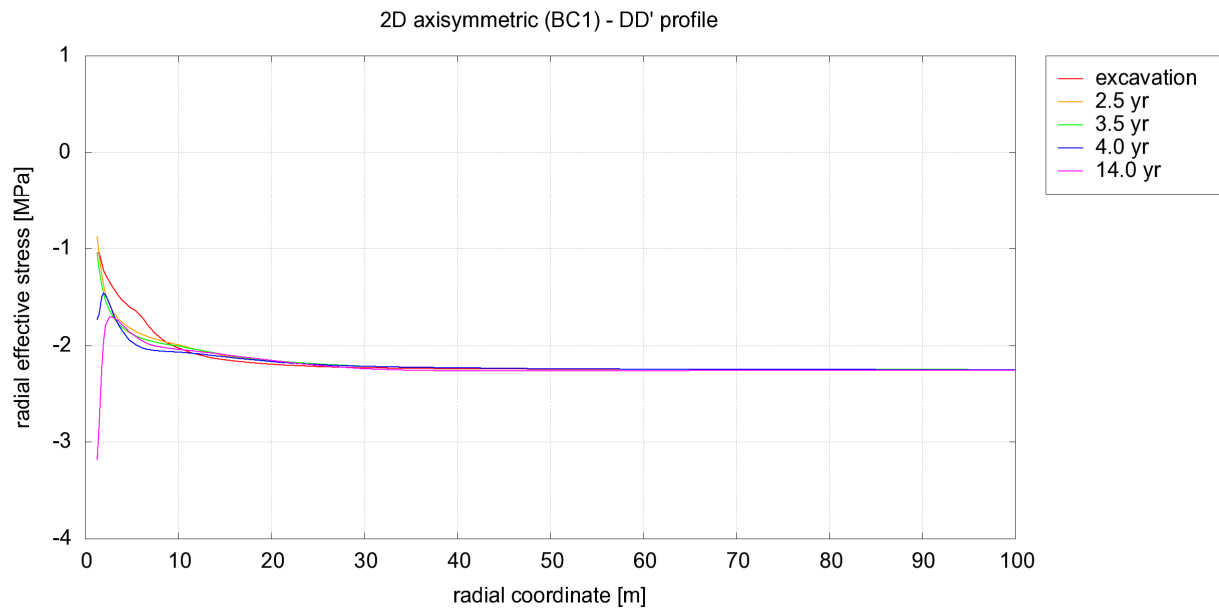


Figure 91: Radial effective stress along DD' (radial) profile

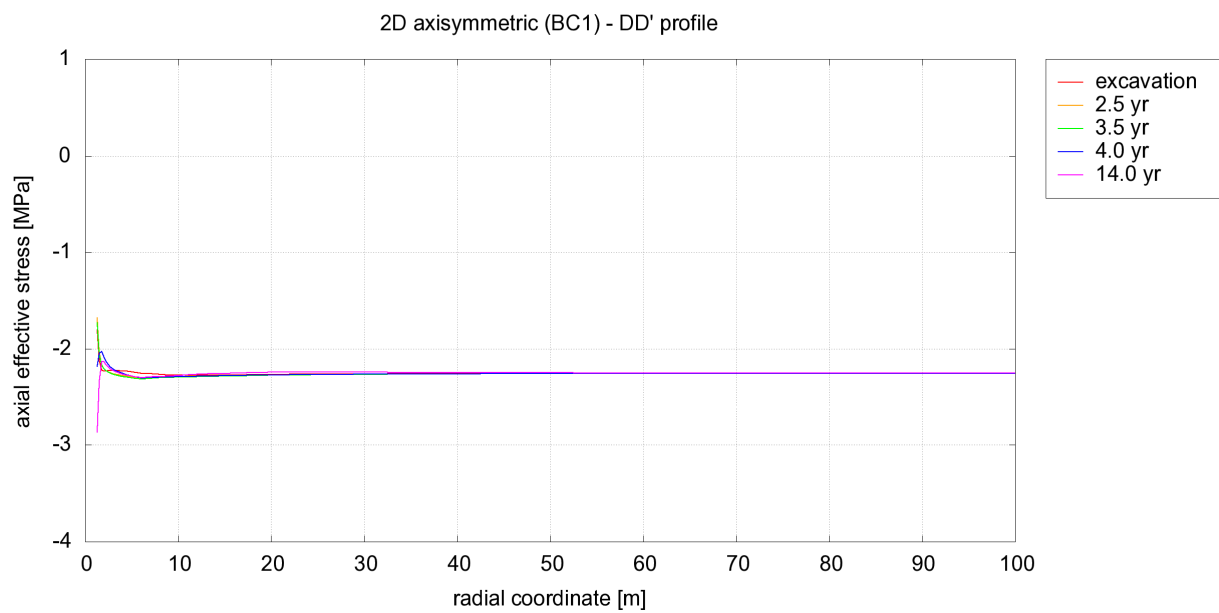


Figure 92: Axial effective stress along DD' (radial) profile

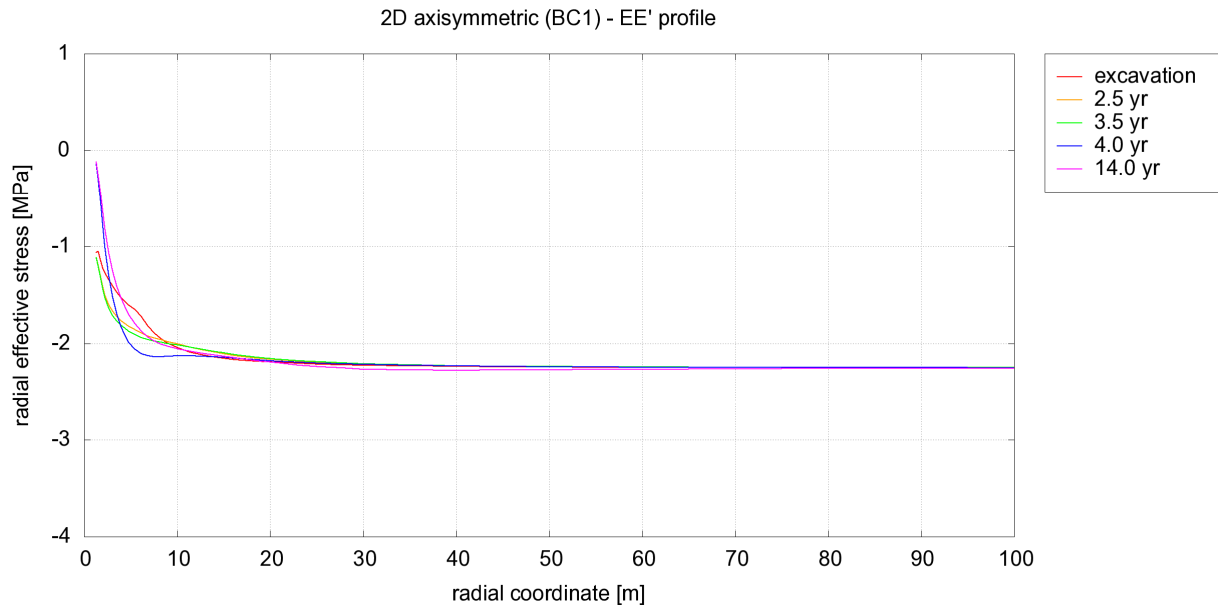


Figure 93: Radial effective stress along EE' (radial) profile

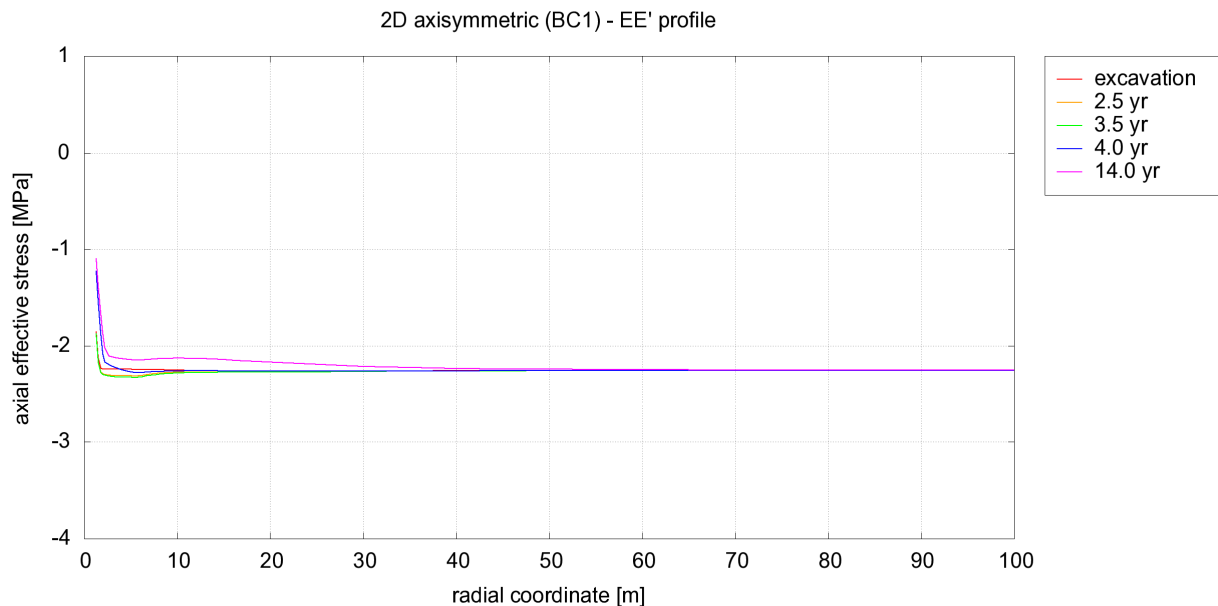


Figure 94: Axial effective stress along EE' (radial) profile

Mean and deviatoric stresses and stress path at sensors location

The Figure 95 and Figure 96 show the evolution in time at sensors location of the mean and the deviatoric effective stresses, respectively. Since the initial stress state is isotropic, the initial values of p' and q are:

- mean effective stress $p' = -2.25$ MPa
- deviatoric effective stress $q = 0$ MPa

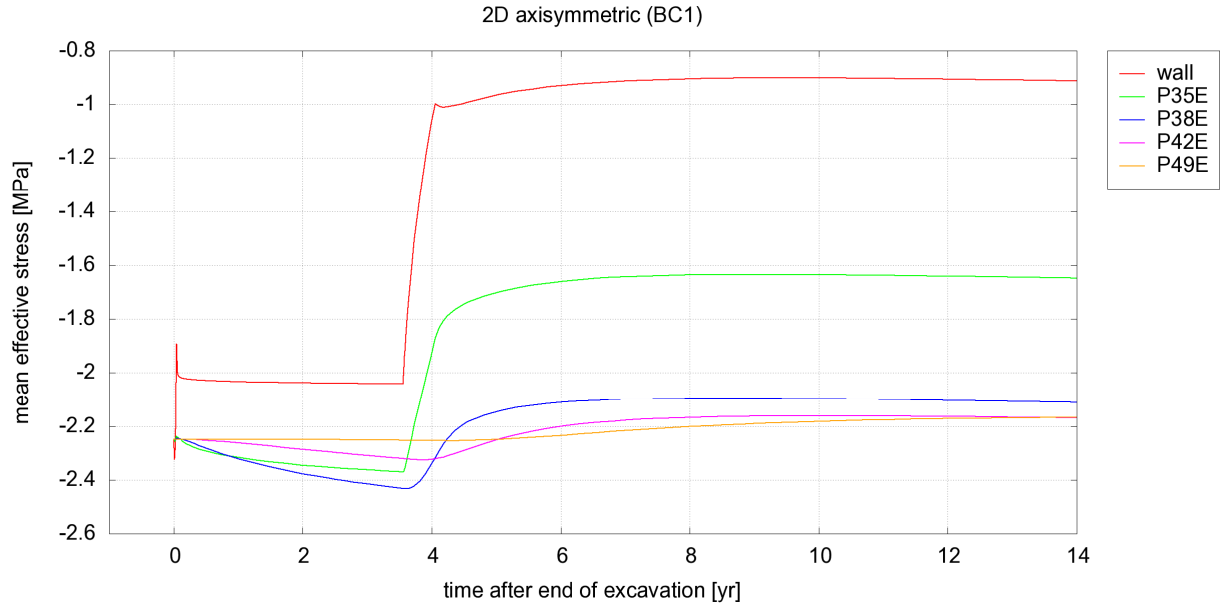


Figure 95: Evolution in time of mean effective stress p' at sensors location

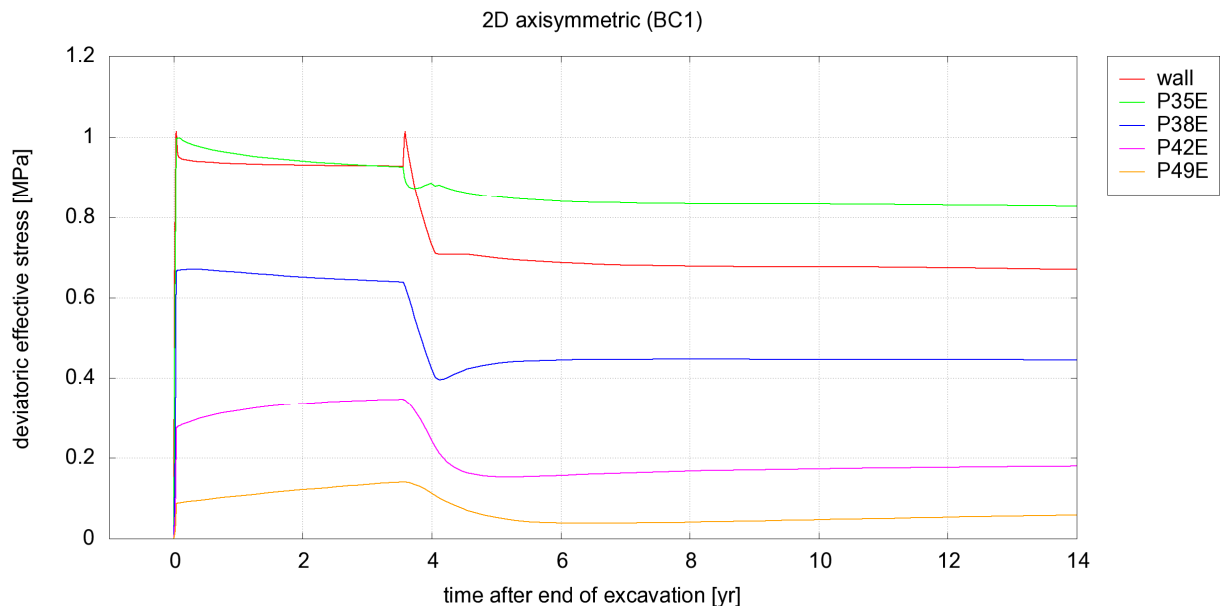


Figure 96: Evolution in time of mean effective stress q at the sensors location

The different phases of the calculation are clearly identified: first the excavation (almost instantaneous at this time scale), a 3.5 years period before the heater experiment and finally the heater test during the 10.5 last years.

To better understand what is happening during these phases, the next figures represent the stress path at the sensors location in the plane of the two invariants of the effective stresses, $I_1 = 3p'$ and $I_2 = \sqrt{3}q$.

As the Figure 97 shows, the plastic domain is reached at the wall and for the two first sensors P35E ($r = 2.2$ m) and P38E ($r = 4.7$ m). The two next sensors P42E ($r = 8.9$ m) and P49E ($r = 16.2$ m) remain in the elastic domain all of the time.

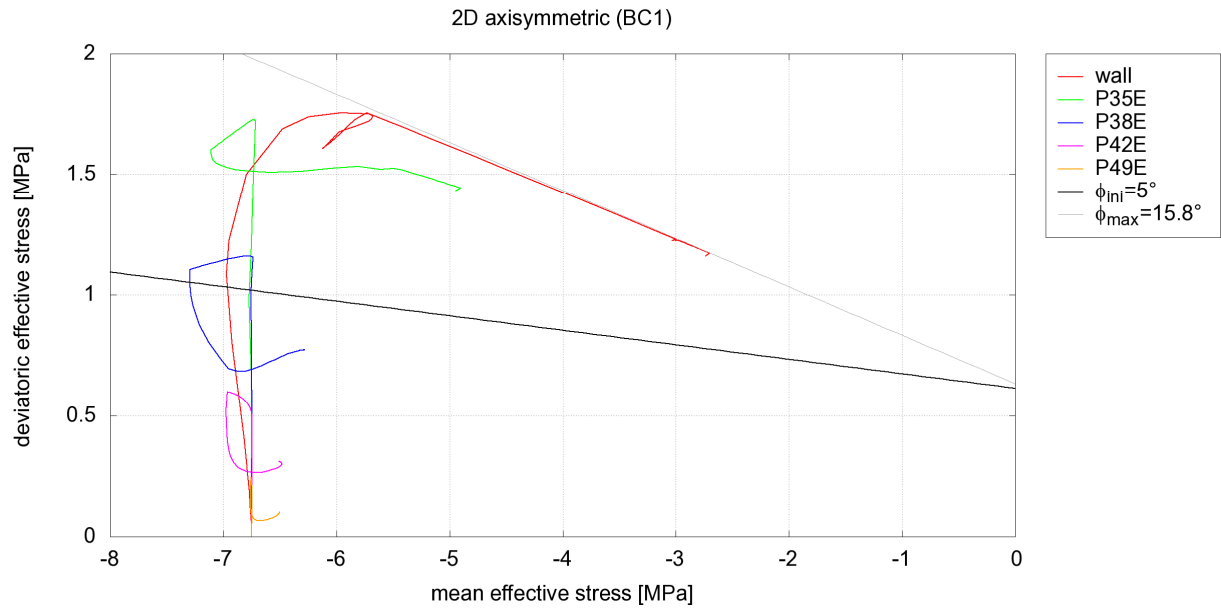


Figure 97: Stress path in the I_1 - I_2 invariants space at the sensors location

The complete history of the stress paths at each sensor location is detailed in Figure 98 to Figure 102.

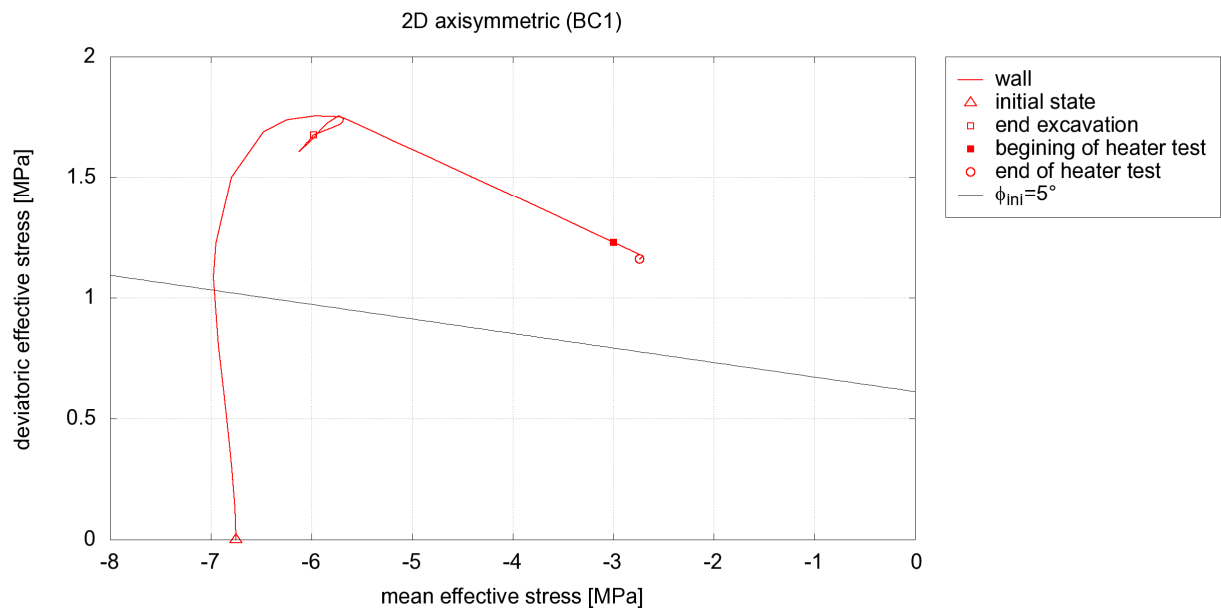


Figure 98: Stress path in the I_1 - I_2 invariants space at the wall (Boom clay / PRACLAY gallery interface)

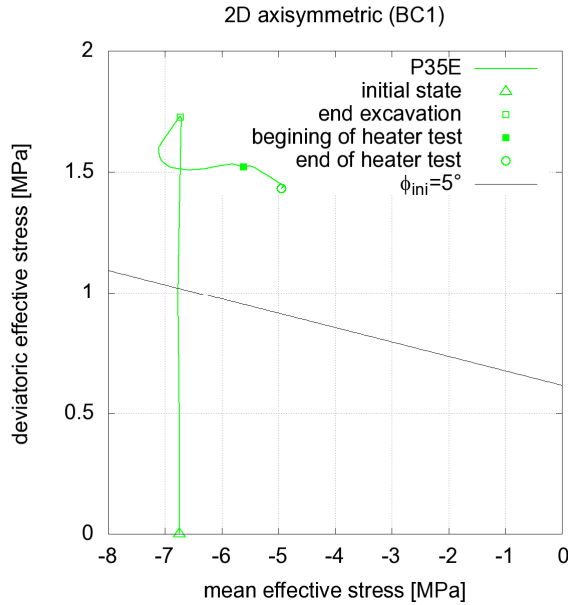


Figure 99: Stress path in the I_1 - I_2 invariants space at sensor P35E

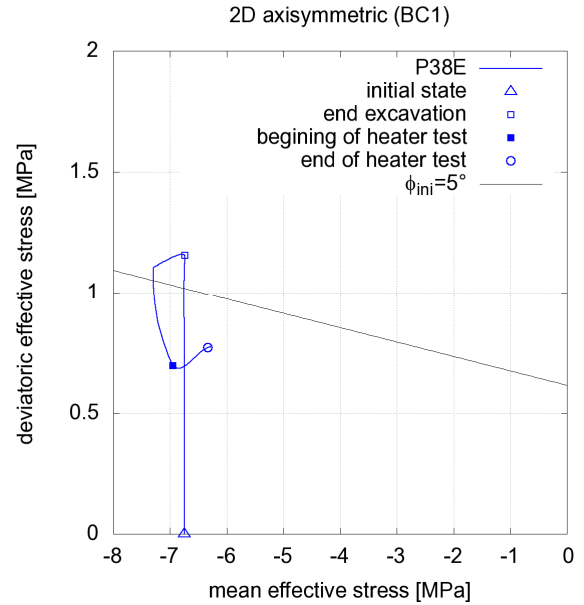


Figure 100: Stress path in the I_1 - I_2 invariants space at sensor P38E

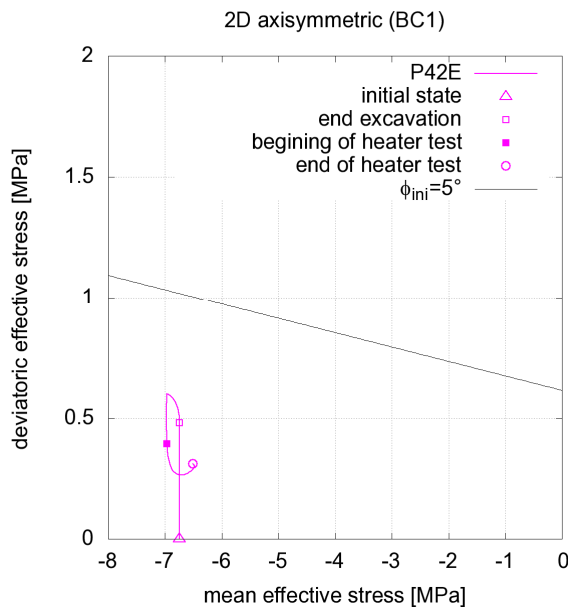


Figure 101: Stress path in the I_1 - I_2 invariants space at sensor P42E

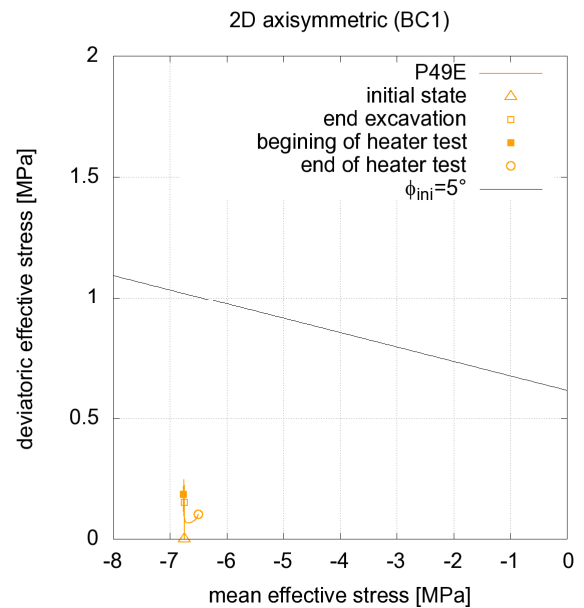


Figure 102: Stress path in the I_1 - I_2 invariants space at sensor P49E

The use of BC2 instead of BC1 does not change significantly the stress path, as illustrated in the Figure 103.

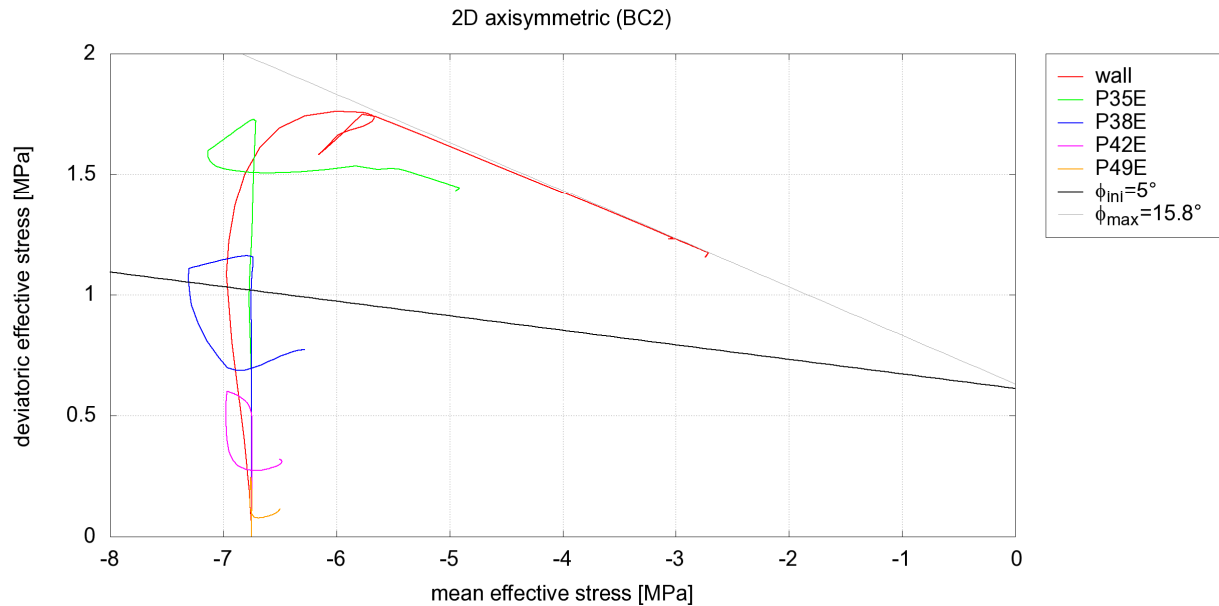


Figure 103: Stress path in the I_1 - I_2 invariants space at the sensors location using BC2

Plastic zone extent

The Figure 104 and the Figure 105 represent the Coulomb's friction angle at the end of the excavation and at the end of the heater experiment, respectively. No significant difference can be observed when comparing these figures, including the comparison of the use of BC1 and BC2.

The extent of the plastic zone is an annular zone around the PRACLAY gallery, the thickness of which being about 2.6 m.

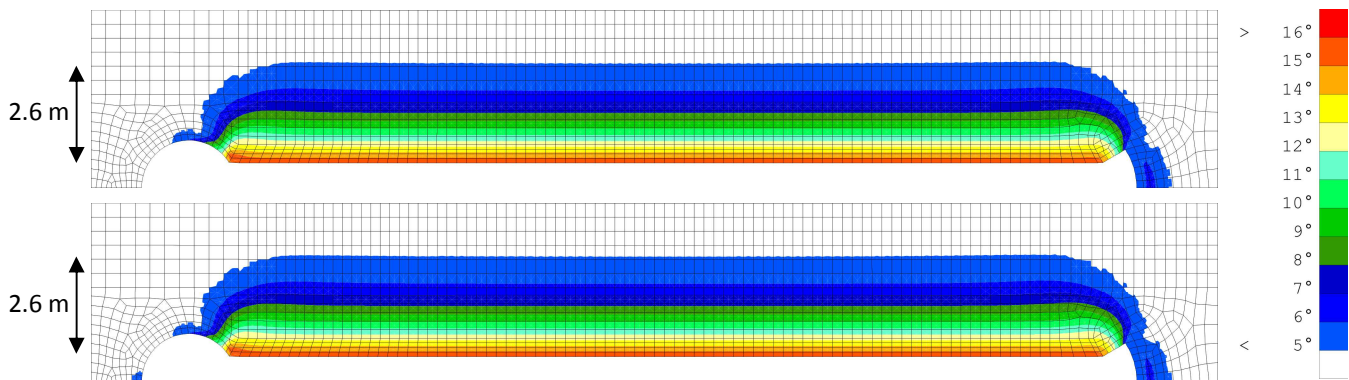


Figure 104: Actualized ("hardened") Coulomb's friction angle at the end of the excavation. Initial value is 5° (in white). Above: using BC1 – Below: using BC2

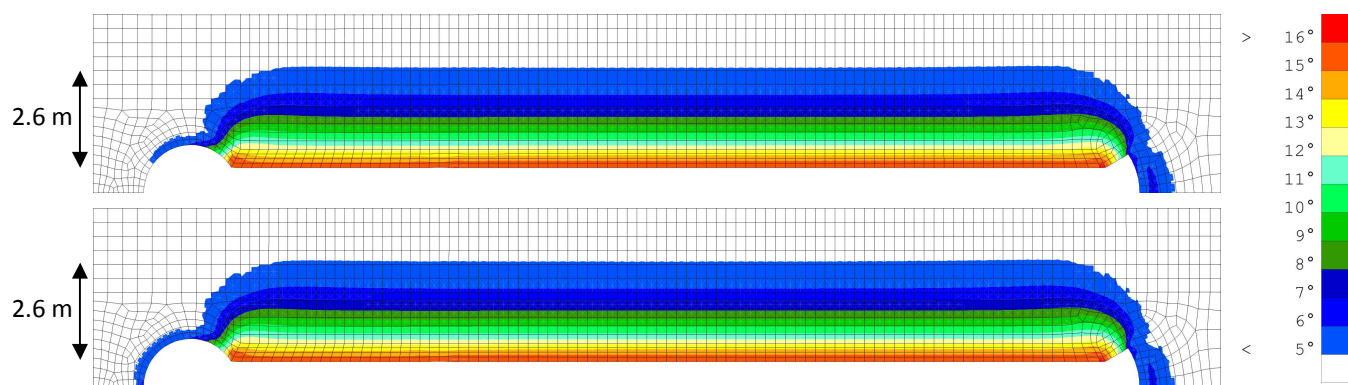


Figure 105: Actualized ("hardened") Coulomb's friction angle at the end of the heater experiment.
Initial value is 5° (in white). Above: using BC1 – Below: using BC2

4.3 3D modelling

Partners active in this model: ULg – CIMNE

4.3.1 Additional information about the 3D model

As described in the terms of the problem (cf. section 3.5, p. 45), “The geometry of the 3D modelling should be inspired by the geometry of the two preceding cases. This modelling effort should concentrate on the anisotropic effects in the Boom clay”.

The exercise of 3D modelling is therefore relatively free in order to make it accessible by the teams who can manage such approach. Here are some details of the 3D model by ULg.

Geometry

The geometry conforms to the description of the PRACLAY gallery in Figure 27.

The extent of the model is

- 250 m long, in the horizontal direction of the PRACLAY gallery axis, denoted x -direction
- 100 m wide, in the second horizontal direction, along connecting gallery axis, denoted y -direction
- 100 m high, in the vertical direction, denoted z -direction.

Taking into account the assumed double symmetry of the problem (no gravity in the model), the PRACLAY gallery is approximately centred in the model, as depicted in Figure 106.

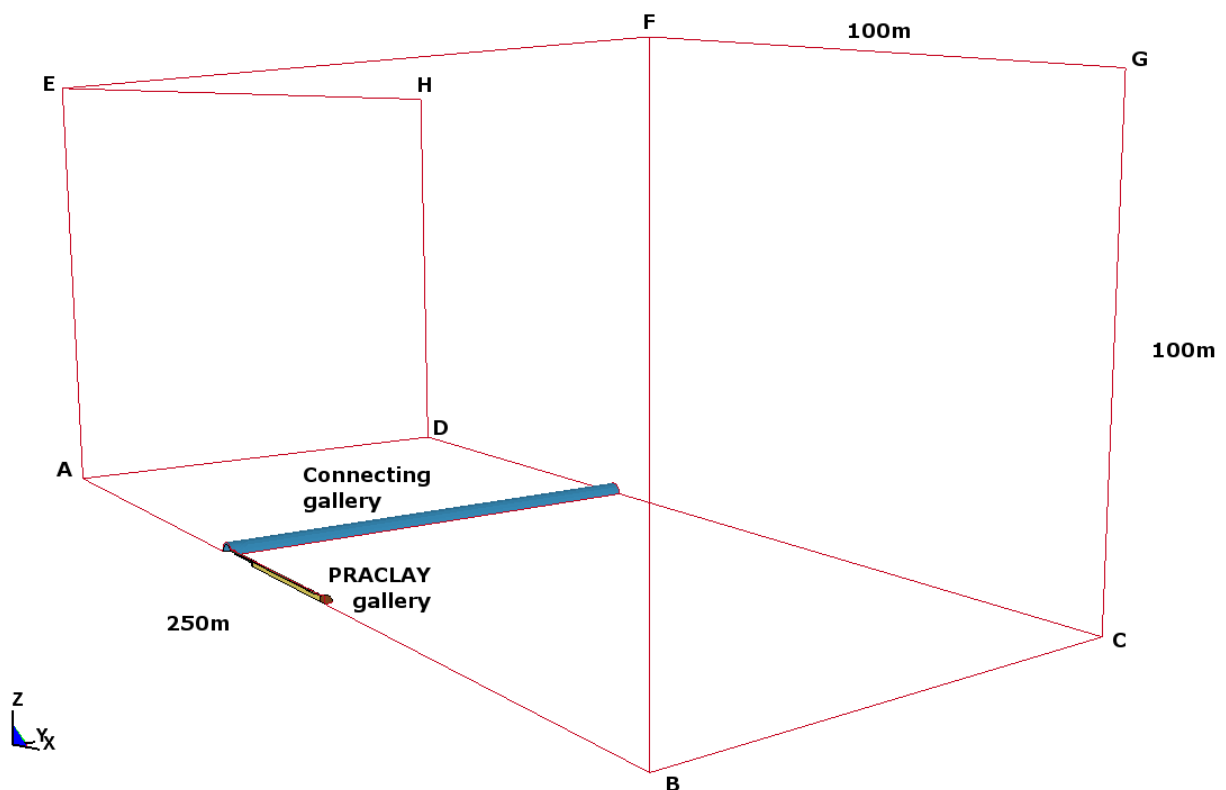


Figure 106: 3D model extent

In addition to the Boom clay, the same material components of the liner are considered, like in the 2D axisymmetric model (cf. Table 12). They are illustrated in the Figure 107.

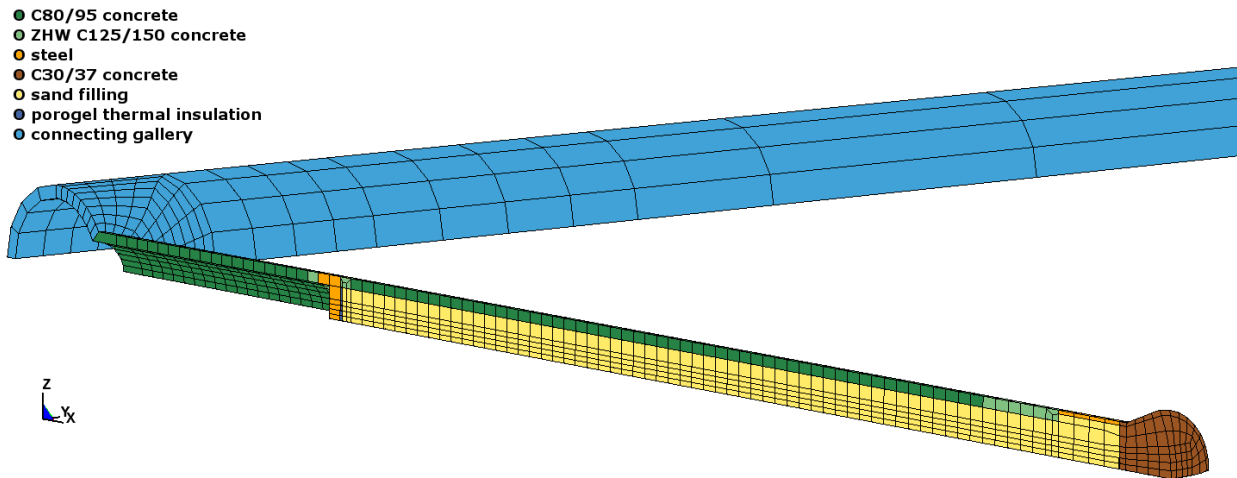


Figure 107: Detailed view of the 3D modelling of (1/4 of) the PRACLAY and connecting galleries

Initial conditions

The initial conditions are similar to those in the 2D plane strain model, i.e. considering the clay as homogeneous and isotropic, fully saturated, but taking into account the anisotropy of the initial stresses, as described in Table 1:

- Initial vertical total stress: $\sigma_{zz} = 4.5$ MPa (in compression)
- Initial horizontal total stresses: $\sigma_{xx} = \sigma_{yy} = 3.825$ MPa (in compression)

In the liner, the initial state is the one described in the section 3.4.2 for the 2D axisymmetric model.

Parameters

The material parameters are identical to those defined in the 2D axisymmetric model, cf. section 3.4.3

Boundary conditions and description of the calculation

Boundary conditions are similar to those defined in the 2D models, but only the second type of mechanical boundary conditions has been considered (denoted BC2). They are:

- Mechanical boundary conditions:
 - no z -displacement on the face ABCD (horizontal symmetry plane)
 - no y -displacement on the face ABFE (vertical symmetry plane)
 - no x -displacement at one node (to avoid rigid body motion)
 - external normal (compressive) loading to balance initial total stress:
 - $q_x = 3.825$ MPa on ADHE and $q_x = -3.825$ MPa on BCGF
 - $q_y = -3.825$ MPa on DCGH
 - $q_z = -4.5$ MPa on EFGH

- Hydraulic and thermal boundary conditions: all boundaries are impervious and adiabatic, except when the prescribed values (pore water pressure and temperature) are defined in accordance with the 5 successive phases of the experiment and summarized in the 2D axisymmetric case (cf. section 0).

Note:

To make easier the comparison of the 3D model with the 2D models, the following results concern profiles denoted “ABC” (horizontal) and “GFE” (vertical) that correspond to those defined in the 2D plane strain model. They are located in the plane $x = 22.75$ m, which corresponds to the mid-plane of the ring 44, in accordance with the profiles presented in the results of the 2D axisymmetric model.

Hence, the notations “ABC” and “GFE” do not refer to the letters used in the Figure 106, but in the Figure 31.

4.3.2 Pore water pressure

Due to the anisotropy of the initial stresses, the pore water pressure profiles along the ABC-horizontal and GFE-vertical directions differ as soon as the excavation of the PRACLAY gallery is executed.

Like in the 2D plane strain model, a peak of p_w (about 2.4 MPa) can be observed in Figure 108 for the ABC-horizontal profile after excavation (red curve), while the p_w profile is monotonic along the GFE-vertical direction (red crosses). A detailed view in the vicinity of the gallery is shown in the Figure 109. This difference tends to disappear as soon as the heating effect becomes more and more marked.

The maximum level of p_w at the end of the heater test is about 2.5 MPa, in both horizontal and vertical profiles, and it is located at 8 to 9 m from the gallery axis.

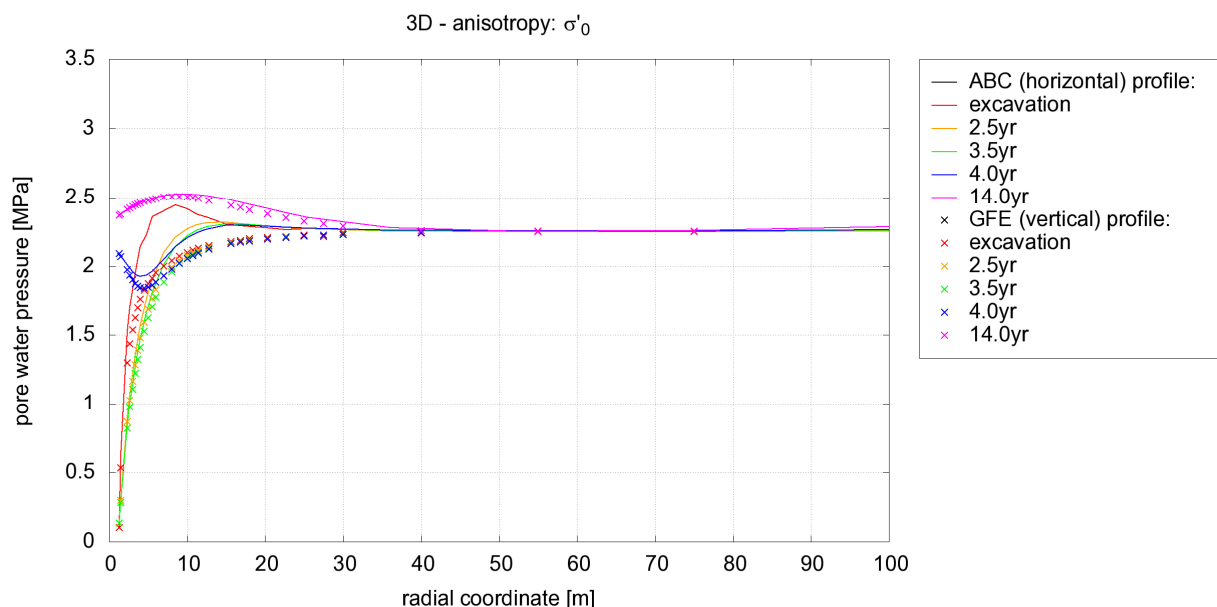


Figure 108: Pore water pressure along “ABC” (horizontal) and “GFE” (vertical) profiles in the mid-plane of ring 44

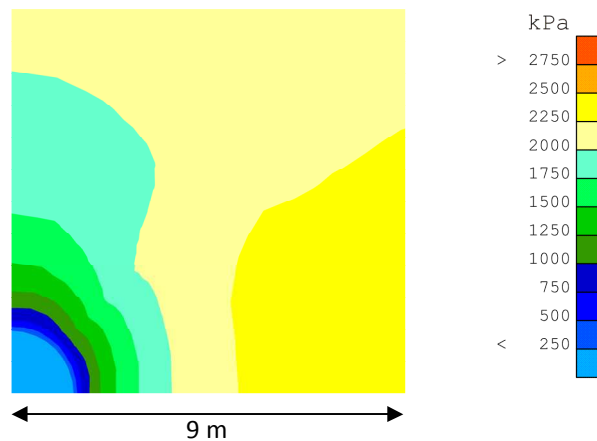


Figure 109: Pore water pressure at the end of the excavation.
Detailed view in the mid-plane of the ring 44 around the excavated gallery.

The evolution in time of p_w at the sensors is plotted in the Figure 110. The three main parts of the PRACLAY experiment are clearly visible: excavation – 3.5 years of stabilization – heater test (0.5 year to heat up the system and 10 additional years of observation). It is noticeable that the p_w during the last 6 to 8 years stabilizes around 2.4-2.5 MPa for all sensors, except P49E (the most distant one) the p_w of which being slowly increasing (in the same range as the p_w of the other sensors).

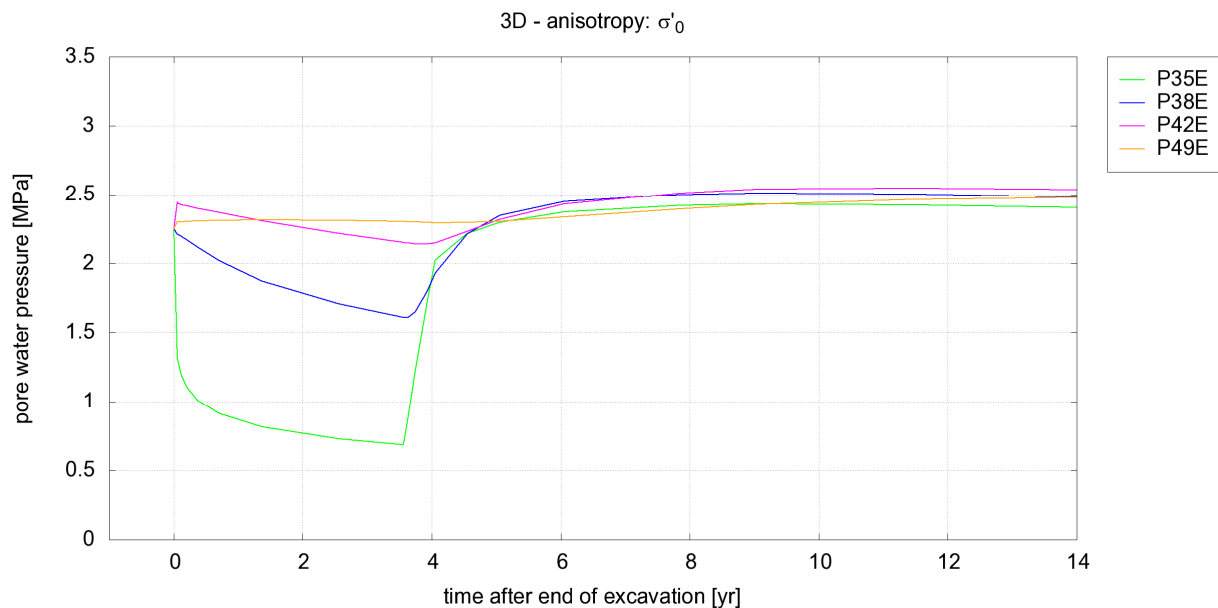


Figure 110: Evolution in time of pore water pressure at sensors location

4.3.3 Temperature

The temperature profiles are identical in both horizontal and vertical directions, as depicted in the Figure 111. The effect of heating is visible up to 40 m from the gallery axis, but the heating remains under 5°C from 20 m and over.

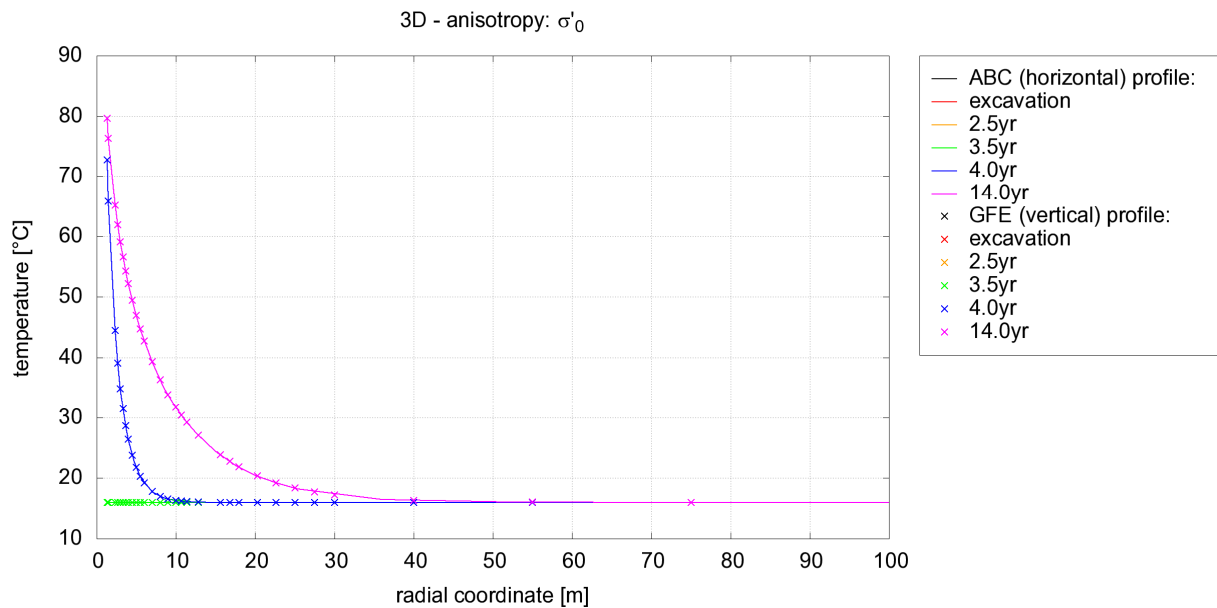


Figure 111: Temperature along “ABC” (horizontal) and “GFE” (vertical) profiles in the mid-plane of ring 44

The Figure 112 shows the evolution of the temperature at the sensors location.

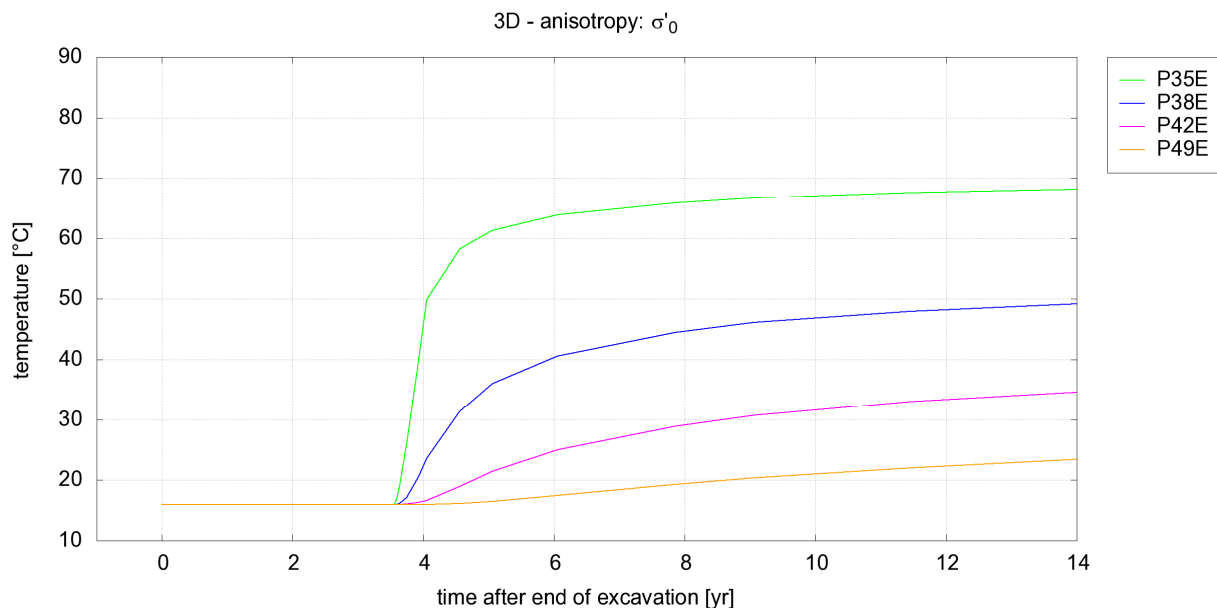


Figure 112: Evolution in time of temperature at sensors location

4.3.4 Radial displacement

As shown in the Figure 113, the radial displacement at the wall reaches -6 cm (convergence of the Boom clay up to contact with the liner), in both directions. The effect of the anisotropy of initial stresses remains visible during all the experiment, the radial displacement being different in both directions, even at the end of the heat test.

For radial coordinates over 50 m the magenta curve representing the radial displacement after 14 years along the ABC-horizontal exhibits a behaviour probably linked to a too much coarse mesh.

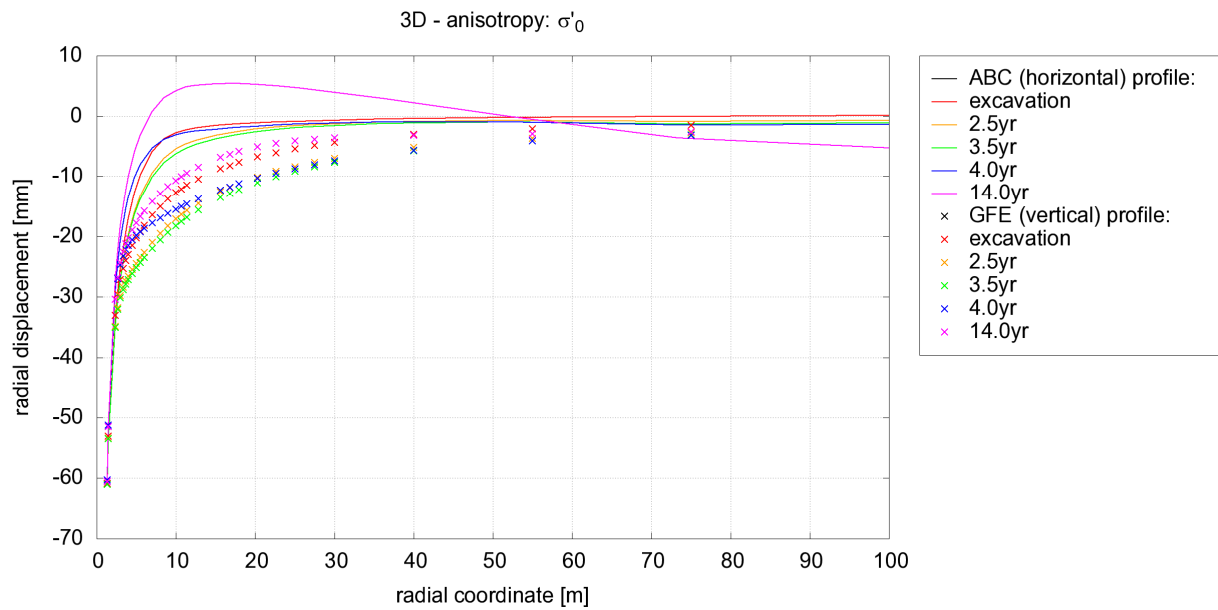


Figure 113: Radial displacement along “ABC” (horizontal) and “GFE” (vertical) profiles in the mid-plane of ring 44

4.3.5 Effective stresses

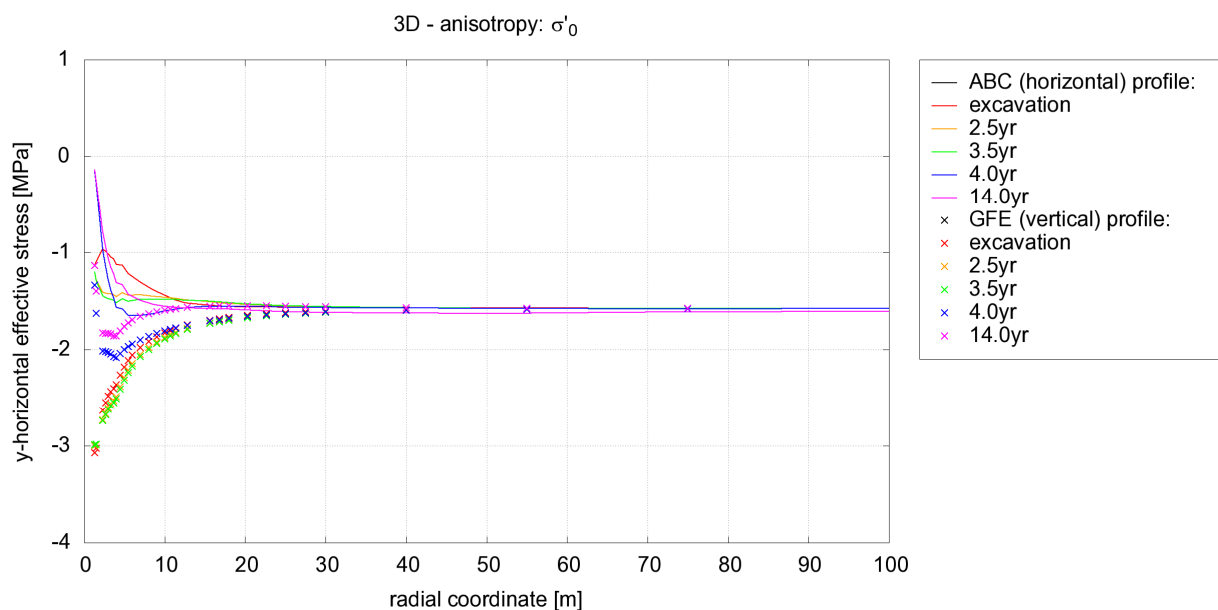


Figure 114: y-horizontal effective stress along “ABC” (horizontal) and “GFE” (vertical) profiles in the mid-plane of ring 44

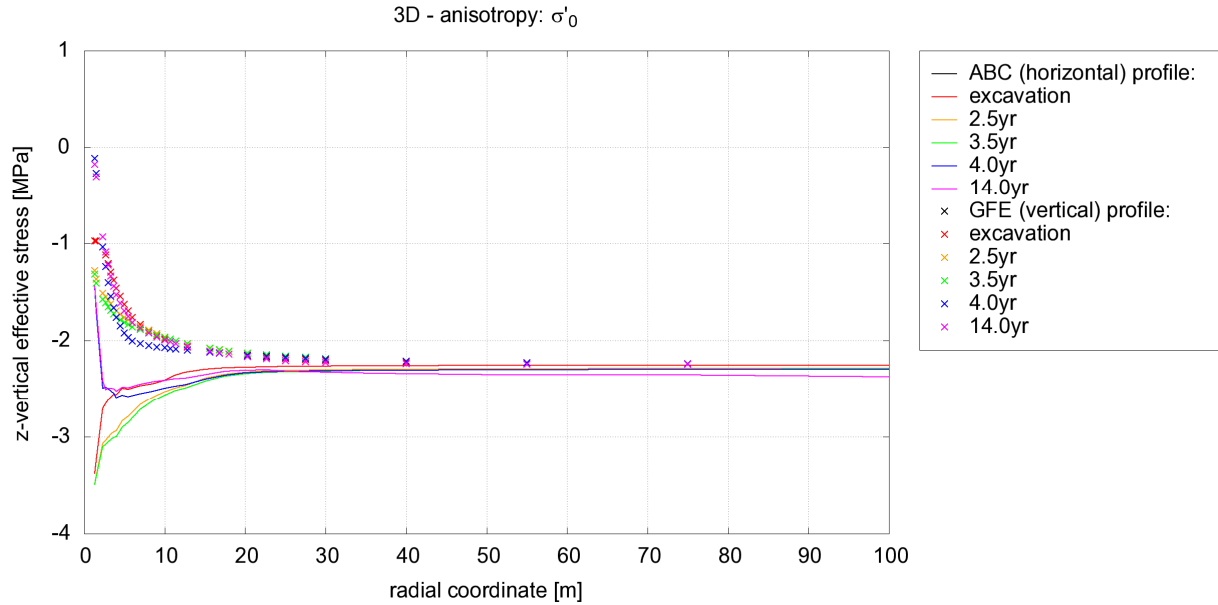


Figure 115: z-vertical effective stress along “ABC” (horizontal) and “GFE” (vertical) profiles in the mid-plane of ring 44

Mean and deviatoric stresses and stress path at sensors location

The Figure 116 and Figure 117 represent the evolution of the mean and deviatoric effective stresses at sensors location. The initial values are:

- initial mean effective stress $p' = \frac{1}{3} \sigma'_{ii} = -1.8 \text{ MPa}$
- initial deviatoric effective stress $q = \sqrt{\frac{1}{2} \hat{\sigma}'_{ij} : \hat{\sigma}'_{ij}} \approx 0.39 \text{ MPa}$

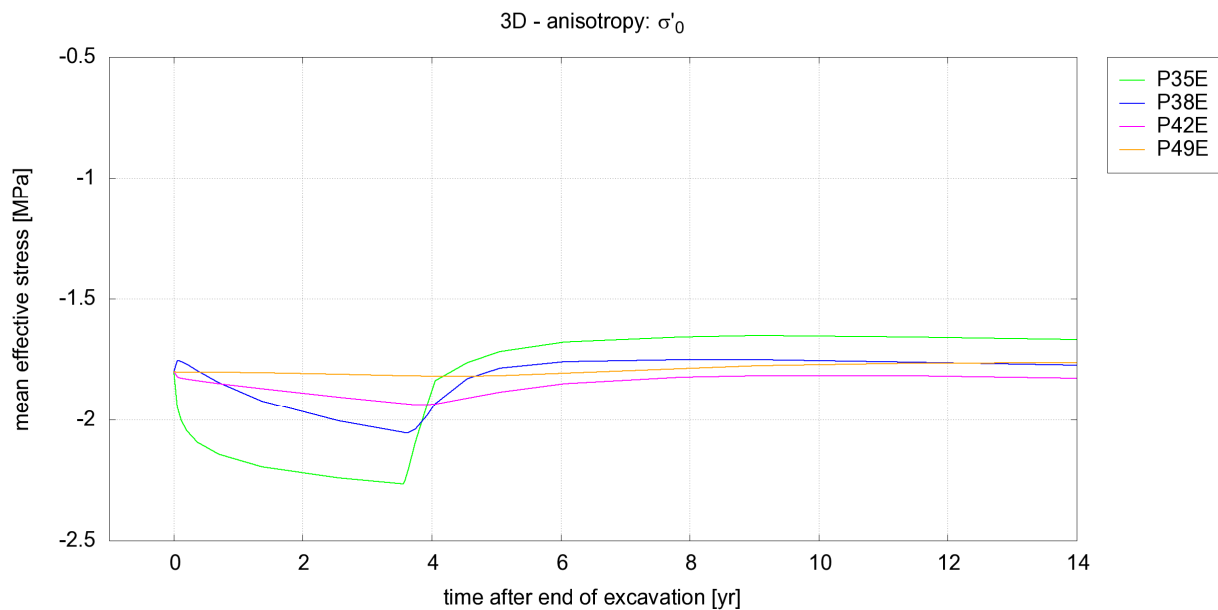


Figure 116: Evolution in time of mean effective stress p' at sensors location

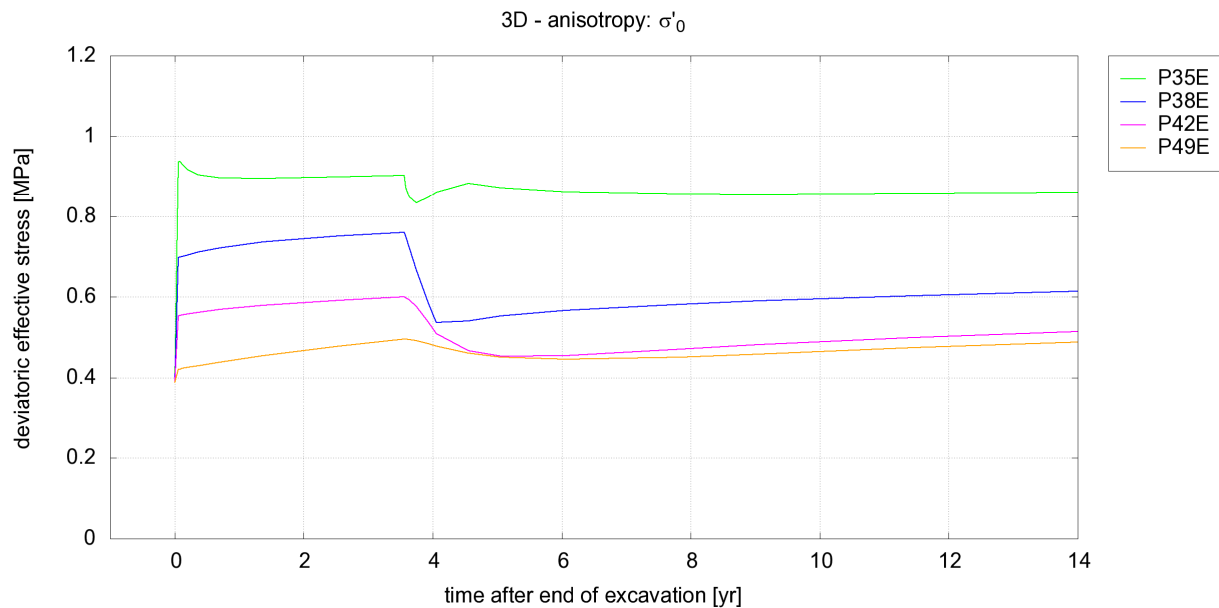


Figure 117: Evolution in time of deviatoric effective stress q at sensors location

The Figure 118 illustrates the stress path at sensors location in the plane of the two (effective) stress invariants I_1 and I_2 . This figure shows that the plastic domain is reached at the location of all sensors, except P49E, which is located about 16 m far from the gallery axis and remains in the elastic domain.

The stress path during all successive phases (excavation, stabilization, heating) is detailed in Figure 119 to Figure 122 for each of the sensor locations.

Note that the first phase of the simulated experiment – the excavation of the PRACLAY gallery – has been performed in one time step to avoid oscillations in the pore water pressure field due to numerical reasons. This approach implies that the stress path during this phase is represented by a segment of straight line from the initial stress state to the stress state “at the end of excavation”. Hence, no details are available concerning the stress path during the convergence of Boom clay entering in contact with the liner. To overcome this problem, a finer mesh is required in order to compute smaller time steps, but this would lead to much memory and computing time consuming simulations, even though the present ones are already memory and CPU expensive.

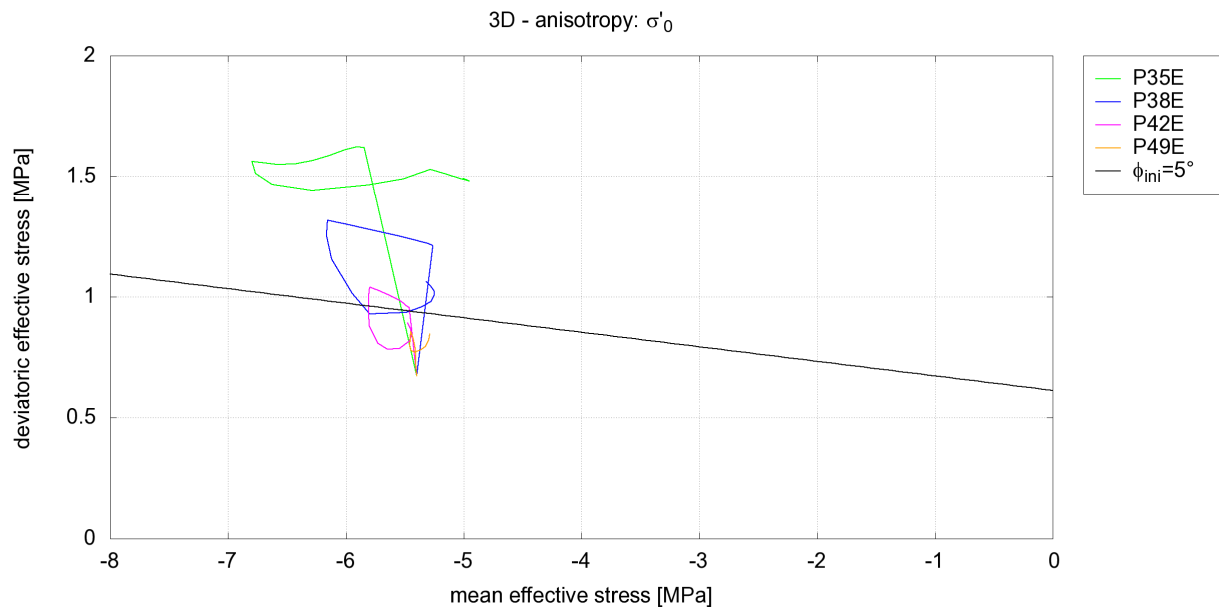


Figure 118: Stress path in the I_1 - I_2 invariants space at sensors location

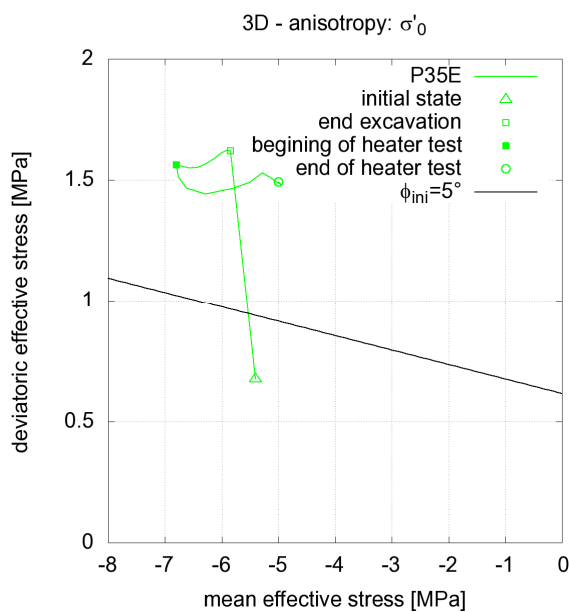


Figure 119: Stress path in the I_1 - I_2 invariants space at sensor P35E

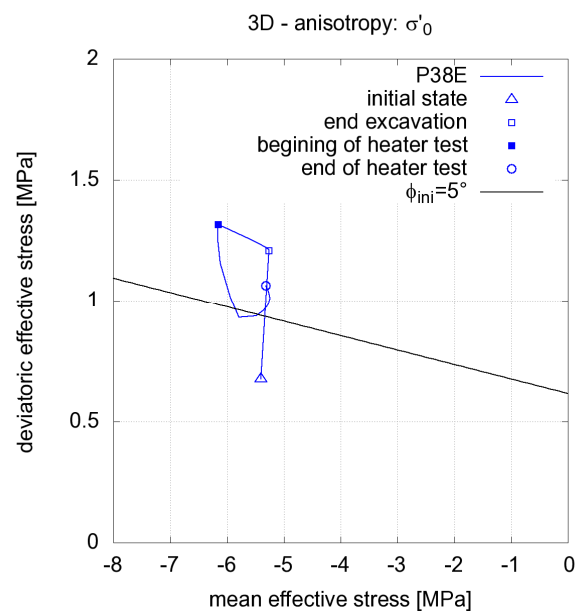


Figure 120: Stress path in the I_1 - I_2 invariants space at sensor P38E

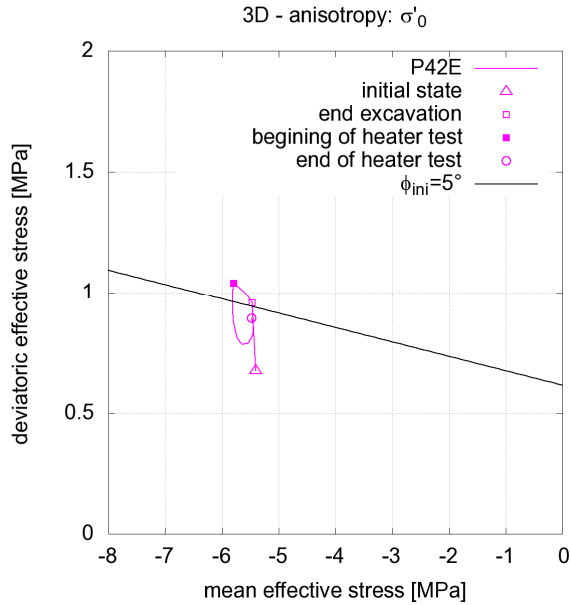


Figure 121: Stress path in the I_1 - I_2 invariants space at sensor P42E

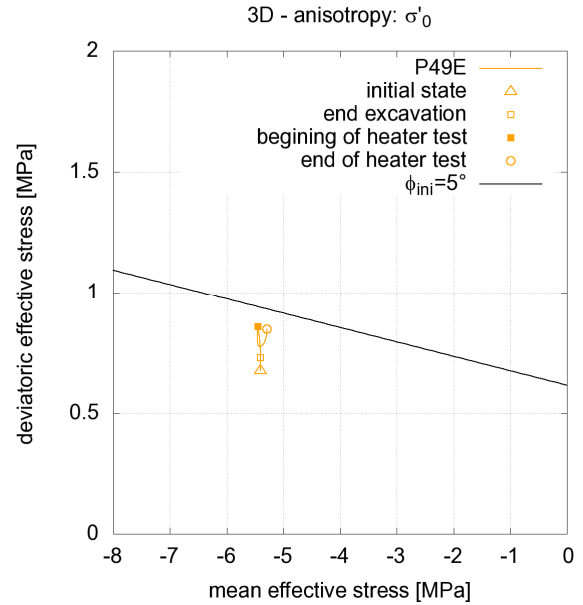


Figure 122: Stress path in the I_1 - I_2 invariants space at sensor P49E

Plastic zone extent

The Figure 123 shows the actualized (hardened) Coulomb's friction angle at the end of the excavation. The extent of the plastic zone is an annular zone around the PRACLAY gallery, the thickness of which varying approximately from 3 m in the vertical direction to 10 m in the horizontal direction.

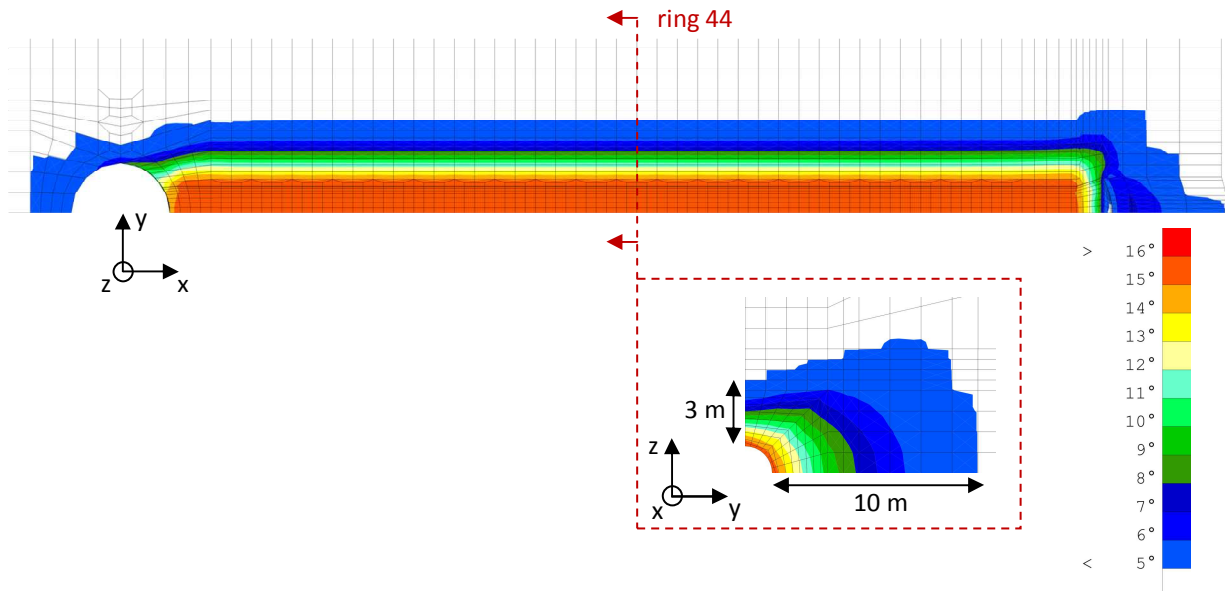


Figure 123: Actualized Coulomb's friction angle at the end of the excavation. Initial value is 5° (in white).

5 Comparison of 2D and 3D models

5.1.1 Pore water pressure

The comparison of the p_w profiles obtained using the 3 different approaches leads to two main conclusions summarized on the following figures:

- At the end of the gallery excavation (Figure 124), the anisotropy of the initial stresses implies a higher p_w along the horizontal profile. Both 2D plane strain and 3D models include this anisotropy and they provide very similar results: the same difference between horizontal and vertical p_w profiles and the same overpressure (peak) along the horizontal profile (the same maximum value as well as the same location). With the 2D axisymmetric model, which does not take into account the anisotropic initial stresses, the p_w profile is in-between.
- At the end of the experiment (Figure 125), the difference between the horizontal and vertical profiles is not so large anymore, as predicted by those models including this anisotropy, i.e. 2D plane strain and 3D models. The main difference is now between the 2D plane strain model that predicts a maximum p_w at the wall (about 2.7 MPa) and both 2D axisymmetric and 3D models that agree on a maximum p_w around 2.5 MPa and located at about 9 to 10 m from the gallery axis.

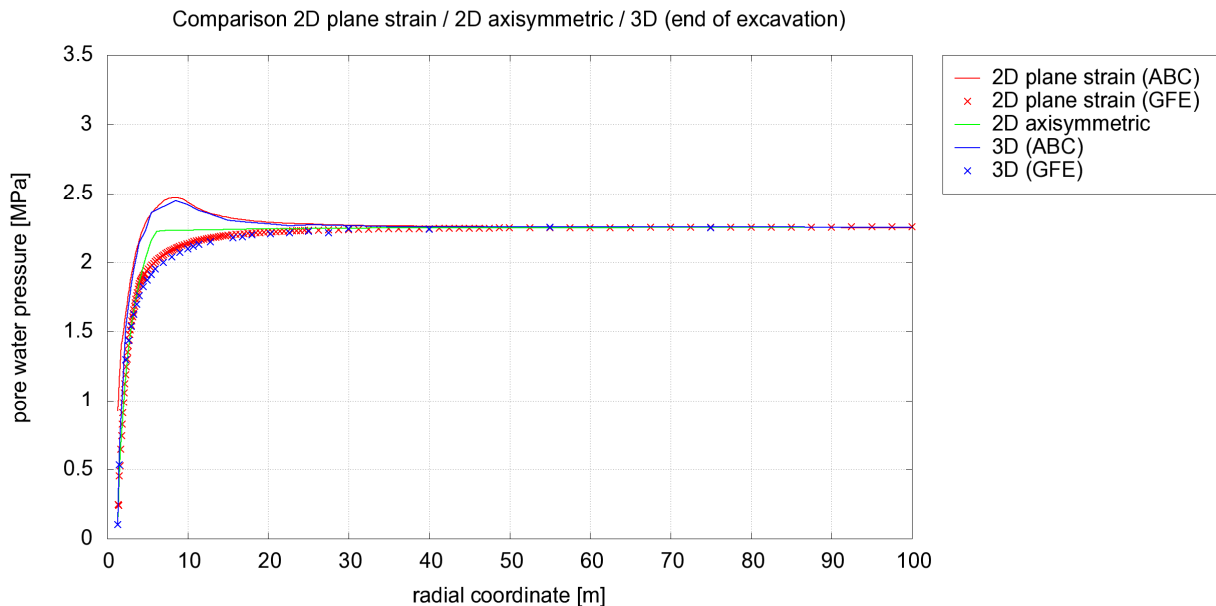


Figure 124: Comparison of the p_w horizontal and vertical profiles at the end of the excavation with the 2D plane strain, 2D axisymmetric and 3D models (using BC2 in all models)

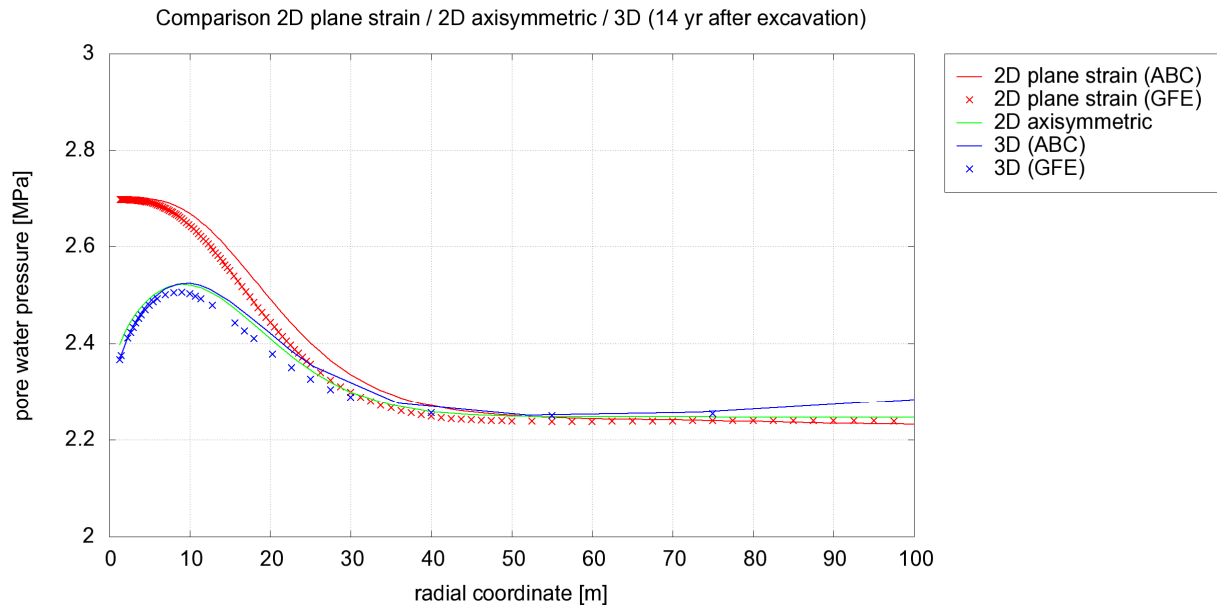


Figure 125: Comparison of the p_w horizontal and vertical profiles at the end of the experiment with the 2D plane strain, 2D axisymmetric and 3D models (using BC2 in all models)

Hence, the 3D model is the more complete than 2D models and it should indicate the most realistic results among the three approaches. In the short term results, the 2D plane strain model is in good agreement with the 3D model (since the anisotropy could be introduced).

In the long term results, the effect of anisotropy of the initial stresses is not as important as just after excavation. The 2D axisymmetric and 3D models are therefore in good agreement, since the diffusion of p_w along the axial direction is allowed in the 2D axisymmetric model and not in the 2D plane strain one.

Nevertheless, we should keep in mind that no other anisotropy but initial stresses is included in the 3D model. Otherwise, if some other anisotropic properties were taken into account (such as intrinsic permeability or thermal conductivity), we would expect to see a difference between the 2D axisymmetric and the 3D approaches.

5.1.2 Temperature

The temperature profiles in all the models are very close, as illustrated in the Figure 126, and no anisotropy can be observed since thermal properties are isotropic in all models (hence vertical and horizontal profiles are superposed in the figure).

The main difference is observed when comparing the 2D plane strain model with the two other models. Since there is no heat diffusion in the direction of the gallery axis in this model, the temperature is a little bit higher than the temperature predicted by the 2D axisymmetric and 3D model, that are in very good agreement on this. The gap between the different approaches is maximum between 10 and 20 m and it reaches a few degrees (about 2°C).

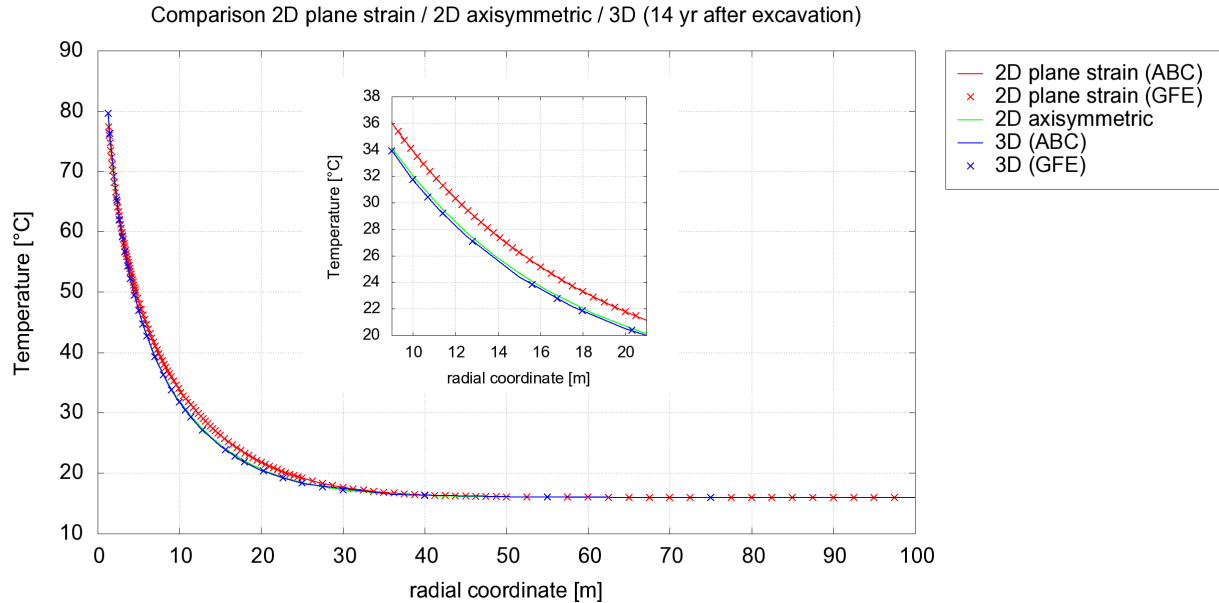


Figure 126: Comparison of the horizontal and vertical temperature profiles at the end of the experiment with the 2D plane strain, 2D axisymmetric and 3D models (using BC2 in all models)

5.1.3 Radial displacement

The comparison of the radial displacement at the end of the excavation using the different models (cf. Figure 127) is very similar to the analysis of the p_w profiles. The 2D plane strain and 3D models give the same different curves along the horizontal and vertical profiles and the 2D axisymmetric model is again in-between. The reason is still a question of anisotropic initial stresses.

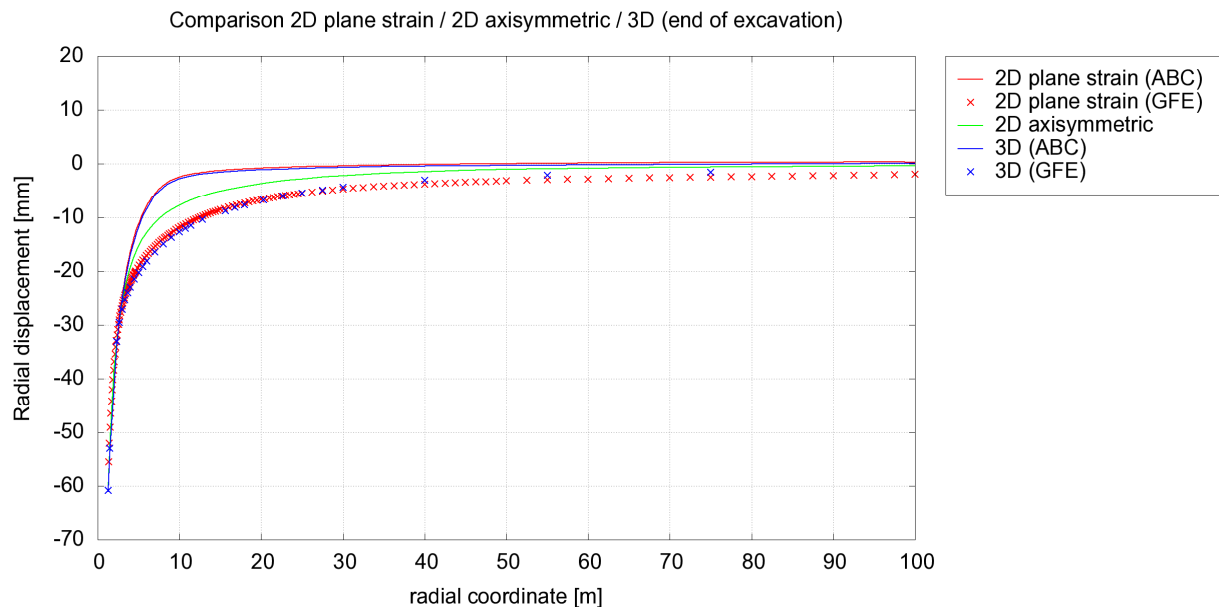


Figure 127: Comparison of the radial displacement along horizontal and vertical profiles at the end of the excavation with the 2D plane strain, 2D axisymmetric and 3D models (using BC2 in all models)

Observing the same profiles at the end of the experiment (Figure 128) is now different from the profiles of p_w 14 years after the excavation of the gallery: the agreement between 2D

axisymmetric and 3D models is not as good as in the Figure 125. The reason comes from the fact that the radial displacement is a cumulated value during all the experiment and the history in the 2D axisymmetric and 3D models is not exactly the same, more especially in terms of plasticity as described in the next section. Even though similar pressure levels (and stress levels) can be observed at the end of the experiment in the two approaches (as in the Figure 125), the plastic strain might be very different and so the corresponding displacement profiles might do (Figure 128).

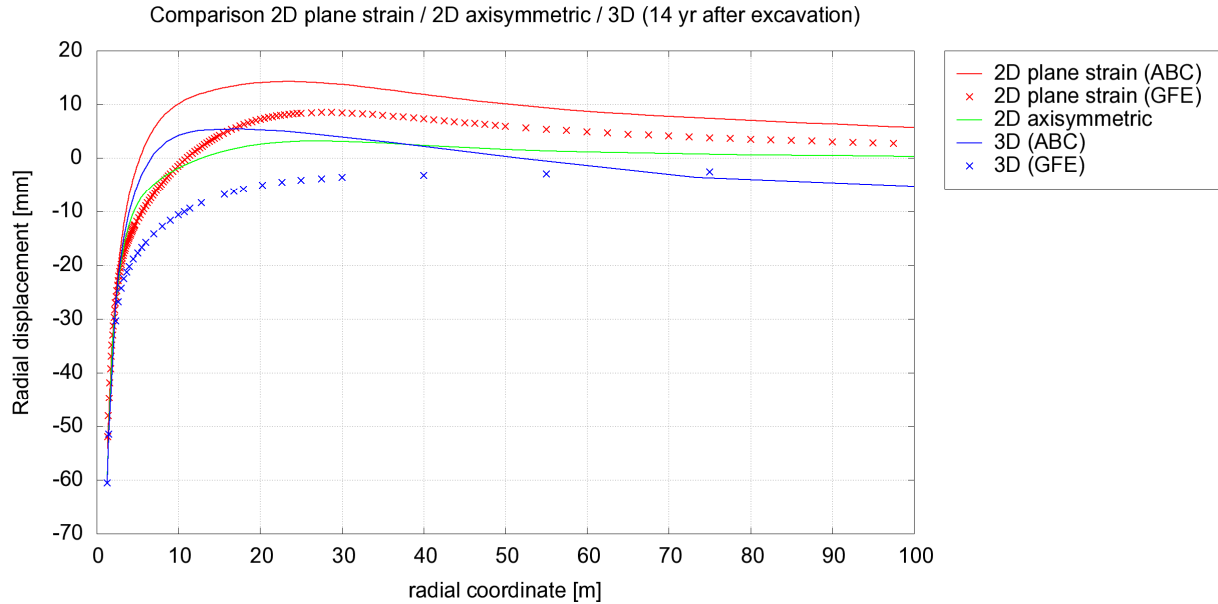


Figure 128: Comparison of the radial displacement along horizontal and vertical profiles at the end of the experiment with the 2D plane strain, 2D axisymmetric and 3D models (using BC2 in all models)

5.1.4 Effective stress path

The main difference between the models comes from the initial stress state. As the initial effective stresses are isotropic in the 2D axisymmetric model, the stress path start from another initial point in the invariants space:

- in the 2D plane strain and 3D models:

$$I_{1,ini} = -5.4 \text{ MPa} \quad \text{and} \quad I_{2,ini} = 0.675 \text{ MPa}$$

- in the 2D axisymmetric model:

$$I_{1,ini} = -6.75 \text{ MPa} \quad \text{and} \quad I_{2,ini} = 0 \text{ MPa}$$

Considering the initial drained friction angle $\phi_{ini} = 5^\circ$, the stress state reaches more quickly the plastic domain in the 2D plane strain and 3D models than in the 2D axisymmetric model. As a consequence, the sensor P42E remains in the elastic domain according to the 2D axisymmetric model, while it enters the plastic domain according the two other models, as shown in the Figure 131.

For all four sensors, the 2D plane strain and the 3D models are in relatively good agreement (cf. Figure 129 to Figure 132), the main drawback of the 3D model being the lack of a complete path during the excavation because of numerical reasons, as already explained in section 4.3.5.

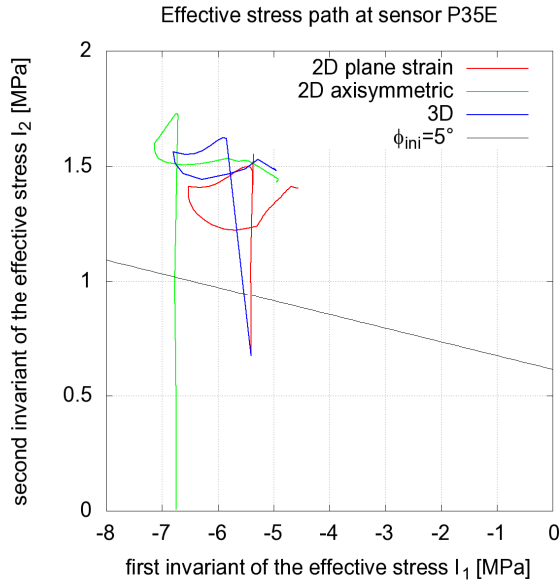


Figure 129: Stress path in the I_1 - I_2 invariants space at sensor P35E

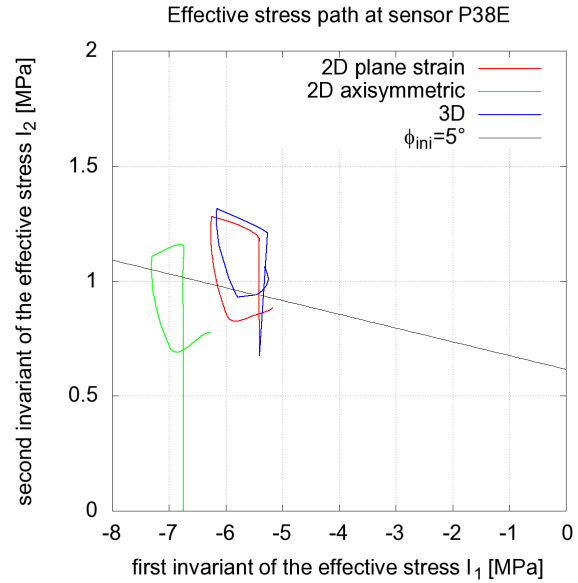


Figure 130: Stress path in the I_1 - I_2 invariants space at sensor P38E

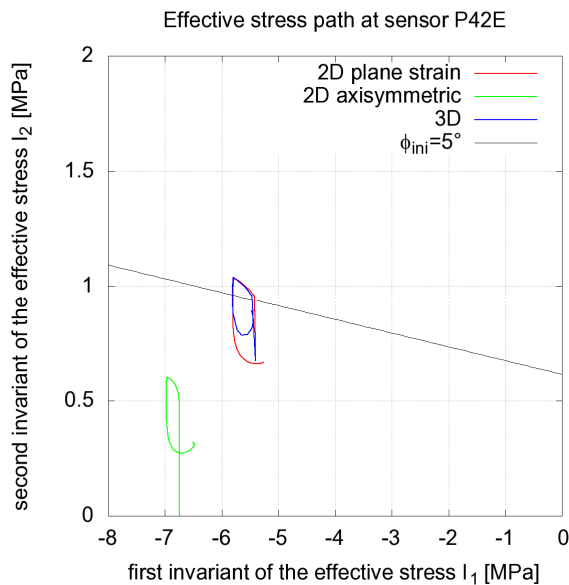


Figure 131: Stress path in the I_1 - I_2 invariants space at sensor P42E

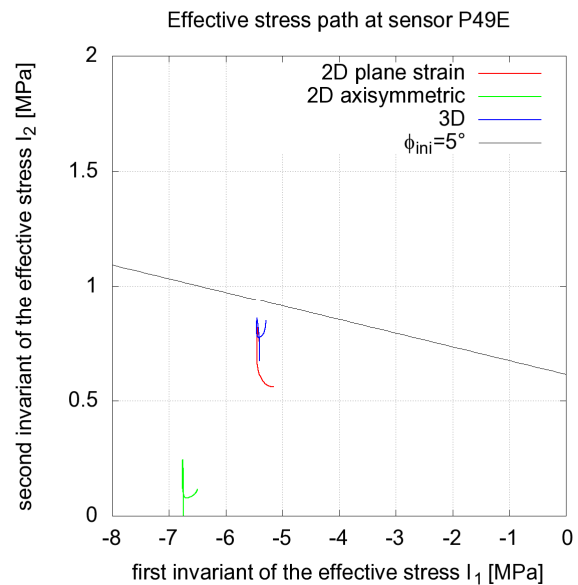


Figure 132: Stress path in the I_1 - I_2 invariants space at sensor P49E

5.1.5 Plastic zone extent

The 2D axisymmetric model predicts a less extended plastic zone, the thickness of which being 2.6 m (cf. Figure 104 and Figure 105).

The 2D plane strain and 3D models are in good agreement, predicting a plastic zone extending up to 3 m along the vertical direction and about 3 times deeper in the horizontal direction, up to 9 m - 11 m (cf. Figure 60 - Figure 61 in 2D plane strain, and Figure 123 in 3D).

6 Specific aspects highlighted by different labs

This section provides some additional results obtained by different labs who further investigated the problem by including specific aspects (different constitutive laws, effect of the boundary conditions, anisotropic material parameters, etc).

6.1 EPFL

The EPFL team carried out the computations with an additional objective in mind; to assess the influence of non-linear thermo-elasticity and thermo-plasticity on the THM response of the repository.

6.1.1 Mechanical model

The ACMEG-T constitutive model accommodates non-linear thermo-elasticity coupled with a multi-dissipative thermo-plasticity in order to reproduce most thermo-mechanical features. The elastic part of the deformation increment $d\boldsymbol{\varepsilon}^e$ is expressed as following:

Erreur ! Des objets ne peuvent pas être créés à partir des codes de champs de mise en forme.

\mathbf{D} is the mechanical elastic tensor defined by the non-linear bulk and shear modulus, K and G , respectively,

$$K = K_{ref} \left(\frac{p'}{p_{ref}} \right)^{n^e} ; G = G_{ref} \left(\frac{p'}{p_{ref}} \right)^{n^e}$$

where p' is the mean effective stress, n^e the non-linear elasticity exponent, p'_{ref} the reference pressure, K_{ref} and G_{ref} the bulk and shear modulus at the reference pressure, respectively. $\boldsymbol{\beta}'_T$ is the thermal expansion tensor. Considering an isotropic thermal dilatation, one can express the thermal expansion tensor as $\boldsymbol{\beta}'_T = 1/3 \beta'_s \mathbf{I}$ with β'_s being the volumetric thermal expansion coefficient of the solid skeleton.

Using the concept of multi-mechanism plasticity, the total irreversible strain increment $d\boldsymbol{\varepsilon}^p$ is induced by two coupled dissipative processes: an isotropic and a deviatoric plastic mechanism. Each of them produces plastic strain increment, $d\boldsymbol{\varepsilon}^{p,iso}$ and $d\boldsymbol{\varepsilon}^{p,dev}$, respectively. The yield limit of each mechanism, restricting the elastic domain in the effective stress space, takes the following expressions (Fig. 1):

$$f_{iso} = p' - p'_c r_{iso} = 0 ; f_{dev} = q - M p' \left(1 - b \ln \frac{p' d}{p'_c} \right) r_{dev} = 0$$

where q is the deviatoric stress. The variables b and d govern the shape of the deviatoric yield limit and M is the slope of critical state line in the $(p' - q)$ plane, which may depend on temperature:

$$M = M_0 - g(T - T_0) ; M_0 = \frac{6 \sin \phi'_0}{3 - \sin \phi'_0}$$

where ϕ'_0 is the friction angle at critical state at reference temperature T_0 and g defines the linear evolution of M with temperature, M_0 being the value of M at initial temperature.



Each of the yield limits evolves through the generation of plastic strain which is the hardening variable. During loading, the volumetric plastic strain governs the evolution of p'_c and r_{iso} , while deviatoric plastic strains control the evolution of r_{dev} . The preconsolidation pressure, p'_c , depends on the volumetric plastic strain ϵ_v^p and temperature.

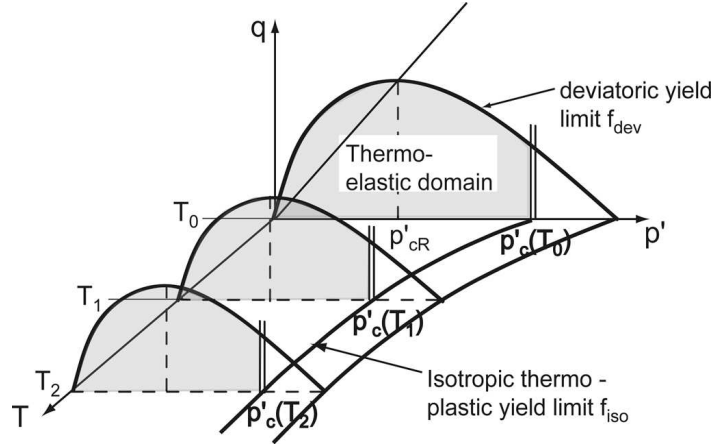


Figure 133: Yield limits for the ACMEG-T thermo-mechanical elasto-plastic framework

$$p'_c = p'_{c0T_0} \exp(\beta \epsilon_v^p) \left(1 - \gamma_T \log \frac{T}{T_0} \right)$$

where p'_{c0T_0} is the initial value of the preconsolidation pressure at the reference temperature, T_0 , while β and γ_T are material parameters.

According to the bounding surface theory, r_{iso} and r_{dev} correspond to the degree of plastification (mobilised hardening) of the isotropic and deviatoric yield limits, respectively. This enables a progressive evolution of the isotropic yield limit during loading and a partial comeback of this limit during unloading. The evolution of r_{iso} during loading is linked to the volumetric plastic strain induced by the isotropic mechanism $\epsilon_v^{p,iso}$:

$$r_{iso} = r_{iso}^e + \frac{\epsilon_v^{p,iso}}{c + \epsilon_v^{p,iso}} \quad \text{and} \quad dr_{iso} = \frac{(1 - r_{iso})^2}{c} d\epsilon_v^{p,iso}$$

where c and r_{iso} are material parameters. In the same way, the evolution of r_{dev} during loading is linked to the deviatoric plastic strain ϵ_d^p :

$$r_{dev} = r_{dev}^e + \frac{\epsilon_d^p}{a + \epsilon_d^p} \quad \text{and} \quad dr_{dev} = \frac{(1 - r_{dev})^2}{a} d\epsilon_d^p$$

where a and r_{dev} are material parameters.

The flow rule of the isotropic mechanism is associated, while the deviatoric one is not and assumes the following forms:

$$d\epsilon^{p,iso} = \frac{\lambda_{iso}^p}{3} \mathbf{I}$$

$$d\boldsymbol{\varepsilon}^{p,dev} = \lambda_{dev}^p \frac{1}{Mp'} \left[\frac{\partial q}{\partial \boldsymbol{\sigma}'} + \alpha \left(M - \frac{q}{p'} \right) \frac{1}{3} \mathbf{I} \right]$$

The plastic multipliers, λ_{iso}^p and λ_{dev}^p , are determined using Prager's consistency equation for multi-dissipative plasticity. α is a material parameter.

6.1.2 Parameters

Specific thermo-mechanical parameters were determined to accommodate ACMEG-T.

Thermo-mechanical characteristics		Boom Clay
Bulk modulus at the reference pressure [MPa]	K_{ref}	130
Shear modulus at the reference pressure [MPa]	G_{ref}	130
Non-linear elasticity exponent [-]	n_e	0.4
Volumetric thermal expansion coefficient of the solid skeleton [-]	β'_s	1.3.10 ⁻⁵
Plastic compressibility [-]	β	18
Material parameter defining the shape of the isotropic yield limit with respect to temperature [-]	γ_T	0.55
Material parameter [-]	c	0.015
Radius of the isotropic elastic nuclei [-]	r_{iso}	0.001
Material parameter [-]	b	0.8
Material parameter [-]	d	1.3
Friction angle at critical state at reference temperature [°]	ϕ'_0	16
Slope of the linear evolution of M with temperature [°C ⁻¹]	g	0.0085
Parameter controlling the dilatancy rule [-]	α	0.1
Material parameter [-]	a	0.007
Radius of the deviatoric elastic nuclei [-]	r_{dev}	0.3

Table 36: Thermo-mechanical parameters used for the ACMEG-T model (François et al., 2009)

6.1.3 Output results

In the following, some of the 2D results of EPFL will be briefly presented to highlight the influence of non-linear thermo-elasticity and thermo-plasticity on the THM response of the repository.

The obtained pore pressures and stress fields differ from those obtained by the other teams. The differences are mainly due to the non-linear elasticity and the thermo-plasticity of the ACMEG-T model. An increase in rigidity as well as progressive plasticity induced by heating, causing an increase of the preconsolidation pressure, is considered in ACMEG-T. This causes an increase in excess pore water pressures, and consequently in effective stresses.

Profile AA

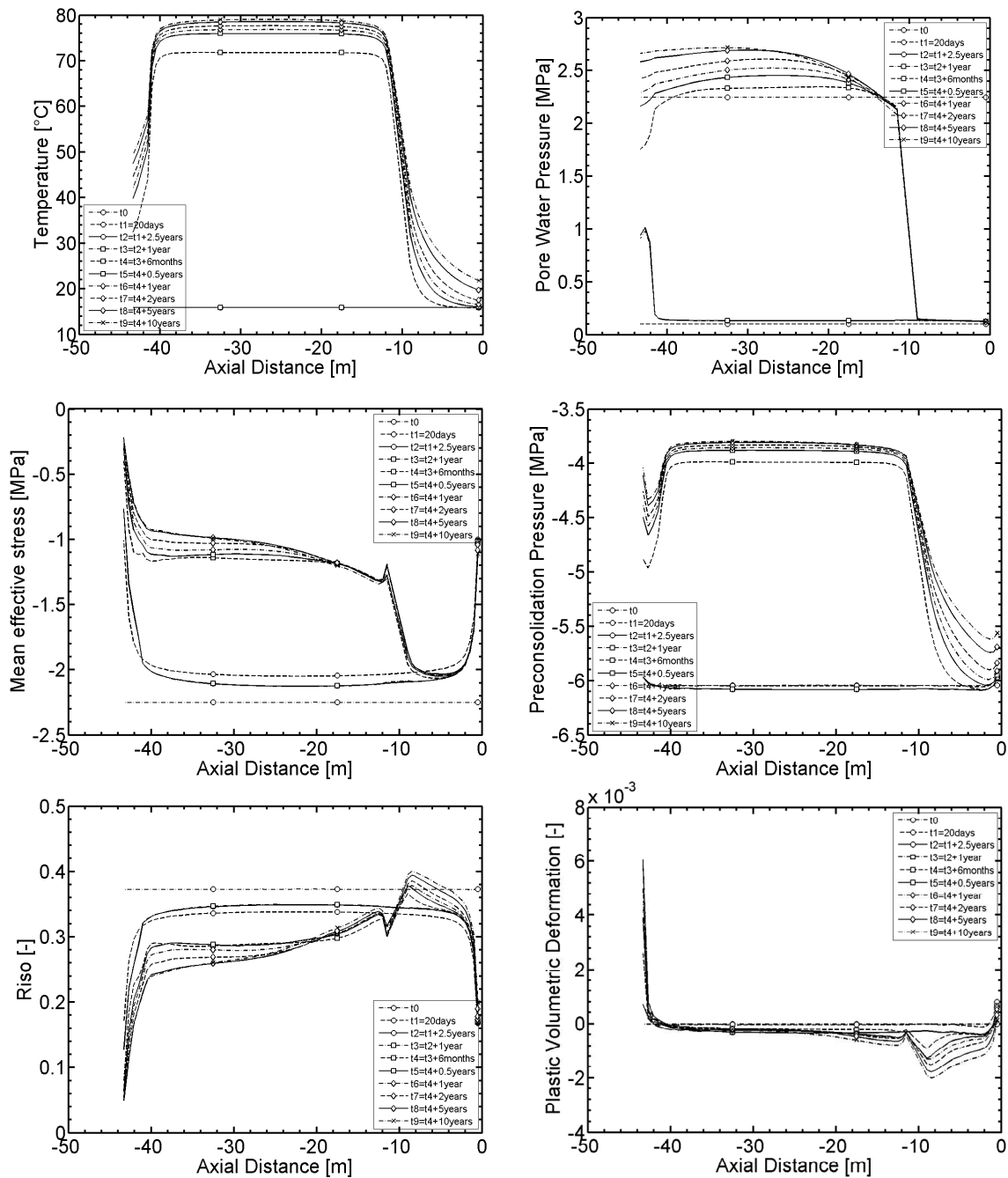


Figure 134: Profiles AA of temperature, pore water pressures, mean effective stresses, preconsolidation pressure, degree of mobilization of the isotropic mechanism and plastic volumetric deformation and in the 2D modelling

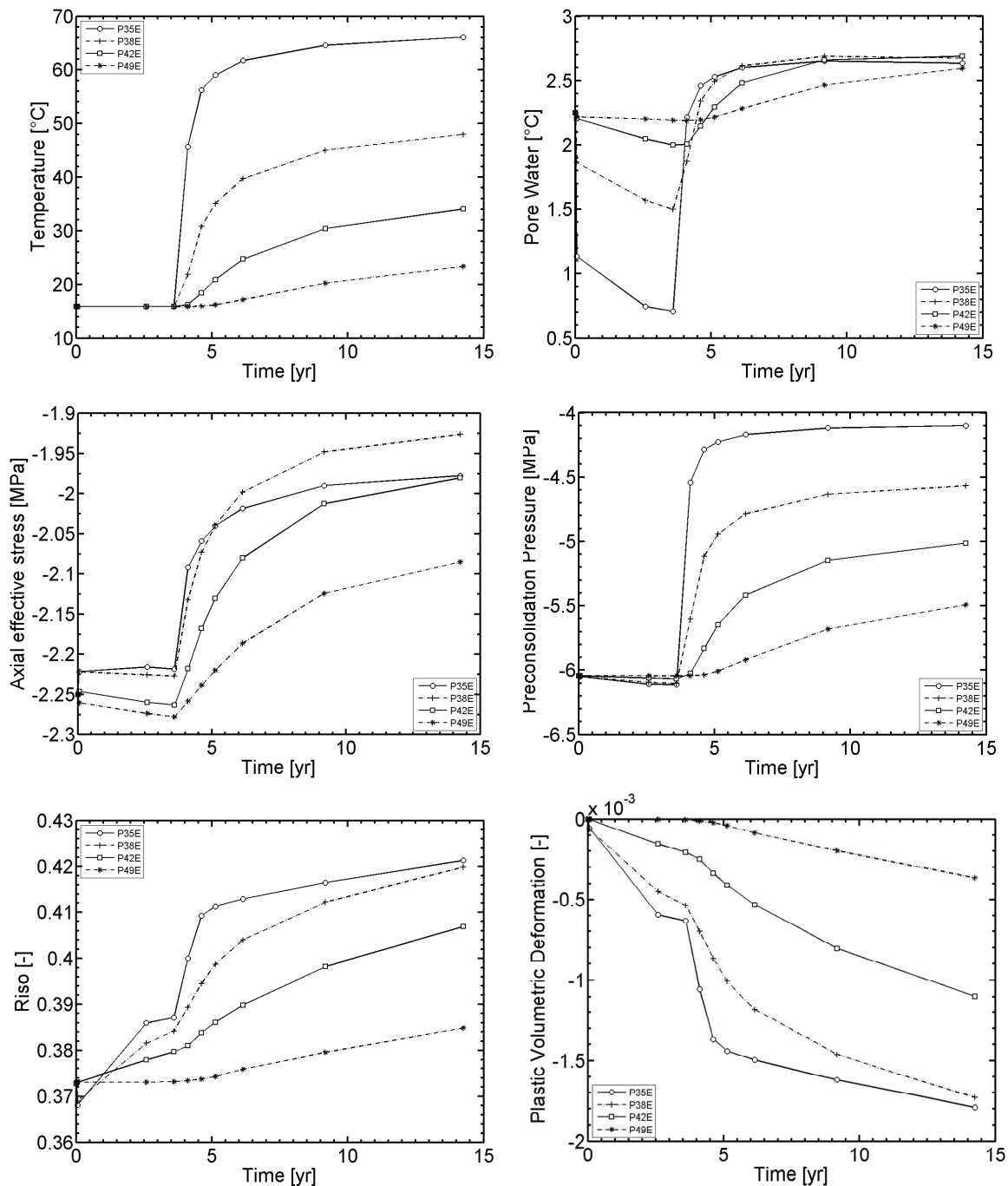


Figure 135: Time evolution at sensors of temperature, pore water pressure, axial effective stresses, preconsolidation pressure, degree of mobilization of the isotropic mechanism and plastic volumetric deformation in the 2D modelling

6.1.4 Conclusions

Modelling of the PRACLAY experiment in 1D and 2D configurations enables visualizing the main characteristics of the soil response under the imposed loading. These results should be analysed in light of results obtained with different constitutive models and in different configurations.

6.2 ULg

6.2.1 Comparisons between three different thermo-plastic models

The first modelling realised by ULg have considered thermo-elasticity during the heating phase, but we know that the behaviour of clay submitted to an increase of temperature is much complicated and it is needed to take into account the thermo-plasticity. So, this section describes results of the 2D plane strain modelling using three different thermo-mechanical constitutive laws in order to investigate the effect of the consideration of thermo-plasticity.

The constitutive laws are the following: Drucker-Prager with thermo-plasticity (described previously), TSOIL and ACMEG-T. TSOIL consists in a combination of a cap model and two different plastic mechanisms reproducing the basic features of the thermo-plasticity of soils. These mechanisms are based on the work realised by CERMES. The second law is ACMEG-T which is developed at EPFL (cf. 6.1.1). For more information concerning these laws, we refer to the deliverable D10 describing the constitutive laws.

The Table 37 and the Table 38 give the mechanical and the thermo-mechanical parameters used with TSOIL. Concerning the Drucker-Prager part of the cap model, the hardening of the friction angle is not considered.

Geomechanical characteristics		Boom Clay
Young elastic modulus [MPa]	E_0	300
Poisson ratio [-]	ν	0.125
Specific mass [kg/m ³]	ρ	2682
Cohesion [kPa]	c	300
Friction angle [°]	ϕ	18
Dilatancy angle [°]	ψ	0
Preconsolidation pressure [MPa]	p_c	6
Compression index [-]	λ	0.178
Biot's coefficient [-]	b	1

Table 37: Mechanical parameters for TSOIL

Thermo-mechanical properties		Boom Clay
Critical temperature [°C]	T_c	2000
Initial temperature [°C]	T_0	16
Hardening parameters [Pa ⁻¹]	β	3.8E-6
Parameters linked with $\epsilon_v^{t,p}$	a	0.937
Shape parameters for LY [°C ⁻¹]	α_0	3.93E-3
HC curve	c_I	0.52245
HC curve	c_I	-0.02197

Table 38: Thermo-mechanical parameters for TSOIL

The parameters used for ACMEG-T model are those in the Table 39. Some of them slightly differ from those in the table Table 36 in order to reproduce as closely as possible the Drucker-Prager model and to highlight the only effect of thermo-plastic model.

Elastic parameters		Boom Clay
Bulk modulus at the unity effective stress [MPa]	K_{ref}	133
Shear modulus at the unity effective stress [MPa]	G_{ref}	133
Nonlinear elasticity exponent [-]	n_e	0
Thermal expansion coefficient [$^{\circ}\text{C}^{-1}$]	β'_s	$1 \cdot 10^{-5}$
Isotropic plastic parameters		
Plastic compressibility [-]	β	18
Material parameter defining the shape of the isotropic yield limit with respect to temperature [-]	γ_T	0.55
Material parameter [-]	c	0.012
Radius of the isotropic elastic nuclei [-]	r_{iso}^e	0.001
Deviatoric plastic parameters		
Material parameter [-]	b	0.6
Material parameter [-]	d	1.3
Friction angle [$^{\circ}$]	ϕ'_0	16
Average slope of variation of friction angle at critical state [-]	g	0.0085
Parameter controlling the dilatancy rule [-]	α	1
Material parameter [-]	a	0.007
Radius of the deviatoric elastic nuclei [-]	r_{dev}^e	0.3

Table 39: Mechanical parameters for ACMEG-T

The comparison of the TSOIL model with the Drucker-Prager with thermo-elasticity does not show significant differences in term of evolution of pore water pressure. The Figure 97 presents the pore water pressure distribution along the profile ABC during the heating phase for both models. It may be observed that the differences are not predominant.

The Figure 98 presents the distribution of the pore water pressure according profile GEF during the heating phase. The same conclusions as previously may be done. The thermo-plasticity does not seem to play a key role in this modelling.

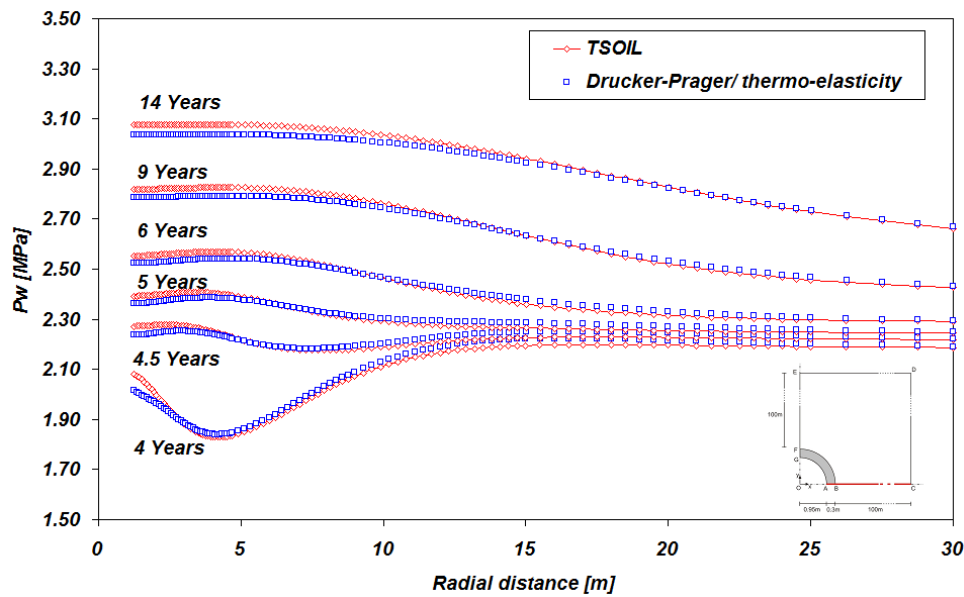


Figure 97: Comparison between TSOIL and Drucker-Prager with thermo-elasticity.
Comparison of the pore water pressure distribution during the heating phase according profile ABC

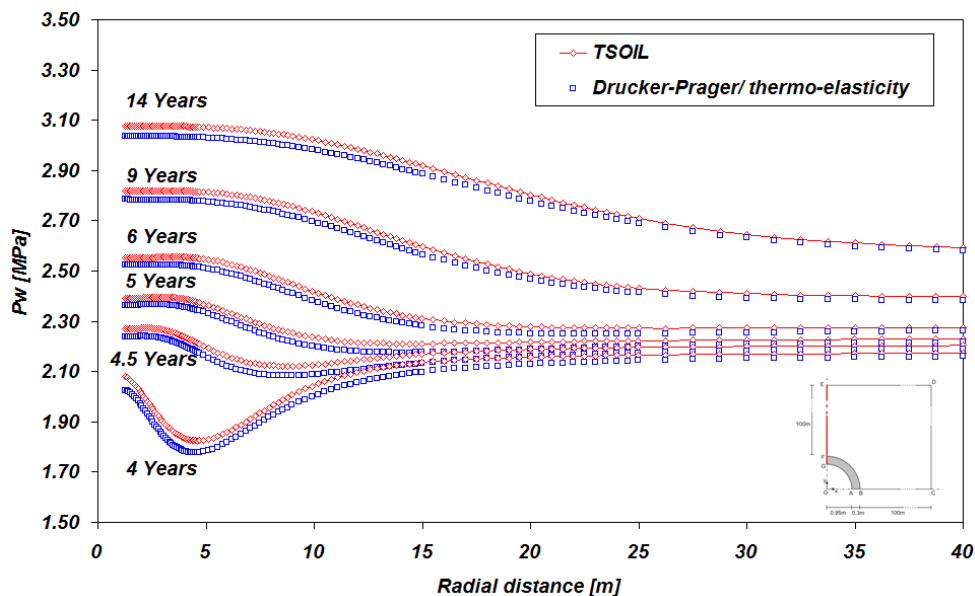


Figure 98: Comparison between TSOIL and Drucker-Prager with thermo-elasticity.
Comparison of the pore water pressure distribution during the heating phase according profile GEF

This similitude in the results is explained by the fact that the temperature mainly induced thermo-elastic strain in both cases and that the amount of volumetric strain induced by temperature is weak. The Figure 99 presents the stress path in the (p', T) plane of a point located at the wall of the cavity. The plateau corresponds to the process of excavation and stabilisation. After the stabilisation, the temperature increases at the wall. As a consequence, a decrease of the mean effective stress is observed due to the excess pore water pressure generated by heating. So, the stress path reaches the initial TY curve which creates thermo-plastic strains. Then, hardening occurs and the TY curve moves upwards. The mean stress continues to decrease, moves leftwards and, finally, leaves the TY curve to reach the thermo-elastic domain. The stress path

leaves rapidly the thermo-plastic limit so that the amount of volumetric plastic strain generated by an increase of temperature is weak. This behaviour explains why the results are similar.

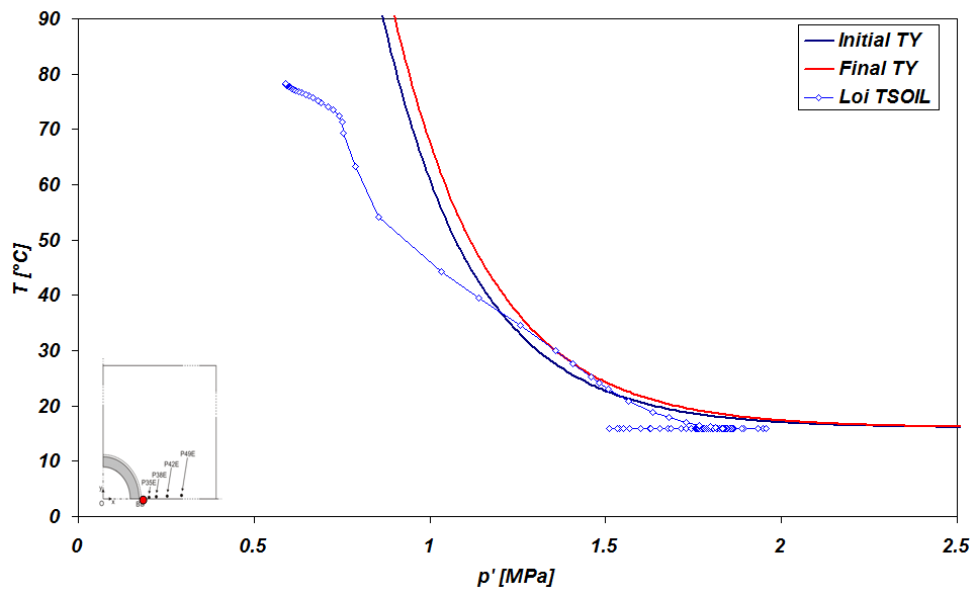


Figure 99: Stress path in the (p', T) plane for a point located at the wall.

The Figure 100 presents a comparison between the three different thermo-mechanical models: TSOIL, ACGEG-T and Drucker-Prager with thermo-elasticity. The comparison shows that there is not a lot of difference in term of excess pore water pressure prediction. The explanation of this similitude is the same as previously. The amount of thermo-plastic strains is weak so that the evolutions of pore water pressure are relatively the same.

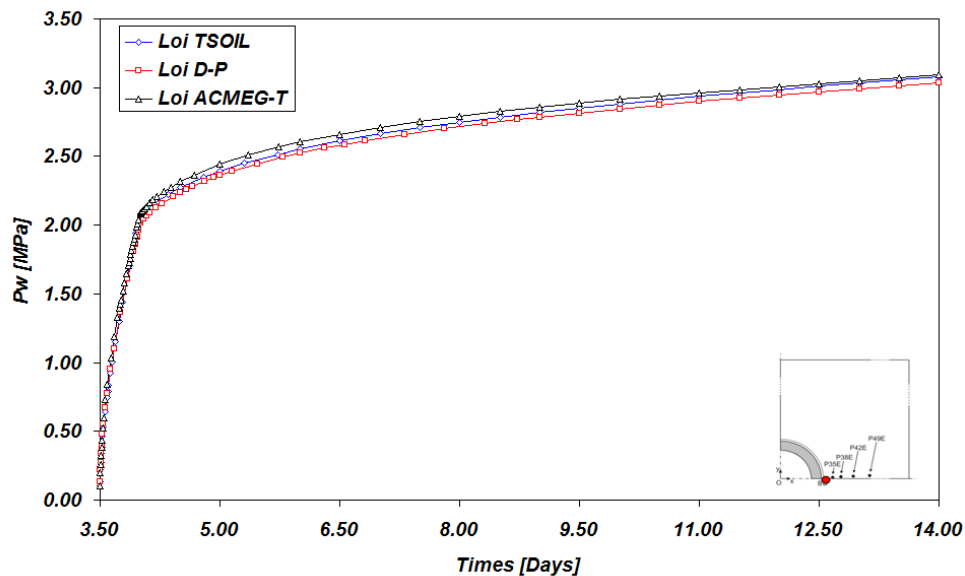


Figure 136: Evolution of the pore water for the three models.
This evolution is taken for the same point as previously located at the wall.

6.2.2 Effect of additional anisotropic properties: anisotropic thermal conductivity and anisotropic intrinsic permeability (3D model)

The material properties in the 3D model introduced in the section 4.3 are mainly based on the properties used in the 2D models. Only one source of anisotropy is included: the initial stress state.

The effect of two additional anisotropies in the Boom clay have also been investigated, those are the anisotropy of the thermal conductivity and the intrinsic permeability, leading to 3 different 3D models:

1. 3D_I: 3D model including only the anisotropy of initial stresses (this model is the model introduced in the section 4.3)
2. 3D_{II}: 3D model including the anisotropy of initial stresses and thermal conductivity
3. 3D_{III}: 3D model including the anisotropy of initial stresses, thermal conductivity and intrinsic permeability

The Table 40 summarizes the anisotropic material properties used for the Boom Clay. In this table, the values in **bold** characters are those used when the property is assumed isotropic.

Initial effective stresses [MPa]	$\sigma'_{xx} = \sigma'_{yy}$ σ'_{zz}	2.25 1.575	in 3D _I - 3D _{II} - 3D _{III} models
Thermal conductivity [W.m ⁻¹ .K ⁻¹]	$\lambda_{int,zz}^{sat}$ $\lambda_{int,xx}^{sat} = \lambda_{int,yy}^{sat}$	1.35 1.7	in 3D _{II} - 3D _{III} models
Intrinsic permeability [m ²]	$k_{int,zz}^{sat}$ $k_{int,xx}^{sat} = k_{int,yy}^{sat}$	2.10 ⁻¹⁹ 4.10⁻¹⁹	only in 3D _{III} model

Table 40: Anisotropic material properties of the Boom clay in the 3D models.
The values in **bold** characters are those used in the isotropic case.

The Figure 137 to Figure 139 shows the results at the end of the heater experiment using the 3 different 3D anisotropic models. Concerning the pore water pressure profiles (Figure 137), the influence of the anisotropic thermal conductivity (visible when comparing 3D_I and 3D_{II} models) is smaller than the impact of the anisotropic permeability (comparing 3D_{II} and 3D_{III} models). With the 3D_{III} model (the “most anisotropic” model, in blue), the peaks in pressure become a little bit higher and they tend to become equal along both horizontal and vertical profiles. They remain under 2.6 MPa, approximately 50-75 kPa over the peaks observed with the two other 3D models.

In the Figure 138, the temperature profiles are plotted. The effect of the anisotropic thermal conductivity is visible, as the horizontal and vertical profiles are not equal anymore for the 3D_{II} and 3D_{III} models, though the maximum gap between the two profiles is about 2°C. No difference can be observed between the results of the 3D_{II} and 3D_{III} models (the green and blue curves are perfectly superposed in the Figure 138).

The third figure (Figure 139) illustrates the radial displacement along the horizontal and vertical profiles. Once again, the introduction of additional anisotropic parameters does not affect dramatically the results, which remain quite similar for all 3D_I, 3D_{II} and 3D_{III} models.



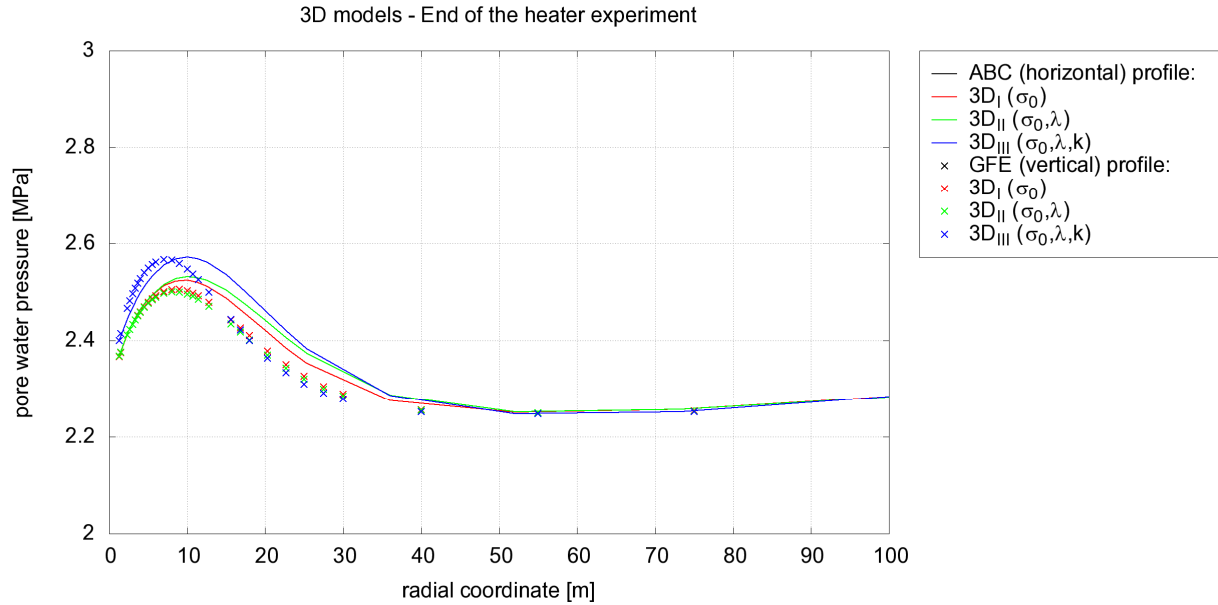


Figure 137: Pore water pressure profiles at the end of the heater experiment.
Effect of the anisotropic parameters.

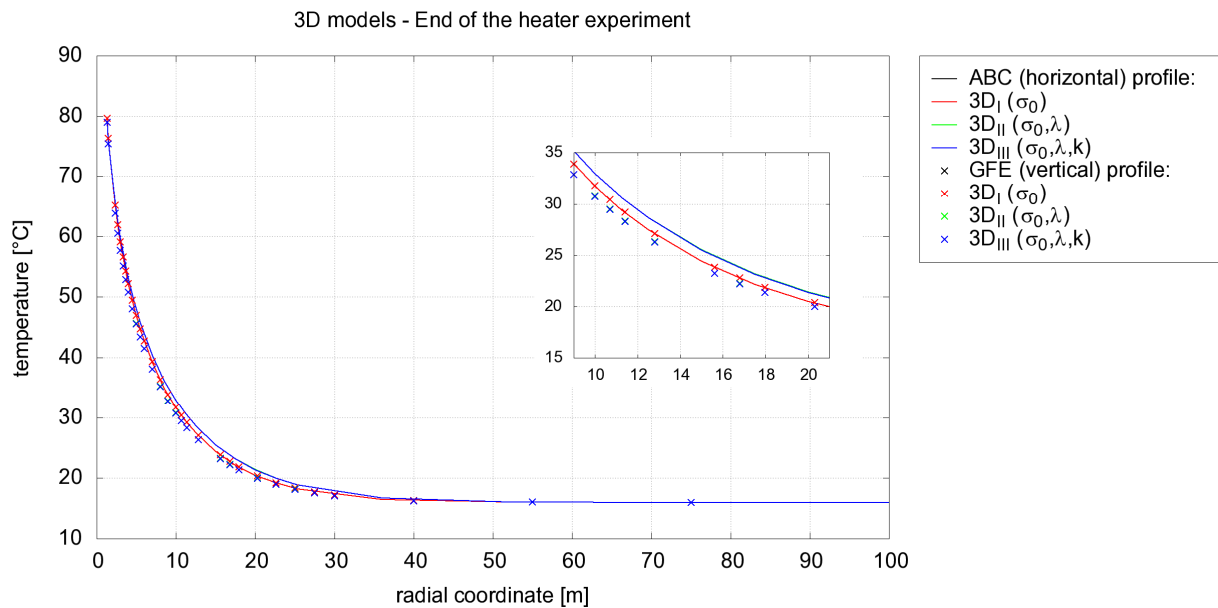
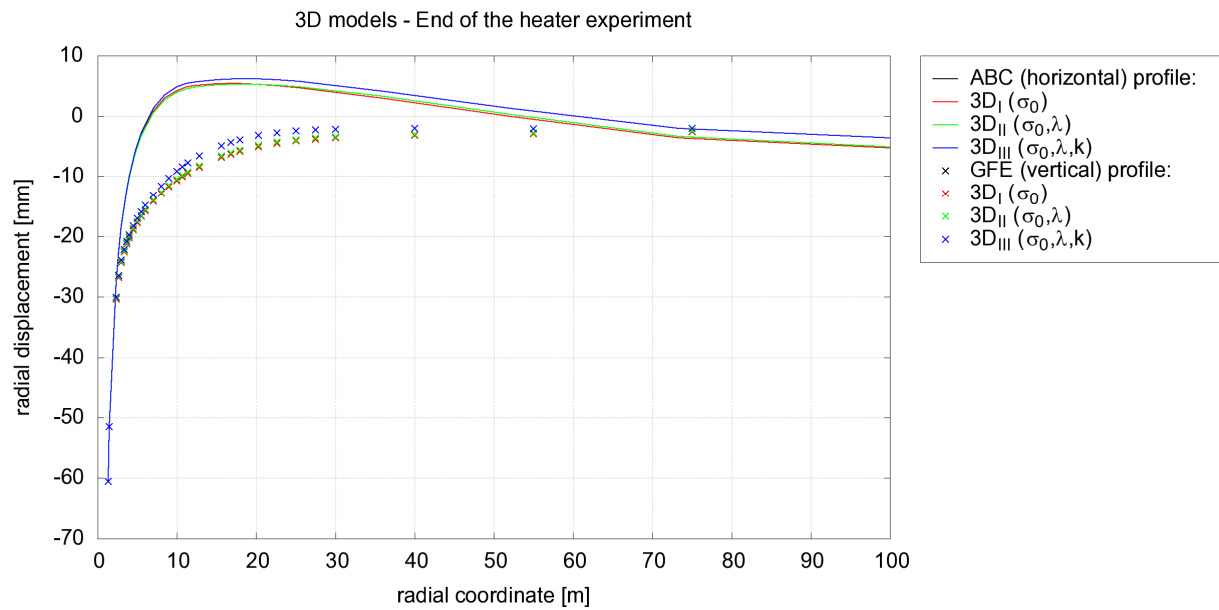


Figure 138: Temperature profiles at the end of the heater experiment.
Effect of the anisotropic parameters.



*Figure 139: Radial displacement profiles at the end of the heater experiment.
Effect of the anisotropic parameters.*

6.3 Euridice

6.3.1 Effect of far-field mechanical boundary condition (BC1 and BC2)

In section 4.1.1, two types of mechanical far-field boundary conditions have been mentioned. To further investigate these two types of boundary conditions, four cases using 2D plane strain model are simulated (see the Table 41, also see Figures 4~5 for the geometry).

Boundaries CD and DE	Case 1	Case 2	Case 3	Case 4
Size	100 m	100 m	300 m	300 m
Thermal B.C.	Adiabatic			
Hydraulic B.C.	Impermeable			
Mechanical B.C.	Constant stress	Fixed displ.	Constant stress	Fixed displ.
Boundary condition	BC2	BC1	BC2	BC1

Table 41: Four cases of 2D plane strain modelling

The four cases have the same thermo-hydraulic boundary conditions, and the differences among the four cases are the far-field mechanical boundary condition and the domain size. It is certain that with the increase of the domain size, the influence of the far-field boundary condition on the near field modelling results decreases.

Some modelling results for the four cases are selected and presented in the Figure 140 to the Figure 143. The Figure 140 presents the pore water pressure profiles along boundary ABC after heating for 10.5 years, the Figure 141 shows the horizontal stress profile along CD after heating for 10.5 years, the Figure 142 shows the pore water pressure evolution with time at point D, and Figure 143 shows the displacement evolution with time at point D. Some observations are made from the four figures:

- After heating for 10.5 years, Case 2 gives higher p_w than the other three cases (Figure 140), and the results for Case 1 and Case 2 are consistent to the results shown in the Figure 35 and the Figure 37. For Case 2 and Case 4 with far-field fixed displacement boundary conditions, the horizontal boundary stresses increase from the initial value of 3.825 MPa to around 4.15 MPa and 3.86 MPa respectively (Figure 141).
- For Case 2 and Case 4 (with fixed displacement at the far field), the evolution of pore water pressure at point D tends to increase linearly with time (Figure 142), and for Case 1 and Case 3 (with constant stress boundary condition at the far field), the evolution of displacement at point D also tends to increase linearly with time (Figure 143).
- Case 2 and Case 4 have the same THM boundary conditions (i.e. BC1), the domain sizes of Case 2 and Case 4 are $100 \times 100 \text{ m}^2$ and $300 \times 300 \text{ m}^2$, respectively, and from the point of numerical modeling, Case 4 should have more reasonable results than Case 2 because of the further boundary. Besides, Case 1 and Case 3 with constant stress far-field boundary conditions give much closer results to those of Case 4 than those of Case 2. Therefore it could be concluded that Case 2 (fixed displacement at the far-field of 100 m) is not a reasonable case.



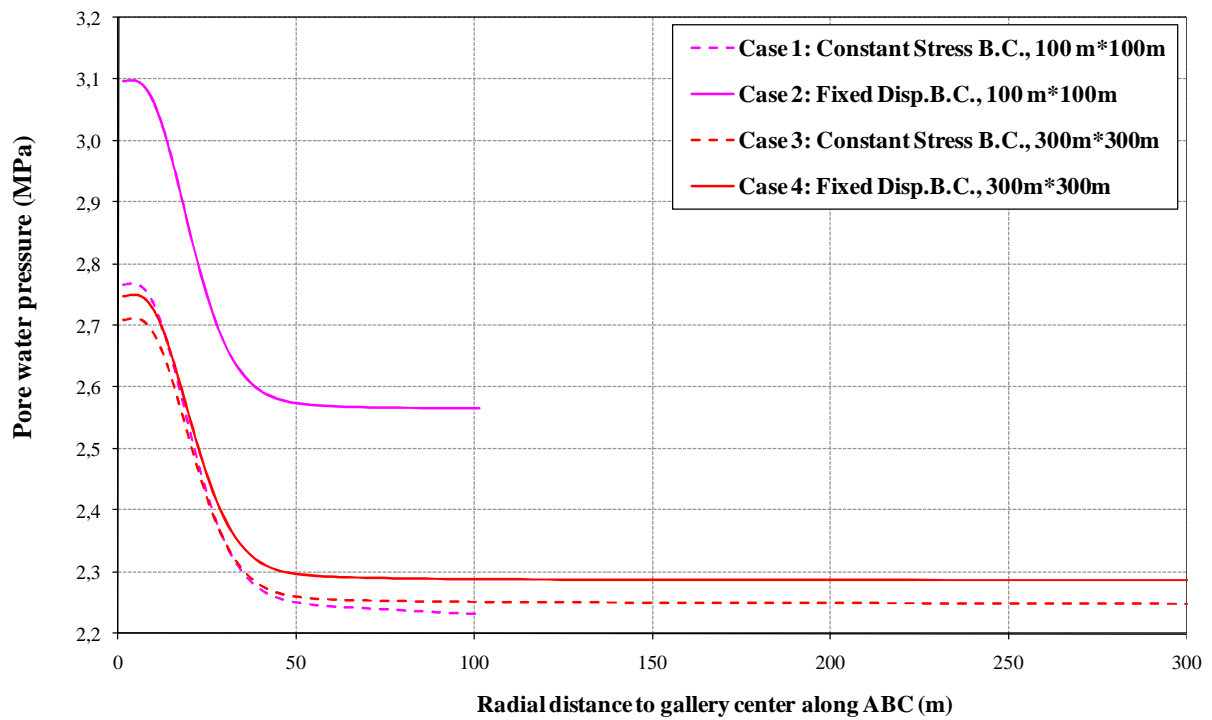


Figure 140: Pore water pressure profiles along boundary ABC for the four cases after heating for 10.5 years

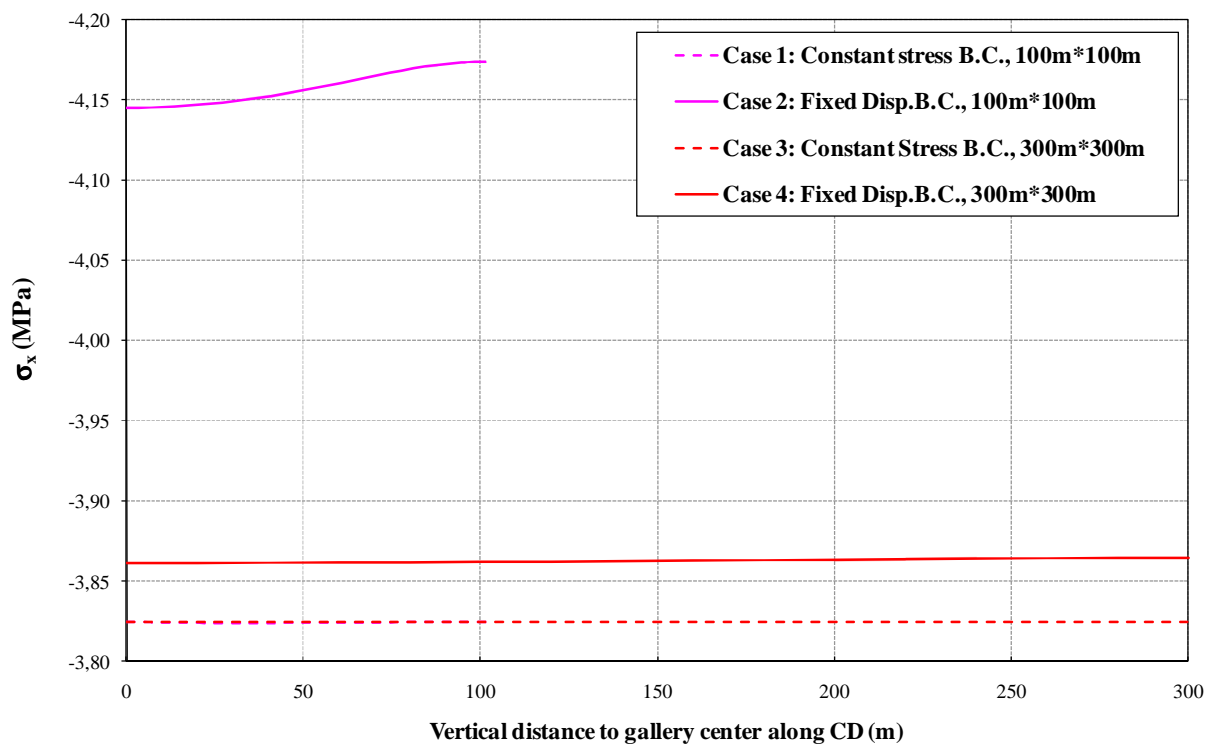


Figure 141: Horizontal stress profiles along CD for the four cases after heating for 10.5 years

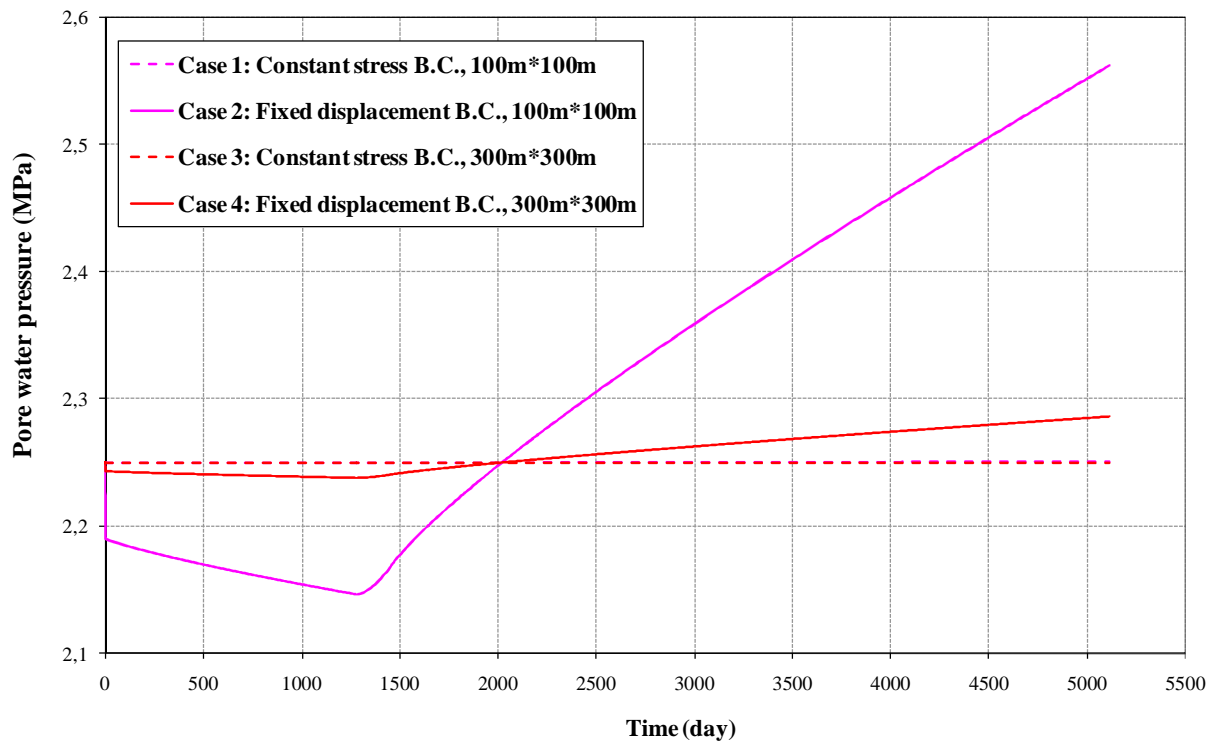


Figure 142: Pore water pressure evolution with time at point D for the four cases

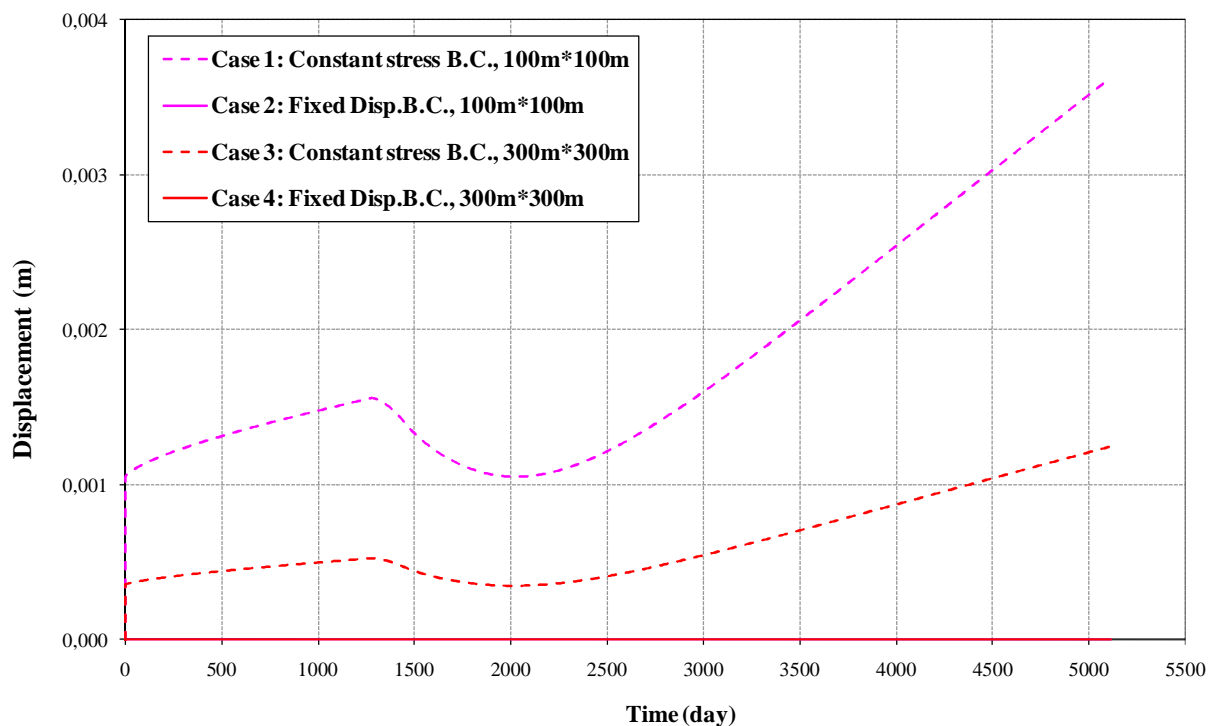


Figure 143: Displacement evolution with time at point D for the four cases

6.3.2 Effect of initial stress anisotropy

The Figure 144 presents the modelled pore water pressure contour just after excavation for Case 1 (see Table 41). In Case 1, initial stress anisotropy is considered with horizontal stress of 3.825 MPa and vertical stress of 4.5 MPa. It is observed that just after excavation, higher than the initial pore pressure (2.25 MPa) was generated to the right or left of the gallery, and the pore water pressure decreases above or below the gallery. For the case considering the initial isotropic stresses, the modelled pore pressure change around the gallery is axisymmetric, having different pattern from that observed in Case 1. Therefore, the non-axisymmetric response of pore pressure after excavation is clearly due to initial stress anisotropy.

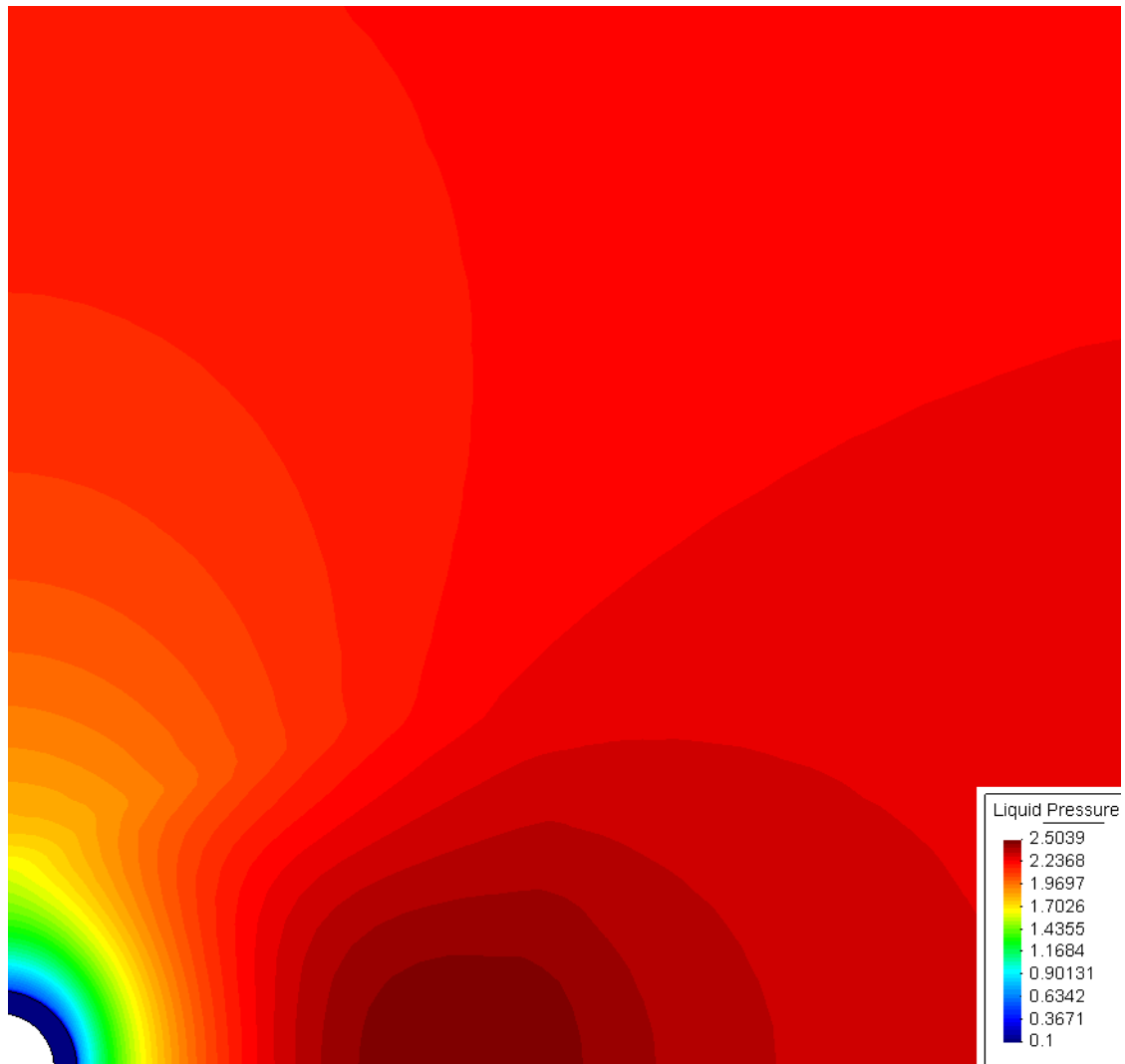


Figure 144: Pore water pressure contour just after excavation

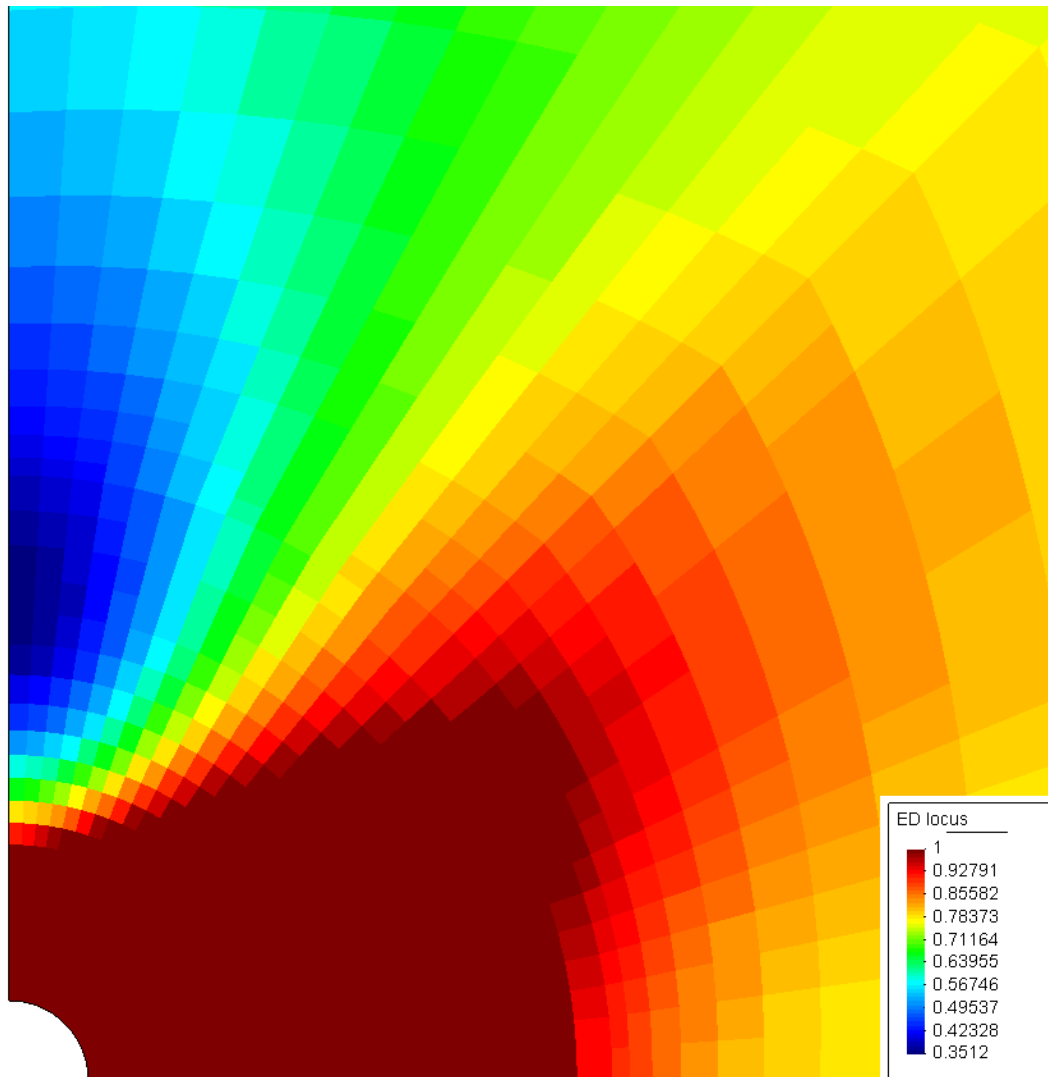


Figure 147: Contour of plastic index (Plastic index is equal to 1 in plastic zone)

The Figure 147 shows the modelled contour of plastic index just after excavation, it can be seen that the plastic zone has larger extent in the horizontal direction than that in the vertical direction, and due to initial stress anisotropy, deviator stresses are bigger to the left or right of the gallery than those at the top or bottom of the gallery. These modelled results can explain the observed larger convergence in the horizontal direction than that in the vertical direction around PRACLAY gallery.

6.3.3 Influence of backfilling materials

For 2D axisymmetric modelling, two cases are studied, and the only difference between the two cases is:

Case 1 does not include the material of backfilling sand in the modelling, and when heating test starts, the interface between sand and liner is considered impermeable; while Case 2 includes the backfilling sand in the geometry, and no specific hydraulic boundary condition between liner and sand is imposed.

The Figure 148 shows the pore water contour before heating test, i.e. 2.5 years after starting heater test. The Figure 149 shows the pore water profiles at different times along the interface between liner and Boom clay. Both figures clearly demonstrate that Case 2 makes the axial distribution of pore pressure much more homogeneous at the region close to the liner than Case 1. This can be explained as:

Very permeable sand is included in the modelling of Case 2, the sand has hydraulic conductivity of several orders higher than those of Boom clay and liner, so it is very fast for the pore water pressure within the sand to become homogeneous, which subsequently imposes almost the same pore water pressure boundary condition for the liner around the sand. But for Case 1, impermeable boundary condition is imposed at the intrados of the liner, which does not have constraint on the axial distribution of the pore water pressure along the liner.

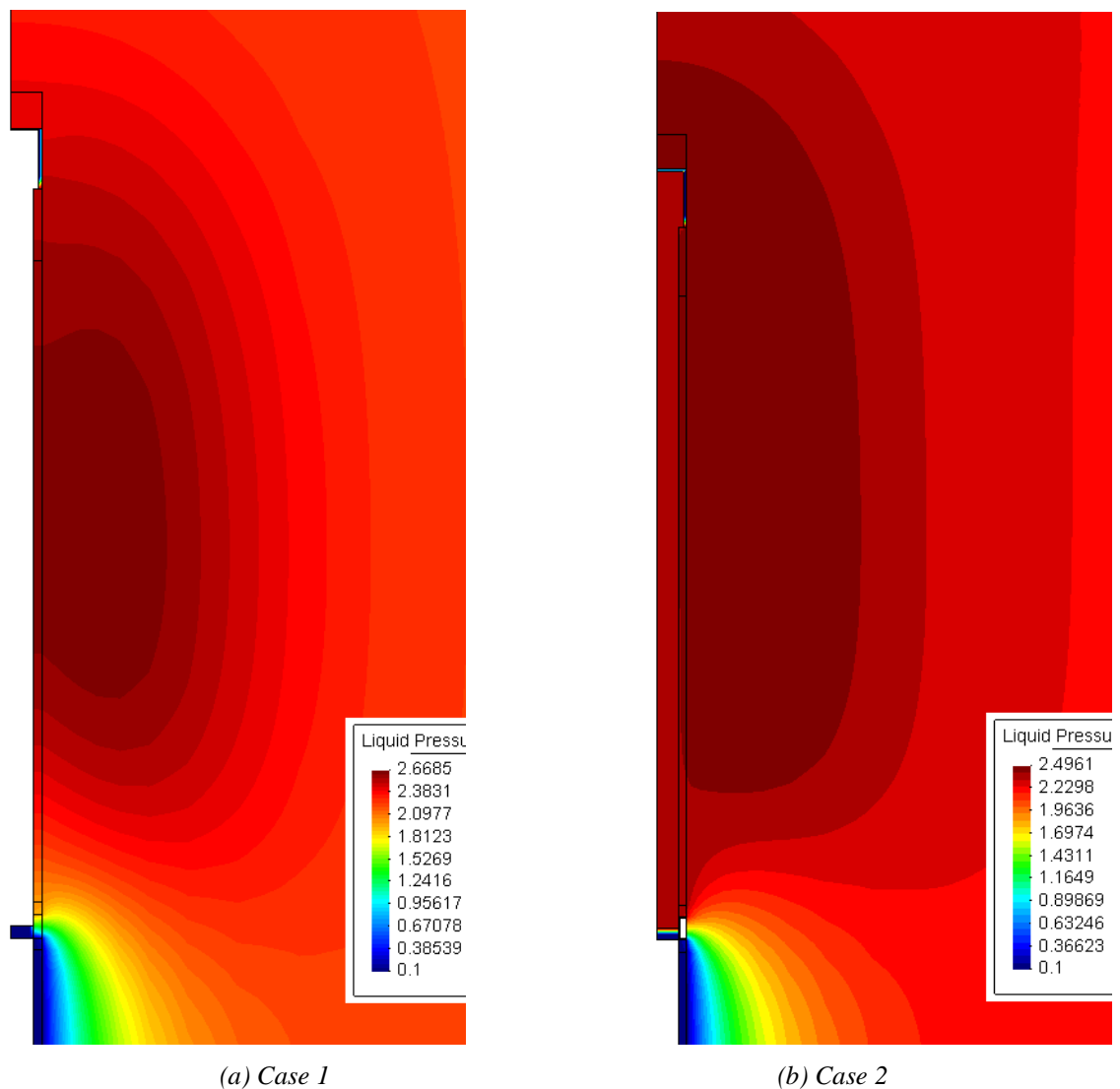
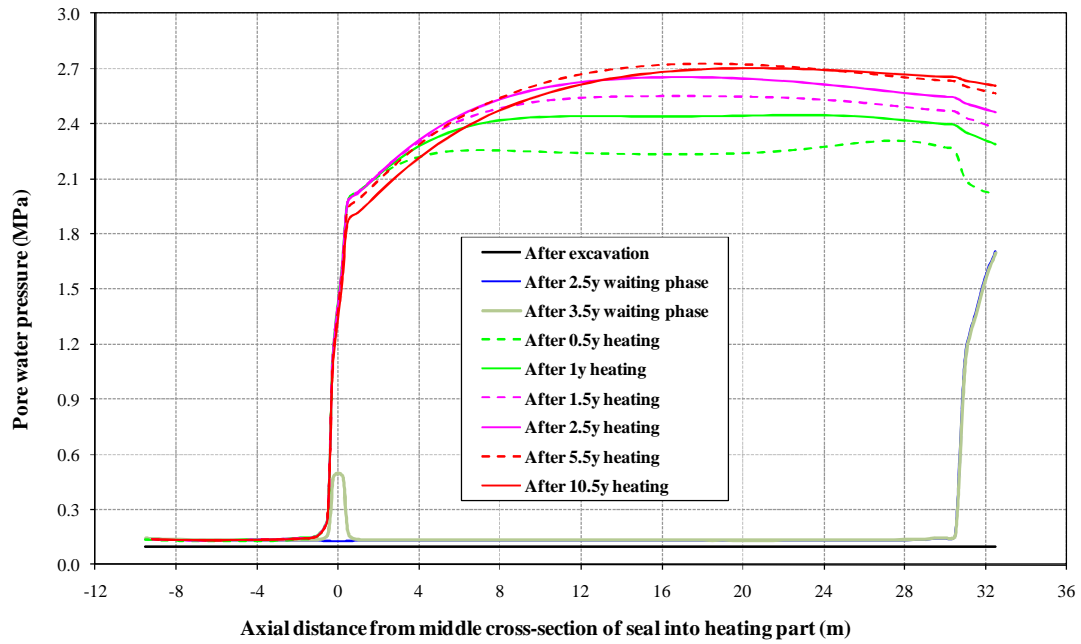
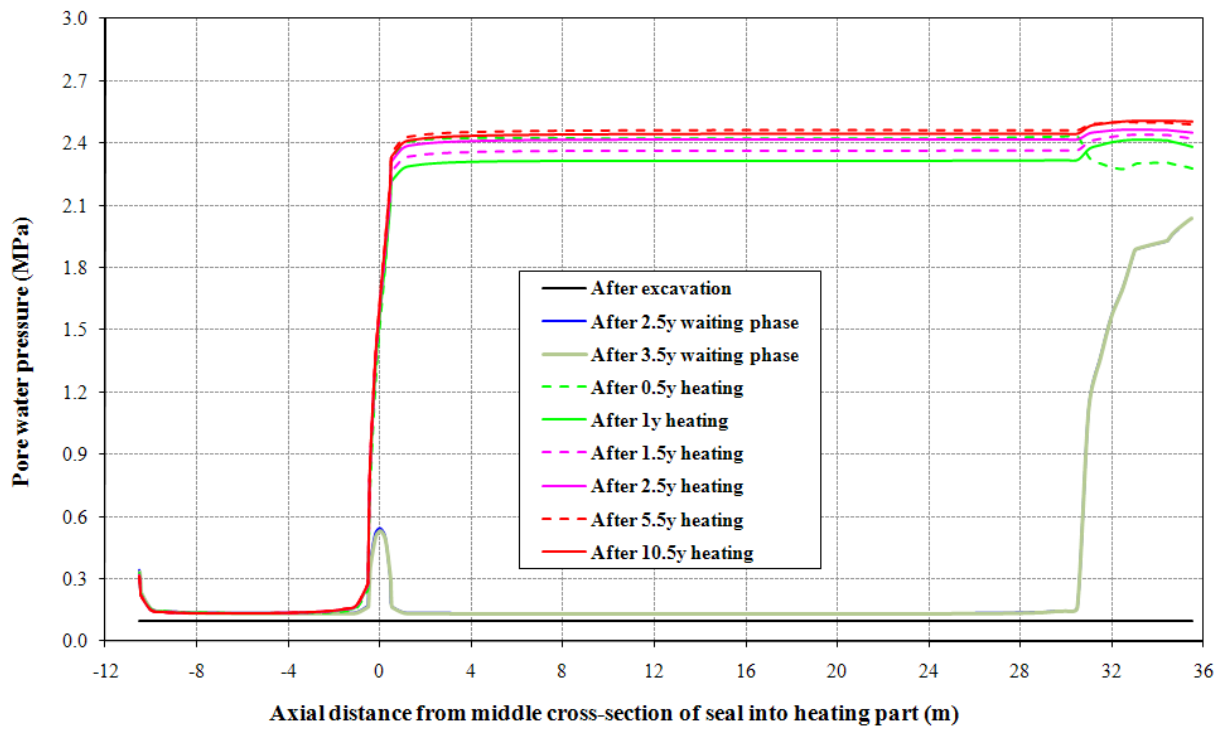


Figure 148: Pore water pressure contour 2.5 years after starting heater test



(a) Case 1 of 2D axisymmetric modelling



(b) Case 2 of 2D axisymmetric modelling

Figure 149: Pore water pressure profiles along the interface between liner and Boom clay

6.4 CIMNE

6.4.1 Initial state around PRACLAY experiment

Studies realized in argillaceous URLs have shown that the hydro-mechanical state prevailing inside the laboratory is highly heterogeneous because it is influenced by the different excavations realized. Moreover, the low permeability of the clay rock delays significantly the reach of the steady state for pore pressure distribution, which affects in turn the stress distribution. It is thus very common that the stress state existing in the rock just before the realization of a new excavation is in an evolving phase and depends on the chronology of previous works.

In this section, the effect of the excavation of the gallery connecting the first to the second access shafts to HADES URL on the hydro-mechanical state around Praclay experiment is studied. This gallery, from which Praclay gallery was excavated in 2007, was excavated between 2001 and 2002. The objective is to evaluate the extension of the perturbed hydro-mechanical zone around the connecting gallery and its evolution in time in order to have an insight into its possible influence on the response of the clay around the PRACLAY test.

Moreover, the follow-up by instrumentation of the excavation of the connecting gallery within the framework of CLIPEX experiment, provide interesting data to adjust the field rock parameters to be used in the modelling of PRACLAY experiment. It has been particularly studied the influence of the anisotropy on the build-up of pore pressure during excavation.

The geometry of the connecting gallery and the schematic location of sensors are depicted in Figure 150. Pore pressure and displacements sensors were installed into 4 instrumentation boreholes labelled from A to D. From the sake of conciseness, comparison between numerical modelling and field measurements will be realized for sensors in borehole A (aligned with the central axis of connecting gallery) and B (close to gallery wall).

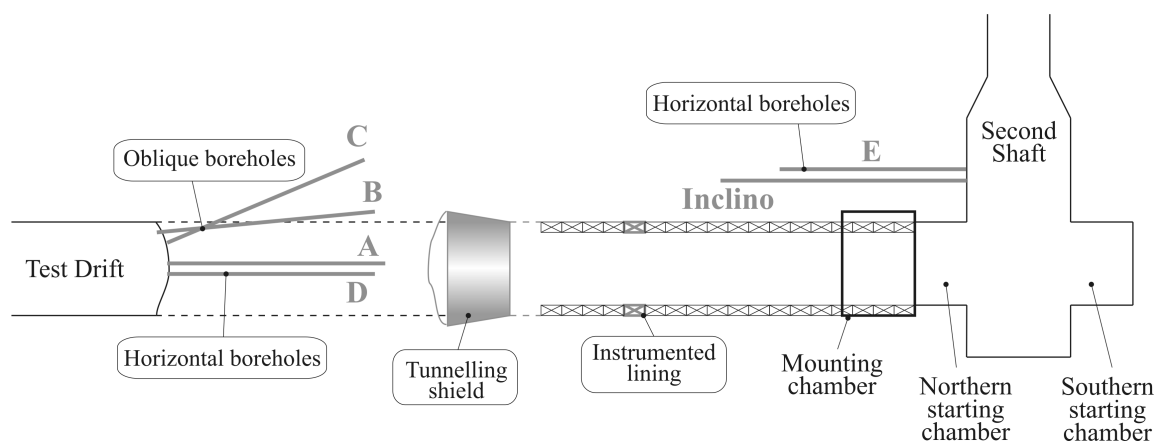


Figure 150: Pore water pressure profiles along the interface between liner and Boom clay

The geometry, mesh, initial and boundary conditions used in the numerical model are shown in Figure 151. To favour sensitivity analysis, an axisymmetric configuration has been considered. Pore pressure is set initially to 2.2 MPa in the whole mesh and maintain constant at 50 m from gallery axis. On the lateral boundary, conditions of null displacement and null wall flow have been imposed. Four main stages are considered in the analysis: an initial stage to insure equilibrium, a stage for the excavation of the test drift excavation (realized in 1987 and left open 14 years), a stage for the step-by-step excavation of the connecting gallery (whole duration 35 days) and one final stage from the end of the excavation of the connecting gallery to the start of

TIMODAZ

the excavation of Praclay gallery. Excavation of test drift is considered instantaneous. Excavation of the connecting gallery is divided into 28 steps defined in accordance with the real advance of the front. The average rate of advance is 3m/d.

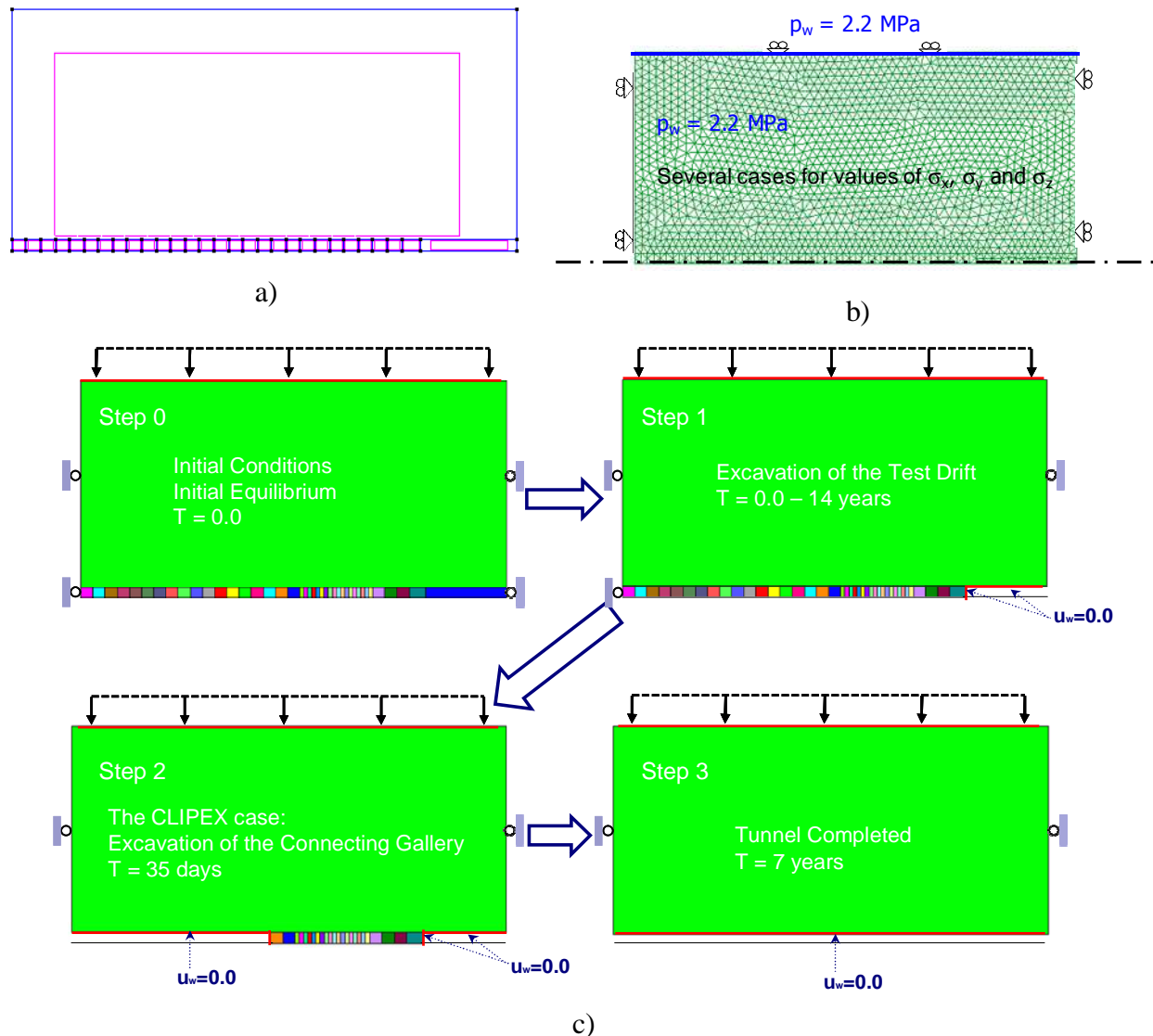


Figure 151: Numerical model for CLIPEX experiment: a) geometry; b) mesh; c) stages of the analysis

In order to study the effect of anisotropy on the response of the rock, eight cases have been simulated, with different assumptions for the stress state and material properties. They are summarized in Table 42. The damage/elastoplastic law developed for argillaceous rocks and presented in Deliverable D10 has been used. Because induration is lower in Boom clay than in Opalinus of Callovo-Oxfordian clay, only the elastoplastic part of the model has been activated. Yield criterion is based on Mohr Coulomb failure criterion. Values of material parameters for the anisotropy are given in Table 43.

Computations	I	II	III	IV	V	VI	VII	VIII
Isotropy	X							
Anisotropy in permeability		X			X	X		X
Anisotropy in stress state			X		X		X	X
Anisotropy in elastic moduli				X		X	X	X

Table 42: Summary of the analyses of CLIPEX experiment.

Parameters		Exp. values
Young's modulus (MPa) – isotropic case	E'	585
Young's modulus (MPa) – anisotropic case	E'_h	700
Young's modulus (MPa) – anisotropic case	E'_v	350
Poisson's ratio	ν'	0.125
Friction angle ($^\circ$)	ϕ'	18
Cohesion (MPa)	c'	0.3
Dilation angle ($^\circ$)	ψ'	0-10
Hydraulic conductivity (m/s) – isotropic case	k_w	4.00e-12
Hydraulic conductivity (m/s) – anisotropic case	k_{wh}	6.00 e-12
Hydraulic conductivity (m/s) – anisotropic case	k_{wv}	3.00 e-12
Porosity (%)	n	39

Table 43: Isotropic and anisotropic properties of Boom clay considered in the analyses

When the stress state is considered isotropic, an initial value equal to 4.5 MPa is considered in all the mesh. In the computations assuming an anisotropic stress state, the initial values are: -3.82 MPa for the horizontal stress and -4.16 MPa (average of the horizontal and vertical stress) for the stress in the vertical plane.

Figure 152 shows a comparison between the pore pressure computed by the full anisotropic model (case VIII of Table 42) and the isotropic model (case I) for one sensor located in borehole A. It evidences the capability of the anisotropic model to capture the peak in pore pressure as the front approaches the sensors. This is due to the loading originated by the redistribution farther ahead the front of the lateral stress released by the excavation. When the front goes closer to the sensor (less than 6 m), a sudden decrease in pore pressure is observed caused by axial unloading. The effect on pore pressure of the two last steps of excavation before the reach of the sensor can be clearly observed in the Figure. To the opposite, the isotropic model captures only the pore pressure decrease by axial unloading but not the previous peak by lateral loading.

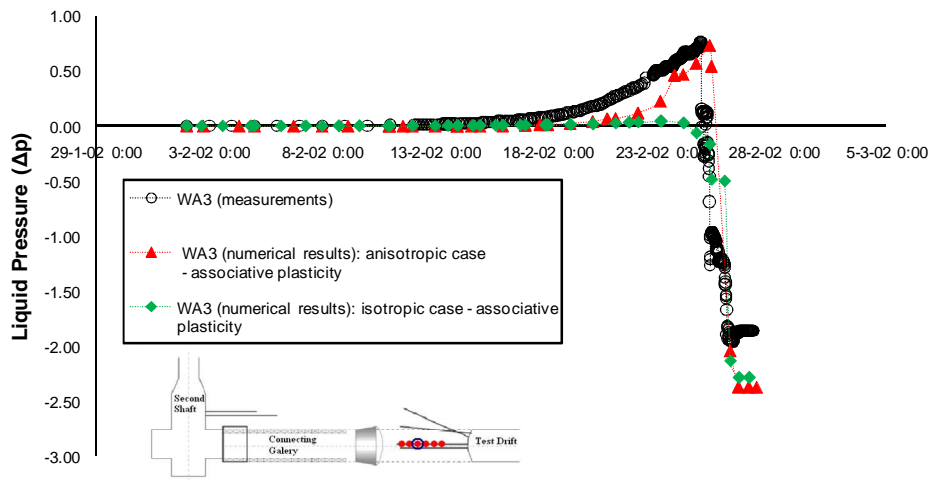
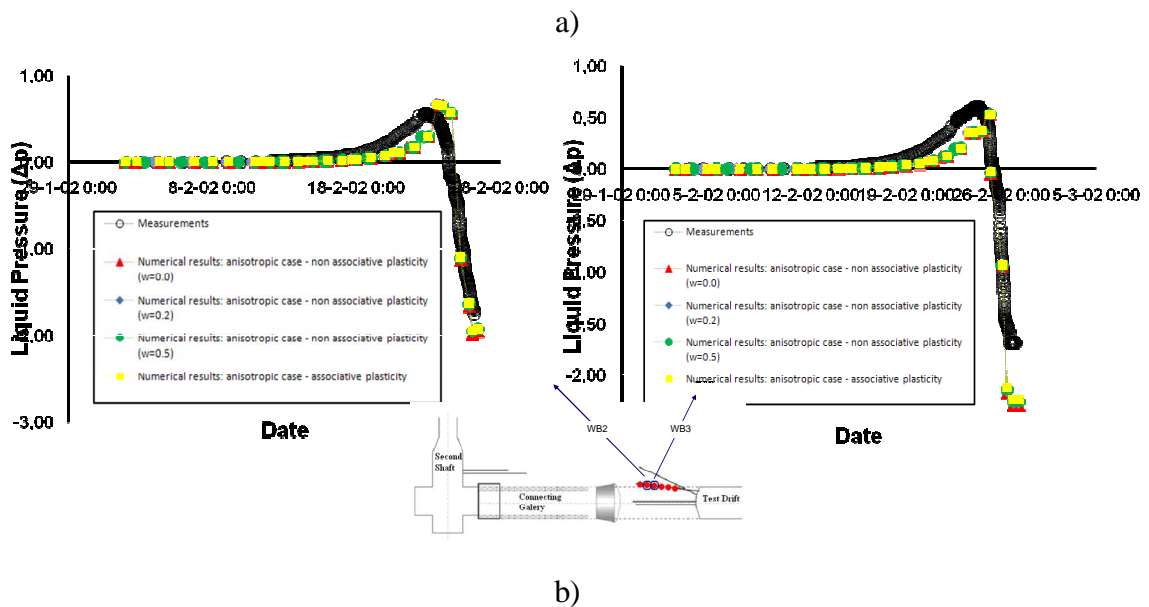
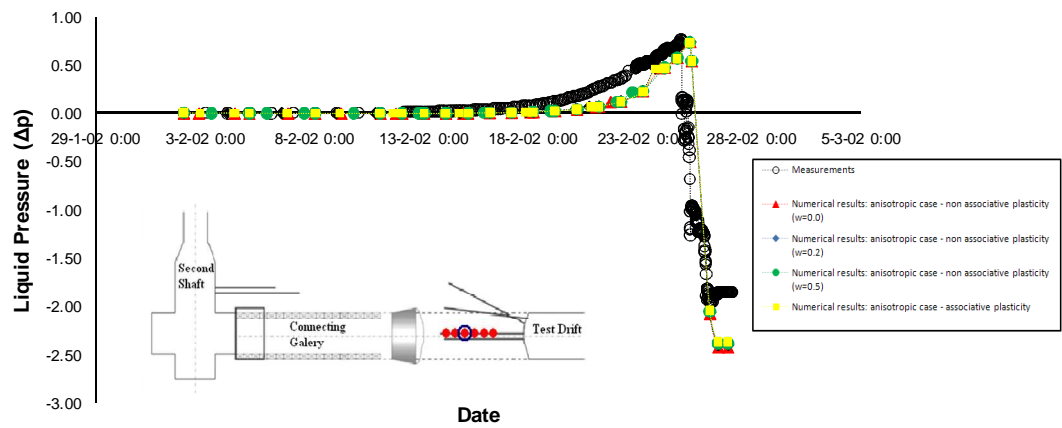


Figure 152: Computed pore pressure vs measurement at sensor A3 for the isotropic and full anisotropic model.



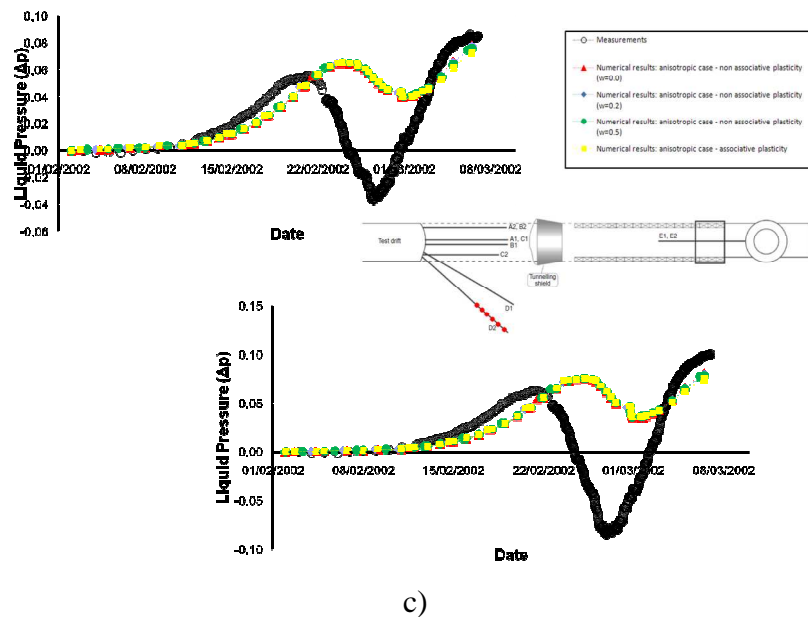


Figure 153: Computed pore pressure vs measurement at five sensors along borehole a) A, b) B and c) C for the full anisotropic model and three values of dilatancy

In Figure 153, pore pressures computed by the full anisotropic model are further compared with pore pressure measurements at sensors located on the sides of the excavation. Agreement is good for sensors close to the gallery wall (borehole B). For sensors farther in the rock (borehole C), the trend of evolution, characterized by a cycle of increase/decrease in pore pressure, is well reproduced but the magnitude of change in pore pressure is not totally captured.

Results of a sensitivity analysis on the value of dilatancy angle are also reported in the Figure 153. Whatever is the value of ψ ($\psi = 0$ – red symbols, 3.6° – in blue, 9° – in green, 18° – full dilatancy in yellow), the computed evolutions of pore pressure almost identical. This has been confirmed by comparison of pore pressure maps around the excavation at different times (not presented here). The dilatancy angle appears thus to have little influence on the hydraulic field around Clipex experiment.

A final analysis was performed to identify whether anisotropy in permeability, stress state or moduli control mainly the pore pressure field. As a representative example, comparison between computed pore pressures and measurements at sensor A4 is reported in Figure 154 for three models: the full anisotropic model, the model considering anisotropy only in elastic moduli and the model considering anisotropy in all variables (permeability, stress state) but in elastic moduli. The figure indicates that the peak in pore pressure ahead the front is controlled almost exclusively by the anisotropy in moduli.

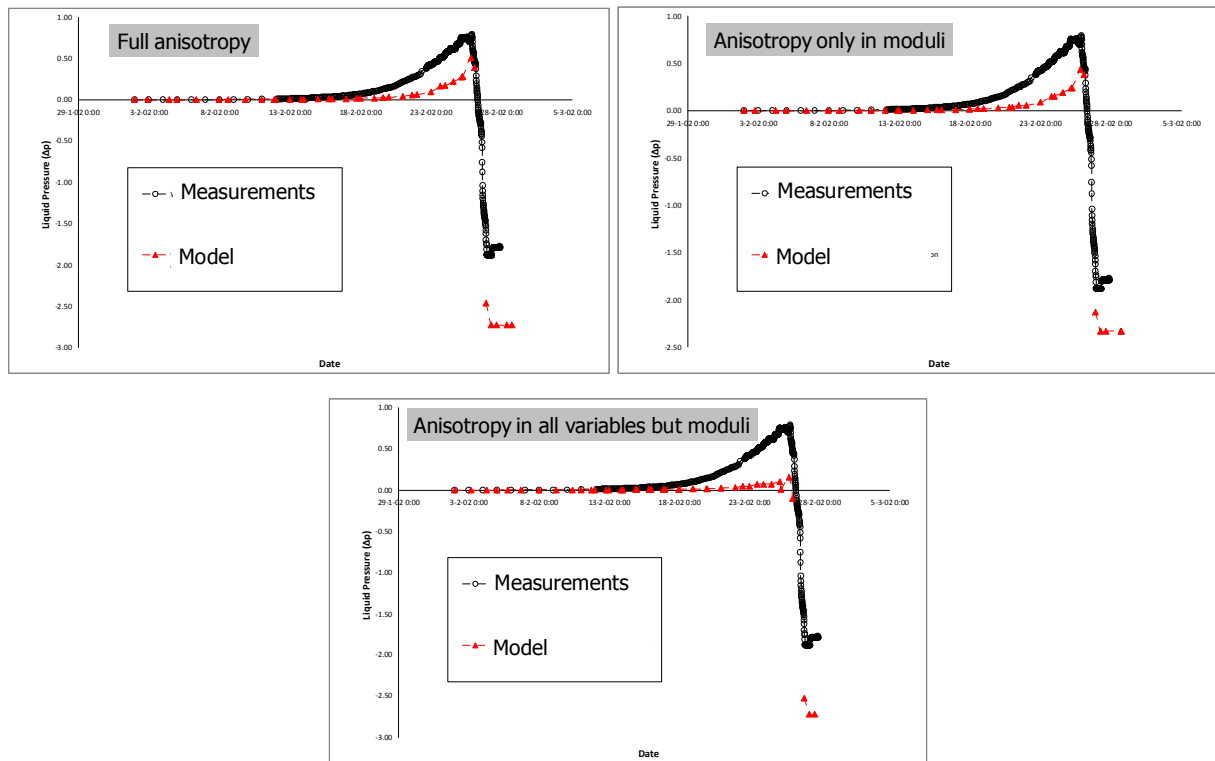


Figure 154: Computed pore pressure vs measurement at sensor A4 for a) the full anisotropic model b) model with anisotropy only in moduli and c) model with anisotropy in all variables but in moduli

Figure 155 shows a comparison between displacements computed by the full anisotropic model and measurements at sensors A1 and A4. Agreement is reasonable although the magnitude of displacement provided by the model appears to be lesser than the measured one. It is however difficult to put forward reasons for such a discrepancy because of the possible sliding of the extensometer chain during excavation (Bastiaens et al, 2003).

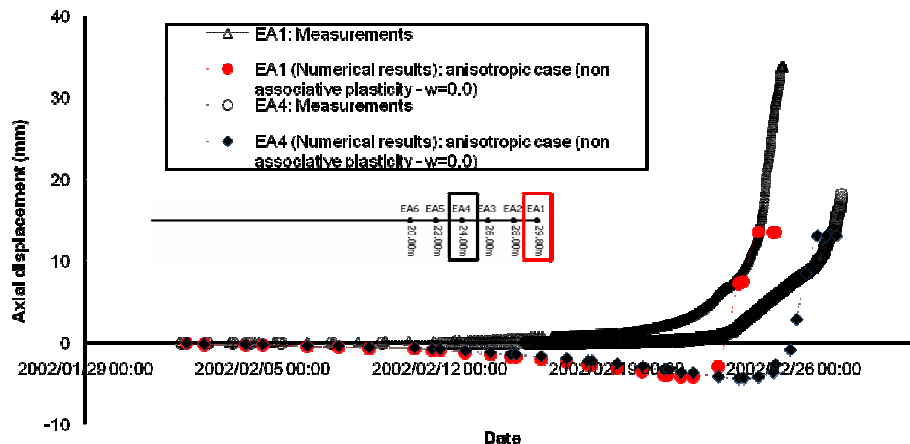


Figure 155: Comparison between displacement computed by the full anisotropic model and measurements at sensor A1 and A4

The comparisons with field measurements suggest that the model supply acceptable results, which provides a reasonable validation of the assumptions done and the values used for material properties. The full anisotropic model will now be used to assess the stress state in the Praclay zone at time of the excavation of Praclay gallery.

Figure 156 shows the profile of pore pressure along the centre axis of Praclay gallery previous to its excavation. It evidences an increase of pressure in a zone at a distance from the connecting gallery wall between 20 and 50m, that is around the second middle of Praclay heater. Magnitude of the increase reaches a maximum of 500 kPa (with respect to value of pore pressure in the far field) at 28m from the connecting gallery.

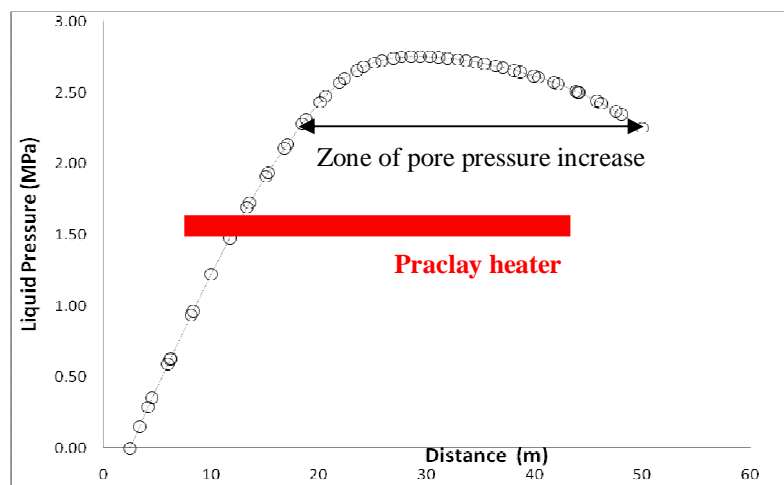


Figure 156: Profile of pore pressure along the centre axis of Praclay gallery previous to its excavation

Profiles of stresses are depicted in Figure 157 (directions of stresses are taken with respect to the axis of the connecting gallery). They evidence a mechanical perturbation due to the connecting gallery that extends up to approximately one fourth of Praclay heater.

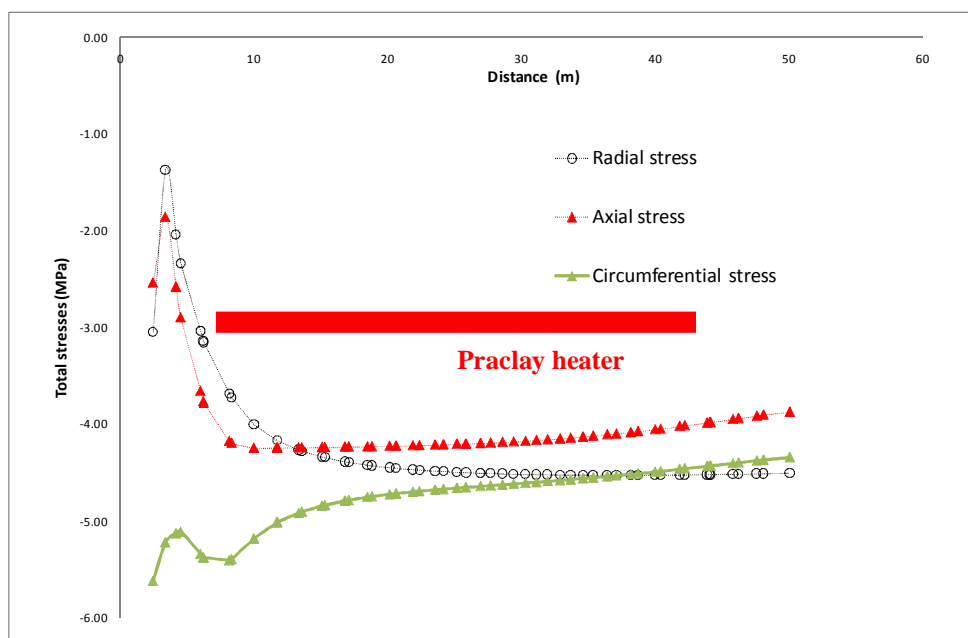


Figure 157: Profile of stresses along the centre axis of Praclay gallery previous to its excavation

6.4.2 Effect of anisotropy in the thermal field around PRACLAY experiment

A three dimensional analysis of Praclay experiment has been conducted considering anisotropy in permeability, stress state and thermal conductivity and moduli. Mesh and geometry are depicted in Figure 158. Boundary conditions are null displacement, water flow and heat flow at the outer boundaries. At the boundary of the heater, temperature and null water flow and null normal displacement are imposed.

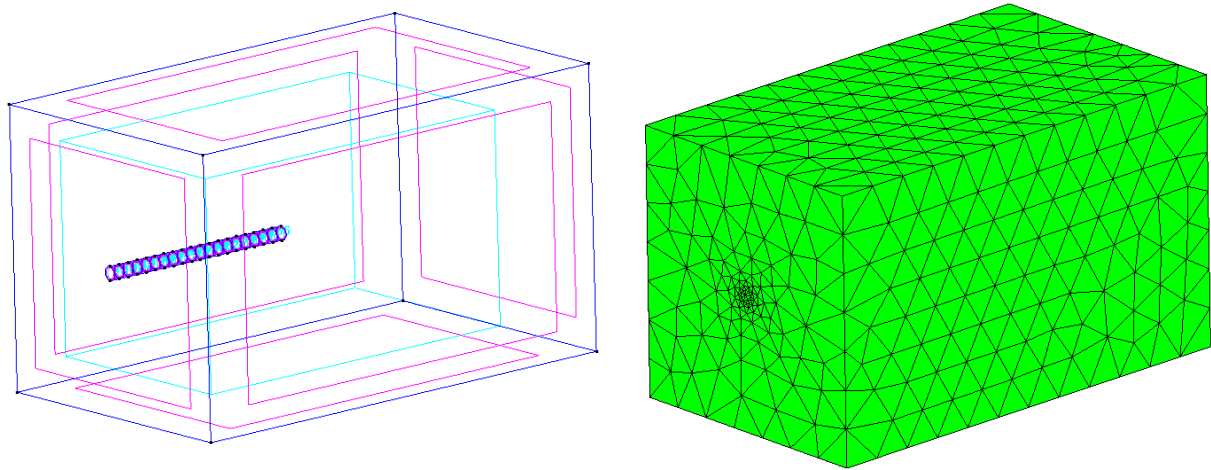


Figure 158: Geometry and mesh used in the 3D modelling of Praclay experiment

Properties of the material are those presented in Table 43. In addition, a thermal conductivity equal to 1.4 in the horizontal plane and 1 in the vertical direction is used. These values are taken from the analysis of Atlas experiment presented in Annex 3.

A map of the temperature field at 14 years is drawn in Figure 159. The anisotropic development of the thermal bulb can be observed. Loss of heat is less in the horizontal direction because of the greater thermal conductivity. Time evolution of temperature at three points insight the rock (along a horizontal axis orthogonal to heater at the middle of its length and at 0, 2.8 and 6.5 m from the contact between the heater and the host rock) is given on Figure 160.

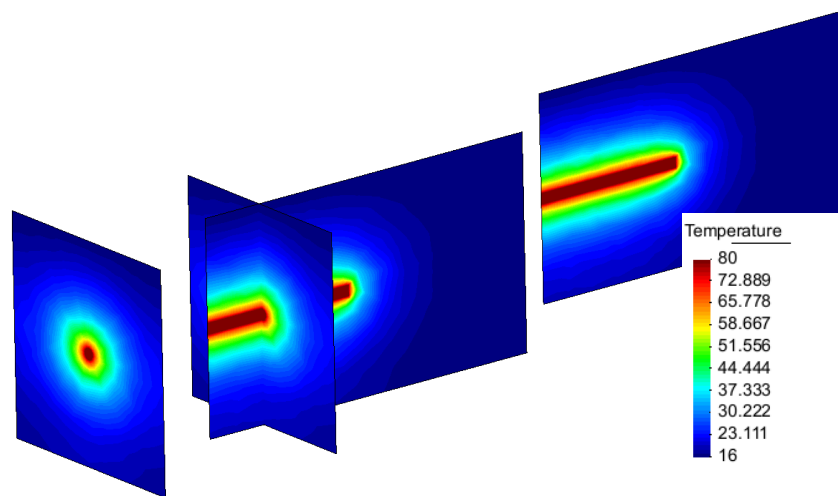


Figure 159: Thermal field at 14 years

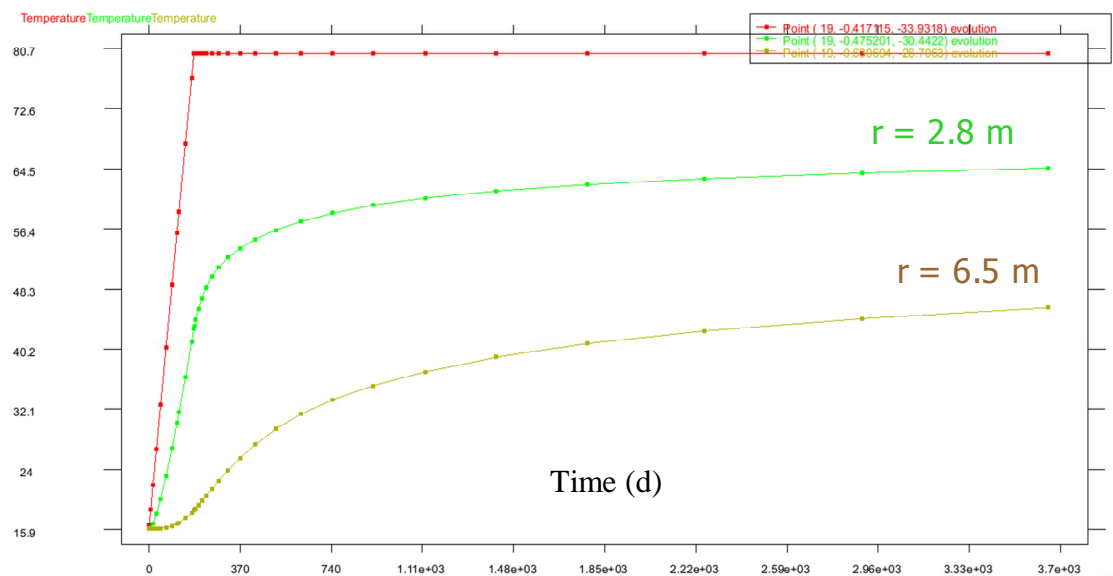


Figure 160: Evolution of temperature

The effect of temperature on the hydraulic field is illustrated in Figure 161 by the map of pore pressure at 4 years. Time evolution of water pressure is depicted in Figure 162 at 6 points inside the rock, 3 along the horizontal direction and 3 along the vertical direction. Due to the conjunction of anisotropy in the thermal, hydraulic and mechanical properties of Boom clay, pore pressure increase around the heater is heterogeneous. Highest pressures develop in the vertical directions. Along the horizontal plan, zone close to the heater experiments an increase in pore pressure while depression of water pressure can be observed farther in the rock.

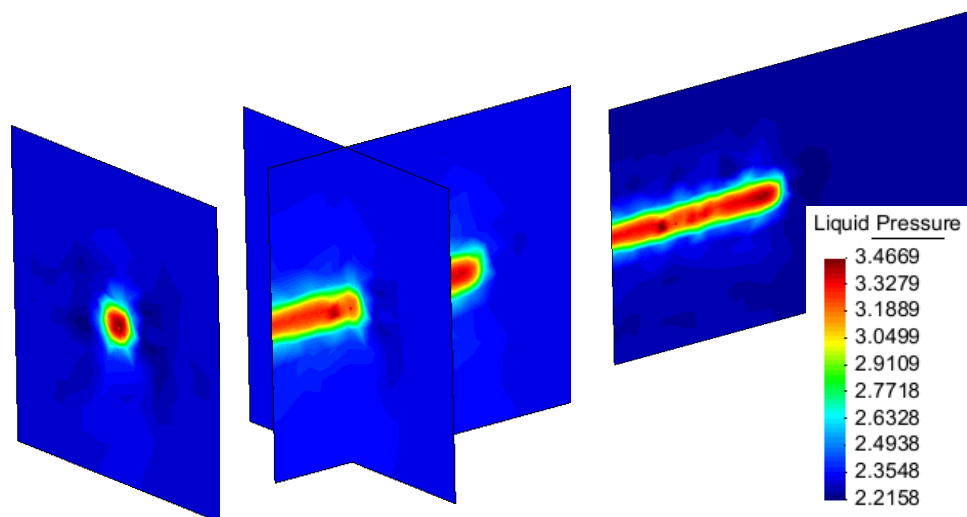
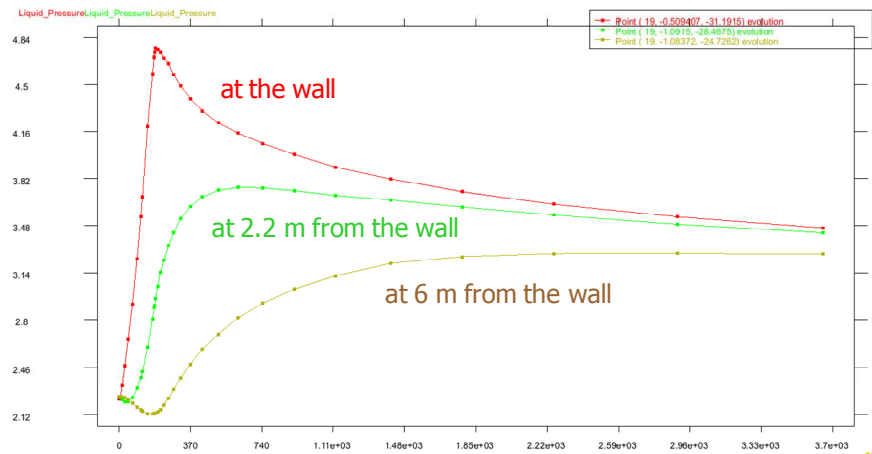
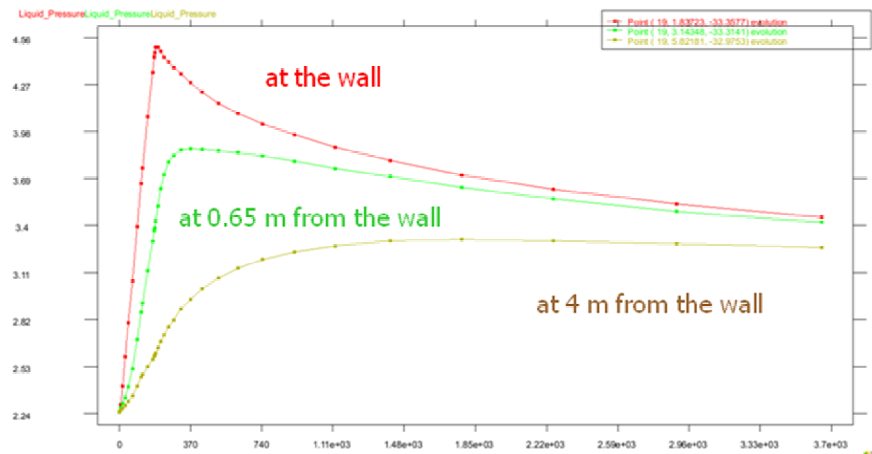


Figure 161: Three dimensional map of pore pressure at 4 years.

Figure 163 shows finally the development of the plastic zone at 14 years, resulting from the anisotropic thermo-hydro-mechanical response of the clay formation. It develops preferentially along the horizontal direction (asymmetry is an artefact of the computation that evidences the influence of boundary conditions – heating borehole is not centred in the mesh).



(a)



(b)

Figure 162: Time evolution of pore pressure at 6 points in a vertical section orthogonal to Praclay borehole at mid-length of the heater. a) points along the horizontal direction; b) points along the vertical direction

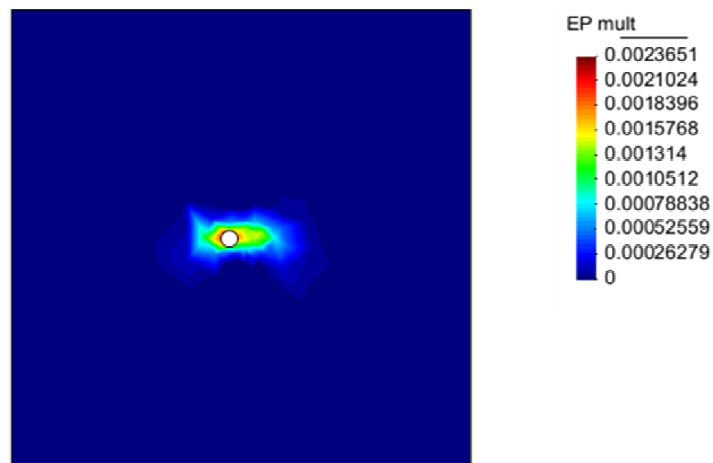


Figure 163: Development of the plastic zone around the heater at 14 years

7 References

- Bastiaens W., Bernier F., Buyens M., Demarche M., Li X.L., Linotte J.M. and Verstricht J., 2003. The Connecting Gallery – the extension of the HADES underground research facility at Mol, Belgium. EURIDICE report 03-294.
- Demarche, M. and Bel, J., 2003. The PRACLAY project: redefinition of the PRACLAY-experiment. NIROND note 2003-1397.
- François, B., Laloui, L. and Laurent, C. 2009. Thermo-hydro-mechanical simulation of ATLAS in situ large scale test in Boom Clay. Computers and Geotechnics. **36**, p. 626-640
- NIROND, 1997. The PRACLAY Demonstration Test. NIROND report 97-06.
- NIROND, 2003. EBS architecture for disposal of category B and C waste in Boom Clay. Progress report on activities between October 1st 2001 and December 31st 2002. NIROND report 2003-01.
- NIROND, 2004. Multicriteria analysis on the selection of a reference EBS design for vitrified high level waste. NIROND report 2004-03.
- Van Humbeek, H., Verstricht, J., Li, X.L., De Cannière, P., Bernier, F. and Kursten, B., 2009. The OPHELIE mock-up. EURIDICE report 09-134.
- Van Marcke, P., Li, X.L., Bastiaens, W. Verstricht, J., Chen, G., De Preter, P. The design and installation of the PRACLAY In-Situ Experiment (in progress).

